

# ***GDSA Repository Systems Analysis Investigations in FY2021***

## **Spent Fuel and Waste Disposition**

***Prepared for  
U.S. Department of Energy  
Spent Fuel and Waste Science Technology  
Tara LaForce, Eduardo Basurto, Kyung W. Chang,  
Richard Jayne, Rosie Leone, Michael Nole, Frank  
V. Perry, Emily Stein***

***Sandia National Laboratories***

***September 1, 2021  
M2SF-20SN010304062  
SAND2021-11691 R***



#### **DISCLAIMER**

This information was prepared as an account of work sponsored by an agency of the U.S. Government. Neither the U.S. Government nor any agency thereof, nor any of their employees, makes any warranty, expressed or implied, or assumes any legal liability or responsibility for the accuracy, completeness, or usefulness, of any information, apparatus, product, or process disclosed, or represents that its use would not infringe privately owned rights. References herein to any specific commercial product, process, or service by trade name, trade mark, manufacturer, or otherwise, does not necessarily constitute or imply its endorsement, recommendation, or favoring by the U.S. Government or any agency thereof. The views and opinions of authors expressed herein do not necessarily state or reflect those of the U.S. Government or any agency thereof.

#### **DISCLAIMER**

This is a technical report that does not take into account contractual limitations or obligations under the Standard Contract for Disposal of Spent Nuclear Fuel and/or High-Level Radioactive Waste (Standard Contract) (10 CFR Part 961). For example, under the provisions of the Standard Contract, spent nuclear fuel in multi-assembly canisters is not an acceptable waste form, absent a mutually agreed to contract amendment.

To the extent discussions or recommendations in this report conflict with the provisions of the Standard Contract, the Standard Contract governs the obligations of the parties, and this report in no manner supersedes, overrides, or amends the Standard Contract.

This report reflects technical work which could support future decision making by DOE. No inferences should be drawn from this report regarding future actions by DOE, which are limited both by the terms of the Standard Contract and Congressional appropriations for the Department to fulfill its obligations under the Nuclear Waste Policy Act including licensing and construction of a spent nuclear fuel repository.

Sandia National Laboratories is a multi-mission laboratory managed and operated by National Technology & Engineering Solutions of Sandia, LLC., a wholly owned subsidiary of Honeywell International, Inc., for the U.S. Department of Energy's National Nuclear Security Administration under contract DE-NA0003525.



**U.S. DEPARTMENT OF  
ENERGY**



**Sandia National Laboratories**



## APPENDIX E NFCSC DOCUMENT COVER SHEET<sup>1</sup>

Name/Title of Deliverable/Milestone/Revision No. GDSA Repository Systems Analysis Investigations in FY2021 / M2SF-20SN010304062

Work Package Title and Number GDSA - Repository Systems Analysis – SNL / SF-20SN01030406

Work Package WBS Number. 1.08.01.03.04

Responsible Work Package Manager Tara LaForce *Tara LaForce*

Date Submitted 9/1/2021

Quality Rigor Level for Deliverable/Milestone <sup>2</sup>	<input type="checkbox"/> QRL-1	<input type="checkbox"/> QRL-2	<input checked="" type="checkbox"/> QRL-3	<input type="checkbox"/> QRL-4
	<input type="checkbox"/> Nuclear Data			Lab QA Program <sup>3</sup>

This deliverable was prepared in accordance with Sandia National Laboratories  
(Participant/National Laboratory Name)

QA program which meets the requirements of

DOE Order 414.1       NQA-1       Other

**This Deliverable was subjected to:**

<input checked="" type="checkbox"/> Technical Review	<input type="checkbox"/> Peer Review
<b>Technical Review (TR)</b>	<b>Peer Review (PR)</b>
<b>Review Documentation Provided</b>	<b>Review Documentation Provided</b>
<input type="checkbox"/> Signed TR Report or,	<input type="checkbox"/> Signed PR Report or,
<input type="checkbox"/> Signed TR Concurrence Sheet or,	<input type="checkbox"/> Signed PR Concurrence Sheet
or,	
<input checked="" type="checkbox"/> Signature of TR Reviewer(s) below	<input type="checkbox"/> Signature of PR Reviewer(s)

below

**Name and Signature of Reviewers**

Richard Jayne *Richard Jayne*

Michael Nole *Michael Nole*

Alex Salazar *Alex Salazar III*

**NOTE 1:** Appendix E should be filled out and submitted with the deliverable. Or, if the PICS:NE system permits, completely enter all applicable information in the PICS:NE Deliverable Form. The requirement is to ensure that all applicable information is entered either in the PICS:NE system or by using the NFCSC Document Cover Sheet.

- In some cases there may be a milestone where an item is being fabricated, maintenance is being performed on a facility, or a document is being issued through a formal document control process where it specifically calls out a formal review of the document. In these cases, documentation (e.g., inspection report, maintenance request, work planning package documentation or the documented review of the issued document through the document control process) of the completion of the activity, along with the Document Cover Sheet, is sufficient to demonstrate achieving the milestone.

**NOTE 2:** If QRL 1, 2, or 3 is not assigned, then the QRL 4 box must be checked, and the work is understood to be performed using laboratory QA requirements. This includes any deliverable developed in conformance with the respective National Laboratory / Participant, DOE or NNSA-approved QA Program.

**NOTE 3:** If the lab has an NQA-1 program and the work to be conducted requires an NQA-1 program, then the QRL-1 box must be checked in the work Package and on the Appendix E cover sheet and the work must be performed in accordance with the Lab's NQA-1 program. The QRL-4 box should not be checked.

## **ACKNOWLEDGEMENTS**

This work was supported by the US Department of Energy (DOE) Office of Nuclear Energy, through the Office of Spent Fuel and Waste Science and Technology (SFWST), within the Office of Spent Fuel and Waste Disposition (DOE NE-8).

Thanks go to our DOE customer for their support of this work. Thank you to David Sevougian (retired) for leading the Repository Systems Analysis team until 2020. Thank you to Terry Miller and Phil Stauffer at Los Alamos National Laboratory for ongoing technical support for LaGrit and for providing the Rock Springs Uplift geological model, and to LianGe Zheng and Jonny Rutqvist of Lawrence Berkeley National Laboratory for input to the shale geomechanical analysis. Thanks to Lindsay McCabe, our OAA for assistance with formatting and referencing this report. Finally, thanks to our technical reviewers, Michael Nole (Section 1, 2, 3.2, 4 and 5), Rick Jayne (Section 6), and Alex Salazar (Section 3.1), for comments and suggestions that improved the report.

This report incorporates principal contributions from the following coauthors:

Eduardo Basurto (Section 5)

Kyung Chang (Section 3)

Tara LaForce (Section 1, 2.2.9, 3.2.1, and 6)

Rosie Leone (Section 2.1)

Richard Jayne (Section 2.2)

Michael Nole (Section 3.1)

Frank Perry (Section 4)

Emily Stein (Section 2)

## EXECUTIVE SUMMARY

The Spent Fuel and Waste Science and Technology (SFWST) Campaign of the U.S. Department of Energy Office of Nuclear Energy, Office of Spent Fuel and Waste Disposition (SFWD), has been conducting research and development on generic deep geologic disposal systems (i.e., geologic repositories). This report describes specific activities in the Fiscal Year (FY) 2021 associated with the Geologic Disposal Safety Assessment (GDSA) Repository Systems Analysis (RSA) work package within the SFWST Campaign. The overall objective of the GDSA RSA work package is to develop generic deep geologic repository concepts and system performance assessment (PA) models in several host-rock environments, and to simulate and analyze these generic repository concepts and models using the GDSA Framework toolkit, and other tools as needed.

A summary of the specific objectives in FY2021 is to:

- Develop the technical bases for representing generic repository reference case concepts in GDSA Framework simulations for deep geologic disposal in any of four possible host-rock environments: argillite, crystalline, bedded salt, and unsaturated zone formations.
- Ensure that generic repository concepts include potential disposal of large, high-decay-heat waste packages.
- Incorporate relevant near field and far field processes as well as geologic/material properties and stratigraphic information developed in conjunction with geologic framework models (GFM)s).
- Perform GDSA Framework performance assessment (PA) simulations and, in collaboration with the GDSA Uncertainty and Sensitivity Analysis Methods work package, associated uncertainty and sensitivity analyses for generic repository reference case concepts containing high-decay-heat waste packages.
- Include, as needed, detailed coupled processes in the EBS (engineered barrier system), (e.g., waste form and waste package degradation, EBS flow and transport, disturbed rock zone (DRZ) evolution) and natural system (e.g., near-field and far-field flow and transport, multi-phase flow).
- Reference case development, simulation, and analysis, as appropriate, for international collaborations, including for example, DECOVALEX, the Integration Group for the Safety Case (IGSC) sensitivity analysis task group, and the long-standing US-German collaboration on PA methodology applied to generic repositories in salt.

Section 1 of this report is a brief introduction. Section 2 discusses progress to date on the international Development of COupled models and their VALidation against Experiments (DECOVALEX) 2023 Task F performance assessment comparison, which is being led by the GDSA team on behalf of the US DOE's SFWST Campaign. Section 3 describes two small-scale reference case studies: the first is a continuation of the damage zone evolution study and the second is a near-DPC thermal study on unstructured meshes. Section 4 develops a shallow-geosphere model for the crystalline environment. Section 5 discusses deterministic simulations of a PA-scale model for the unsaturated alluvium reference case. Finally, Section 6 documents the continuing investigation into PFLOTRAN simulations on Voronoi meshes, including four benchmark cases and a complex model of subsurface flow.

## Contents

Acknowledgements .....	iv
Executive Summary.....	vi
Nomenclature.....	xvii
1. Introduction.....	1
1.1 References .....	5
2. DECOVALEX REFERENCE CASES .....	7
2.1 Crystalline reference case.....	7
2.1.1 Benchmark Cases .....	8
2.1.2 Proposed Conceptual Model.....	20
2.2 Salt reference case .....	20
2.2.1 Geologic Setting .....	21
2.2.2 Inventory.....	22
2.2.3 Engineered Barrier System.....	27
2.2.4 Natural Barrier System .....	37
2.2.5 Geochemical Environment.....	39
2.2.6 Containment Rock Zone.....	42
2.2.7 Initial Conditions .....	43
2.2.8 Outputs for Comparison .....	44
2.2.9 Analytical benchmark for overburden transport.....	45
2.3 References .....	50
3. Small-scale reference case studies .....	54
3.1 Buffer and DRZ evolution.....	54
3.1.1 Model setting.....	54
3.1.2 THC coupling integrated with stress-dependent permeability .....	58
3.1.3 Effects of shale permeability .....	61
3.1.4 Geomechanical analysis .....	62
3.1.5 Near-field multiphysics mechanism.....	66
3.1.6 Future study .....	67
3.2 Thermal DPC studies.....	67
3.2.1 VoroCrust mesh generation.....	67
3.2.2 Modeling results .....	69
3.2.3 Future study.....	70
3.3 References .....	70
4. Conceptual model of the Shallow Geosphere in a Crystalline Rock Environment .....	72
4.1 Introduction .....	72
4.2 Crystalline Rock Environments in the US.....	72
4.3 Representative Region for Identifying Features in the Conceptual Model of the Shallow Geosphere .....	75
4.4 Regional Geology and Hydrology.....	77
4.4.1 Geology .....	77

4.4.2	Hydrology .....	77
4.5	Data to Support the Crystalline Conceptual Model.....	78
4.5.1	Topography and Surficial Geology .....	78
4.5.2	Characteristics of Crystalline Rocks .....	82
4.5.3	Characteristics of Surficial Deposits .....	85
4.6	Comparison between the Shallow Crystalline Environment in the US and Forsmark, Sweden.....	88
4.6.1	Glacial Deposits.....	88
4.6.2	Shallow Horizontal Fractures .....	90
4.7	Conceptual Model of the Stratigraphy and Hydrology of the Shallow Geosphere .....	90
4.8	Conclusions .....	92
4.9	References .....	93
5.	Unsaturated Alluvium .....	97
5.1	Model Setting .....	97
5.2	Simulation.....	99
5.2.1	New PFLOTRAN Solver and Options .....	101
5.2.2	Initial Conditions .....	103
5.2.3	Boundary Conditions.....	104
5.2.4	Material Properties .....	104
5.3	Simulation Results and Discussion.....	104
5.4	Conclusions and Considerations for Future Work .....	111
5.5	References .....	112
6.	Investigation into simulations on Voronoi meshes .....	113
6.1	FY 2021 Improvements to VoroCrust.....	113
6.2	Four Test Cases Revisited .....	113
6.2.1	Meshing .....	114
6.2.2	Test case simulations.....	116
6.2.3	Error analysis.....	123
6.3	Wyoming uplift simulation.....	130
6.3.1	Meshing .....	130
6.4	Conclusions and Future Work .....	138
6.4.1	Future PFLOTRAN/VoroCrust integration studies.....	138
6.4.2	Future VoroCrust development .....	138
6.5	References .....	139

## FIGURES

	Page
Figure 1-1. Information flow and the role of performance assessment for RD&D prioritization during a single stage of repository development. (Taken from Sevougian et al. 2019b) .....	3
Figure 1-2. Schematic the GDSA Framework. The RSA work packages focuses primarily on flow and transport modelling, but also works closely with VoroCrust, dfnWorks and Dakota for processing and computational support. (Mariner et al. 2020).....	4
Figure 2-1. Fracture-Matrix system from (Tang et al. 1981), z represents distance along the fracture and x represents distance into the matrix.....	8
Figure 2-2. Concentrations in the fracture (above) and in the matrix 2 m into the fracture (below) for low velocity case (0.01 m/d) .....	11
Figure 2-3. Concentrations in the fracture (above) and in the matrix 2 m into the fracture (below) for fast velocity case (0.1 m/d).....	12
Figure 2-4. Steady state flow field for 4-Fracture DFN .....	13
Figure 2-5. Left: Upscaled permeability for uniform ECPM mesh. Matrix cells are inactive and not shown. Right: Upscaled permeability for octree ECPM mesh. ....	15
Figure 2-6. (A) Uniform ECPM liquid pressure solution. Matrix cells are inactive and not shown. (B) Octree ECPM liquid pressure solution. ....	15
Figure 2-7. Breakthrough curves from teams participating in Crystalline Task F for 4-Fracture DFN.....	16
Figure 2-8. E-W stochastic fractures (1), N-S stochastic fractures (2), subhorizontal fractures (3), and deterministic fractures (4). ....	17
Figure 2-9. Steady state flow field for 4-Fracture DFN with stochastic fractures. ....	18
Figure 2-10. Breakthrough curves for DFN (solid line) and ECPM (dashed line). ....	19
Figure 2-11. Breakthrough curve comparison of 4-Fracture DFN and 4-Fracture DFN with stochastic fractures with a conservative tracer.....	20
Figure 2-12. Geological cross-section with model units for the generic salt reference case. The model units are simplified from Bertrams et al. (2020b).....	22
Figure 2-13. Heat vs. time for POLLUX-10 after 100 yr OoR; plotted using values in Table 2-4.....	25
Figure 2-14. Heat vs. time for a single HLW canister aged 130 y; plotted using values in Table 2-6.....	26
Figure 2-15. Schematic of the waste repository in a generic salt dome. ....	28
Figure 2-16. Schematic of the POLLUX-10 waste container. 1. Shielding body; 2. Shielding cover; 3. Inner tank; 4. Primary cover; 5. Secondary (welded) cover; 6. Welding seam; 7. Damping element; 8. Moderator plate (graphite); 9. Moderator staff; 10. Bushings with fuel rods; 11. Trunnion; 12. Guide plate (from Bertrams et al. 2020a). ....	31
Figure 2-17. Stainless steel canister for vitrified HLW.....	32
Figure 2-18. Canister dimensions for vitrified HLW. ....	33

Figure 2-19. Dimensions for vertical borehole emplacement for vitrified HLW canisters.....	34
Figure 2-20. Shaft seal for generic salt dome repository (GRS 415). .....	36
Figure 2-21. Schematic for initial conditions at $t = 0s$ after waste package emplacement. The orientation and design of the repository and geologic cross section were chosen to provide a symmetry boundary that modelers can choose to leverage to reduce the computational resources required for the presented scenario. ....	44
Figure 2-22. Schematic of chemical diffusion and transport from a planar source in a uniform flow field. Taken from Batu (2006.) .....	46
Figure 2-23. Tracer distribution for proposed DECOVALEX salt analytical benchmark problem after 250 years. Top Left: solution without retardation or decay in the tracer source. Top Right: solution with retardation factor $R_d = 3.165 \text{ m}^3/\text{kg}$ , representative of Cs(I) retardation and no decay in the tracer source. Bottom: Solution without retardation and with time-dependent tracer source $\gamma = -0.05$ .....	49
Figure 2-24. Simulated tracer distribution for DECOVALEX salt analytical benchmark problem after 250 years without retardation or decay in the tracer source. Left: Simulation on a 720,000 grid-cell cubic structured mesh. Right: Simulation on a 1,031,736 grid-cell unstructured Voronoi mesh. Rectangular outline indicates the extent of the domain where the analytical solution is calculated on Figure 2-23.....	50
Figure 3-1. (A) Schematic description of the model domain consisting of waste package (wp), buffer/spacer, disturbed rock zone (DRZ), and shale host rock. (B) Numerical domain of 15 m (width in x-axis) $\times$ 12.5 m (length in y-axis) $\times$ 75 m (height in z-axis) with unstructured grids to model a quarter of the cylindrical repository centered at depth of 500 m. ....	55
Figure 3-2. Stress-dependent permeability functions: exponential (green line), cubic-law (orange line), and Two-part Hooke's Law Model (TPHM; blue region). The constant DRZ permeability is indicated by a black solid line. For the TPHM function, the larger soft-part fraction increases permeability in general. ....	58
Figure 3-3. Evolution of liquid saturation (solid lines) within the buffer and corresponding changes in swelling stress (dashed lines) acting on the DRZ for three permeability functions: (1) Exponential function (Exp; green), (2) Modified cubic function (Cubic; orange), and two-part Hooke's law model (TPHM; blue). Black line shows the reference case with a constant DRZ permeability and is very similar to Exp result.....	59
Figure 3-4. Evolution of physical quantities at the DRZ cell nearest the buffer for three cases with different stress-dependent permeability functions: (A) gas pressure, (B) gas saturation, (C) liquid pressure, (D) liquid saturation and swelling stress, (E) temperature, and (F) permeability. The host rock permeability is indicated by a black dash line in Figure F. ....	60
Figure 3-5. Sensitivity tests on shale host rock permeability: reference case ( $1 \times 10^{-19} \text{ m}^2$ ; left column) and less permeable shale ( $1 \times 10^{-21} \text{ m}^2$ ; right column). Temporal evolution of DRZ permeability (A–B), Cl <sup>-</sup> concentration and liquid saturation within buffer (C–D) and DRZ (E–F), respectively. ....	62
Figure 3-6. Schematic description of swelling-induced stresses acting on the repository system in all directions. The color of wp, engineered barrier, and DRZ follows the model domain shown in Figure 3-1B.....	63

Figure 3-7. Geomechanical analysis of the DRZ stability: (A, C) schematic description of shear and tensile failure under the normal and reverse faulting stress states, respectively, and (B, D) lower and upper limits of  $\sigma_{swell}$  to prevent shear and tensile failure at given repository conditions and stress states; swelling stress staying between limits means that buffer swelling stabilizes the DRZ over time. .... 64

Figure 3-8. Voronoi mesh for unsaturated alluvium DPC thermal study. Left: surface mesh on  $x=10m$  plane for the entire length of the model. Top Right: surface mesh on  $x = 10$  m plane near the DPC. Bottom Right: isometric view of the surface mesh near the DPC. .... 68

Figure 3-9. Results of gas pressure (A, B) and gas saturation (C, D) from PFLOTRAN models using unstructured grids and Voronoi meshes at  $t = 100$  years. .... 70

Figure 4-1. Distribution of exposed or near-surface crystalline rocks (red) in the conterminous US from Perry et al. (2014). Crystalline rock occurrences are classified by smoothed local slope using a 3 km grid, illustrating that crystalline rocks in the eastern half of the US occur more frequently in areas of low topographic relief (slope  $<1$  degree). The limit of Wisconsin glaciation is the southern extent of the most recent North American ice sheet. .... 73

Figure 4-2. Distribution of Paleozoic granitic plutons in Maine and boundaries of reference areas that include the Sebago Lake Pluton (southwestern Maine) and Passadumkeag River Pluton (southeastern Maine). Granitic plutons intrude several northeast trending metamorphic terranes. .... 76

Figure 4-3. Topography and surface features of the Sebago Lake Pluton reference area. Blue features are lakes and streams. .... 79

Figure 4-4. Surficial geology of the Sebago Lake Pluton reference area. .... 80

Figure 4-5. Topography and surface features of the Passadumkeag River Pluton reference area. Blue features are lakes and streams. Cross-hatched green areas are wetlands. .... 81

Figure 4-6. Surficial geology of the Passadumkeag River Pluton reference area. .... 82

Figure 4-7. Examples of horizontal fractures in crystalline rocks of southern Maine. Left: Groundwater flow (icicles) from a horizontal fracture exposed in a roadcut near Falmouth, Maine (MGS 2012). Right: horizontal fractures exposed in a quarry face in the Vinalhaven Pluton, Hurricane Island, Maine (Lemmond 2016). .... 84

Figure 4-8. Horizontal fractures and lenticular sheet structure in granite in quarry near Sullivan, Maine (Dale 1907). The sheets vary in thickness from 1-3 meters, except near tapered ends. .... 84

Figure 4-9. Exposures of unsorted till deposits in southern Maine (Thompson 2015). .... 85

Figure 4-10. Exposures of glacial outwash sand and gravel deposits in southern Maine (Thompson 2015) ..... 86

Figure 4-11. Distribution of sand and gravel aquifers in Maine. .... 87

Figure 4-12. Exposure of the Presumpscot Formation (Marine silt and clay) in southern Maine (Thompson 2015). .... 88

Figure 4-13. East-west cross-section of surficial deposits and bedrock in a coastal area to the southeast of the Sebago Lake Pluton. From Nielsen and Locke (2012).....	91
Figure 4-14. Conceptual model of stratigraphy and fracture systems of the shallow geosphere. Vertical scale is highly exaggerated.....	92
Figure 5-1. A schematic showing a potential unsaturated zone geologic repository. Figure 5-2 of Mariner et al. (2018). A possible location for a repository would be in the playa deposits, which are impermeable fine-grained sediments and are located towards the center of this schematic. Also notice the lithologic heterogeneity depicted here that is expected in basin-fill valleys where alluvial fans, fluvial systems, spring discharge areas, and playas are common features.....	98
Figure 5-2. Schematic cross section of the unsaturated zone model (Mariner et al., 2018). UZ = unsaturated zone; SZ = saturated zone.....	99
Figure 5-3. Configuration of the repository and natural barrier system that was generated using Cubit, simulated in PFLOTRAN and visualized on ParaView. Turquoise color (material ID 3) represents the upper basin fill confining (ubf_conf) units (the centermost contains the repository as seen there), green (material ID 4) represents UBF, dark blue (material ID 2) represents the UBF aquifer, and blue (material ID 1) represents LBF. Distances along the axes are in meters, where 1000 m is land surface and 0 m is the bottom of the model domain. The left side of the figure represents a western direction. ....	100
Figure 5-4. XY slice through the repository colored by material ID. The repository is assumed to be 250 meters below the surface. The zoom in box on the top left shows a close-up of four waste packages (WPs), colored in red, buffer in yellow, DRZ in burgundy, and ubf_conf in turquoise. Visualized using ParaView.....	101
Figure 5-5. Text from the PFLOTRAN input deck used to set up the final simulations. Bold text represents the keywords used for the new solver and characteristic curve smoothing options. Lighter text is included to show where these keywords are located within the input deck. ....	103
Figure 5-6. XY slice through the repository colored by temperature (°C) at years 0.5, 10, and 300 for the 10 mm/yr. infiltration rate simulation. Temperature range has been scaled over all timesteps. ....	106
Figure 5-7. XY slice through the repository colored by gas pressure (Pa) at years 0.5, 10, and 300 for the 10 mm/yr. infiltration rate simulation. Pressure range has been scaled over all timesteps. ....	107
Figure 5-8. XY slice through the repository colored by liquid saturation at years 0.5, 10, and 300 for the 10 mm/yr. infiltration rate simulation. Saturation range has been rescaled over all timesteps. ....	108
Figure 5-9. Temperature, gas saturation, gas pressure and liquid saturation history plots at observation point “Fwp_inside” for the two final PFLOTRAN simulations.....	109
Figure 5-10. Zoomed XZ slice showing equilibrated gas saturation through the center of the half-symmetry repository showing grid orientation effects. ....	111

Figure 6-1. Stratigraphy for all four Test Case volumes. Top Left: Test case 1 with 4 horizontal layers. Top Right: Test Case 2 with a pinch-out. Bottom Left: Test Case 3 with an interior lens. Bottom Right: Test Case 4 with layering and an offset fault..... 114

Figure 6-2. Test structure 1 layered example. Left: Surface mesh. Right: Interior mesh on a slice on the plane  $y=10$ . Permeabilities shown are for Test Case 1.2. .... 115

Figure 6-3. Test structure 2 pinch out example. Left: Surface mesh. Right: Interior mesh on a slice on the plane  $y=10$ . Permeabilities shown are for Test Case 2.2. .... 115

Figure 6-4. Test structure 3 interior lens example. Left: Surface mesh. Right: Interior mesh on a slice on the plane  $y=10$ . Permeabilities shown are for Test Case 3.2. .... 116

Figure 6-5. Test structure 4 offset fault example. Left: Surface mesh. Right: Interior mesh on a slice on the plane  $x=10$ . Permeabilities shown are for Test Case 4.2. .... 116

Figure 6-6. Steady-state pressure for Test Case 1.2 (top left), 2.2 (top right), 3.2 (bottom left) and 4.2 (bottom right). Test Cases 1-3 are shown on the XZ plane on a slice through the plane  $y=10$ , while solution for Test Case 4 is shown on the YZ plane on a slice through the plane  $x=10$ . .... 119

Figure 6-7. Steady-state liquid pressure for Test Case 1.3 (top left), 2.3 (top right), 3.3 (bottom left) and 4.3 (bottom right). Test Cases 1-3 are shown on the XZ plane on a slice through the plane  $y=10$ , while solution for Test Case 4 is shown on the YZ plane on a slice through the plane  $x=10$ . .... 120

Figure 6-8. Steady-state liquid saturation for Test Case 1.3 (top left), 2.3 (top right), 3.3 (bottom left) and 4.3 (bottom right). Test Cases 1-3 are shown on the XZ plane on a slice through the plane  $y=10$ , while solution for Test Case 4 is shown on the YZ plane on a slice through the plane  $x=10$ . .... 121

Figure 6-9. Steady-state liquid pressure for Test Case 1.4 (top left), 2.4 (top right), 3.4 (bottom left) and 4.4 (bottom right). Test Cases 1-3 are shown on the XZ plane on a slice through the plane  $y=10$ , while solution for Test Case 4 is shown on the YZ plane on a slice through the plane  $x=10$ . .... 122

Figure 6-10. Steady-state liquid saturation for Test Case 1.4 (top left), 2.4 (top right), 3.4 (bottom left) and 4.4 (bottom right). Test Cases 1-3 are shown on the XZ plane on a slice through the plane  $y=10$ , while solution for Test Case 4 is shown on the YZ plane on a slice through the plane  $x=10$ . .... 123

Figure 6-11. Liquid pressure and saturation profiles for equivalent monitoring points vs log of time for heterogeneous two-phase Test Case 4.4..... 125

Figure 6-12. Side view of the equilibrated saturation (top) and pressure (bottom) distribution near the monitoring points (10,10,-7.5) and (1,10,-7.5) for heterogeneous two-phase Test Case 4.4. Very small scales have been chosen in the colorbars to emphasize the difference in quantities between the two points. .... 126

Figure 6-13. Side view of the equilibrated pressure and saturation distribution for heterogeneous two-phase Test Case 2.4 on a slice through  $y=10$  m. Top: simulated result on the coarse mesh. Middle: simulated result on the intermediate mesh. Bottom: simulated result on the fine mesh. .... 128

Figure 6-14. Side view on a slice along the plane  $x=15$  m of the equilibrated pressure (left) and saturation (right) distribution near the monitoring point (15, 10 ,-8) for heterogeneous two-phase Test Case 2.4. The range  $z = (-7.5,-10)$  m and  $y = (8,18)$

m is shown. The green circle indicates the centroid of the monitoring point cell. Top: simulated result on the coarse mesh. Middle: simulated result on the intermediate mesh. Bottom: simulated result on the fine mesh. Very small temperature and pressure ranges have been chosen to emphasize differences between the simulated result in this area. .... 129

Figure 6-15. Geological surfaces for the Rock Springs uplift from geological mapping software..... 131

Figure 6-16. Top: Clipped region containing only the Phosphoria top, Weber top, and Madison top surfaces integrated into a water-tight volume with a flat base. Middle: Surface mesh of the reservoir. Bottom: Reservoir layers colored by material type. The Phosphoria caprock is shown in gray, Weber sandstone injection interval is blue and crystalline basement is red. .... 131

Figure 6-17. Top: isometric view of the Weber sandstone in the full simulation model. Bottom Left: Top mesh for the full Weber sandstone layer. Bottom Right: Top mesh for the Weber sandstone layer near the injection wells showing finely refined region gradually coarsening away from the wells. Injection wells are shown as red circles on all subfigures. .... 133

Figure 6-18. Slice through two of the injection wells at y=8500m showing the refined mesh near the wells. The Phosphoria caprock is shown in gray, Weber sandstone injection interval is blue and crystalline basement is red. Injection well locations are shown as red circles..... 134

Figure 6-19. Isometric view of the liquid saturation in the Weber sandstone after 10 years of injection. Only the Weber formation is shown and slice is at y=8500m. Green circles mark two of the well locations, which are 1 km apart..... 136

Figure 6-20. Top view of the liquid saturation at the top of the Weber Sandstone. Green circles mark well locations. Top: 2.5 years of CO<sub>2</sub> injection. Middle: 10 years. Bottom: 100 years. .... 137

## TABLES

	<b>Page</b>
Table 2-1. Parameters for Fracture Transport with Matrix Diffusion .....	10
Table 2-2. Parameters for Transport in a 4-Fracture DFN. ....	14
Table 2-3. Inventory of selected radionuclides in PWR SNF at 100 y OoR. ....	23
Table 2-4. Heat output per POLLUX-10 cask as function of time. ....	24
Table 2-5. Inventory of selected radionuclides in HLW aged 130y. ....	26
Table 2-6. Heat output per HLW canister as function of time. ....	27
Table 2-7. Dimensions for components of repository layout. ....	29
Table 2-8. Instant release fractions from Johnson et al. (2005) cited in Sassani et al. (2016). ....	29
Table 2-9. SNF dissolution rates; log triangular distribution from Werme et al. (2004) cited in Sassani et al. (2016, Section 3.2.1). ....	30
Table 2-10. Material properties for use in initial flow and transport simulations. ....	37
Table 2-11. Hydraulic, thermal, and mechanical parameters for geologic units. ....	38
Table 2-12. Relative permeability parameters for salt, crushed salt, and shaft seal. Additional materials will be added as needed. ....	39
Table 2-13. Element solubility calculated at T = 25° C in concentrated brine (Wang and Lee 2010 as cited in Clayton et al. 2011). ....	40
Table 2-14. Anhydrite $K_{ds}$ compiled by Clayton et al. (2011). ....	41
Table 2-15. $K_{ds}$ for basin fill and overburden (from Baeyens et al. 2014). ....	42
Table 2-16. $K_{ds}$ for the bentonite component of the shaft seal (from Baeyens et al. 2014). ....	42
Table 2-17. Hydraulic, thermal, and mechanical parameters for DECOVALEX Task F salt analytical benchmark. ....	48
Table 3-1. Material properties .....	56
Table 3-2. Parameter values for different permeability functions. ....	57
Table 4-1. Crystalline Regions in the US after Mariner et al. (2011). ....	74
Table 4-2. Comparison of permeability estimates for glacial deposits. Values are for horizontal permeability. ....	89
Table 4-3. Representative values of properties included in the conceptual model. ....	92
Table 5-1. Parameter values used in final simulations (Modified from Sevougian et al. 2019a, Table 4-7). Modifications include backfill unsaturated thermal conductivity is now set to 1.0 (previously set to 2.0) and included a row of values for the upper basin fill DRZ. ....	104
Table 5-2. Results for the final PFLOTRAN simulations at observation point “Fwp_inside”. ....	110
Table 6-1. Parameters for the 16 simulations on four test structures (after Gross et al. (2019)). RICHARDS mode is single-phase isothermal flow. GENERAL mode is full two- phase flow with thermal capability. All GENERAL mode simulations in the	

---

present work are isothermal with temperature $T=20^{\circ}\text{C}$ . Variable permeability properties and their distribution are given in Tables 6-2 and 6-3 and 6-4. ....	117
Table 6-2. Permeability for Test Case 1.2, 2.2, 3.2 and 4.2. Porosity is 0.1 for all materials. Permeabilities are also shown in Figures 6-2 to 6-5. ....	118
Table 6-3. Santa Fe and Otowi rock properties and two-phase flow parameters (after Gross et al. (2019)). ....	120
Table 6-4. Permeability for Test Case 1.4, 2.4, 3.4 and 4.4. Properties are given in Table 6-3. ....	122
Table 6-5. Monitoring point locations for Test Cases 1.1-4.4. All points with the same ID are expected to have the same solution due to symmetry of the problem. ....	124
Table 6-6. Difference in Test Case 2.4 solutions at monitoring points in meshes with different resolution. The monitoring point used as benchmark are those with N/A. (-) indicates that the monitoring point is not in the mesh. ....	127
Table 6-7. Monitoring point locations for ten realizations of Test Case 3.4. Minimum and maximum pressure difference from the base case are shown, along with the mesh that had the largest or smallest difference. ....	130
Table 6-8. Rock parameters for the Rock Springs Uplift example. ....	135
Table 6-9. Fluid flow parameters for the Rock Springs Uplift example. ....	135

## NOMENCLATURE

1D, 2D, 3D	one-, two-, and three-dimensional
CPU	central processing unit
DECOVALEX	Development of COupled models and their VALidation against Experiments
DFN	discrete fracture network
DOE	U.S. Department of Energy
DRZ	disturbed rock zone
EBS	engineered barrier system
ECPM	equivalent continuous porous medium
EDZ	excavation disturbed zone
Eq.	equation
FEP	feature, event, and process
FY	fiscal year
GB	gigabytes
GDSA	Geologic Disposal Safety Assessment
GFM	geologic framework model
gpm	gallons per minute
HDF5	hierarchical data format, version 5
HLW	high-level radioactive waste
HPC	high-performance computing
$K_D$	distribution coefficient
km	kilometer
LANL	Los Alamos National Laboratory
m	meter
MB	megabytes
mm	millimeter
mol	mole
MPa	megapascal
MTHM	metric tons of heavy metal
NA	not applicable
NBS	natural barrier system
NE	Office of Nuclear Energy
NEA	Nuclear Energy Agency
NM	New Mexico
NT	Newton's method
NTR	Newton trust region
NTRDC	Newton Trust Region Dogleg-Cauchy
OoR	out of reactor
PA	performance assessment
PDE	partial differential equation
PETSc	Portable Extensible Toolkit for Scientific Computation
PFLOTRAN	massively parallel reactive flow and transport model for describing subsurface processes (pflotran.org)
pH	negative logarithm of hydrogen ion activity
PWR	pressurized water reactor

---

QA	quality assurance
RAM	random access memory
R&D	research and development
RSA	Repository Systems Analysis
s	seconds
S&T	Storage and Transportation
SDA	SFWD Document Archive
SFWD	Spent Fuel and Waste Disposition
SFWST	Spent Fuel and Waste Science and Technology
SKB	Swedish Nuclear Fuel and Waste Management Company
SNF	spent nuclear fuel
SNL	Sandia National Laboratories
TBD	to be determined
TH	thermal-hydrological
THC	thermal-hydrologic-chemical
THM	thermal-hydrologic-mechanical
THMC	thermal-hydrologic-mechanical-chemical
ULR	unclassified limited release
UNF	used nuclear fuel
UQ	uncertainty quantification
U.S.	United States of America
USA	United States of America
UR	unclassified unlimited release
W	watt
WF	waste form
WP	waste package
yr	year

(This page left intentionally blank.)



## 1. INTRODUCTION

The Spent Fuel and Waste Science and Technology (SFWST) Campaign of the U.S. Department of Energy (DOE) Office of Nuclear Energy, Office of Spent Fuel and Waste Disposition (SFWD), is conducting research and development (R&D) on geologic disposal of spent nuclear fuel (SNF) and high-level radioactive waste (HLW). Two of the highest priorities for SFWST disposal R&D are design concept development and disposal system performance assessment (PA) modeling (DOE 2012, Table 6). Generic design (or reference-case) concepts being considered for SNF and HLW disposal since 2010 include mined repository concepts in bedded salt, argillite (shale), and crystalline rock. An additional option begun three years ago is a potential mined repository in unsaturated alluvium. The PA R&D since 2012 has mostly focused on disposal of commercial spent nuclear fuel (CSNF) inventory packaged in smaller waste packages, such as 4-pressurized water reactor (PWR) and/or 12-PWR waste packages. However, since 2019 a greater emphasis is given to simulating disposal of higher decay-heat waste packages containing 21, 24, or 37 PWR assemblies.

This report describes accomplishments for the Fiscal Year (FY) 2021 in the development of generic repository reference cases and PA modeling and analysis. Prior development and accomplishments are summarized at a high-level in Mariner et al. (2019), with much more detail provided in Mariner et al. (2018), Mariner et al. (2017), Mariner et al. (2016), Mariner et al. (2015), Sevougian et al. (2016), Sevougian et al. (2014), Sevougian et al. (2013), Sevougian et al. (2012), Freeze et al. (2013), Vaughn et al. (2013), Sevougian et al. (2019a), Sevougian et al. (2019b) and LaForce et al. (2020).

Sassani et al. (2020) details a 5-year disposal research R&D plan that “provides a strategic guide to the work within the R&D technical areas, focusing on the highest priority technical thrusts” for the SFWST Campaign. The plan discusses the need to focus on four areas (Sassani et al. 2020):

- Capabilities Development and Demonstration
- International Collaboration and Underground Research Laboratories
- Engineered Barrier System Representations
- Evaluation of Potential Direct Disposal of large, high-energy waste packages

The objective of the GDSA Repository Systems Analysis work package is to develop generic deep geologic repository concepts and system Performance Assessment (PA) models in line with the current 5-year plan (Sassani et al. 2020) for several host-rock environments, and to simulate and analyze these generic repository concepts and models using the GDSA Framework toolkit (Mariner et al. 2019), and other tools as needed.

Figure 1-1 shows the flow of information and the role of PA for R&D. The repository systems analysis (RSA) work package focuses primarily on the reference case components and technical bases and process models, as indicated by the dashed blue lines. Figure 1-2 shows the GDSA framework, which is used by the RSA work package for simulation studies. The piece of the GDSA framework addressed by RSA in FY21 is flow and transport modelling and investigating the suitability of the VoroCrust meshing software for the workflow. The work accomplished in FY21 applies to the goals of capabilities development and demonstration, international collaboration, engineered barrier systems, and evaluation of disposal of large, high-energy waste packages. The specific goals for FY21 are:

- The GDSA team is leading Task F of the DECOVALEX 2023 project on behalf of the US DOE’s SFWST Campaign. This project has 9 international partners for the crystalline case and 3 for the salt case. Both cases involve collaborative development of reference case scenarios for post-closure PA for deep geologic repositories. An overview of the progress to date is in Section 2.

- The study on the impact of buffer swelling on the disturbed rock zone (DRZ) in a shale reservoir in LaForce et al. (2020) was continued. This study involves PFLOTRAN implementation of a reduced order model for permeability evolution in the DRZ in response to increased stress from the swelling buffer and the impact on tracer transport. The results of this study are in Section 3.1.
- RSA has been collaborating within Sandia to conduct a near-DPC thermal study (Jones et al. 2021). A study of unsaturated alluvium PFLOTRAN simulation cases from that work on a Voronoi mesh is in Section 3.2.
- A near-surface conceptual model of the geosphere above the crystalline rock environment has been undertaken with the goal of improving coupling with the near-surface and biosphere, as presented in Section 4.
- The unsaturated alluvium PA-model has been run to completion using newly developed solvers (Nole et al. 2021). Two deterministic models of the full complexity conceptual model from Sevougian (2019) have been completed, as shown in Section 5.
- VoroCrust Voronoi meshing continues to be studied in a stepwise process to improve GDSA capability and to further the goal of having all open-source software in the GDSA Framework workflow. This work is presented in Section 6.

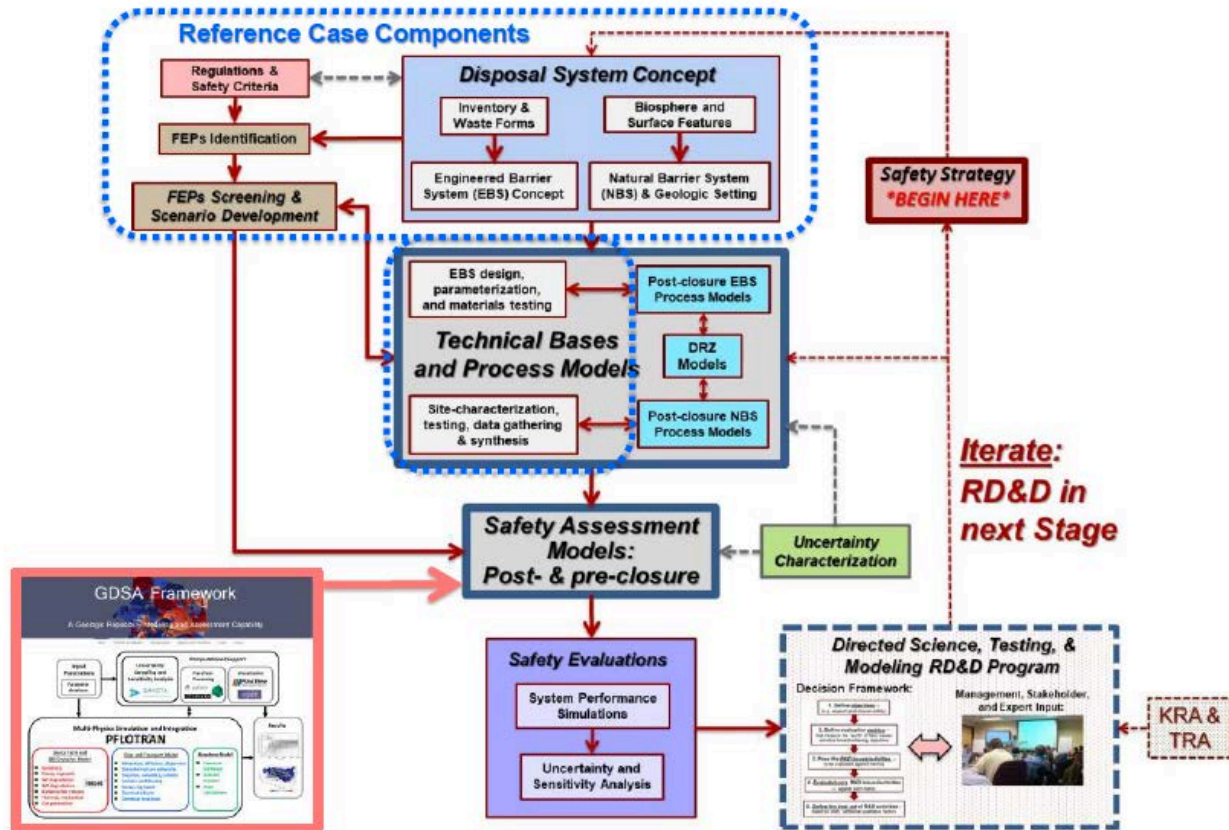


Figure 1-1. Information flow and the role of performance assessment for disposal R&D prioritization during a single stage of repository development. (Taken from Sevougian et al. 2019b)

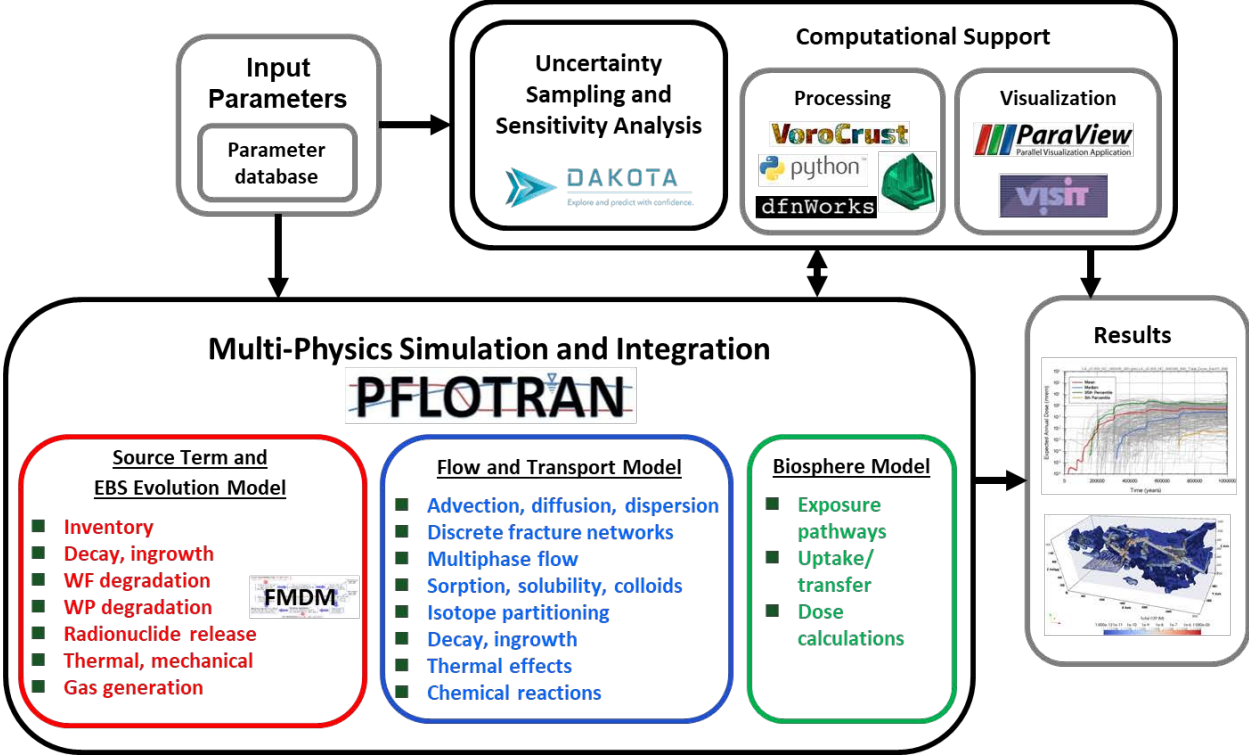


Figure 1-2. Schematic the GDSA Framework. The RSA work packages focuses primarily on flow and transport modelling, but also works closely with VoroCrust, dfnWorks and Dakota for processing and computational support. (Mariner et al. 2020)

## 1.1 References

- DOE (U.S. Department of Energy). 2012. *Used Fuel Disposition Campaign Disposal Research and Development Roadmap*. FCR&D-USED-2011-000065, REV 1, U.S. DOE Office of Nuclear Energy, Used Fuel Disposition, Washington, D.C.
- Freeze, G., Gardner, P., Vaughn, P., Sevougian, S.D., Mariner, P., Mousseau, V. and Hammond, G. 2013. *Enhancements to Generic Disposal System Modeling Capabilities*. FCRD-UFD-2014-000062. SAND2013-10532P. Sandia National Laboratories, Albuquerque, NM
- LaForce, T., Chang, K.W., Perry, F.V., Lowry, T.S., Basurto, E., Jayne, R., Brooks, D., Jordan, S., Stein, E., Leone, R., and Nole, M. 2020. *GDSA Repository Systems Analysis Investigations in FY2020*. M2SF-20SN010304052, SAND2020-12028 R. Sandia National Laboratories, Albuquerque, NM.
- Mariner, P. E., Connolly, L. A., Cunningham, L. J., Debusschere, B. J., Dobson, D. C., Frederick, J. M., Hammond, G. E., Jordan, S. H., LaForce, T. C., Nole, M. A., Park, H. D., Perry, F. V., Rogers, R. D., Seidl, D. T., Sevougian, S. D., Stein, E. R., Swift, P. N., Swiler, L. P., Vo, J., and Wallace, M. G. 2019. *Progress in Deep Geologic Safety Assessment in the U.S. since 2010*, M2SF-19SN010304041, U.S. Department of Energy, Spent Fuel and Waste Science and Technology Campaign, Office of Spent Fuel and Waste Disposition, Washington, DC.
- Mariner, P. E., Stein, E. R., Sevougian, S. D., Cunningham, L. J., Frederick, J. M., Hammond, G. E., Lowry, T. S., Jordan, S., and Basurto, E. 2018. *Advances in Geologic Disposal Safety Assessment and an Unsaturated Alluvium Reference Case*, SFWD-SFWST-2018-000509, SAND2018-11858R. Sandia National Laboratories, Albuquerque, NM.
- Mariner, P. E., Stein, E. R., Frederick, J. M., Sevougian, S. D., and Hammond, G. E. 2017. *Advances in Geologic Disposal System Modeling and Shale Reference Cases*. SFWD-SFWST-2017-000044 / SAND2017-10304R. Sandia National Laboratories, Albuquerque, NM.
- Mariner, P. E., Stein, E. R., Frederick, J. M., Sevougian, S. D., Hammond, G. E., and Fascitelli, D. G. 2016. *Advances in Geologic Disposal System Modeling and Application to Crystalline Rock*, FCRDUFD-2016-000440, SAND2016-96107R. Sandia National Laboratories, Albuquerque, NM.
- Mariner, P. E., Gardner, W. P., Hammond, G. E., Sevougian, S. D. and Stein, E. R. 2015. *Application of Generic Disposal System Models*. SAND2015-10037R; FCRD-UFD-2015-000126. Sandia National Laboratories, Albuquerque, NM.
- Nole, M., Leone, R.C., Park, H.D., Paul, M., Salazar, A., Hammond, G.E., and Lichtner, P.C. 2021. *PFLOTRAN Development FY2021*. SAND2021- 8709 R. Sandia National Laboratories, Albuquerque, NM.
- Sassani, D., Birkholzer, J., Camphouse, R., Freeze, G., Stein, E. R., 2020. *SFWST Disposal Research R&D 5-Year Plan*. SAND 2020-XXXXXX. Sandia National Laboratories, Albuquerque, NM.
- Sevougian, S. D., Stein, E. R., LaForce, T., Perry, F. V., Lowry, T. S., Cunningham, L. J., Nole, M., Haukwa, C. B., Chang, K. W. and Mariner, P. E. 2019a. *GDSA Repository Systems Analysis Progress Report*. SAND2019-5189R. Sandia National Laboratories, Albuquerque, NM.

- Sevougian, S. D., Stein, E. R., LaForce, T., Perry, F. V., Nole, M., Haukwa, C. B., and Chang, K. W. 2019b. *GDSA Repository Systems Analysis FY19 Update*. SAND2019-11942R. Sandia National Laboratories, Albuquerque, NM.
- Sevougian, S. D., Mariner, P. E., Connolly, L. A., MacKinnon, R. J., Roger, R. D., Dobson, D. C., and Prouty, J. L. 2019c. *DOE SFWST Campaign R&D Roadmap Update*. M2SF-19SN010304042 SAND2019-5179R. Sandia National Laboratories, Albuquerque, NM.
- Sevougian, S. D., Stein, E. R., Gross, M. B., Hammond, G. E., Frederick, J. M. and Mariner, P. E. 2016. *Status of Progress Made Toward Safety Analysis and Technical Site Evaluations for DOE Managed HLW and SNF*, SAND2016-11232 R; FCRD-UFD-2016-000082, Rev. 1. Sandia National Laboratories, Albuquerque, NM.
- Sevougian, S. D., Freeze, G. A., Gardner, W. P., Hammond, G. E. and Mariner, P. E., 2014. *Performance Assessment Modeling and Sensitivity Analyses of Generic Disposal System Concepts*. FCRD-UFD-2014- 000320, SAND2014-17658. Sandia National Laboratories, Albuquerque, NM.
- Sevougian, S. D., Freeze, G. A., Vaughn, P., Mariner, P. E., and Gardner, W.P., 2013. *Update to the Salt R&D Reference Case*. FCRD-UFD-2013-000368, SAND2013-8255P. Sandia National Laboratories, Albuquerque, NM.
- Sevougian, S. D., Freeze, G. A., Gross, M. B., Lee, J., Leigh, C. D., Mariner, P. E., MacKinnon, R. J. and Vaughn, P. 2012. *TSPA Model Development and Sensitivity Analysis of Processes Affecting Performance of a Salt Repository for Disposal of Heat-Generating Nuclear Waste*. FCRD-UFD-2012-000320 Rev. 0, U.S. Department of Energy, Office of Used Nuclear Fuel Disposition, Washington, DC.
- Vaughn, P., Sevougian, S. D., Hardin, E. L., Mariner, P. E., and Gross, M. B. 2013. *Reference Case for Generic Disposal of HLW and SNF in Salt, in Proceedings of the 2013 International High-Level Radioactive Waste Management Conference*, Albuquerque, NM, April 28 – May 2, 2013, American Nuclear Society, La Grange Park, Illinois. ([www.ans.org](http://www.ans.org)).

## 2. DECOVALEX REFERENCE CASES

DECOVALEX (DEveloping COupled models and their VALidation against Experiments; <https://decovallex.org>) is an international collaboration initiated in 1992 for the purpose of improving understanding of the coupled thermal, hydrologic and mechanical (THM) processes affecting repository evolution. In recent years chemical processes have also been considered. DECOVALEX activities run in 4-year phases. SNL is leading Task F, on behalf of the US DOE's SFWST Campaign, for the DECOVALEX-2023 phase. Task F is a comparison of the models and methods used in deep geologic repository performance assessment (PA).

Teams participating in Task F will compare post-closure performance assessment approaches to physics simulation, uncertainty propagation, and sensitivity analysis on two generic reference case repositories: one in a fractured crystalline host rock and one in a domal salt formation. In Year 1, nine teams from six countries participated in discussion of the crystalline reference case and benchmarking exercises, and three teams (from three countries) participated in development of the salt reference case comparison. In Year 2 (this year), each reference case has gained the participation of an additional team.

The primary objectives of Task F are to build confidence in the models, methods, and software used for post-closure PA, and/or to bring to the fore additional research and development needed to improve PA methodologies. Although a direct comparison cannot be made between simulations of a crystalline repository and simulations of a salt repository, it is expected that lessons learned regarding, for instance, methods of coupling process models, propagating uncertainty, or conducting sensitivity analysis will be transferable between concepts.

For each reference case, a common set of conceptual models and parameters describing features, events, and processes (FEPs) that impact performance will be given, and teams will be responsible for determining how best to implement and couple the models. The comparison will be conducted in stages, beginning with a comparison of key outputs of individual process models, followed by a comparison of a single deterministic simulation of the full reference case, and moving on to uncertainty propagation and uncertainty and sensitivity analysis. The Task Specification (Stein et al. 2021) provides background information, a summary of the proposed reference cases, and a staged plan for the analysis.

In the first year of the project, the crystalline teams focused on benchmarking, especially simulations of transport in fractured rock, and the salt teams developed a repository reference case and phased modeling approach. The crystalline benchmarking exercises and the domal salt reference case are described in the following sections.

### 2.1 Crystalline reference case

A preliminary description of the DECOVALEX crystalline reference case and the choices to be made regarding features and processes to be simulated is available in Stein et al. (2021). Teams participating in the Crystalline Task F completed several benchmark cases related to flow and transport through fractured rock. The benchmark cases provide an opportunity to understand differences in model implementation that affect how a problem can be specified, what results can be obtained, and the influence modeling choices have on calculated values of performance measures in relatively simple systems. Results from several benchmark cases completed for the Crystalline Task F are outlined below.

## 2.1.1 Benchmark Cases

### 2.1.1.1 Fracture Transport with Matrix Diffusion

The matrix diffusion benchmark case is based on the analytical solution by Tang et al. (1981), for the problem of transport of a radionuclide in a single fixed-aperture fracture, with diffusion into the rock matrix, which is assumed to be infinite. Matrix diffusion is the migration of dissolved solutes from flowing fractures into the pore space of the rock matrix (and vice versa). The fracture-rock matrix system is represented in Figure 2-1. The governing equations are derived from mass conservation of the radionuclide and the following assumptions are made:

1. The width of the fracture is much smaller than its length.
2. Transverse diffusion and dispersion within the fracture assure complete mixing across the fracture width at all times.
3. The permeability of the porous matrix is very low and transport in the matrix will be mainly by molecular diffusion.
4. Transport along the fracture is much faster than transport within the matrix.

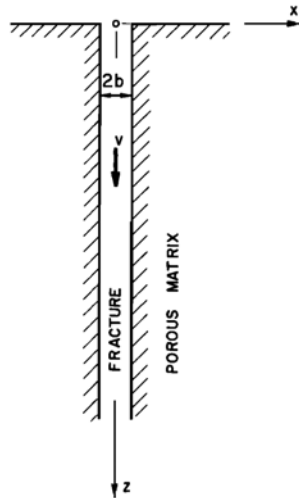


Figure 2-1. Fracture-Matrix system from (Tang et al. 1981),  $z$  represents distance along the fracture and  $x$  represents distance into the matrix.

The governing equations are as follows:

$$\frac{\partial c}{\partial t} + \frac{v}{R} \frac{\partial c}{\partial z} - \frac{D}{R} \frac{\partial^2 c}{\partial z^2} + \lambda c + \frac{J}{bR} = 0 \quad (2-1)$$

$$\frac{\partial c'}{\partial t} - \frac{D'}{R'} \frac{\partial^2 c'}{\partial z^2} + \lambda c' = 0 \quad (2-2)$$

Where  $c$ ,  $c'$  are the concentration of solute in solution in the fracture and rock matrix respectively ( $M/L^3$ ),  $R'$  is the retardation factor in the matrix,  $\lambda$  is the decay constant, and  $z$  is the distance along the fracture. Where  $v$  is average linear groundwater velocity in the fracture ( $L/T$ ) and  $D$  is the hydrodynamic dispersion coefficient in the fracture given by:

$$D = \alpha_L v + D^* \quad (2 - 3)$$

The effective diffusion coefficient,  $D'$  is given by:

$$D' = \tau D^* \quad (2 - 4)$$

where  $\tau$  is tortusity in the matrix and  $D^*$  is the diffusivity in water. The diffusive mass flux  $J$  (M/L<sup>2</sup>/T), from the fracture in the rock matrix is given by, at  $x = b$ :

$$J = -\phi D' \frac{\partial c'}{\partial x} \quad (2 - 5)$$

Where  $x$  is the distance into the matrix. The initial conditions are given by:

$$c(z, 0) = c'(x, z, 0) = 0 \quad (2 - 6)$$

The boundary conditions are given by:

$$c(0, t) = c_0 \quad (2 - 7)$$

$$c(\infty, t) = 0 \quad (2 - 8)$$

$$c'(b, z, t) = c(z, t) \quad (2 - 9)$$

$$c'(\infty, z, t) = 0 \quad (2 - 10)$$

The analytical solution is then derived in the Laplace domain. Material and fluid properties solution are listed in Table 2-1. The analytical solution was coded in Python for comparison. PFLOTTRAN uses a multiple continuum model which models a primary continuum (fracture) coupled to a secondary continuum (matrix) using a Dual Continuum Disconnected Matrix (DCDM) model (Nole et al. 2021; Iraola et al. 2019).

Concentration profiles along the fracture and the rock matrix ( $x \geq b$ ) are compared to the analytical solution at 100, 1000 and 10000 days over 101 cells. The first set is compared with slow velocity  $v_1 = 0.01$  m/d along a 10 m domain for the fracture and at  $z = 2$  m with a domain of 2 m for the matrix. A second set is compared with fast velocity  $v_2 = 0.1$  m/d along a 10 m domain for the fracture and at  $z = 2$  m with a domain of 1 m for the matrix. The simulation ran with a maximum time step size of 0.1 days for 10000 days and 100 and 200 cells in the secondary continuum for the fast and slow velocity, respectively.

The analytical solution and PFLOTTRAN simulation result at the low velocity case are compared in Figure 2-2. Comparisons are shown for along the fracture and into the matrix at a distance 2 m down the fracture. Tracer concentrations are normalized to the inlet concentration value. By 10000 days the tracer can be seen as far as ~5-6 m down the fracture, by then the curve has almost converged on the steady state solution. The tracer penetrates to ~1 m into the matrix at 2 m down the fracture. The PFLOTTRAN simulations are verified to agree between 0.1-15% relative error for concentrations in the fracture with higher values of relative error being associated with small concentrations values further along the fracture. When only looking at concentrations above 0.1 the greatest relative error is ~8%.

For the high velocity case (Figure 2-3), tracer can be seen 10 m down the fracture at 1000 and 10000 days. At 100 days there is tracer ~5 m down the fracture. In the matrix at 2 m down the fracture tracers can be detected at 10000 days ~0.5 m into the matrix and less than ~0.25 m for 100 and 1000 days. The PFLOTTRAN simulations agree between 0.05-15% relative error in the fracture, with larger relative errors again being associated with smaller concentration values, looking at values between 0-5 m down the fracture relative error is less than 1%.

**Table 2-1. Parameters for Fracture Transport with Matrix Diffusion.**

Parameter	Value	Units
Diffusion coefficient in water ( $D^*$ )	$1.6 \times 10^{-9}$	m <sup>2</sup> /s
Tortuosity ( $\tau$ )	0.1	–
Fracture width ( $2b$ )	$10^{-4}$	m
Dispersivity ( $\alpha_L$ )	0.5	m
Half-life ( $t_{1/2}$ ), equivalent to Decay constant ( $\lambda$ )	12.35 $1.779 \times 10^{-9}$	y s
Retardation factor in matrix ( $R'$ )	1.0	–
Retardation factor in fracture ( $R$ )	1.0	–
Porosity in matrix ( $\phi$ )	0.01	–
Concentration, $c_0(z=0)$	1.0	mol/L
Average linear velocity ( $v_1$ )	0.01	m/d
Average linear velocity ( $v_2$ )	0.1	m/d

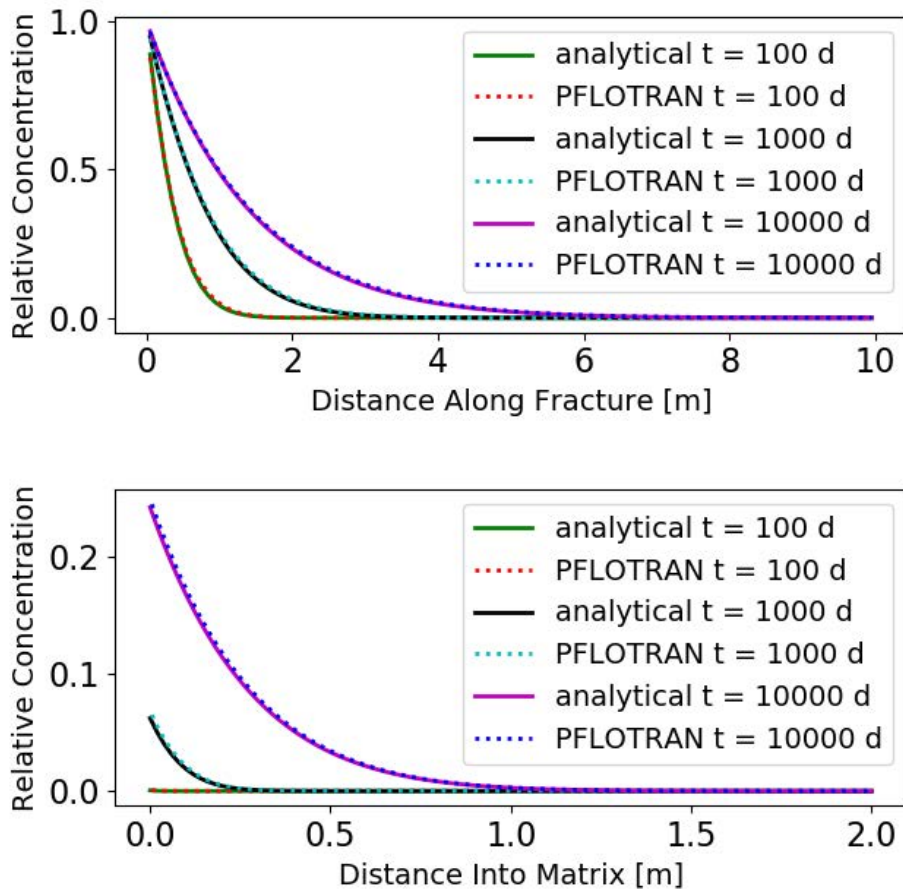


Figure 2-2. Concentrations in the fracture (above) and in the matrix 2 m into the fracture (below) for low velocity case (0.01 m/d).

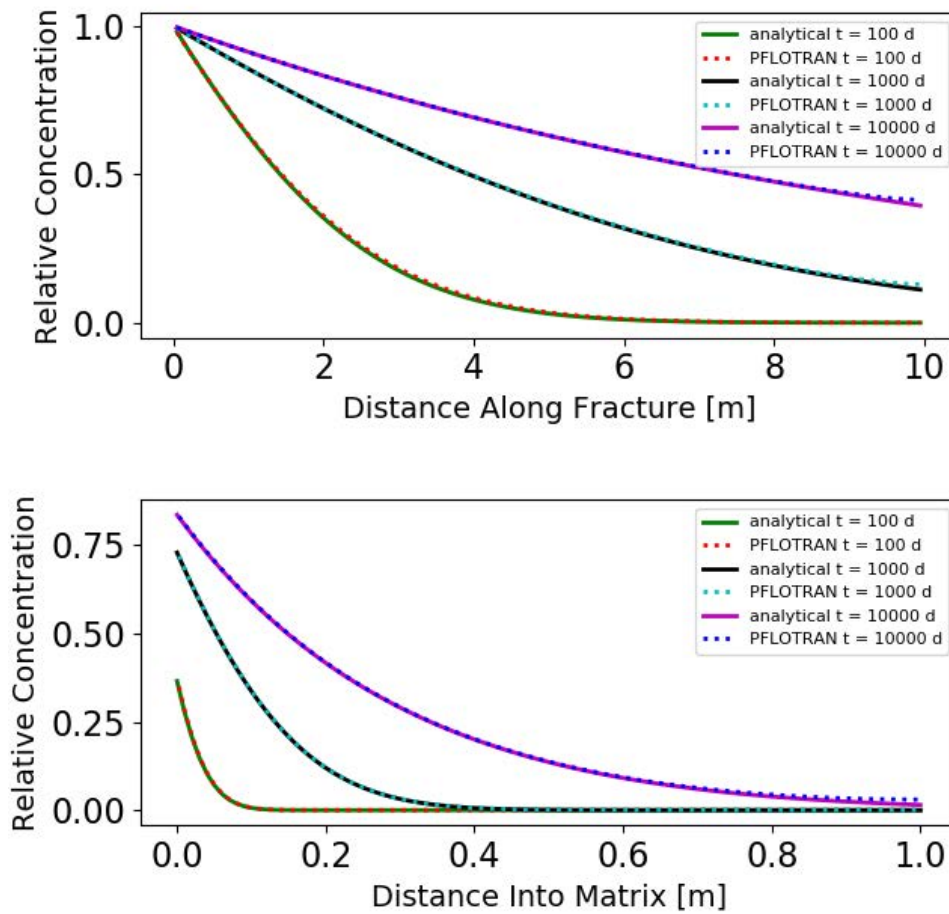


Figure 2-3. Concentrations in the fracture (above) and in the matrix 2 m into the fracture (below) for fast velocity case (0.1 m/d).

**2.1.1.2 Transport in a 4-Fracture DFN**

The four-fracture test problem shown in Figure 2-4 provided an opportunity for teams to practice generating deterministic fractures, upscaling to an Equivalent Continuous Porous Medium (ECPM) and simulating particle tracking. The test problem (built based on an example provided with dfnWorks (Hyman et al. 2015)) models advection and diffusion of a conservative tracer through four fractures within a cubic domain. It is assumed flow and transport only occur in the fractures; matrix diffusion is neglected. Groundwater flow is simulated by a steady state (saturated, single-phase) flow driven by a pressure gradient along the x-axis. Constant pressure (Dirichlet) boundary conditions are applied on the inflow and outflow faces. For simplicity, gravity is not included. No-flow boundary conditions are applied at all other faces of the domain.

The fractures were generated using Los Alamos National Laboratories (LANL) dfnWorks (Hyman et al. 2015). After generating the fractures, dfnWorks uses PFLOTRAN to solve for the steady state flow field

solution. We then modelled the four-fracture benchmark case using the DFN approach and two different methods of upscaling to an Equivalent Continuous Porous Medium (ECPM).

An initial pulse of tracer is inserted uniformly along the single fracture on the west face ( $x = -500$ ) of the domain at time zero; the concentration at the west face is zero for all other times. The tracer then exits the domain through the two fractures on the east face ( $x = 500$ ). In particle tracking, the mass of each particle is equal. On the inflow face  $1.0 \times 10^4$  particles were introduced. For comparison, normalized breakthrough curves (total mass that's crossed the east face divided by the initial mass at the west face) over 30 years were generated at the outflow face. Since breakthrough curves are normalized to initial mass, the concentration of the initial pulse was irrelevant. The parameters and values used can be found in Table 2-2. Figure 2-4 shows the fracture domain pressure solution in the DFN.

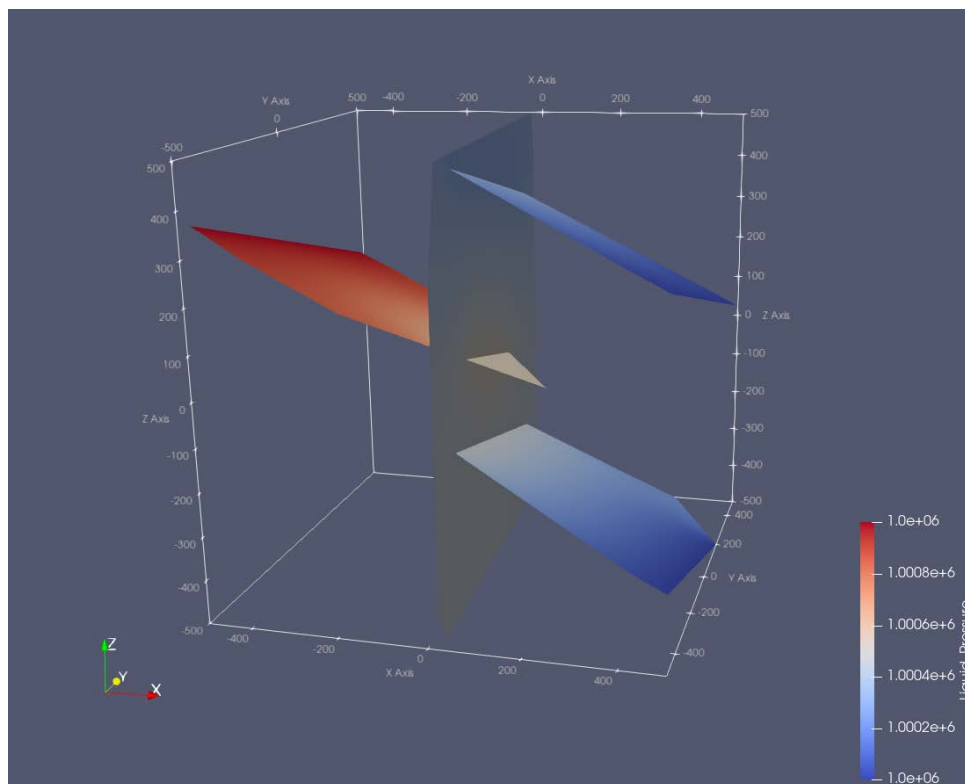


**Figure 2-4. Steady state liquid pressure solution for 4-Fracture DFN.**

Two different transport methods were used with the DFN approach. The first utilizes dfnWorks particle tracking software dfnTrans (Lagrangian reference frame). The dfnTrans software takes the flow field and fracture information and outputs particle travel times in the domain. The second method uses the advection-dispersion equation (ADE) in PFLOTRAN (Eulerian reference frame) with 175920 cells in the domain.

With the ECPM approach two different methods of upscaling were used. The first method used a python script called mapdfn.py (Stein et al. 2017) which creates a uniform grid. Using output from dfnWorks (apertures, permeabilities, radii, the unit vector defining the normal vector to the fractures, and coordinates of the fracture center) along with user input defining the domain and grid cell size, mapDFN outputs upscaled anisotropic permeability, porosity, and tortuosity based on the intersection of fractures within grid cells. A cell length of 20 m was chosen which resulted in a total of 9704 active cells. The

matrix cells were made inactive when modelling. Figure 2-5 shows the upscaled permeability for the uniform ECPM.

The second method used dfnWorks octree meshing. This method returns a spatially variable Delaunay tetrahedral mesh and is refined only where there are fractures (Sweeney et al. 2020). We used an edge length of 160 m, representing the largest cell size of the background mesh cells and 3 refinement levels. This resulted in ~20 m grid cells for a total of 30086 cells. The matrix cells remained active when modelling but tracer was only injected into the fracture. Figure 2-5 shows the upscaled permeability for the octree ECPM while Figure 2-6 shows the liquid pressure solution for both upscaling methods.

The breakthrough curves for the Sandia team are shown in Figure 2-7. The results show good agreement between the models and with the other teams (not shown). Most teams chose to only model the tracer via an ECPM. The tracer can first be seen on the outflow face at ~0.5 years and is fully through the model after ~10 years. Differences between results could be due to mesh size chosen for the ECPM, numerical diffusion, or general upscaling methods.

**Table 2-2. Parameters for Transport in a 4-Fracture DFN.**

Parameter	Value	Units
Pressure (inlet, x = -500)	$1.001 \times 10^6$	Pa
Pressure (outlet, x = 500)	$1 \times 10^6$	Pa
Fracture 1 Aperture	$1 \times 10^{-3}$	m
Fracture 2 Aperture	$1 \times 10^{-3}$	m
Fracture 3 Aperture	$1 \times 10^{-3}$	m
Fracture 4 Aperture	$5 \times 10^{-4}$	m
Fracture 1 Permeability	$8.333 \times 10^{-8}$	m <sup>2</sup>
Fracture 2 Permeability	$8.333 \times 10^{-8}$	m <sup>2</sup>
Fracture 3 Permeability	$8.333 \times 10^{-8}$	m <sup>2</sup>
Fracture 4 Permeability	$2.083 \times 10^{-8}$	m <sup>2</sup>
Porosity in a fracture ( $\phi$ )	1.0	–
Tortuosity in a fracture ( $\tau$ )	1.0	–
Diffusion coefficient in water ( $D_m$ )	$1.6 \times 10^{-9}$	m <sup>2</sup> /s

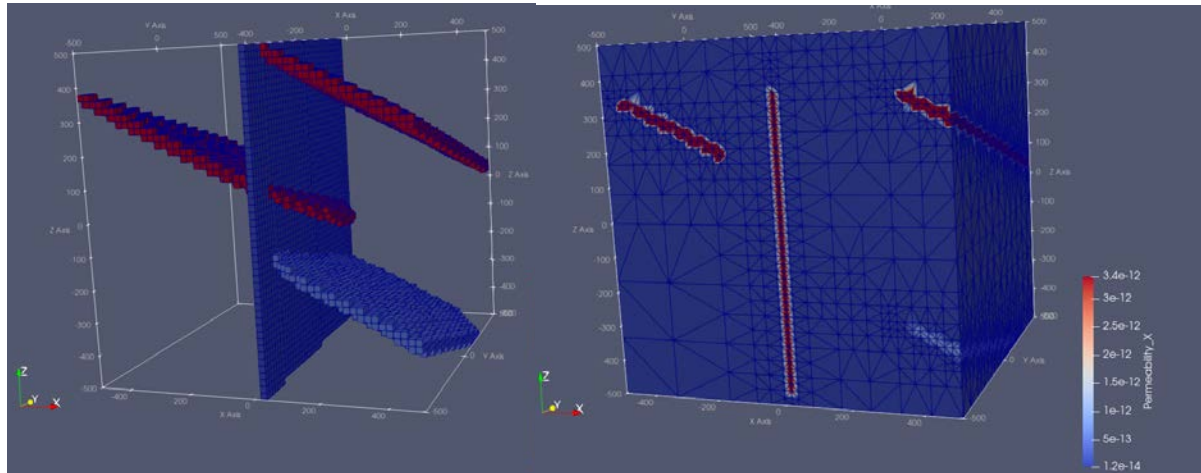


Figure 2-5. Left: Upscaled permeability for uniform ECPM mesh. Matrix cells are inactive and not shown. Right: Upscaled permeability for octree ECPM mesh.

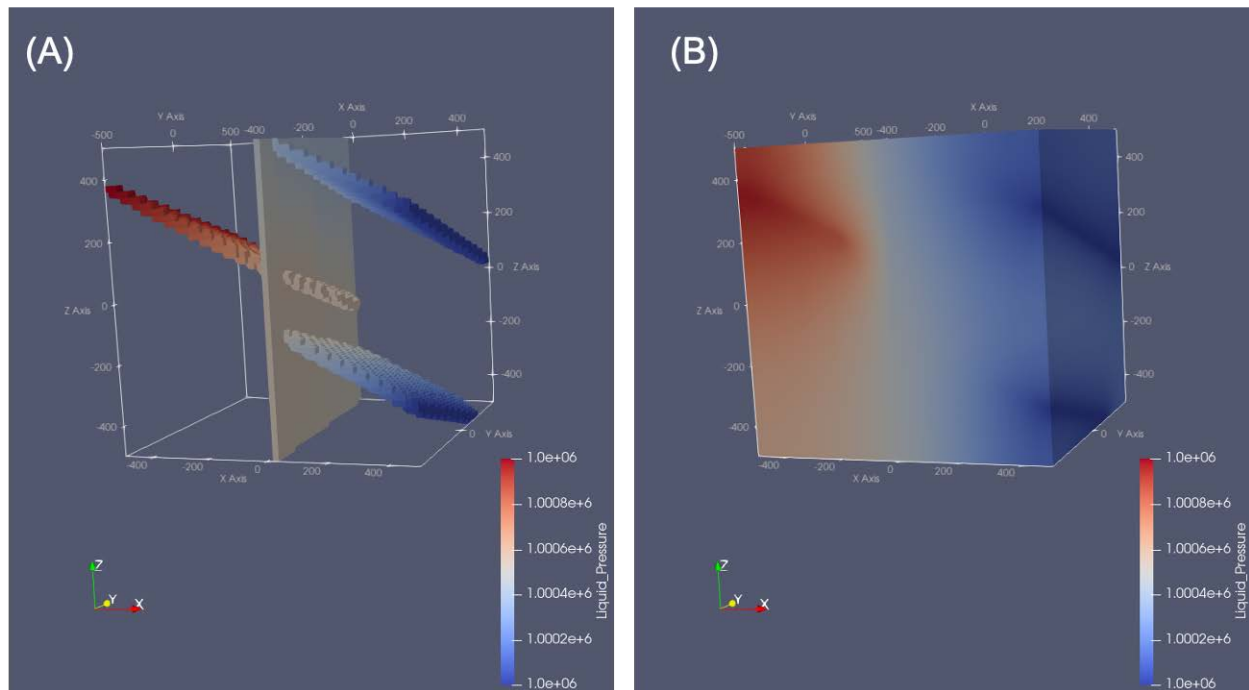


Figure 2-6. (A) Uniform ECPM liquid pressure solution. Matrix cells are inactive and not shown. (B) Octree ECPM liquid pressure solution.

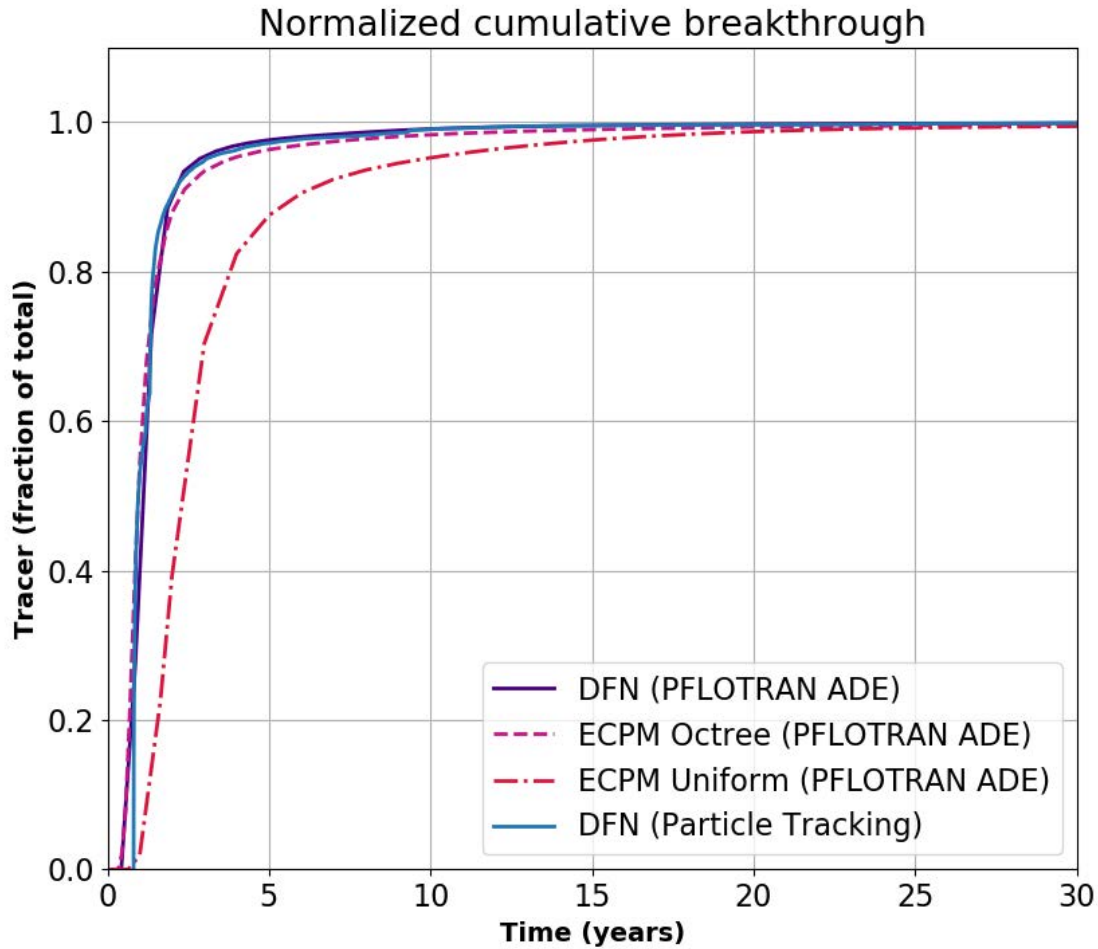


Figure 2-7. Sandia team breakthrough curves for the Crystalline Task F 4-Fracture DFN.

### 2.1.1.3 Transport in a 4-Fracture DFN with Stochastic Fractures

The four-fracture benchmark case is then extended by adding stochastically-generated fracture sets to the model domain. The stochastic fractures were generated based on Central Hydraulic Unit West (CHUW) Case A distributions from Posiva WR 2012-42 (Hartley et al. 2012, Table D-4) corresponding to Depth Zone 4, which applies at repository depth (Hartley et al. 2016, Table 3-1). The domain, including stochastically-generated fractures, were provided to the teams. The problem models advection and diffusion of a conservative, decaying, and adsorbing tracer through the four deterministic fractures and stochastic fractures within a cubic domain. The problem uses the same assumptions for flow and transport as the four-fracture benchmark case and the domain coordinates remain the same.

Three fracture families, two subvertical and one subhorizontal, were defined. For each fracture family, fracture radius was sampled from a truncated power law distribution, and fracture orientation was sampled from a Fisher distribution. Although a bivariate Bingham distribution is given for the subhorizontal fracture family in Posiva WR 2012-42, the option is not yet implemented in dfnWorks and

we proceeded by substituting a Fisher distribution for this initial test problem. Fractures were assumed to be randomly distributed in space, with a fracture intensity for each fracture family expressed as fracture area per unit volume of rock, defined as P32. Figure 2-8 shows the three stochastic fracture families along with the deterministic fractures.

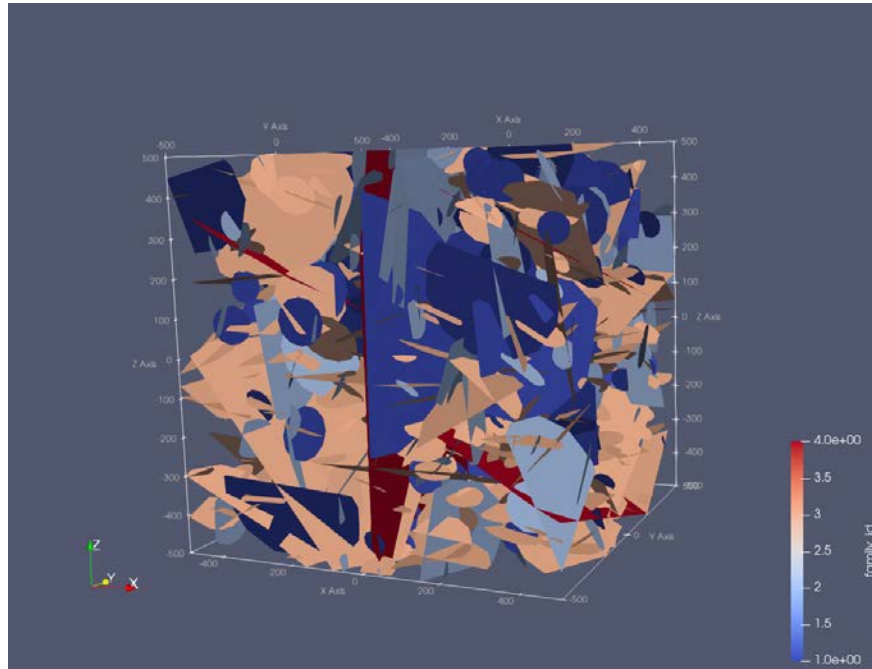


**Figure 2-8. E-W stochastic fractures (1), N-S stochastic fractures (2), subhorizontal fractures (3), and deterministic fractures (4).**

Posiva employed truncated power law distributions with a minimum radius of 0.04 m and a maximum radius of 564 m in calibrating P32 and fracture transmissivity to borehole flow measurements (Hartley et al. 2011), but employed larger minimum fracture radii (8.46 m in the far field and 0.5 m in the vicinity of the repository) in generating DFNs for flow and transport modeling (Hartley et al. 2012). Similarly, to generate fractures for this test problem, we increased the minimum fracture radius from 0.04 m to 30 m and adjusted P32 accordingly using the method in Hedin (2008).

In this test problem, fracture transmissivity ( $T$  [m<sup>2</sup>/s]) was correlated with fracture radius ( $r$  [m]) according to:

$$T = ar^b \quad (2 - 11)$$

Here  $a$  and  $b$  are dimensionless constants with values equal to  $2.2 \times 10^{-9}$  and 0.8, respectively (Hartley et al. 2012, Table D-4).

Fracture aperture was calculated from transmissivity using the cubic law (as in Bear et al. 1993):

$$T = \frac{\rho g B^3}{\mu 12} \quad (2 - 12)$$

$B$  is fracture aperture [m] (equal to  $2b$  in Figure 2-1),  $\rho$  is the density of water [kg/m<sup>3</sup>],  $g$  is acceleration due to gravity [m/s<sup>2</sup>], and  $\mu$  is the viscosity of water [Pa s].

The decaying tracer has a half-life of 100 years. The adsorbing tracer has a retardation coefficient in the fracture of 5. The retardation coefficient ( $R$  [-]) is defined as (Tang et al. 1981):

$$R = 1 + \frac{K_f}{b} \quad (2 - 13)$$

Where  $b$  is half the fracture aperture, and  $K_f$  is the linear distribution coefficient in the fracture, defined as (Freeze and Cherry 1979):

$$K_f = \frac{\text{mass sorbed/area fracture}}{\text{mass dissolved/volume water}} \quad (2 - 14)$$

As in the four-fracture benchmark, the fractures were generated using Los Alamos National Laboratories (LANL) dfnWorks (Hyman et al. 2015). However, in this case the DFN was modeled only using the ADE method and only one method of upscaling was used (uniform grid mapdfn.py python script). The DFN flow field is seen in Figure 2-9. The DFN used 4647375 cells and ran in ~3 hours on 288 processors on a parallel super-computer. The ECPM used 49685 cells and ran in ~1.5 minutes on 288 processors.

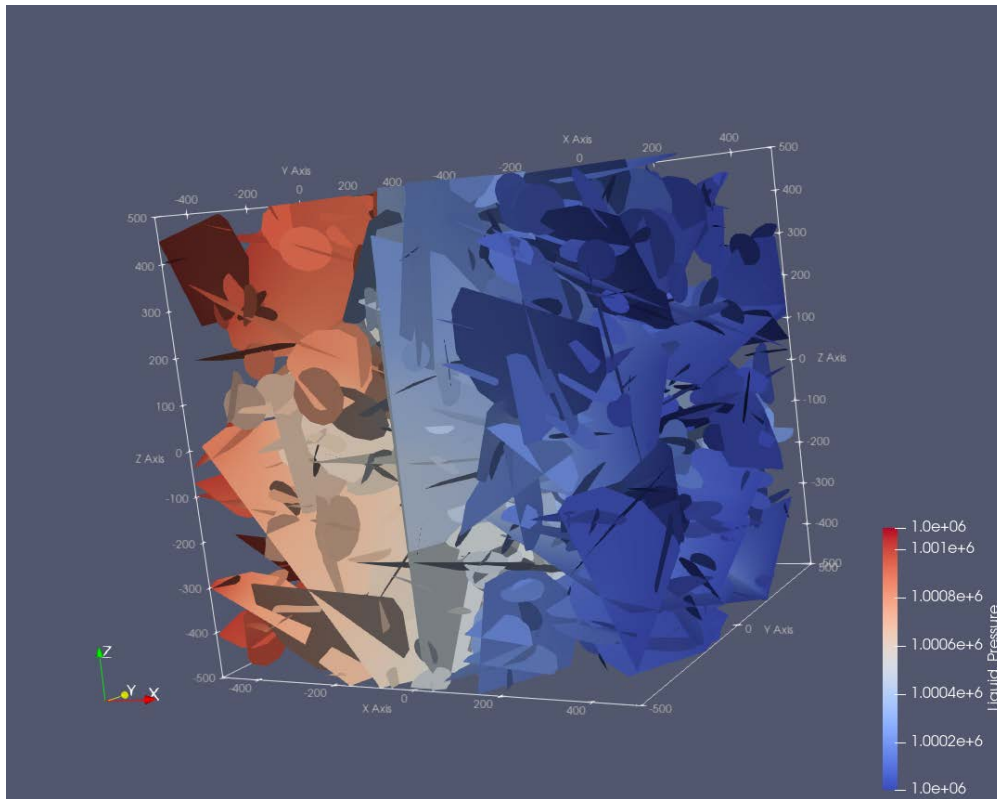


**Figure 2-9. Steady state liquid pressure distribution for 4-Fracture DFN with stochastic fractures.**

An initial pulse of tracer was inserted uniformly along the fractures on the west face ( $x = -500$ ) of the domain at time zero; the concentration at the west face is zero for all other times. The tracer then exited the domain through the fractures on the east face ( $x = 500$ ). For comparison, normalized breakthrough curves (total mass that has crossed the east face divided by the initial mass at the west face) are generated at the outflow face and compared over 1000000 years. Since breakthrough curves are normalized to initial mass, the concentration of the initial pulse is inconsequential.

The breakthrough curves for the SNL team can be seen in Figure 2-10. Tracer initially breaks through at ~0.5 years except for the sorbing DFN tracer, which initially breaks through at ~3 years. In the ECPM all

the tracer exits the domain earlier than the DFN, at ~1000 years for the conservative tracer. The same trend can be seen for the sorbing tracer as well. The decaying tracer for the DFN and ECPM exits the domain at ~320 years at a fraction of tracer of ~0.75. In order to assess the impact of the stochastic fractures on the domain, the four-fracture conservative breakthrough curves for ECPM and DFN compared to the four-fractures plus stochastic fractures are plotted in Figure 2-11. When adding the stochastic fractures to the domain we can see a bump in the breakthrough curve around 2.5 years for the DFN and around 8 years for the ECPM where the curves deviate from the four-fractures only breakthrough curve. This implies this delayed breakthrough time in the four-fracture plus stochastic fracture example is due to the addition of the stochastic fractures.

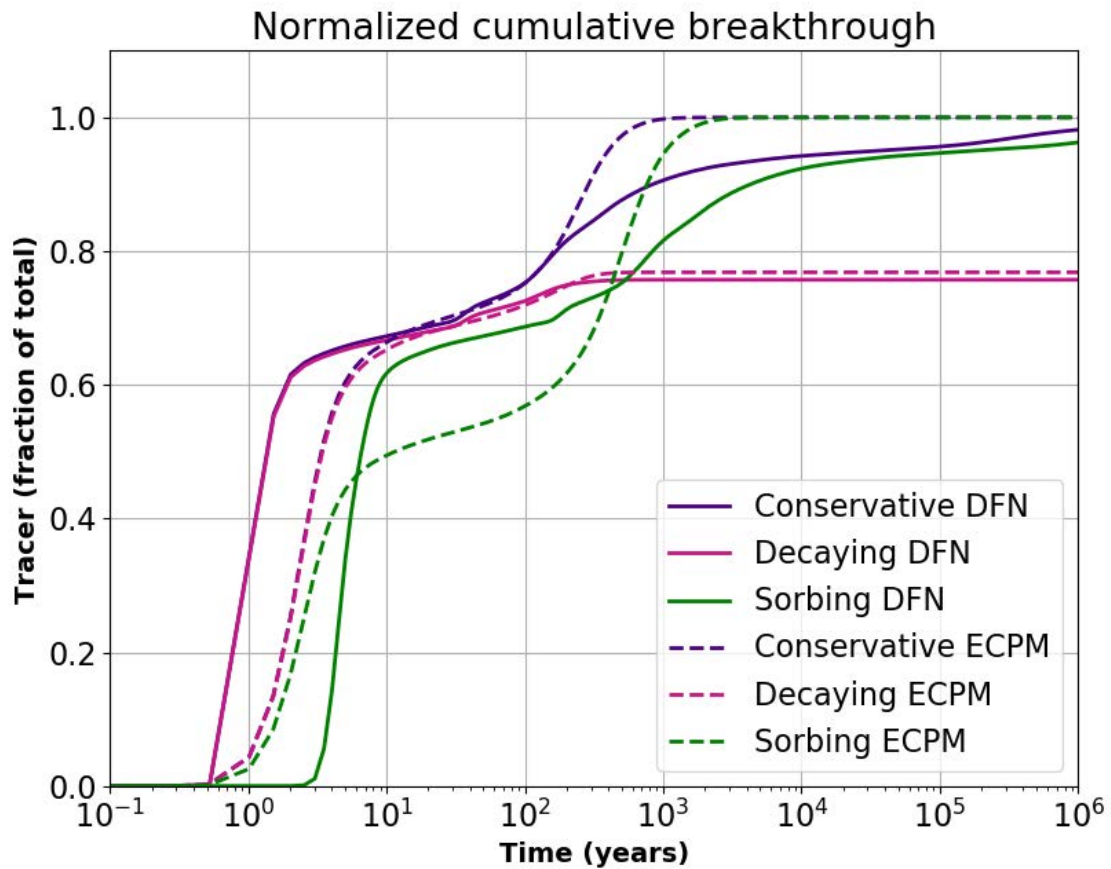


Figure 2-10. Breakthrough curves for DFN (solid line) and ECPM (dashed line).

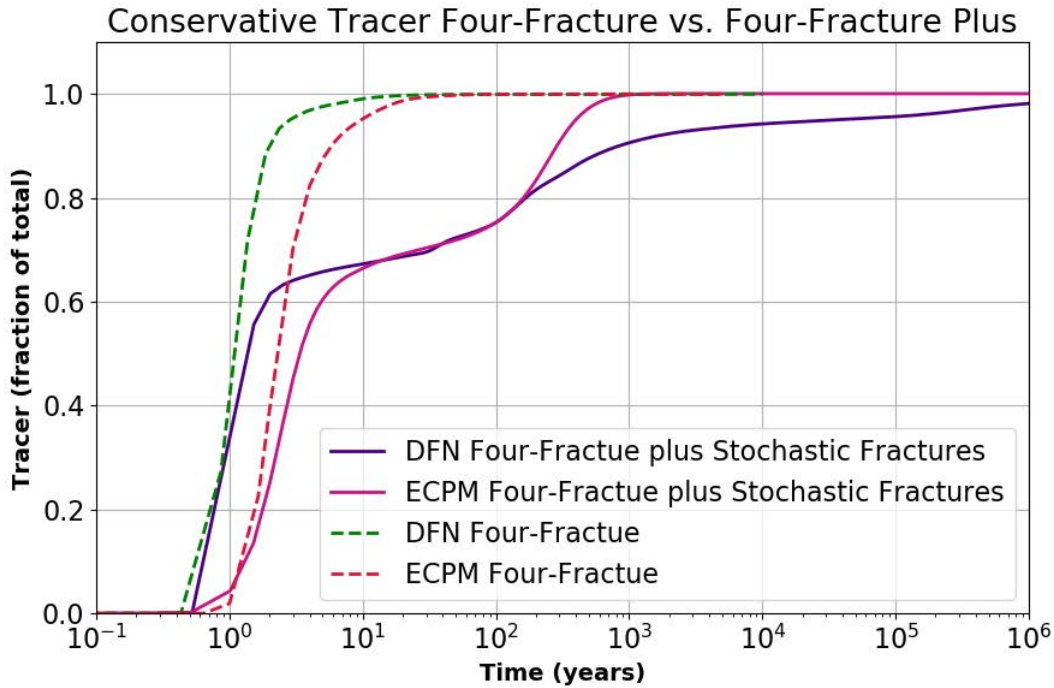


Figure 2-11. Breakthrough curve comparison of 4-Fracture DFN and 4-Fracture DFN with stochastic fractures with a conservative tracer.

### 2.1.2 Proposed Full Performance Assessment Model

The parameters stated here are as of June 2021 and are subject to change throughout the project. The volume of interest will be around 5 x 2 x 1 km<sup>3</sup> and a ~20 m/km slope over 2 km distance where the water table follows the topography. First transport will be done with a uniform source term across the repository to identify fast flow paths. Next, waste packages will be placed at the shortest distance to the preferential flow paths. Around 2500 waste packages will be simulated and ~50 waste packages will fail after a specified amount of time. Vertical emplacement will be used rather than horizontal emplacement. Both concentration and flux values will be used as a comparison.

## 2.2 Salt reference case

The salt reference scenario presented here will not focus on an undisturbed scenario for a salt repository. It has been shown through multiple performance assessments RESUS, KOMTESS, ISIBEL and VSG (Bollingfehr et al., 2008; Beuth et al., 2012; Bollingfehr et al., 2017; Bollingfehr et al., 2018; Bertrams et al., 2020a) that there are no radiological consequences within 1,000,000 years within salt formations because of their very low permeability and moisture content. Additionally, the integrity of rock salt is given for at least 1,000,000 years for salt rock barriers greater than 200 m in thickness (which is the scenario presented here), which provides no pathway through permeable anhydrite, boudinage, or isolated salt blocks. As a result, here we present a disturbed scenario in which the shaft seals fail 1000 years after repository closure, allowing an influx of brine down the shafts and into the repository.

For this task a staged development of models is planned, building up to a full PA. This stepwise process is done to ensure the validity of each team's modeling efforts as complexities are added. The planned staged development is:

1. Flow + radionuclide mobilization and transport (problem description will include variably saturated initial conditions)
2. + drift convergence (salt creep and backfill consolidation will be considered)
3. + heat flow and temperature-dependence of drift convergence
4. + model uncertainty in backfill consolidation model
5. (+ gas generation)

The description of the engineered and natural barrier systems will be updated as the exercise progresses so that necessary information is available at each stage of model development.

### **2.2.1 Geologic Setting**

The salt reference case considers a mined repository for spent nuclear fuel (SNF) and vitrified high-level waste (HLW). The repository is mined at a depth of 850 m below the ground surface. The generic geological cross section of a salt dome developed for the RESUS project (Bertrams et al. 2020b) is simplified to 6 homogeneous geologic units for use in this reference case (Figure 2-12). It is assumed that the salt dome geometry shown in Figure 2-12 extends for 9 km perpendicular to the plane of the cross section. The ground surface is at about 50 m above mean sea level (amsl) and the top of the salt dome is roughly -150 m amsl. The base of the salt diapir base is at about -3150 m and is underlain by basement rock, which extends to the base of the section at about -5500 m.

The geometry of the salt dome cross section will be provided to teams as a geometry file. Hydrologic, mechanical, and thermal properties of the upper five units are given in Section 2.2.4. Teams are expected to develop model domains that are considerably shallower than the section shown here. Thus, properties of the basement unit will not be needed.

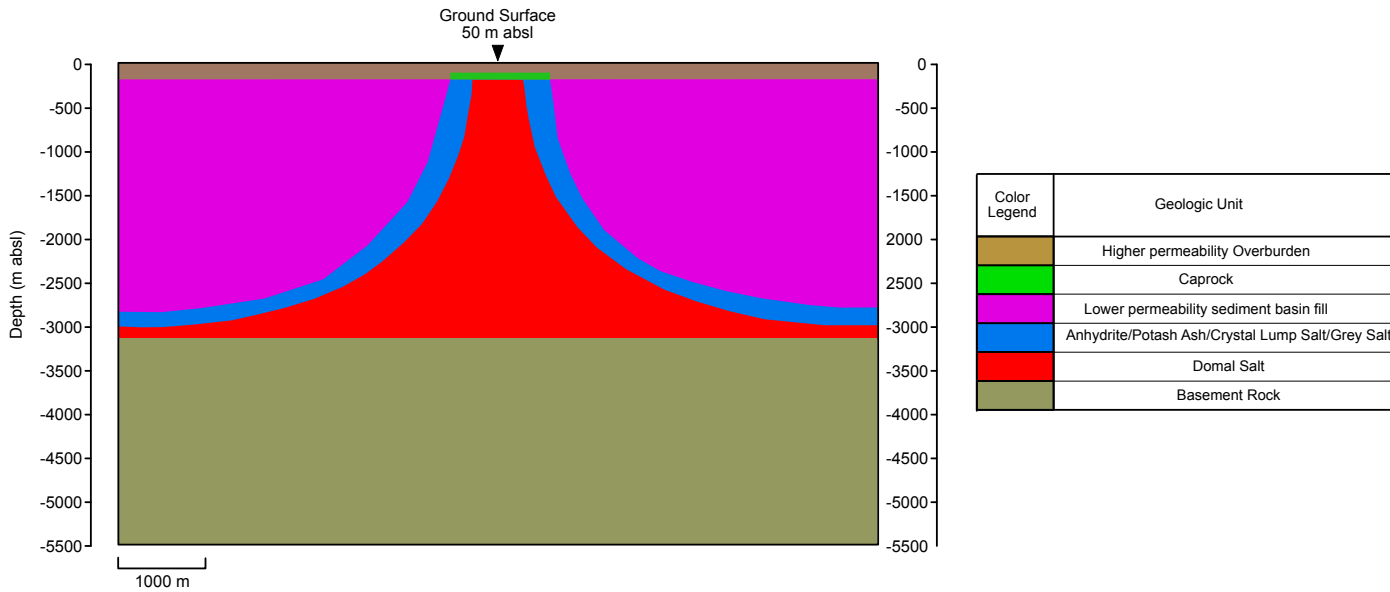


**Figure 2-12. Geological cross-section with model units for the generic salt reference case. The model units are simplified from Bertrams et al. (2020b). The repository is at a depth of 850 m in the domal salt.**

## 2.2.2 Inventory

To reduce the computational burden of this comparison exercise, the salt reference case assumes fairly small inventories of SNF and HLW. For the same reason, the radionuclides included in transport simulations are limited to a small set of mobile, long-lived fission products ( $^{129}\text{I}$  and  $^{235}\text{Cs}$ ) and a single transuranic decay chain ( $^{241}\text{Am} \rightarrow ^{237}\text{Np} \rightarrow ^{233}\text{U} \rightarrow ^{229}\text{Th}$ ), which includes ingrowth and decay of long-lived  $^{237}\text{Np}$ .

Additional radionuclides may be added as model development progresses.

### 2.2.2.1 Spent Nuclear Fuel

The reference case assumes that the inventory of SNF consists entirely of pressurized water reactor (PWR) assemblies packaged in 500 POLLUX-10 casks (described in Section 2.2.3.2), each of which contains (as the name suggests) 10 assemblies. Each assembly contains 0.435 metric tons heavy metal (MTHM) for a total of 2175 MTHM. To place this value in context, it is 3.1% of the 70,000 MTHM repository specified by the U.S. Nuclear Waste Policy Act and 20.7% of the total SNF inventory expected in Germany (Bertrams et al., 2020).

Following the example of previous reference cases developed in the U.S. program (e.g., Mariner et al. 2015; LaForce et al. 2020), the initial radionuclide inventory and heat of decay versus time for SNF is calculated assuming an initial enrichment of 4.73 wt%  $^{235}\text{U}$  and 60 GWd/MTHM burn-up (Appendix C, Carter et al. 2013). A storage time of 100 years out of reactor (OoR) prior to emplacement in the repository is assumed. In the U.S., the average burn-up of SNF assuming decommissioning without replacing existing nuclear power plants is predicted to be 54 GWd/MTHM (Carter et al. 2013). Therefore, the assumption of 60 GWd/MTHM results in a conservatively high heat load and will be used in later simulations, the first round of simulations will not include heat.

Inventories of radionuclides at the time of emplacement (Table 2-3) are expressed as grams radionuclide per MTHM and grams radionuclide per grams total waste. The former ratio includes only the initial mass of heavy metal (i.e., U) in the denominator; the latter ratio includes the total mass of the UO<sub>2</sub> ceramic waste form in the denominator. Table 2-3 also provides the atomic weight and decay constant for each radionuclide (isotope).

The heat of decay versus time for a POLLUX-10 cask containing 10 PWR assemblies (Table 2-4 and Figure 2-13) is calculated from the complete radionuclide inventories provided by Carter et al. (2013, Appendix C). At the time of emplacement (100 y OoR), the power output per POLLUX-10 cask is about 2400 W.

The first stage of model development (flow and transport) does not require implementation of a heat source term.

See Section 2.2.3.2 for characterization of the UO<sub>2</sub> waste form and the POLLUX-10 cask.

**Table 2-3. Inventory of selected radionuclides in PWR SNF at 100 y OoR.**

Isotope	Inventory (g/MTHM) <sup>1</sup>	Inventory (g/g waste) <sup>2</sup>	Atomic weight (g/mol) <sup>3</sup>	Approximate Decay Constant (1/s) <sup>4</sup>
<sup>241</sup> Am	1.46E+03	1.01E-03	241.06	5.08E-11
<sup>243</sup> Am	2.69E+02	1.87E-04	243.06	2.98E-12
<sup>238</sup> Pu	2.84E+02	1.97E-04	238.05	2.56E-10
<sup>239</sup> Pu	7.40E+03	5.14E-03	239.05	9.01E-13
<sup>240</sup> Pu	4.11E+03	2.85E-03	240.05	3.34E-12
<sup>242</sup> Pu	8.17E+02	5.67E-04	242.06	5.80E-14
<sup>237</sup> Np	1.40E+03	9.72E-04	237.05	1.03E-14
<sup>233</sup> U	4.33E-02	3.01E-08	233.04	1.38E-13
<sup>234</sup> U	5.11E+02	3.55E-04	234.04	8.90E-14
<sup>236</sup> U	6.27E+03	4.35E-03	236.05	9.20E-16
<sup>238</sup> U	9.10E+05	6.32E-01	238.05	4.87E-18
<sup>229</sup> Th	1.48E-05	1.03E-11	229.03	2.78E-12
<sup>230</sup> Th	1.04E-01	7.22E-08	230.03	2.75E-13
<sup>226</sup> Ra	3.99E-05	2.77E-11	226.03	1.37E-11
<sup>36</sup> Cl	5.01E-01	3.48E-07	35.97	7.30E-14
<sup>99</sup> Tc	1.28E+03	8.89E-04	98.91	1.04E-13
<sup>129</sup> I	3.13E+02	2.17E-04	128.9	1.29E-15
<sup>135</sup> Cs	7.72E+02	5.36E-04	134.91	9.55E-15

<sup>1</sup>from Carter et al. (2013, Table C-2)

<sup>2</sup>(g isotope/g waste) = (g isotope/MTHM)/(g waste/MTHM), where g waste = g all isotopes

<sup>3</sup>Weast and Astle (1981)

<sup>4</sup>Decay constants from ORIGEN (Croff, 1983)

Table 2-4. Heat output per POLLUX-10 cask as function of time.

Time (y) <sup>a</sup>	Heat (W)	Time (y) <sup>a</sup>	Heat (W)
0.0E+00	2.381E+03	4.5E+02	5.673E+02
1.0E+00	2.356E+03	5.0E+02	5.326E+02
2.0E+00	2.332E+03	6.0E+02	4.750E+02
3.0E+00	2.309E+03	7.0E+02	4.287E+02
4.0E+00	2.286E+03	8.0E+02	3.904E+02
5.0E+00	2.263E+03	9.0E+02	3.582E+02
6.0E+00	2.241E+03	1.0E+03	3.309E+02
7.0E+00	2.219E+03	1.2E+03	2.875E+02
8.0E+00	2.197E+03	1.4E+03	2.555E+02
9.0E+00	2.176E+03	1.6E+03	2.315E+02
1.0E+01	2.156E+03	1.8E+03	2.134E+02
2.0E+01	1.969E+03	2.0E+03	1.996E+02
3.0E+01	1.814E+03	2.5E+03	1.770E+02
4.0E+01	1.683E+03	3.0E+03	1.636E+02
5.0E+01	1.572E+03	3.5E+03	1.546E+02
6.0E+01	1.478E+03	4.0E+03	1.476E+02
7.0E+01	1.396E+03	4.5E+03	1.416E+02
8.0E+01	1.325E+03	5.0E+03	1.363E+02
9.0E+01	1.263E+03	6.0E+03	1.267E+02
1.0E+02	1.208E+03	7.0E+03	1.182E+02
1.2E+02	1.116E+03	8.0E+03	1.104E+02
1.4E+02	1.041E+03	9.0E+03	1.032E+02
1.6E+02	9.778E+02	1.0E+04	9.672E+01
1.8E+02	9.243E+02	1.5E+04	7.151E+01
2.0E+02	8.780E+02	2.0E+04	5.491E+01
2.5E+02	7.846E+02	2.5E+04	4.362E+01
3.0E+02	7.128E+02	3.0E+04	3.568E+01
3.5E+02	6.552E+02	3.5E+04	2.989E+01
4.0E+02	6.076E+02	4.0E+04	2.552E+01
4.5E+02	5.673E+02	4.5E+04	2.213E+01
5.0E+02	5.326E+02	5.0E+04	1.942E+01
6.0E+02	4.750E+02	6.0E+04	1.539E+01
7.0E+02	4.287E+02	7.0E+04	1.259E+01
8.0E+02	3.904E+02	8.0E+04	1.058E+01
9.0E+02	3.582E+02	9.0E+04	9.126E+00
1.0E+03	3.309E+02	1.0E+05	8.065E+00
1.2E+03	2.875E+02	2.0E+05	5.337E+00
1.4E+03	2.555E+02	3.0E+05	5.021E+00
1.6E+03	2.315E+02	4.0E+05	4.624E+00
1.8E+03	2.134E+02	5.0E+05	4.196E+00
2.0E+03	1.996E+02	6.0E+05	3.802E+00
2.5E+03	1.770E+02	7.0E+05	3.463E+00
3.0E+03	1.636E+02	8.0E+05	3.180E+00
3.5E+03	1.546E+02	9.0E+05	2.944E+00
4.0E+03	1.476E+02	1.0E+06	2.749E+00

<sup>a</sup> Time of emplacement (100 y OoR) is 0 y in this table.

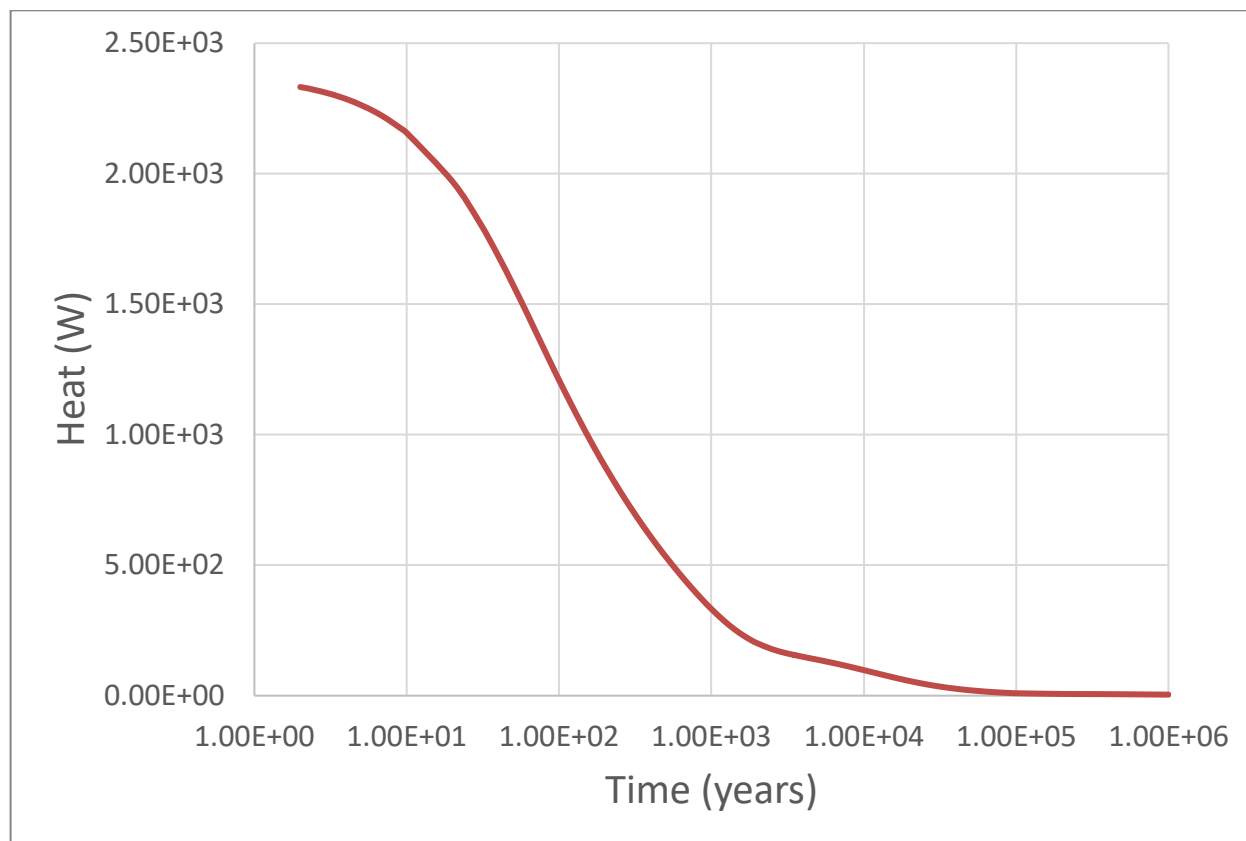


Figure 2-13. Heat vs. time for POLLUX-10 after 100 yr OoR; plotted using values in Table 2-4.

### 2.2.2.2 High Level Waste

The salt reference case includes vitrified high-level waste resulting from the reprocessing of spent nuclear fuel. The characteristics of the vitrified waste form are based on the COGEMA vitrified waste from the Dutch fuel cycle (GRS 2012). In total, the operation of two nuclear power plants in the Netherlands is expected to result in 478 canisters of vitrified HLW. The reference case assumes a nominal inventory of 500 HLW canisters, each containing 400 kg of waste. The waste, which is 11.3% fission products and 2.2% actinides by mass, is aged 130 years before emplacement in the repository.

Selected radionuclide inventories at the time of emplacement (waste aged 130 y) expressed in Bq per canister, grams per canister, and grams per gram vitrified waste (glass) are given in Table 2-5.

The heat of decay versus time for an HLW canister containing 400 kg waste (Table 2-6 and Figure 2-14) is calculated from the complete radionuclide inventories provided by (Kienzler et al., 2012). At the time of emplacement, the power output per canister is about 120 W.

The first stage of model development (flow and transport) does not require implementation of a heat source term.

See Section 2.2.3.3 for characteristics of the glass waste form and the stainless-steel canister.

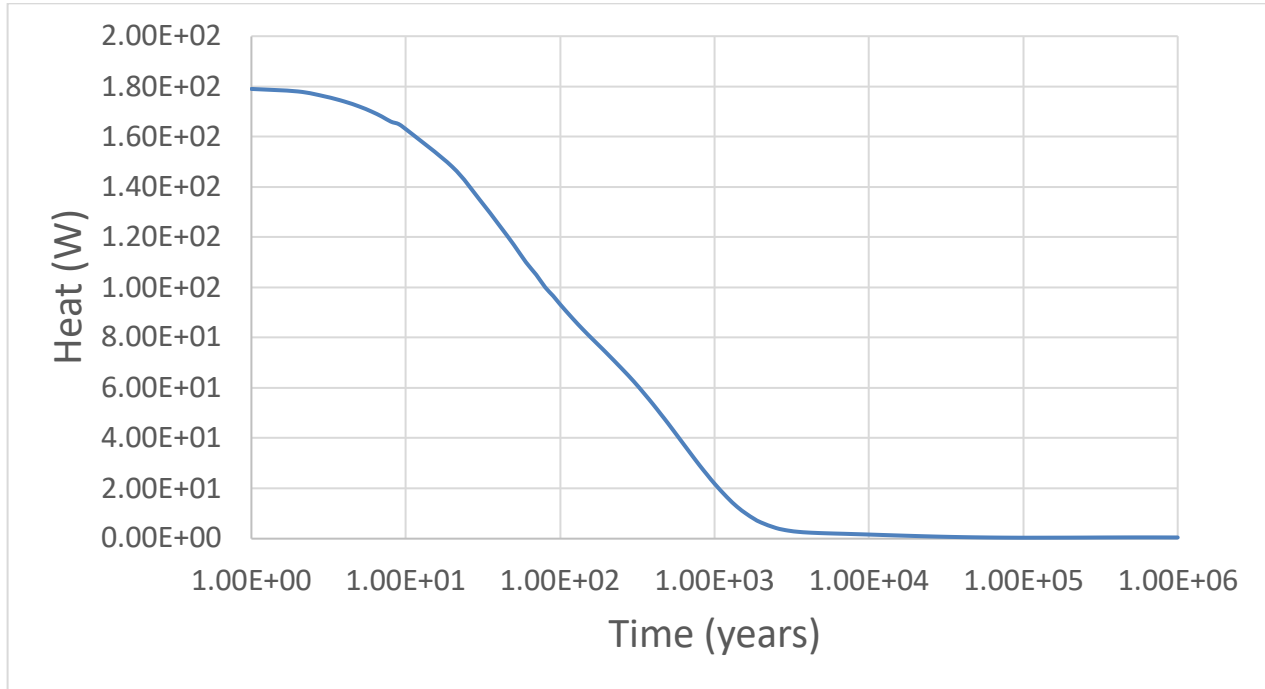


Figure 2-14. Heat vs. time for a single HLW canister aged 130 y; plotted using values in Table 2-6.

Table 2-5. Inventory of selected radionuclides in HLW aged 130y.

Isotope	Inventory (Bq/canister) <sup>a</sup>	Inventory (g/canister)	Inventory (g/g glass) <sup>b,c</sup>
<sup>241</sup> Am	1.06E+14	8.35E+02	2.09E-03
<sup>243</sup> Am	2.57E+12	3.48E+02	8.71E-04
<sup>238</sup> Pu	4.78E+11	7.55E-01	1.89E-06
<sup>239</sup> Pu	1.44E+11	6.26E+01	1.57E-04
<sup>240</sup> Pu	2.31E+11	2.74E+01	6.85E-05
<sup>242</sup> Pu	1.01E+09	7.15E+00	1.79E-05
<sup>237</sup> Np	4.80E+10	1.84E+03	4.60E-03
<sup>233</sup> U	3.20E+06	8.93E-03	2.23E-08
<sup>234</sup> U	4.77E+08	2.06E+00	5.16E-06
<sup>236</sup> U	4.21E+07	1.76E+01	4.40E-05
<sup>238</sup> U	5.53E+07	4.45E+03	1.11E-02
<sup>229</sup> Th	1.17E+04	1.49E-06	3.72E-12
<sup>230</sup> Th	1.68E+05	2.25E-04	5.62E-10
<sup>226</sup> Ra	1.03E+02	2.82E-09	7.04E-15
<sup>36</sup> Cl	-	-	-
<sup>99</sup> Tc	1.25E+12	1.99E+03	4.98E-03
<sup>129</sup> I	-	-	-
<sup>135</sup> Cs	3.01E+10	7.07E+02	1.77E-03

<sup>a</sup> Radionuclide inventory in COGEMA glass from GRS, 2012.  
<sup>b</sup> assuming 400 kg vitrified waste per canister  
<sup>c</sup> Refer to Table 2-3 for atomic weights and decay constants.

Table 2-6. Heat output per HLW canister as function of time.

Time (y) <sup>a</sup>	Heat (W)	Time (y) <sup>a</sup>	Heat (W)
0.0E+00	1.17E+02	1.4E+03	1.26E+01
1.0E+00	1.79E+02	1.6E+03	9.89E+00
2.0E+00	1.78E+02	1.8E+03	7.84E+00
3.0E+00	1.76E+02	2.0E+03	6.35E+00
4.0E+00	1.74E+02	2.5E+03	4.15E+00
5.0E+00	1.72E+02	3.0E+03	3.12E+00
6.0E+00	1.70E+02	3.5E+03	2.62E+00
7.0E+00	1.68E+02	4.0E+03	2.36E+00
8.0E+00	1.66E+02	4.5E+03	2.21E+00
9.0E+00	1.65E+02	5.0E+03	2.10E+00
1.0E+01	1.63E+02	6.0E+03	1.95E+00
2.0E+01	1.48E+02	7.0E+03	1.84E+00
3.0E+01	1.35E+02	8.0E+03	1.73E+00
4.0E+01	1.25E+02	9.0E+03	1.64E+00
5.0E+01	1.17E+02	1.0E+04	1.55E+00
6.0E+01	1.10E+02	1.5E+04	1.20E+00
7.0E+01	1.05E+02	2.0E+04	9.68E-01
8.0E+01	1.00E+02	2.5E+04	8.00E-01
9.0E+01	9.66E+01	3.0E+04	6.79E-01
1.0E+02	9.32E+01	3.5E+04	5.90E-01
1.2E+02	8.77E+01	4.0E+04	5.23E-01
1.4E+02	8.33E+01	4.5E+04	4.71E-01
1.6E+02	7.97E+01	5.0E+04	4.30E-01
1.8E+02	7.66E+01	6.0E+04	3.72E-01
2.0E+02	7.38E+01	7.0E+04	3.35E-01
2.5E+02	6.77E+01	8.0E+04	3.11E-01
3.0E+02	6.25E+01	9.0E+04	2.96E-01
3.5E+02	5.77E+01	1.0E+05	2.87E-01
4.0E+02	5.34E+01	2.0E+05	3.19E-01
4.5E+02	4.94E+01	3.0E+05	3.67E-01
5.0E+02	4.58E+01	4.0E+05	3.94E-01
6.0E+02	3.93E+01	5.0E+05	4.07E-01
7.0E+02	3.38E+01	6.0E+05	4.10E-01
8.0E+02	2.91E+01	7.0E+05	4.07E-01
9.0E+02	2.52E+01	8.0E+05	4.00E-01
1.0E+03	2.18E+01	9.0E+05	3.92E-01
1.2E+03	1.65E+01	1.0E+06	3.82E-01

<sup>a</sup> Time of emplacement (aged 130 y) is 0 y in this table.

## 2.2.3 Engineered Barrier System

### 2.2.3.1 Repository Layout

The repository, located at a depth of 850 m, is accessed by two shafts that extend vertically out of the salt dome formation through the cap rock and to the surface. The access shafts are designed this way based on the design of the shaft seal as it is specifically engineered to be an effective seal within a salt formation. Within the repository there are three sets of 25 emplacement drifts with a drift spacing of 35 m. For heat-generating waste, the waste package spacing is 3 m end-to-end in an emplacement drift 90 m long with a total of 10 waste packages per drift for a total of 500 POLLUX-10 waste packages. The vitrified waste emplacement area consists of 25 emplacement drifts with 35 m drift spacing, each drift containing 10 vertical boreholes with a center-to-center spacing of 4.5 m in an emplacement drift 45 m long with two

waste packages per borehole for a total of 500 vitrified waste packages (Table 2-7). The spacing of the drifts and waste packages is sufficient to ensure that peak temperatures do not exceed 100°C (Figure 2-15). The dimensions of drifts within the repository are the same, at 7 m width and 4 m height. The infrastructure has a total volume of 240000 m<sup>3</sup>, with dimensions of 240 m × 250 m × 4 m. The infrastructure is utilized during the construction and emplacement phases of disposal. During the post-closure phase this area is filled with gravel to allow for excess fluid or gas buildup to accumulate.

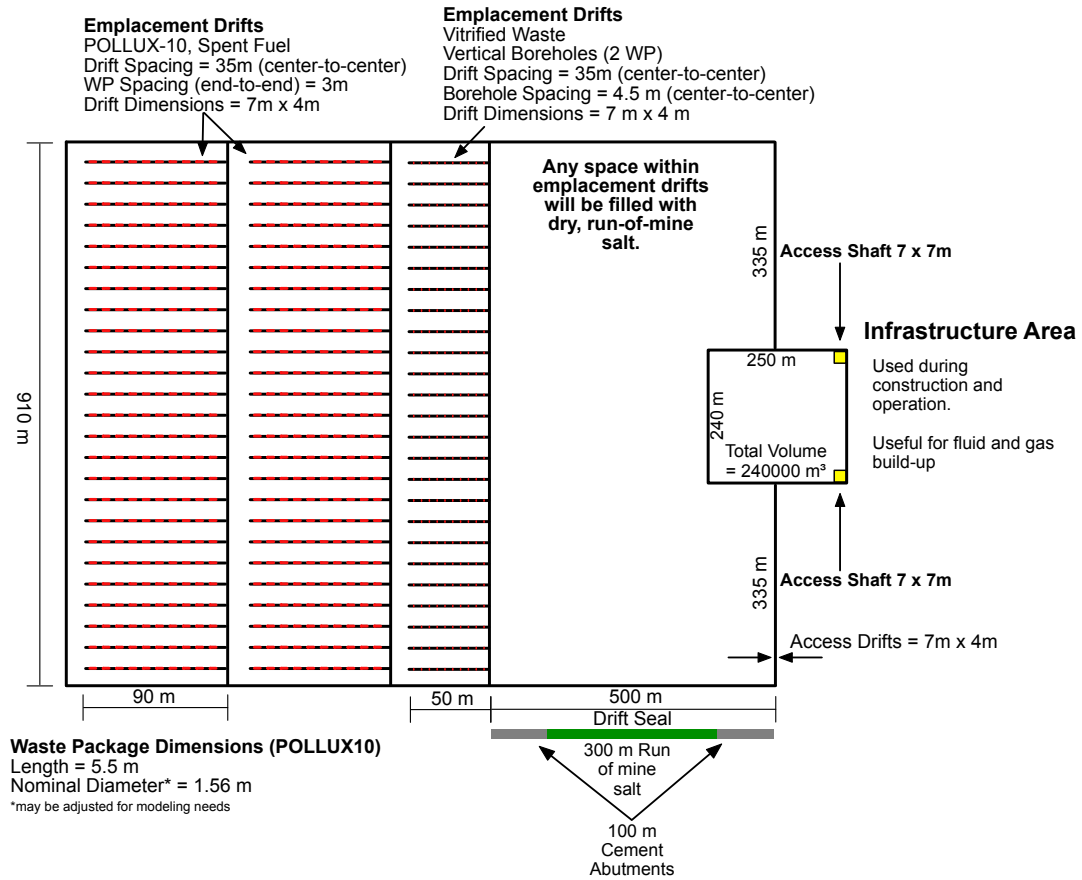


Figure 2-15. Schematic of the waste repository in a generic salt dome.

Table 2-7. Dimensions for components of repository layout.

	Number	Width (m)	Height (m)	Length (m)	Spacing (m)
SNF Drifts	50	7	4	90	35 (center-to-center)
HLW Drifts	25	7	4	50	35 (center-to-center)
Access Shafts	2	7	850	7	240 – (7*2) (edge-to-edge)
Infrastructure Area	1	240	4	250	-
POLLUX-10	500	-	1.56*	5.5	3 (end-to-end)
Boreholes	250	1.5 <sup>†</sup>	-	1.5 <sup>†</sup>	4.5 (center-to-center)
Drift Seals	2	7	4	500	-

\*diameter of POLLUX-10 cask; may be adjusted for modeling needs  
<sup>†</sup>diameter of borehole

### 2.2.3.2 Spent Nuclear Fuel Waste Form and Waste Container

#### SNF Waste Form

The SNF waste form is spent uranium oxide (UO<sub>2</sub>) fuel pellets encased in tubes of Zircaloy cladding. UO<sub>2</sub> is a polycrystalline ceramic material that is stable to high temperatures and has the potential for slow degradation in the disposal environment (Freeze et al. 2013). The reference case neglects any protection that the Zircaloy cladding may provide.

In the reactor, fuel undergoes physical changes due to heating, radiation damage, and the build-up of fission products. Concentration of lighter elements along margins of the UO<sub>2</sub> matrix and in gaps in the waste form results in radionuclide release in two fractions: instant-release (upon failure of the waste canister) and slow-release (as the UO<sub>2</sub> matrix degrades).

Radioisotopes such as Nickel-60 accumulate in the metal components of a fuel assembly due to irradiation. These are neglected in this simplified comparison exercise.

*Safety function:* Slow degradation of the UO<sub>2</sub> waste form limits radionuclide release.

#### Instant Release Fraction

The salt reference case considers two radionuclides (<sup>129</sup>I and <sup>135</sup>Cs) with nonzero instant release fractions (IRF). The best estimate and pessimistic values for IRF of iodine and cesium from 60 GWd/MTHM-burnup SNF are 10% and 16% (Johnson et al. 2005 cited in Sassani et al. 2016). These values plus those for other light elements are listed in Table 2-8. The salt reference case assumes an IRF of 10% for both <sup>129</sup>I and <sup>135</sup>Cs, as this is the best estimate in Sassani et al. (2016).

Table 2-8. Instant release fractions from Johnson et al. (2005) cited in Sassani et al. (2016).

Element	Best Estimate IRF (%)	Pessimistic IRF (%)
C	10	–
Cl	5	–
Sr, Tc	7	11
I, Cs	10	16

***UO<sub>2</sub> Degradation Model***

The reference case assumes that fuel matrix (UO<sub>2</sub>) dissolution occurs when the POLLUX-10 container fails (and the disposal drift is completely liquid saturated, for simplicity). Dissolution proceeds at a fractional rate of 10<sup>-7</sup>/yr. This rate is the mode of a log triangular distribution (Table 2-9) appropriate for fuel 3,000-10,000 years OoR and strongly reducing conditions (Werme et al. 2004; Ollila 2008); for a complete discussion refer to Sassani et al. (2016, Section 3.2.1). Congruent release of radionuclides is assumed, and radionuclide inventories in the waste form are updated with time to account for decay and ingrowth.

**Table 2-9. SNF dissolution rates; log triangular distribution from Werme et al. (2004) cited in Sassani et al. (2016, Section 3.2.1).**

<b>Parameter</b>	<b>Rate (yr<sup>-1</sup>)</b>	<b>Time to 50% dissolution (yr)</b>	<b>Time to 99% dissolution (yr)</b>
Min	10 <sup>-8</sup>	6.93 x 10 <sup>7</sup>	4.61 x 10 <sup>8</sup>
Mode	10 <sup>-7</sup>	6.93 x 10 <sup>6</sup>	4.61 x 10 <sup>7</sup>
Max	10 <sup>-6</sup>	6.93 x 10 <sup>5</sup>	4.61 x 10 <sup>6</sup>

**POLLUX-10 Cask**

A POLLUX® type container is utilized as the reference container. The POLLUX® container was conceived and designed for final disposal in salt (Figure 2-16). It consists of an inner and an outer container. The inner container is made of fine-grained structural steel (material 1.6210) and is tightly sealed by a bolted primary cover and a welded secondary cover. The interior is divided into several chambers, into each of which a fuel rod can be inserted with fuel rods of two PWR-BE or six BWR-BE. Figure 2-16 shows an example of a POLLUX® container with the drawn fuel rods from ten PWR fuel assemblies (POLLUX®-10). The outer shielding vessel, like the primary and secondary covers, is made of nodular cast iron (material 0.7040). This shielding vessel has no sealing function to perform and is closed with a bolted cover. In the shell, rods made of polyethylene are inserted in radially distributed holes to reduce the neutron dose rate. The structural container design and the choice of materials ensure the basic requirements for retrievability in the operational phase. Therefore, the POLLUX-10 cask is assumed to contain the waste for 500 years and to provide no containment after 500 y (BMU 2010).

The cask shown below has a length of 5.517 m and a diameter of 1.56 m. For the reference case, a nominal length of 5.5 m is assumed. The diameter of 1.56 m is retained, although it is recognized that individual teams may need to adjust the cross-sectional area of the cask to simplify modeling.

*Safety function:* The Pollux-10 cask contains the waste for 500 years; it provides no safety function after 500 years.

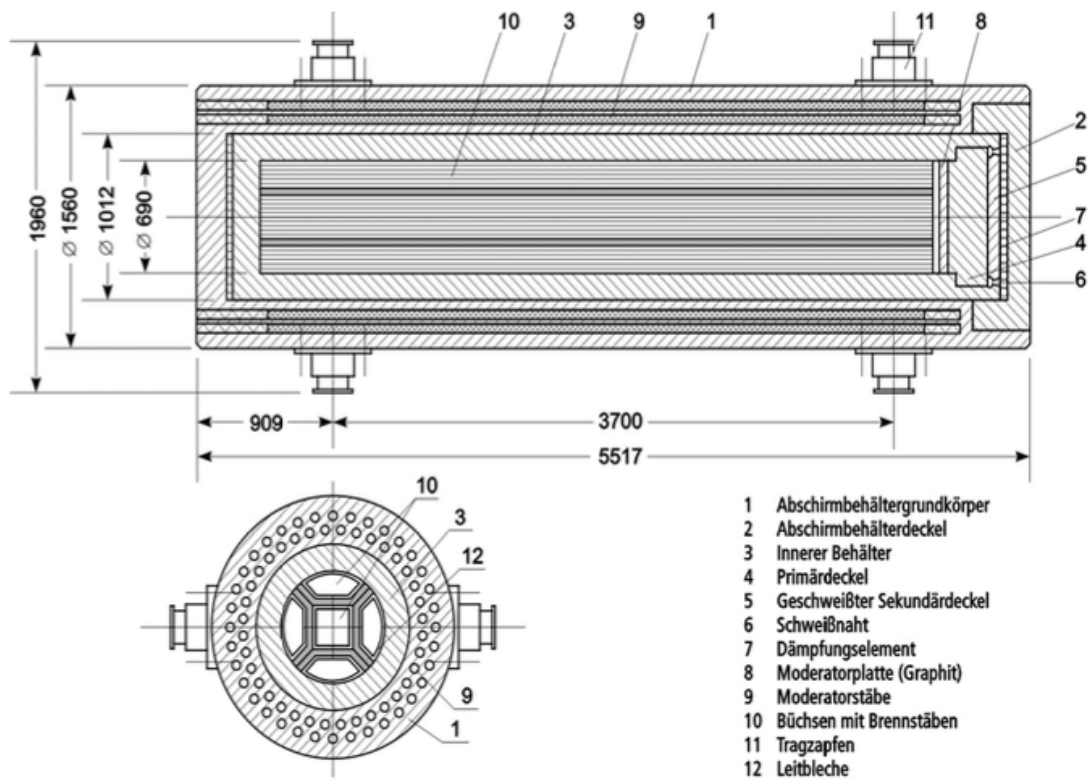


Figure 2-16. Schematic of the POLLUX-10 waste container. 1. Shielding body; 2. Shielding cover; 3. Inner tank; 4. Primary cover; 5. Secondary (welded) cover; 6. Welding seam; 7. Damping element; 8. Moderator plate (graphite); 9. Moderator staff; 10. Bushings with fuel rods; 11. Trunnion; 12. Guide plate (from Bertrams et al. 2020a).

### 2.2.3.3 HLW and Waste Container

#### Vitrified HLW in Stainless Steel Canister

The vitrified (glass) waste is formed in stainless steel canisters with a height of 1.335 m and an outer diameter of 0.430 m (Figure 2-17). The canisters have a mass of 100 kg when empty. Each canister contains a nominal inventory of 400 kg of vitrified waste. The reference case assumes that the thin-walled stainless steel canister provides no containment function, i.e., the glass waste form dissolves when brine is present.

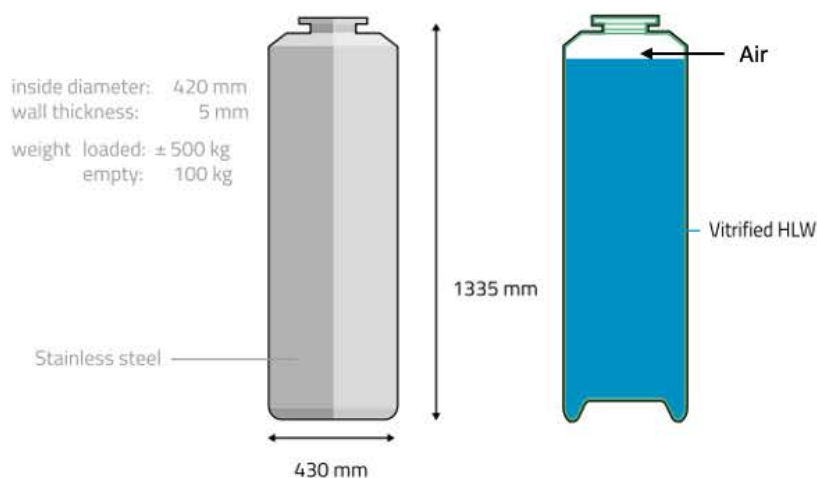


Figure 2-17. Stainless steel canister for vitrified HLW.

### *Glass dissolution model*

Glass dissolution rate depends on many factors, including local pore fluid chemistry, temperature, and glass surface area; and will slow with time as pore fluids become saturated with  $\text{SiO}_{2(\text{aq})}$  and a surface alteration layer forms (Sassani et al. 2016, Section 3.2.2). This latter stage of dissolution (stage II dissolution, Vienna et al. 2013) is typically assumed to represent long-term dissolution rates for repository modeling (Sassani et al. 2016). The salt reference case uses an empirical rate law fitted to temperature (Kienzler et al. 2012) to model the long-term dissolution of glass:

$$R = 560 \times \exp\left(\frac{-7397}{T}\right) \quad (2 - 15)$$

Where the dissolution rate,  $R$ , has the units  $\text{kg m}^{-2} \text{d}^{-1}$  and  $T$  is temperature in Kelvin. The rate law is appropriate for dilute and saline solutions.

Initial flow and transport simulations assume a reference temperature of  $38^\circ \text{C}$  (Bauer et al. 2011).

The surface area of the glass is calculated from the cylindrical geometry of the glass and an exposure factor ( $f_{\text{exposure}}$ ), a number greater than 1 that accounts for additional reactive surface area due to cracking and roughness (Sassani et al. 2016):

$$S = f_{\text{exposure}}A \quad (2 - 16)$$

where  $S$  is the reactive surface area of the glass and  $A$  is the geometric surface area of the glass. Surface area decreases with time, and can be calculated as a function of the specific geometric surface area ( $s_a$  [ $\text{m}^2/\text{kg}$ ]) and the remaining mass of glass ( $M$  [ $\text{kg}$ ]):

$$A = s_a M \quad (2 - 17)$$

Given a nominal density of  $2754 \text{ kg/m}^3$  for COGEMA glass (Kienzler 2012), a mass of 400 kg, and a diameter of 0.42 m, the glass cylinder has a volume of  $0.145 \text{ m}^3$  and a geometric surface area of  $1.66 \text{ m}^2$ . Kienzler et al. (2012) estimates  $f_{\text{exposure}} = 10$ . Therefore, the specific geometric surface area is  $0.004 \text{ m}^2/\text{kg}$  and the specific reactive surface area is 10 times larger. A triangular distribution for  $f_{\text{exposure}}$  is proposed by Strachan (2014) with a minimum and mode of 4 and a maximum of 17. This distribution may be applied to the reference case when we address uncertainty.

Congruent release of radionuclides is assumed, and radionuclide inventories in the waste form are updated with time to account for decay and ingrowth.

*Safety function:* Slow dissolution of the glass waste form limits radionuclide release.

### 2.2.3.4 HLW Emplacement

#### HLW Overpack

Each vitrified HLW canister is placed in an overpack. The overpack has a total length of 1.745 m, with a 0.20-m-long, air-filled crumple zone at the top (Figure 2-18).

*Safety function:* The HLW overpack is not assigned a post-closure safety function.

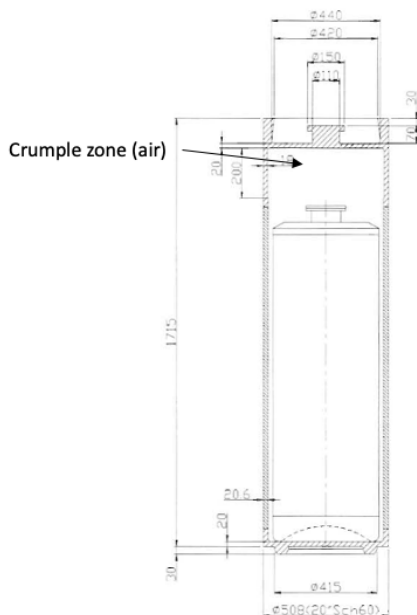
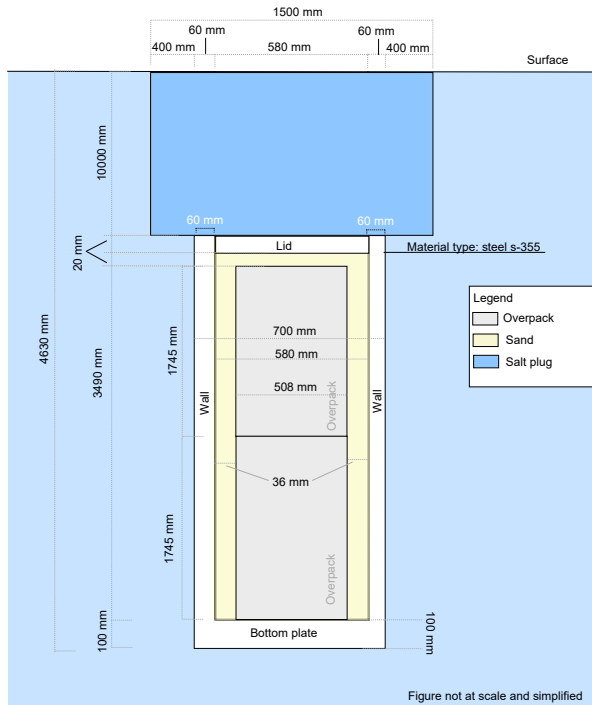


Figure 2-18. Canister dimensions for vitrified HLW.

#### Vertical Emplacement Borehole

Two overpacks are emplaced in a vertical borehole, one on top of the other, in the floor of a waste emplacement drift. The emplacement borehole is 14-m in length (Figure 2-19) (Poley 1999). The two overpacks sit in the lowest 4 m of the borehole, where the borehole is 0.7 m in diameter, lined with steel and backfilled with sand. A salt plug sits in the upper 10 m of the borehole, which is 1.5 m in diameter.



**Figure 2-19. Dimensions for vertical borehole emplacement for vitrified HLW canisters.**

The lower borehole (containing vitrified HLW in canisters and overpacks, sand backfill, and steel lining) will be assigned bulk properties. Bulk porosity is estimated from the void space in the HLW canister, overpack, and sand backfill. Permeability is left up to each modeling team to determine. As the staged modeling progresses, it is proposed that representative thermal and mechanical properties be based on the properties of borosilicate glass.

The salt plug is assigned the same properties as the run-of-mine salt that backfills the drift as discussed in the next section. This assumption results in conservatively high permeability and porosity, because in practice, the salt plug would be pre-compacted at the time of emplacement.

*Safety function:* The salt plug provides shielding during the operational phase of the repository and limits radionuclide transport after closure. Materials within the lower borehole have no post-closure safety function.

### 2.2.3.5 Disposal Drift Backfill

To ensure durable and long-term stable void filling, the backfill material should be the salt run of mine rock produced during excavation, and thus the same salt rock as the surrounding geologic barrier. Due to the compaction of the salt run of mine rock backfill, the backfill will develop a sealing effect over time that is comparable to that of the surrounding, undisturbed geological barrier. The time required to reach the final states ranges from several tens to several thousands of years, depending on the convergence rate, moisture content and ambient temperature (Bertrams et al., 2020). For this reason, additional geotechnical closure structures such as shaft and drift closures are provided, which have a specified sealing effect immediately after closure of the repository. In particular, the access of surface, overburden and formation waters to the emplacement areas must be prevented at the time of closure of the repository or must be sufficiently small.

*Safety function:* Upon reconsolidation of the backfill, its low permeability and porosity limit the volume of water that comes in contact with waste and limit radionuclide transport.

### **2.2.3.6 Infrastructure Area Gravel Backfill**

The shaft landing station and the infrastructure area are backfilled with gravel which has negligible compaction capabilities, and which forms permanent pore storage to significantly delay an increase in brine pressure at the drift seals. The infrastructure area (Figure 2-15) will be backfilled with gravel and will act as a reservoir for fluids intruding from the host rock or via the shafts. The access drifts are separated from the infrastructure area by drift seals. They are to be backfilled with run-of-mine salt with a moisture content of 0.6 % to enhance the backfill compaction. The fluid pressure will be mainly controlled by the enclosed mine air.

*Safety function:* The gravel backfill provides a high porosity reservoir for fluids intruding from the host rock or via the shafts, thus allowing fluids to accumulate in the infrastructure area without causing increased pore fluid pressures in other areas of the repository.

### **2.2.3.7 Drift Seals**

Immediately after emplacement of a repository container in a drift, the remaining drift space will be backfilled with naturally dry run of mine salt rock. Crosscuts, directional drifts and borehole crossover drifts are backfilled with natural dry run of mine salt rock. The directional drifts are sealed with two drift seals near the shaft, and the cavity between the drift seals is backfilled with moistened run of mine salt.

For reasons of long-term stability, the drift closures are of Sorel concrete, analogous to the lowest sealing element of the shaft closure (see Section 2.2.3.8). In each directional section, two sealing elements, each 100 m long, are provided, which are fixed by abutments, also made of Sorel concrete. Moistened run of mine salt is placed between the two sealing elements along a 300 m section. This type of positioning between two sealing elements prevents the moisture from the run of mine salt from being squeezed out by the convergence of the rock towards the emplacement areas or infrastructure area. The moisture of the salt crust accelerates its compaction and thus the reduction of its permeability. The section seals are positioned in the directional sections between the emplacement areas and the infrastructure area.

The development considered for the generic repository system assumes that the run of mine salt introduced into the drifts as backfill will, by reaction, develop a hydraulic sealing effect in the long term that is comparable to that of the existing, undisturbed geological rock salt barrier. Depending on the convergence rate, moisture content and ambient temperature, the time required to achieve the necessary low boundary porosity ranges from a few thousand to a few tens of thousands of years (Bertrams et al., 2020b). Therefore, the repository concept additionally provides for geotechnical closure structures such as shaft and drift closures made of salt or Sorel concrete, which have a specified sealing effect immediately after closure of the repository. In this way, the access of surface, overburden and formation waters to the emplacement areas is already prevented or kept sufficiently small at the time of closure of the repository.

*Safety function:* Provide long-term separation of surface, overburden, and/or formation waters from emplacement drifts keeping liquid saturation near waste packages minimal.

### **2.2.3.8 Shaft Design**

Access to the repository is provided by two shafts connecting the infrastructure area to the ground surface. The shafts are 850 m tall with a 7 m by 7 m cross section. A layered shaft seal design similar to the illustration in Figure 2-20 with properties from Table 2-10 may be implemented as model development progresses. This design contains segments designed to seal and segments designed to act as reservoirs. The uppermost sealing segment is bentonite, which would limit advection due to its low permeability and retard radionuclide transport due to adsorption.

For the initial simulation of flow and transport, distinct features of the shaft seal are ignored, and bulk hydrologic properties are assumed. The assumed bulk permeability of the shaft seal changes at the time of failure: Prior to shaft seal failure, the bulk permeability is  $5 \times 10^{-17} \text{ m}^2$ ; after shaft seal failure at 1000 years, the bulk permeability is  $5 \times 10^{-15} \text{ m}^2$ .

*Safety function:* The shaft seals limit ingress of water to the repository and limit advective radionuclide transport. In the shaft seal failure scenario, the shaft seals fail to perform these safety functions.

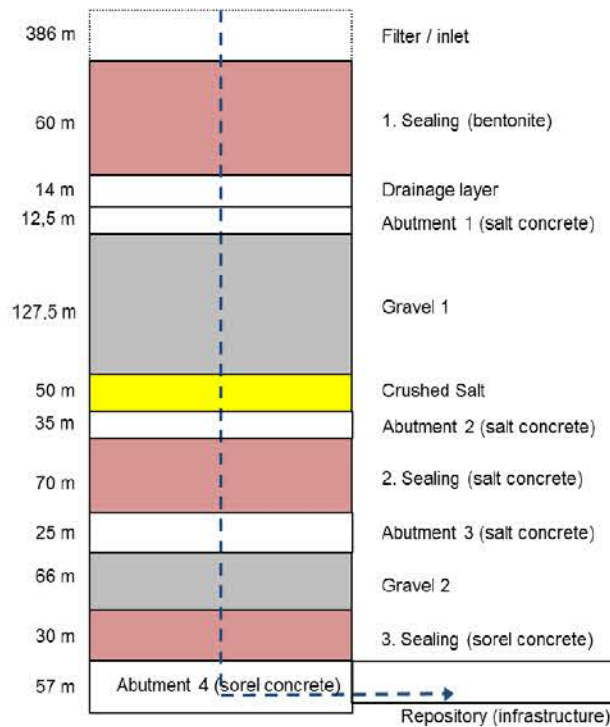


Figure 2-20. Shaft seal for generic salt dome repository (GRS 415).

**Table 2-10. Material properties for use in initial flow and transport simulations.**

	Intrinsic Permeability (m <sup>2</sup> )	Porosity (-)	Tortuosity (-) <sup>j</sup>	Effective Diffusion Coefficient (m <sup>2</sup> /s) <sup>k</sup>	Compressibility (1/Pa) <sup>m</sup>	Grain Density (kg/m <sup>3</sup> )	Specific Heat Capacity (J/(kg*K))	Thermal Conductivity (W/(m*K))
POLLUX-10 cask (bulk) <sup>c</sup>	TBD <sup>a</sup>	TBD <sup>a</sup>	TBD <sup>a</sup>	TBD <sup>a</sup>	TBD <sup>a</sup>	7000	506	32
HLW emplacement borehole (bulk) <sup>d</sup>	TBD <sup>a</sup>	0.14	0.14	4.5e-11	TBD <sup>a</sup>	2750	830	1.15
Crushed salt <sup>e</sup>	8.35E-15	0.1	0.1	2.3E-11	1.00E-08	2200	880	NA <sup>b</sup>
Sorel cement (drift seals) <sup>f</sup>	5.00E-17	0.13	0.13	3.9E-11	1.00E-09	2450	727	2.13
Gravel (infrastructure area) <sup>g</sup>	1.00E-14	0.3	0.3	2.1E-10	1.00E-08	2700	800	2
Shaft seals before failure <sup>h</sup>	5.00E-17	0.24	0.24	1.3E-10	1.00E-08	NA <sup>b</sup>	NA <sup>b</sup>	NA <sup>b</sup>
Shaft seals after failure								

<sup>a</sup> To be determined by the individual modeling teams.

<sup>b</sup> These properties are not applicable to the initial flow and transport simulations and may require discussion.

<sup>c</sup> Generic values consistent with ductile cast iron (ASTM A536).

<sup>d</sup> Generic values consistent with properties of borosilicate glass.

<sup>e</sup> Estimated after 1000 years of reconsolidation from results in Blanco-Martin et al. 2018. Permeability ( $k$  [m<sup>2</sup>]) is a function of porosity ( $\phi$ ):  $k = 1.89 \times 10^{-10} \times \phi^{4.355}$ .

<sup>f</sup> Permeability from GRS 415 and generic values consistent with MgO cement with silica sand aggregate (Zaleska et al. 2019).

<sup>g</sup> Permeability from GRS 415 and generic values consistent with properties of coarse quartz sand.

<sup>h</sup> Bulk permeability from GRS 415. Volume weighted average porosity estimated from shaft seal design in GRS 415.

<sup>j</sup> Tortuosity ( $\tau$ ) set equal to porosity ( $\phi$ ).

<sup>k</sup> Effective diffusion coefficient,  $D_e = D_m \phi \tau$ , where  $D_m$ , the molecular diffusion coefficient in free water, = 2.3e-9 m<sup>2</sup>/s.

<sup>m</sup> Order of magnitude estimates, subject to future improvement

## 2.2.4 Natural Barrier System

The natural barrier system is comprised of the 5 simplified geologic units illustrated in Figure 2-12: the salt dome (which is the host rock); a mixed evaporite sequence flanking the salt dome; the caprock; the basin fill; and the overburden. The descriptions below are derived from the geologic units described by Bertrams et al. (2020b) unless otherwise noted. Physical properties are summarized in Table 2-11 and 2-12.

### 2.2.4.1 Salt Host Rock

In the geological model of the salt dome, the host rock consists of homogeneous rock salt (halite). The model unit consists of rock salt, which has no flowable pore space and thus no permeability greater than 10<sup>-22</sup> m<sup>2</sup>. Due to the extremely low hydraulic permeability of the salt rock, advective mass transport is negligible, so that mass transport is determined solely by diffusion (Bertrams et al. 2020b).

### 2.2.4.2 Mixed Evaporite Sequence

The flank areas of the salt structure consist of a potash seam, an evaporitic sequence of salt and anhydrite, and a clayey stratum. These complicated alternating geologic formations are very common within salt dome architecture. As a result of this complexity a simplification is made in Figure 2-12 with this group of formations being represented by a single formation defined by bulk thermo-physical properties.

### 2.2.4.3 Caprock

A caprock with a thickness between 55 m to 80 m has formed above the salt structure. The model unit consists largely of gypsum or of the residual formations of the various evaporitic strata following the salt structure. With this formation being dominated by mainly evaporitic strata the permeability is assumed to be low.

### 2.2.4.4 Basin Fill

The basin fill, which is present on both sides of the salt structure and absent directly above the salt structure, mainly consists of a limestone to sandstone sequence with conglomerates throughout. Because of this sequence, this formation is assumed to have a higher permeability and effective porosity.

### 2.2.4.5 Overburden

Above the salt structure and cap rock, the overburden varies in thickness from 55 - 80 m. The overburden consists largely of unconsolidated sediments with higher pore volume relative to the deeper units. Therefore, this model unit is classified as a freshwater aquifer.

Table 2-11. Hydraulic, thermal, and mechanical parameters for geologic units.

	Density (kg/m <sup>3</sup> )	Porosity	Permeability (m <sup>2</sup> )	Heat Capacity (J/kg*K)	Thermal Conductivity (W/m <sup>2</sup> )*	E-Moduli (MPa)*	Poisson*
Overburden	2600	0.2	1.00E-15	800	2.3	100	0.33
Caprock	2200	0.4	1.00E-18	950	2.2	500	0.27
Basin Fill	2500	0.25	1.00E-17	900	2.5	17500	0.27
Anhydrite/Potash	2700	0.05	1.00E-19	750	2.6	25000	0.27
Domal Salt	2200	0.001*	1.00E-22*	880	5.5	25000	0.27
Basement	3000	0.01	1.00E-21*	850	2.7	17000	0.27
*from Bertrams et al., 2020b							
All other parameters taken from general geologic property tables							

**Table 2-12. Relative permeability parameters for salt, crushed salt, and shaft seal. Additional materials will be added as needed.**

	Intact Salt*	Crushed Salt*	Shaft Seal
Relative Permeability Function	Corey	Corey	Corey
Residual Liquid Sat ( $S_{lr}$ )	0.1	0.03	0.03
Residual Gas Sat ( $S_{gr}$ )	0	0	0
Van Genuchten's	0.6	0.6	0.6
Van Genuchten's $P_0$ (MPa)	5.7	1.6	1.6
Van Genuchten's $S_{lr}$	0.01	0.02	0.02
*from Blanco-Martín et al. (2018)			

## 2.2.5 Geochemical Environment

In a complex geologic system, solubility limits and adsorption behavior would be controlled by local porewater chemistry and mineral assemblage. For the salt reference case, simplifying assumptions are made.

### 2.2.5.1 Solubility

Radioelement solubility limits throughout the model domain are held constant at values calculated for a concentrated, reducing brine as in previous salt reference case simulations conducted in the U.S. (e.g., LaForce et al. 2020; Clayton et al. 2011). The calculated range of maximum dissolved concentration for each element is given as a triangular distribution in Table 2-13. The reference case uses the mode of the distribution as the nominal value.

Table 2-13. Element solubility calculated at T = 25° C in concentrated brine (Wang and Lee 2010 as cited in Clayton et al. 2011).

Element	Distribution Type	Maximum Dissolved Concentration (mol kg <sup>-1</sup> )		
		Min	Mode	Max
Am	Triangular	1.85 x 10 <sup>-7</sup>	5.85 x 10 <sup>-7</sup>	1.85 x 10 <sup>-6</sup>
Np	Triangular	4.79 x 10 <sup>-10</sup>	1.51 x 10 <sup>-9</sup>	4.79 x 10 <sup>-9</sup>
Pu	Triangular	1.40 x 10 <sup>-6</sup>	4.62 x 10 <sup>-6</sup>	1.53 x 10 <sup>-5</sup>
Sn	Triangular	9.87 x 10 <sup>-9</sup>	2.66 x 10 <sup>-8</sup>	7.15 x 10 <sup>-8</sup>
Tc	Log-triangular	4.56 x 10 <sup>-10</sup>	1.33 x 10 <sup>-8</sup>	3.91 x 10 <sup>-7</sup>
Th	Triangular	2.00 x 10 <sup>-3</sup>	4.00 x 10 <sup>-3</sup>	7.97 x 10 <sup>-3</sup>
U	Triangular	4.89 x 10 <sup>-8</sup>	1.12 x 10 <sup>-7</sup>	2.57 x 10 <sup>-7</sup>
Cs, I	N/A	Unlimited <sup>a</sup>		
<sup>a</sup> Assumed by Clayton et al. (2011)				

### 2.2.5.2 Adsorption

Adsorption is modeled using linear distribution coefficients ( $K_d$ ) in the units mass/kg soil by mass/m<sup>3</sup> water [m<sup>3</sup>/kg]. Distribution coefficients are material specific.

#### Host rock and repository

The reference case assumes that adsorption does not occur within the halite of the salt dome nor within any of the engineered materials in the repository. This assumption is likely conservative, because corrosion products associated with waste package degradation might provide sorption sites.

#### Mixed evaporite sequence and caprock

Clayton et al. (2011) compiled distribution coefficients for anhydrite and expressed them as uniform and log uniform distributions (Table 2-14). Adsorption in the mixed evaporite sequence and the caprock is modeled using a nominal  $K_d$  equal to the midpoint of each distribution. The midpoint is equivalent to the average of the minimum and maximum for a uniform distribution, or the value obtained by averaging the logs of the minimum and maximum for a log uniform distribution.

Table 2-14. Anhydrite  $K_{ds}$  compiled by Clayton et al. (2011).

Element	Distribution	$K_d$ [ $m^3/kg$ ]		
		Min	Max	Mid
Ac	log uniform	5.0E-03	5.0E-01	5.0E-02
Am	uniform	2.5E-02	1.0E-01	6.3E-02
C	uniform	0.0E+00	6.0E-04	3.0E-04
Cl	constant	0.0E+00	0.0E+00	0.0E+00
Cm	log uniform	5.0E-03	5.0E-01	5.0E-02
Cs	uniform	1.0E-03	2.0E-02	1.1E-02
I	constant	0.0E+00	0.0E+00	0.0E+00
Nb	constant	1.0E-04	1.0E-04	1.0E-04
Np	uniform	1.0E-03	1.0E-02	5.5E-03
Pa	log uniform	1.0E-03	5.0E-01	2.2E-02
Pd	constant	1.0E-04	1.0E-04	1.0E-04
Pu	uniform	7.0E-02	1.0E-01	8.5E-02
Se	uniform	2.0E-04	5.0E-04	3.5E-04
Sn	uniform	2.0E-03	1.0E-02	6.0E-03
Sr	uniform	1.0E-03	8.0E-02	4.1E-02
Tc	uniform	0.0E+00	2.0E-03	1.0E-03
Th	uniform	1.0E-01	1.0E+00	5.5E-01
U	uniform	2.0E-04	1.0E-03	6.0E-04
Zr	log uniform	3.0E-03	5.0E-01	3.9E-02
Pb	constant	0.0E+00	0.0E+00	0.0E+00
Sb	constant	1.0E-02	1.0E-02	1.0E-02

### Basin fill and overburden

Adsorption in the basin fill is modeled using  $K_{ds}$  calculated for the Brauner Dogger sandy limestone sequence (a geologic unit overlying the Opalinus clay). Baeyens et al. (2014) calculated values for a reference porewater composition, and three variants including a high salinity case (Table 2-15). The salt reference case assumes high salinity porewaters and reducing conditions in the basin fill. Therefore, the high salinity  $K_{ds}$  are adopted and reduced oxidation states are assumed for uranium and plutonium (U(IV) and Pu(III)).

Adsorption in the overburden is also modeled using  $K_{ds}$  calculated for the Brauner Dogger sandy limestone sequence. For the overburden, the reference  $K_{ds}$  and higher oxidation states (U(VI) and Pu(IV)) are chosen.

Table 2-15.  $K_{ds}$  for basin fill and overburden (from Baeyens et al. 2014).

Element	$K_d$ [ $m^3/kg$ ]			
	Reference	High pCO <sub>2</sub>	Low pCO <sub>2</sub>	High salinity
I(-I)	0.00E+00	0.00E+00	0.00E+00	0.00E+00
Cs(I)	4.33E-01	4.31E-01	4.35E-01	2.88E-01
Th(IV)	7.59E+00	3.61E+00	1.67E+01	2.23E+01
U(IV) <sup>a</sup>	4.20E-02	1.51E-02	1.96E-01	3.08E-01
U(VI) <sup>b</sup>	7.89E-05	4.12E-05	2.41E-04	7.95E-04
Np(IV)	2.80E+01	2.80E+01	2.80E+01	2.80E+01
Pu(III) <sup>a</sup>	1.54E+00	9.22E-01	2.88E+00	1.49E+00
Pu(IV) <sup>b</sup>	7.28E-03	2.55E-03	3.25E-02	4.70E-03
Am(III)	1.54E+00	9.68E-01	2.87E+00	1.64E+00

<sup>a</sup> Use lower oxidation states in the basin fill.  
<sup>b</sup> Use higher oxidation states in the overburden.

### Shaft seal

Adsorption within the shaft seal is neglected for the initial simulations of flow and transport.

The upper shaft seal contains bentonite, which will sorb some radionuclide species. As staged model development progresses, adsorption in the bentonite will be modeled using  $K_{ds}$  calculated for MX-80 bentonite assuming equilibration with a high salinity porewater (Baeyens et al. 2014), as shown in Table 2-16. Reduced oxidation states are chosen for uranium and plutonium (U(IV) and Pu(III)).

Table 2-16.  $K_{ds}$  for the bentonite component of the shaft seal (from Baeyens et al. 2014).

Element	$K_d$ [ $m^3/kg$ ]
	High salinity
I(-I)	0.00E+00
Cs(I)	1.35E-02
Th(IV)	2.78E+02
U(IV)	3.90E+00
Np(IV)	3.75E+02
Pu(III)	6.68E+01
Am(III)	7.26E+01

### 2.2.6 Containment Rock Zone

The containment rock zone (CRZ) refers to the volume of rock where radioactive pollutants and waste must be contained within, thus keeping them away from the biosphere for as long as possible. The determination of the containment-providing rock zone, in particular its dimensions, is essential for the

assessment of the containment of radionuclides in this zone. The CRZ is part of the geological barrier, and the demonstration of its integrity is essential for the safety assessment. The part of the barriers which are involved in the demonstration of integrity is dependent on the repository system. For domal salt, the demonstration of integrity is carried out for the whole salt dome and also for the shaft and drift seals. As a result, here the CRZ is representative of the volume that encapsulates the 25m from the edge of the repository as well as the access shafts. This CRZ will be used as a performance measure and radionuclide flux across this boundary will be monitored over the entire simulation of this repository scenario.

### 2.2.7 Initial Conditions

Initial conditions for this salt reference case are shown in Figure 2-21 and are summed up as follows:

1. Fluid pressure will be defined as hydrostatic. The scenario presented here focuses on the intrusion of water into the mined repository. However, depending on the equation-of-state (EOS) for the given code, density differences between the fluids may be neglected if the EOS lacks that capability.
2. Temperature will be established by setting a heat flux at the base of the model reflective of the regional heat flow in Germany around Gorleben Salt Dome (110 – 120 mW/m<sup>2</sup>; Hänel 1998) and setting a constant temperature boundary condition at ground surface at the average surface temperature (9°C) which will put the temperature at the depth of the repository ~38°C (Bräuer, et al. 2016).
3. Once hydrostatic conditions are calculated, the mined repository and access shafts will be added and are defined by unsaturated conditions at atmospheric pressure. Because the only moisture added to the system is to sections of run of mine salt, the remaining pore space will be air-filled and is critical to incorporate for the early time behavior of the system.

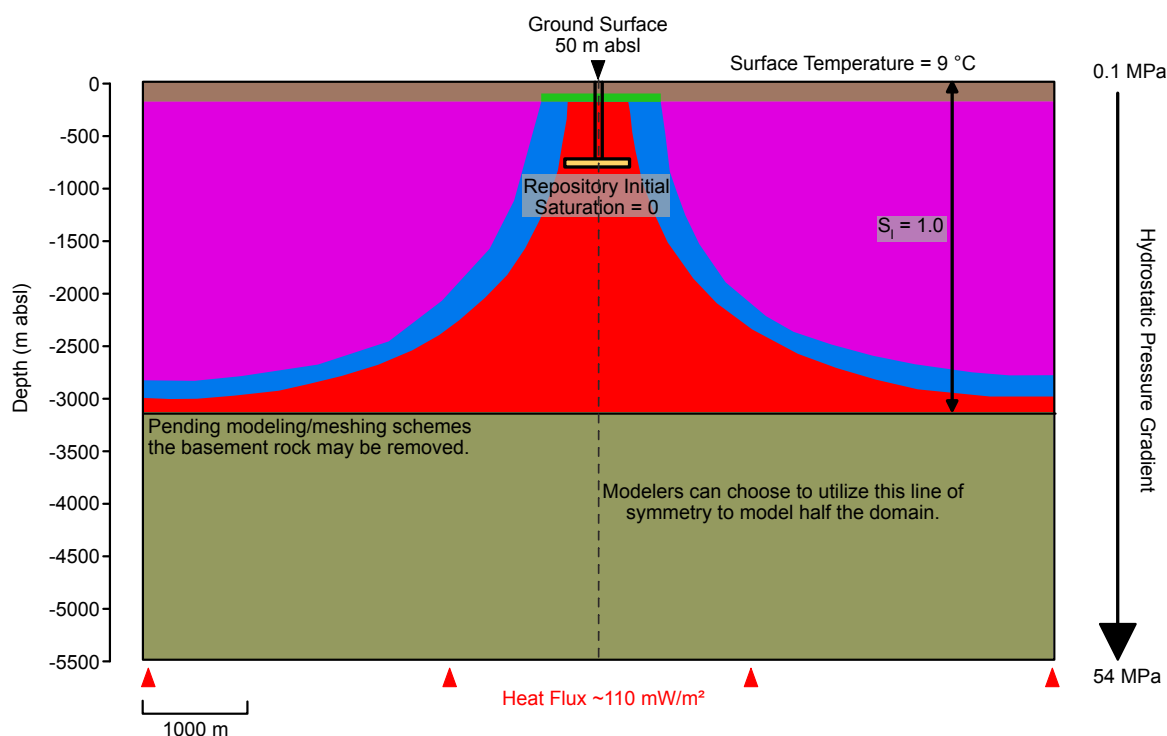


**Figure 2-21. Schematic for initial conditions at  $t = 0s$  after waste package emplacement. The orientation and design of the repository and geologic cross section were chosen to provide a symmetry boundary that modelers can choose to leverage to reduce the computational resources required for the presented scenario.**

## 2.2.8 Outputs for Comparison

This section provides a list of outputs for comparison to compare/contrast modeling schemes, numerical codes, and assumptions made between the participating teams. Some output comparisons are made at a specific point while others are made to be an average over an area. Averages over different areas within the repository are chosen for comparison because the resolution at which participants will model the repository will differ, ultimately making a direct comparison at a single node an inaccurate to compare model outputs.

### 2.2.8.1 Transport comparisons

#### Radionuclide Fluxes

- In shaft across the containment zone boundary
- In shaft at the base of the overburden (aquifer)
- Either end of drift seal

#### Radionuclide concentrations

- Infrastructure area (average/mass)
- Drift seal (average/mass)
- Waste package (one glass and one SNF)
- 50 m and 5 km (or other distances) from shaft in the aquifer (down gradient)

#### Radionuclide source term

- Rate of release for one glass and one SNF

### **2.2.8.2 Flow comparisons**

#### **Saturation/Pressure/Temperature**

- Infrastructure area (average)
- Drift seal (average)
- SNF disposal drift (average)
- Glass disposal drift (average)
- Waste package temperature (once heat is added to simulations)

#### **Liquid Fluxes**

- Same locations for comparisons as radionuclide fluxes

### **2.2.9 Analytical benchmark for overburden transport**

An analytical benchmark for code comparison is needed for the DECOVALEX Task F salt case. As discussed in the preceding section, transport of radionuclides to the overburden by shaft-seal failure is considered as the disruptive scenario for the DECOVALEX salt case. Thus, the proposed benchmark problem has been chosen to be a simplified model of transport of tracers through the overburden from a line source. The analytical solution is one of the example models from Section 3.3.2.2 of Batu (2006).

The conceptual model for the benchmark is shown in Figure 2-22 and the assumptions of the analytical model are (after Batu 2006):

- 1) Unidirectional steady-state groundwater velocity field with flow in the x-direction.
- 2) Solute source is located at  $x = 0$ , planar and perpendicular to the velocity of the flow field.
- 3) Source concentration is a function of z-coordinate and time through an exponential function.
- 4) The medium is infinite in the x-direction and z is in the range  $(0,Z)$ .

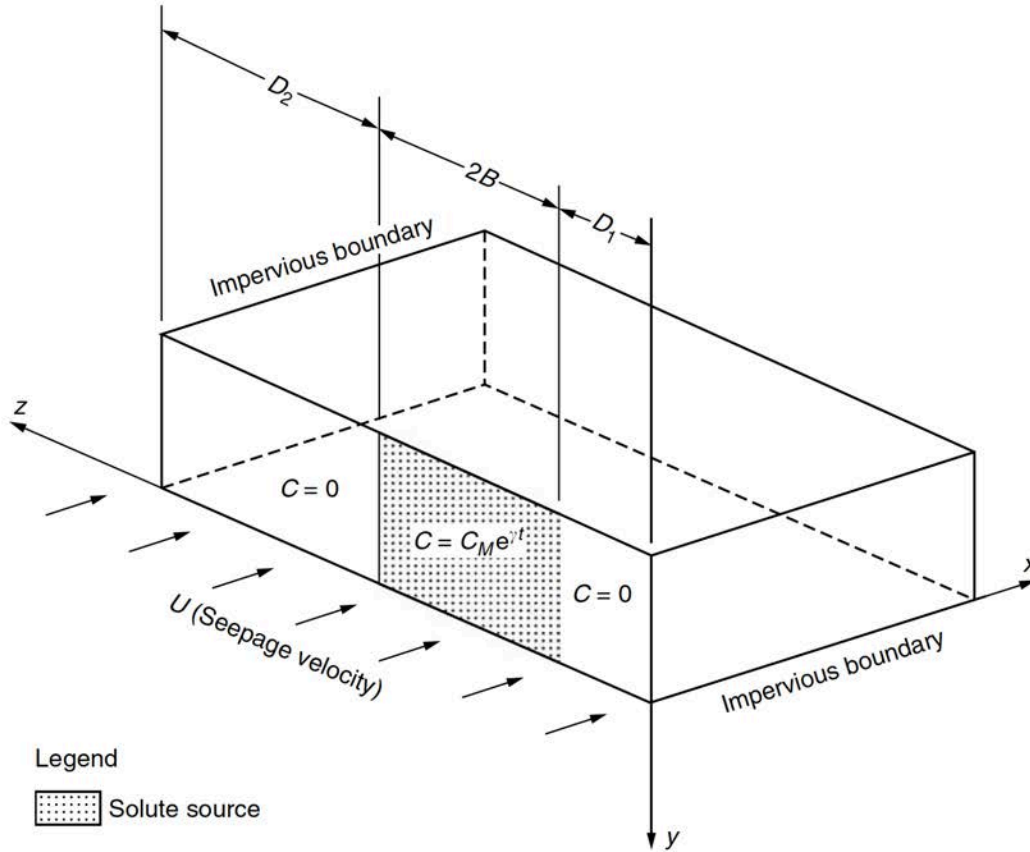


Figure 2-22. Schematic of chemical diffusion and transport from a planar source in a uniform flow field. Taken from Batu (2006).

The governing equation is:

$$\frac{\partial C}{\partial t} = \frac{D_x}{R_d} \frac{\partial^2 C}{\partial x^2} + \frac{D_z}{R_d} \frac{\partial^2 C}{\partial z^2} - \frac{U}{R_d} \frac{\partial C}{\partial x} - vC \quad (2-18)$$

The initial condition is

$$C(x, z, 0) = 0, \quad (2-19)$$

and the boundary condition is

$$C(0, z, t) = \begin{cases} C_m \exp(\gamma t) & D_1 < z < D_1 + 2B \\ 0 & \text{otherwise} \end{cases} \quad (2-20)$$

In this equation  $C_m$  is the initial tracer concentration at the source,  $\gamma$  is the chemical decay rate,  $R_d$  is the retardation factor.  $D_1$  is the distance of the source from the  $z = 0$  axis,  $D_2$  is the distance from the  $z = Z$  outer boundary of the model, and  $B$  is the half-length of the planar source.  $R_d = 1$  for flow without adsorption and  $\gamma = 0$  for a constant rate tracer source.

The solution to this equation is:

$$C(x, z, t) = C_m P_1 [\exp(-P_2) \operatorname{erfc}(P_3 - P_4) + \exp(P_2) \operatorname{erfc}(P_3 + P_4)] \quad (2-21)$$

$$+ \frac{C_m}{\pi} P_5 P_6 \sum_{n=1}^{\infty} P_7 P_n [\exp(-P_8) \operatorname{erfc}(P_3 - P_9) + \exp(P_8) \operatorname{erfc}(P_3 + P_9)]$$

where

$$P_1 = \frac{B}{D_1 + 2B + D_2} \exp\left(\gamma t + \frac{Ux}{2D_x}\right) \quad P_2 = \left(\frac{vR_d}{D_x} + \frac{U^2}{4D_x^2} + \frac{\gamma R_d}{D_x}\right)^{\frac{1}{2}} x$$

$$P_3 = \frac{R_d x}{2(D_x R_d t)^{\frac{1}{2}}} \quad P_4 = \left[\left(v + \frac{U^2}{4D_x R_d} + \gamma\right) t\right]^{\frac{1}{2}} \quad P_5 = \exp\left(\frac{Ux}{2D_x}\right)$$

$$P_6 = \exp(\gamma t) \quad P_7 = \frac{1}{n} \{\sin[\lambda_n (D_1 + 2B)] - \sin(\lambda_n D_1)\} \cos(\lambda_n z)$$

$$P_8 = \left(\frac{vR_d}{D_x} + \frac{D_z}{D_x} \lambda_n^2 + \frac{U^2}{4D_x^2} + \frac{\gamma R_d}{D_x}\right)^{\frac{1}{2}} x \quad P_9 = \left[\left(v + \frac{D_z}{R_d} \lambda_n^2 + \frac{U^2}{4D_x R_d} + \gamma\right) t\right]^{\frac{1}{2}}$$

$$\lambda_n = \frac{n\pi}{D_1 + 2B + D_2}, \quad n = 1, 2, \dots$$

The analytical model domain is intended to be representative of the current iteration of the PA model and the repository is assumed to be exactly centrally located in the domain. Parameters are shown in Table 2-16. The domain for the analytical solution is infinite in the x-direction (flow direction), but concentrations will only be calculated up to X = 4,500 m downstream of the shafts. The model is Z = 8,000 m in the z-direction. Assuming that the waste in the repository is under the center of the salt dome, the shaft centers are 720 m from the center of the structure (See Figure 2-15). The two shafts are 7 m wide each, and they are lumped together so the source is assumed to be 14 m wide. This means  $D_1 = 4000 - 720 - 7 = 3273$  m,  $2B = 14$  m and  $D_2 = 4713$  m. The overburden is 55 m to 80 m thick and thinnest over the repository, as discussed in Section 2.2.4.5, so the analytical model will use 55 m thickness. The background flux rate is 1 m/yr and the overburden is assumed to be completely water-saturated.

The overburden consists largely of unconsolidated sediments with higher pore volume relative to the deeper units.  $D_x = D_o + \alpha u$  where  $u$  is interstitial velocity. Thus  $\alpha = 5.0 \times 10^{-1}$  m,  $D_o = 1 \times 10^{-6}$  m<sup>2</sup>/s and  $D_y = 1.0D_x$  as shown in Table 2-17. The diffusion and dispersivity coefficients are artificially high for this example because the numerical implementation of the analytical solution is accurate only when advective and dispersive transport are of the same order of magnitude. It also ensures that numerical dispersion is smaller than the model diffusion in simulated solutions.

The analytical solution is also calculated for a tracer with retardation factor greater than one and a decaying rate source. A reference partition coefficient,  $K_d$ , value representative of Cs(I) at neutral conditions is chosen (see Table 2-15).  $K_d = 0.433 \text{ m}^3/\text{kg}$  so that  $R_d = 1 + K_d/\phi = 3.165$ . The decay rate of the source is arbitrarily assigned the value  $\gamma = -0.05$ .

**Table 2-17. Hydraulic, thermal, and mechanical parameters for DECOVALEX Task F salt analytical benchmark.**

Parameter	Value
Distance to shaft, $D_1$ [m]	3273
Half-width of combined shaft, $B$ [m]	7
Width of the model in y-direction, $Y$ [m]	8000
Length of the model in x-direction, $X$ [m]	4500
Interstitial velocity [m/yr]	1.0
Dispersivity, $\alpha$ [m]	$5.0 \times 10^{-1}$
Diffusion coefficient, $D_o$ [ $\text{m}^2/\text{s}$ ]	$1 \times 10^{-6}$
Diffusion ratio $D_y/D_x$ [-]	1.0
Concentration at source, $C_m$ [ $\text{kg}/\text{m}^3$ ]	1.0
Retardation factor for Case 2, $R_d$ [ $\text{m}^3/\text{kg}$ ]	3.165
Decay rate for Case 3, $\gamma$ [-]	-0.05
Porosity [-]	0.2
Permeability [ $\text{m}^2$ ]	$1 \times 10^{-15}$

### 2.2.9.1 Analytical model solution

The analytical solution is scripted in python3 for comparison with simulated results. The series solution shown in Eq. 2-21 is challenging to compute numerically. A large number of terms in the infinite series are required for convergence and all analytical solutions shown have  $n = 500$  terms of the series. Furthermore, many of the exponential and error functions contain very large arguments, especially at late time. It is not possible to use regular python float variables because of overflow, and the 'decimal.getcontext().prec' library is required.

The analytical solutions after 250 years are shown in Figure 2-23. As can be seen, the contour plot begins at  $x=200$  m because, even with 500 terms in the series solution, there are numerical artefacts for  $x < 200$  m caused by extremely low concentrations away from the contaminant source.

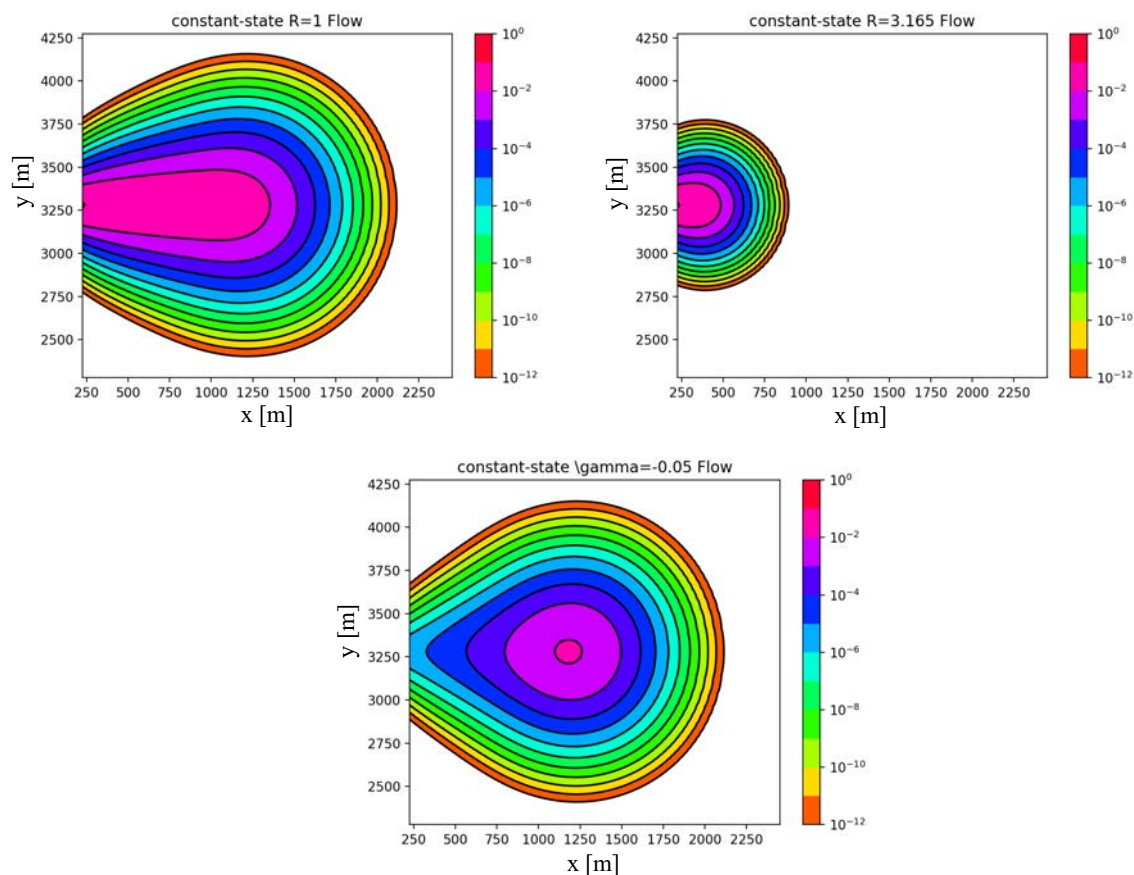


**Figure 2-23. Tracer distribution for proposed DECOVALEX salt analytical benchmark problem after 250 years. Top Left: solution without retardation or decay in the tracer source. Top Right: solution with retardation factor  $R_d = 3.165 \text{ m}^3/\text{kg}$ , representative of Cs(I) retardation and no decay in the tracer source. Bottom: Solution without retardation and with time-dependent tracer source  $\gamma = -0.05$ .**

### 2.2.9.2 Simulated solutions

Simulations are run in the PFLOTRAN RICHARDS mode for the constant tracer source and a tracer with  $R_d = 1.0$ , for no retardation. Simulation parameters are given in Table 2-17. A refined simulation mesh is required to ensure that numerical dispersion in the simulated solution is smaller than the input diffusion and diffusivity (which are artificially high, as discussed above). The simulation mesh extends to  $X = 9,000 \text{ m}$  in the x-direction to approximate a semi-infinite domain in x. Timesteps are also limited to 0.1 year for the duration of the simulation to minimize numerical dispersion.

Two meshes are generated for the simulation. The first mesh is structured and has  $10 \times 10 \text{ m}$  square grid blocks in x and z. The mesh is uniform throughout the domain because mesh refinement and horizontally anisotropic meshing were both observed to bias the simulation result. The final mesh is 2D and has  $800 \times 900 = 720,000$  grid cells. The second mesh is an unstructured Voronoi 3D mesh created by VoroCrust meshing software. All VoroCrust meshes are isotropic, and the mesh is refined in the area where the tracer plume is expected to travel. The unstructured mesh has 1,031,736 grid cells.

The simulated solutions after 250 years are shown in Figure 4-24. As can be seen, both simulations predict a larger plume than the analytical solution, which is shown on the top left of Figure 4-23. Even with the highly refined mesh, the structured mesh is biasing the simulation result and overpredicting tracer movement in the flow direction. The unstructured mesh has a qualitatively better match, but the tracer plume has dispersed in all directions to a greater distance than the analytical solution. These results indicate that numerical dispersion is still impacting the simulated results.

Project partners are currently attempting the simulated solution. However, no results have been quantitatively compared to the analytical or PFLOTRAN simulated solutions yet.

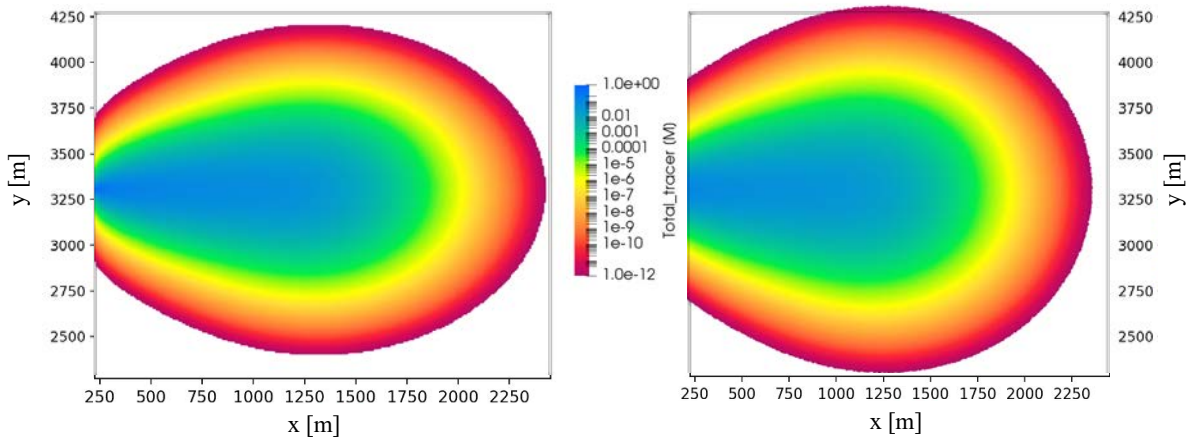


**Figure 2-24. Simulated tracer distribution for DECOVALEX salt analytical benchmark problem after 250 years without retardation or decay in the tracer source. Left: Simulation on a 720,000 grid-cell cubic structured mesh. Right: Simulation on a 1,031,736 grid-cell unstructured Voronoi mesh. Rectangular outline indicates the extent of the domain where the analytical solution is calculated on Figure 2-23.**

## 2.3 References

- Adeniyi, A., Howard, R., Banerjee, K., Bhatt, S. 2020. *GDSA Waste Package Reference Physical and Thermal Characteristics*. M3SF-20OR010304072, Oak Ridge National Laboratory, Oak Ridge, TN.
- Baeyens, B., T. Thoenen, M. H. Bradbury, and M. Marques Fernandes. 2014. *Sorption Data Bases for Argillaceous Rocks and Bentonite for the Provisional Safety Analyses for SGT-E2*. TR 12-04. National Cooperative for the Disposal of Radioactive Waste (NAGRA), Wettingen, Switzerland.
- Batu, Vedat. 2006. *Applied Flow and Solute Transport Modelling in Aquifers*. CRC Taylor and Francis.
- Bear, J., Tsang, C.-F. and de Marsily, G. 1993. *Flow and Contaminant Transport in Fractured Rock*, Academic Press, San Diego, California.

- Beuth, T., Bracke, G., Buhmann, D., Dresbach, C., Keller, S., Krone, J., Lommerzheim, A., Mönig, A., Mrugalla, S., Rübél, A., and Wolf, J. 2012. *Szenarienentwicklung: Methodik und Anwendung. Bericht zum Arbeitspaket 8. Vorläufige Sicherheitsanalyse für den Standort Gorleben*, Gesellschaft für Anlagen und Reaktorsicherheit (GRS) mbH, GRS-284, Köln, ISBN 978-3-939355-60-1.
- Bertrams, N., Bollingerfehr, W., Eickemeier, R., Fahland, S. Flügge, J., Frenzel, B., Hammer, J., Kindlein, J. Liu, W., Maßmann, J., Mayer, K.-M., Mönig, J., Mrugalla, S., Müller-Hoeppe, N., Reinhold, K., Rübél, A., Schubarth-Engel-schall, N., Simo, E., Thiedau, J., Thiemeyer, T., Weber, J.R., Wolf, J. 2020. *Grundlagen zur Bewertung eines Endlagersystems in flach lagernden Salzformationen (S1) - Ergebnisse aus dem Vorhaben RESUS*. BGE TEC 2020.
- Bollingerfehr, W., Filbert, W., Pöhler, M., Tholen, M., and Wehrmann, J. 2008. *Konzeptionelle Endlagerplanung und Zusammen-stellung des endzulagernden Inventars (Design planning of a final repository and summary of the inventory to be stored) – Project ISIBEL*, Peine, April 2008.
- Bollingerfehr, W., Bertrams, N., Buhmann, D., Eickemeier, R., Fahland, S., Filbert, W., Hammer, J., Kindlein, J., Knauth, M., and Wenting, L. 2018. *Concept developments for a generic repository for heat-generating waste in bedded salt formations in Germany*. Synthesis Report (No. BGE TEC 2018-13). BGE TECHNOLOGY GmbH.
- Bollingerfehr, W., Buhmann, D. and Doerr, S. 2017. *Evaluation of methods and tools to develop safety concepts and to demonstrate safety for an HLW repository in salt*. Final Report (No. TEC-03-2017-AB). DBE Technology GmbH.
- Bräuer, S. and Urquhart, A. 2016. *Thermal and physical properties of reconsolidated crushed rock salt as a function of porosity and temperature*. *Acta Geotechnica*, 11(4):913-924.
- Bundesministerium für Umwelt (BMU). 2010. *Naturschutz und Reaktorsicherheit: Sicherheitsanforderungen an die Endlagerung wärmeentwickelnder radioaktiver Abfälle*. Bundesministerium für Umwelt, Naturschutz und Reaktorsicherheit. Stand: 30, September 2010.
- Carter, J., A. J. Luptak, J. Gastelum, C. T. Stockman, and A. Miller. 2013. *Fuel Cycle Potential Waste Inventory for Disposition*. FCR&D-USED-2010-000031 Rev 6. Savannah River National Laboratory, Aiken, SC.
- Clayton, D., G. Freeze, T. Hadgu, E. Hardin, J. Lee, J. Prouty, R. Rogers, W. M. Nutt, J. Birkholzer, H. H. Liu, L. Zheng, and S. Chu 2011. *Generic Disposal System Modeling - Fiscal Year 2011 Progress Report*. SAND 2011-5828P; FCRD-USED-2011-000184. Sandia National Laboratories, Albuquerque, NM.
- Freeze, R. A. and J. A. Cherry, 1979. *Groundwater*, Prentice-Hall, Englewood Cliffs, NJ.
- GRS, 2012. *Radionuclide Inventory of Vitrified Waste after Spent Nuclear Fuel Reprocessing at La Hague*. Gesellschaft für Anlagen- und Reaktorsicherheit, Germany. GRS-294.
- Hartley, L., P. Appleyard, S. Baxter, J. Hoek, D. Roberts, and D. Swan. 2013. *Development of a Hydrogeological Discrete Fracture Network Model for the Olkiluoto Site Descriptive Model 2011*. Working Report 2012-32. Posiva Oy, Eurajaki, Finland.
- Hartley, L., J. Hoek, D. Swan, P. Appleyard, S. Baxter, D. Roberts, and T. Simpson. 2013. *Hydrogeological Modelling for Assessment of Radionuclide Release Scenarios for the Repository System 2012*. Working Report 2012-42. Posiva Oy,

- Hedin, A. 2008. *Semi-analytic stereological analysis of waste package/fracture intersections in a granitic rock nuclear waste repository*, *Mathematical Geosciences*, 40(6):619-637.
- Hyman, J. D., S. Karra, N. Makedonska, C. W. Gable, S. L. Painter, and H. S. Viswanathan. 2015. *DFNWORKS: A discrete fracture network framework for modeling subsurface flow and transport*. *Computers & Geosciences*, 84, 10-19. doi: 10.1016/j.cageo.2015.08.001
- Iraola, A., P. Trinchero, S. Karra and J. Molinero. 2019. *Assessing dual continuum method for multicomponent reactive transport*. *Computers & Geosciences* 130: 11-19.
- Johnson, L. R., C. Ferry, C. Poinssot and P. Lovera. 2005. *Spent fuel radionuclide source term model for assessing spent fuel performance in geological disposal. Part I: Assessment of the Instant Release Fraction*. *Journal of Nuclear Materials* 346: 66-77.
- Kienzler, B., M. Altmaier, C. Bube and V. Metz 2012. *Radionuclide Source Term for HLW Glass, Spent Nuclear Fuel, and Compacted Hulls and End Pieces (CSD-C Waste)*. KIT Scientific Reports 7624. Karlsruhe Institute of Technology, Baden-Württemberg, Germany.
- LaForce, T., Chang, K.W., Perry, F.V., Lowry, T.S., Basurto, E., Jayne, R., Brooks, D., Jordan, S., Stein, E., Leone, R., and Nole, M., 2020. *GDSA Repository Systems Analysis Investigations in FY2020*. M2SF-20SN010304052, SAND2020-12028 R. Sandia National Laboratories, Albuquerque, NM.
- Mariner, P. E., W. P. Gardner, G. Hammond, S. D. Sevougian, and E. R. Stein 2015. *Application of Generic Disposal System Models*. FCRD-UFD-2015-000126; SAND2015-10037R. Sandia National Laboratories, Albuquerque, NM.
- Martín, L.B., Rutqvist, J., and Birkholzer, J.T. 2015. *Long-term modeling of the thermal-hydraulic-mechanical response of a generic salt repository for heat-generating nuclear waste*. *Engineering Geology*, 193:198–211.
- Ollila, K. 2008. *Dissolution of unirradiated UO<sub>2</sub> and UO<sub>2</sub> doped with <sup>233</sup>U in low- and high-ionic strength NaCl under anoxic and reducing conditions*. Working Report 2008-50. Posiva Oy, Eurajoki, Finland.
- Ruebel, A., Buhmann, D., Kindlein, J. and Lauke, T. 2016. *Performance assessment of sealing systems. Conceptual and integrated modelling of plugs and seals* (No. GRS--415). Gesellschaft fuer Anlagen-und Reaktorsicherheit (GRS) gGmbH.
- Sassani, D., J.-H. Jang, P. E. Mariner, L. Price, R. Rechard, M. Rigali, R. Rogers, E. R. Stein, W. Walkow, and P. Weck. 2016. *The On-line Waste Library (OWL): Usage and Inventory Status Report*. FCRD-UFD\_2016-000080 / SAND2016-9485R. Sandia National Laboratories, Albuquerque, NM.
- Stein, E. R., J. M. Frederick, G. E. Hammond, K. L. Kuhlmann, P. E. Mariner, and S. D. Sevougian. 2017. April 9-13, 2017. *Modeling Coupled Reactive Flow Processes in Fractured Crystalline Rock*. Paper presented at the International High-Level Radioactive Waste Management Conference, Charlotte, NC.
- Stein, E. R., R. C. Leone, and S. Nguyen. 2021. *DECOVALEX-2023 Task F Specification Revision 5*. SAND2021-6658 O. Sandia National Laboratories, Albuquerque, NM.
- Strachan, D. 2004. *Defense HLW Glass Degradation Model*. ANL-EBS-MD-000016 REV 02. Sandia National Laboratories, Albuquerque, New Mexico.

- Sweeney, M.R., Gable, C.W., Karra, S., Stauffer, P.H., Pawar, R.J., Hyman, J.D. 2020. *Upscaled discrete fracture matrix model (UDFM): an octree-refined continuum representation of fractured porous media*. *Comput. Geosci.* 24, 293–310. <https://doi.org/10.1007/s10596-019-09921-9>
- Tang DH, Frind, EO and Sudicky EA. 1981. *Contaminant transport in fracture porous media: analytical solution for a single fracture*. *Water Resources Research*, 17(3), 555-564. doi: 10:1029/WR017i003p00555
- Werme, L. O., L. H. Johnson, V. M. Oversby, F. King, K. Spahiu, B. Grambow and D. W. Shoesmith. 2004. *Spent fuel performance under repository conditions: A model for use in SR-Can*. Technical Report TR-04-19. Swedish Nuclear Fuel and Waste Management Co. (SKB), Stockholm, Sweden.
- Vienna, J. D., J. V. Ryan, S. Gin and Y. Inagaki. 2013. *Current understanding and remaining challenges in modeling long-term degradation of borosilicate nuclear waste glasses*. *International Journal of Applied Glass Science* 4(4): 283-294.
- Zaleska, M., M. Pavlikova, and Z. Pavlik. 2019. *Structural, Mechanical and Thermal Properties of Lightweight Magnesium Oxychloride Cement Concrete*. AIP Conference Proceedings 2170(1), published online 05 November 2019.

### 3. SMALL-SCALE REFERENCE CASE STUDIES

This section summarizes research on two separate studies for disposal in shale. The first subsection is a study of DRZ permeability evolution as a result of buffer swelling in a soft shale. A single-waste package simulation model is used to study the DRZ evolution a shale repository in detail. The second study also uses a single-waste package simulation model to study grid orientation affects in an unsaturated alluvium (UZ) repository.

#### 3.1 Buffer and DRZ evolution

There is an ongoing integration effort of repository-scale PA simulations between two modeling capabilities: coupled thermo-hydro-chemical (THC) PFLOTRAN and coupled thermo-hydro-mechanical (THM) TOUGH-FLAC. This has led to the development of a suite of reduced-order models to approximate near-field geomechanical effects in PA simulations. This project was initiated in Section 5.2 of Sevougian et al. (2019b) and continued in Section 3.1 of LaForce et al. (2020).

This section presents an update to an ongoing collaborative project with LBNL to create reduced-order models to approximate near-field geomechanical effects in PA simulations. Geomechanical effects are often localized in the near-field to the near-tunnel environment of the shale that is adjacent to the engineered barrier system and occur relatively early in the post-closure period (100s of years). In the present work, thermally-driven mechanical impacts on DRZ rock properties are approximated by implementing permeability changes as functions of effective stress, which can provide reasonable estimate of stress perturbations without fully coupled THM simulations. Modeling geomechanical behavior at PA-scale can therefore benefit from reduced-order modeling to avoid fully coupled and rigorous geomechanics at a multi-kilometer scale and over hundreds of thousands of years.

##### 3.1.1 Model setting

Three concentric sections of waste package, buffer, and DRZ at radii of 0.42 m, 1.5 m, and 3.17 m, respectively, are modeled in a 15 m (width in x-axis)  $\times$  12.5 m (length in y-axis)  $\times$  75 m (height in z-axis) domain (Figure 3-1). The 75-m thick layer of the model domain represents a portion of the shale host rock, which serves as a natural barrier. The repository extends along the y-axis and is centered at depth of 500 m. The model domain represents a quarter of a waste package and half of the spacing between adjacent drifts (30 m in x-direction) as well as waste packages (20 m in y-direction) in the shale host rock. By invoking closed symmetry conditions at all side boundaries, this configuration represents a waste package that is located in the center of an infinite, symmetrical repository system.

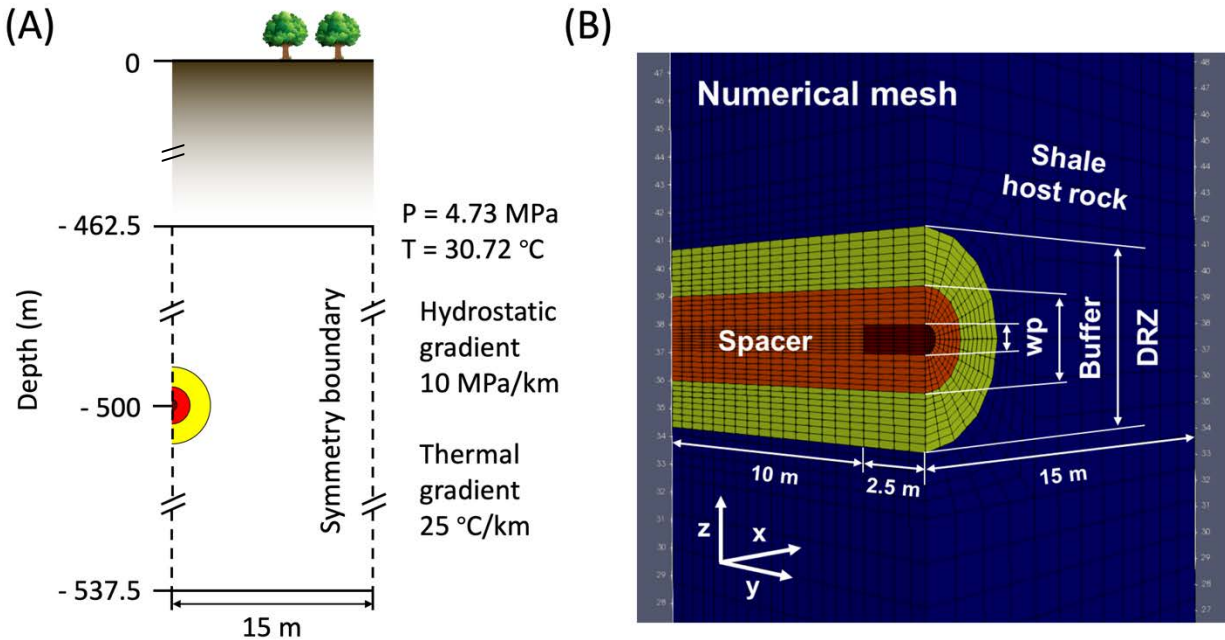


**Figure 3-1. (A) Schematic description of the model domain consisting of waste package (wp), buffer/spacer, disturbed rock zone (DRZ), and shale host rock. (B) Numerical domain of 15 m (width in x-axis)×12.5 m (length in y-axis)×75 m (height in z-axis) with unstructured grids to model a quarter of the cylindrical repository centered at depth of 500 m.**

Initial pressure and temperature throughout the model domain are calculated by applying hydrostatic and geothermal gradients ( $10 \text{ kPa/m}$  and  $0.025^\circ\text{C/m}$ , respectively) in the vertical direction assuming a temperature of  $19^\circ\text{C}$  and atmospheric pressure at the surface ( $462.5 \text{ m}$  above the top of the model domain). For the initial saturation condition, the liquid saturation ( $S_l$ ) is set to  $0.65$  for buffer and DRZ, whereas the shale host rock is fully saturated with liquid. Capillary pressure and relative permeability of liquid and gas phases (subscripts  $l$  and  $g$ , respectively) are calculated by the van Genuchten saturation function (van Genuchten 1980) and Mualem-van Genuchten formulation (Mualem 1976). To consider the effect of saturation changes on thermal behaviors, wet (water-saturated) and dry thermal conductivities are defined to generate saturation-dependent effective thermal conductivity.

Waste package porosity is set to  $50\%$ , which is approximately the fraction of void space within the waste package. Permeability is set several orders of magnitude higher than that of the surrounding materials so that flow through waste packages is uninhibited, although radionuclides are not released until the waste package is breached. The waste package consists of a stainless-steel canister and a stainless-steel overpack; the thermal properties of stainless steel (Shelton 1934) are therefore implemented in the entire waste form region.

The buffer of bentonite/sand mixture is assigned a porosity of  $0.35$  and a permeability of  $1 \times 10^{-20} \text{ m}^2$  (Liu et al. 2016). The shale host rock has a porosity of  $0.2$  and a permeability of  $1 \times 10^{-19} \text{ m}^2$ , whereas the DRZ permeability is an order of magnitude greater than the host rock to represent the changes of mechanical and hydrological properties in response to excavation. For the reference case, the material properties of all formations are constant over time as given in Table 3-1.

Table 3-1. Material properties

	Buffer/Spacer	DRZ	Host rock
Porosity [-]	0.35	0.2	0.2
Permeability [ $\text{m}^2$ ]	$1 \times 10^{-20}$	$1 \times 10^{-18}$	$1 \times 10^{-19}$ , $1 \times 10^{-21}$
Density [ $\text{kg}/\text{m}^3$ ]	2700	2700	2700
Heat capacity	830	830	830
Thermal conductivity (dry)	0.6	0.6	0.6
Thermal conductivity (wet)	1.5	1.2	1.2
Initial gas saturation ( $S_{gi}$ )	0.35	0.35	0.0
Liquid phase diffusion coefficient [ $\text{m}^2/\text{s}$ ]	$1 \times 10^{-9}$		
Gas phase diffusion coefficient [ $\text{m}^2/\text{s}$ ]	$2.1 \times 10^{-5}$		
Saturation function	van Genuchten function		
alpha [ $\text{Pa}^{-1}$ ]	$6.25 \times 10^{-8}$	$6.67 \times 10^{-7}$	$6.67 \times 10^{-7}$
m [-]	0.375	0.333	0.333
Liquid residual saturation ( $S_{rl}$ )	0.1	0.1	0.1
Gas residual saturation ( $S_{rg}$ )	0.1	0.1	0.1

This study excludes chemical reactions and radioactive decay of nuclides, and instead focuses on buffer swelling effects on solute transport by tracer simulation. A single chemical species (chloride ion;  $\text{Cl}^-$ ) is defined as a non-reactive tracer with the solubility limit of  $6159.0 \text{ mol}/\text{m}^3$ -liquid and the precipitated molar density of  $37130.2 \text{ mol}/\text{m}^3$ -mineral. The initial molar concentration of  $\text{Cl}^-$  is set to  $160 \text{ mol}/\text{m}^3$ -liquid for the waste package and buffer and  $332 \text{ mol}/\text{m}^3$ -liquid for the DRZ and shale host rock (Jove-Colon et al., 2016). Note that the initial  $\text{Cl}^-$  concentration in the waste form should match that in the buffer since the waste form is hydraulically connected to the buffer at all times in this model setting.

This near-field model was run in PFLOTRAN GENERAL and NWT (Nuclear Waste Transport) modes that solve two-phase (liquid-gas) miscible flow and solute transport, respectively, coupled to energy for unsaturated conditions in waste package, buffer/spacer, and DRZ. The simulation runs for  $10^6$  years.

The relationship between normal stress across fractures and bulk medium permeability (i.e. fracture + matrix) is highly dependent on fracture and matrix compressibility. There are multiple models in the literature to express this relationship for different shale rocks. In this work, three different models have been implemented in PFLOTRAN relating the DRZ permeability to normal effective stress: (1) an exponential function, (2) a modified cubic-law function, and (3) a Two-part Hooke's Law model (Chang et al., 2021).

The initial permeability values ( $\kappa_0$ ) for each function are unknown, and thus, these permeability values can either be assigned a constant value based on the host rock permeability, or they can be computed for each stress-dependent permeability function assuming that at high swelling stress the permeability of the DRZ approaches host rock permeability. In this study, the latter approach was taken to obtain initial DRZ permeability by assuming that when the buffer becomes fully saturated ( $S_l = 1.0$ , such that  $\Delta S_l = 0.35$ ) and buffer swelling stress reaches a maximum, this is sufficient to close reactivated and/or new fractures within the DRZ and the DRZ permeability approaches that of the host rock.

The DRZ may not completely revert to the original host rock permeability due to inelastic behaviors of fractures even when buffer swelling is at a maximum. However, this assumption provides a physically realistic endpoint permeability from which to compare multiple permeability functions. For each permeability function, the values given in Table 3-2 are employed.

**Table 3-2. Parameter values for different permeability functions**

Exponential function (Exp)		
$C_{exp}$ [1/MPa]	0.18	
$k_0$ [m <sup>2</sup> ]	$1.49 \times 10^{-19}$	
Modified cubic function (Cubic)		
P1 [MPa]	19.3	
m	0.159	
$k_0$ [m <sup>2</sup> ]	$1.38 \times 10^{-18}$	
Two-Part Hooke's model (TPHM)		
$\beta$	1	
$C_e$ [1/MPa]	0.18	
$\phi_e$	0.2	
$\alpha$ [m <sup>2</sup> ]	$1 \times 10^{-16}$	Soft-part initial permeability
$m$	3.0	
$\gamma$	0.005, 0.01, 0.025, 0.05, 0.075	Volume fraction of soft-part
$K_t$ [MPa]	8.0	
$k_{0e}$ [m <sup>2</sup> ]	$1.1969 \times 10^{-20}$	Hard-part initial permeability

Figure 3-2 shows the evolution of DRZ permeability given the change in effective stress ( $\max(\Delta\sigma_{eff}) = 4.998$  MPa) for three functions with the material properties from Table 3-2. The exponential function reduces permeability constantly (Exp; green line), whereas the cubic function starts with an order of magnitude increase in initial permeability and then converges with Exp (Cubic; orange line) as effective stress increases in a log-linear space. For the Two-part Hooke's law model, the influence of soft-part initial permeability on the permeability evolution is negligible with the parameters implemented in this study, such that the DRZ permeability is governed by an exponential function for the hard part (TPHM; blue region). Note that the typical experimental observation of permeability-effective stress relationship will be matched by transition from a power law to an exponential law as the effective stress increases (Zheng et al. 2015). The increase in soft-part fraction ( $\gamma$ ) from 0.005 to 0.075 gives larger permeability in general, but larger reduction in permeability at larger effective stress. The DRZ permeability from all three functions approaches the host rock permeability ( $1 \times 10^{-19}$  m<sup>2</sup>) at the maximum effective stress, as assumed in the derivation of initial permeability for each function.

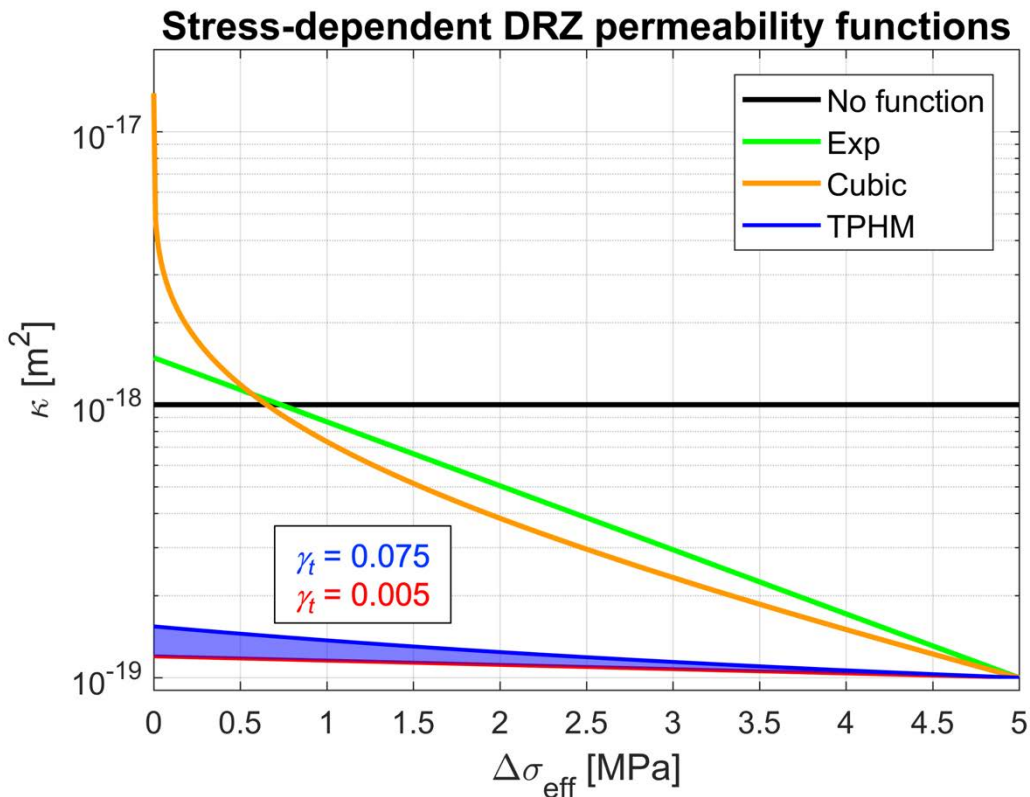


Figure 3-2. Stress-dependent permeability functions in PFLOTRAN: exponential (green line), cubic-law (orange line), and Two-part Hooke’s Law Model (TPHM; blue region). The constant DRZ permeability is indicated by a black solid line. For the TPHM function, the larger soft-part fraction increases permeability in general.

The constant DRZ permeability is lower than that in the Exp and Cubic functions at low effective stress range ( $\Delta\sigma_{\text{eff}} < 0.7$  MPa in this study). Overall, declining trends of stress-dependent permeability suggest that the constant-permeability setting may overestimate the rate of heat transfer or fluid flow through DRZ as effective stress increases. Therefore, the geomechanical impact on the DRZ permeability evolution should be carefully included in THC models to properly characterize the buffer swelling process in a shale repository system.

### 3.1.2 THC coupling integrated with stress-dependent permeability

The waste package temperature peaks at approximately 3 years, reaching a high of about 82 °C for the unsaturated shale repository. If the repository is assumed to be fully saturated as an initial condition, higher temperatures may be reached due to larger wet thermal conductivities assigned for buffer/DRZ/host rock. As the surrounding DRZ undergoes the heating-cooling process due to radioactive decays in the waste package, the swelling stress acting on the DRZ is calculated using the change in average liquid saturation within the buffer over time (Figure 3-3). The increase in swelling stress can be described as a linear function of the change in average liquid saturation within the buffer as follows:

$$\Delta\sigma_{\text{swell}} = 3K\Delta S_l\beta_{\text{sw}}, \quad (3-1)$$

where  $K$  [Pa] is the bulk modulus,  $\Delta S_l$  is the change of liquid saturation within the buffer from the initial state, and  $\beta_{sw}$  is a dimensionless moisture swelling coefficient.  $\beta_{sw}$  is approximately 0.238 for a buffer material with a dry-density of  $1.6 \times 10^3$  kg/m<sup>3</sup>, initial liquid saturation of 0.65, bulk modulus of 20 MPa, and maximum swelling stress of 5 MPa (Rutqvist et al. (2011)).

Different DRZ permeability functions result in different swelling stress and liquid saturation profiles throughout the performance period of the repository, but they eventually converge to the maximum swelling stress when the buffer is entirely saturated with water. This change of swelling-stress as a linear function of change in saturation within the buffer (See Eq. 3-1) is similar to the changes in radial effective stress acting on the adjacent host rock observed from fully coupled THM simulations (see Figures 6 and 9a of Sasaki and Rutqvist (2021)).

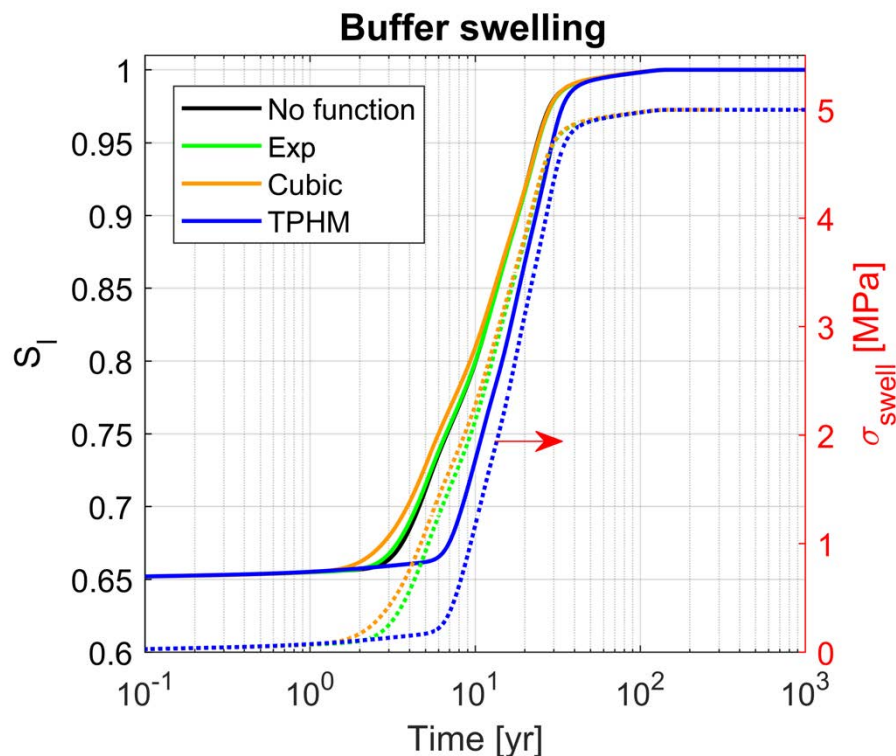


**Figure 3-3. Evolution of liquid saturation (solid lines) within the buffer and corresponding changes in swelling stress (dashed lines) acting on the DRZ for three permeability functions: (1) Exponential function (Exp; green), (2) Modified cubic function (Cubic; orange), and Two-part Hooke’s law model (TPHM; blue). The black line shows the reference case with a constant DRZ permeability and is very similar to Exp result.**

The temporal evolution of pressure, temperature, and saturation of the gas and liquid phases are obtained at the DRZ cell nearest the waste package for three permeability function cases: the exponential function (Exp), the modified cubic-law function (Cubic), and the Two-part Hooke's law model function (TPHM) (Figure 3-4). At early times, as the DRZ becomes heated, higher permeability causes faster pressurization and imbibition within the DRZ (faster increases in gas pressure and saturation) for Exp and Cubic permeability functions; Figures 3-4A and 3-4B). The initial permeability from the exponential function is the most similar to the constant permeability benchmark, with the closest agreement in saturation and

pressure profiles. At later times, the TPHM gives the highest gas pressure and saturation with the slowest re-saturation (Figure 3-4C).

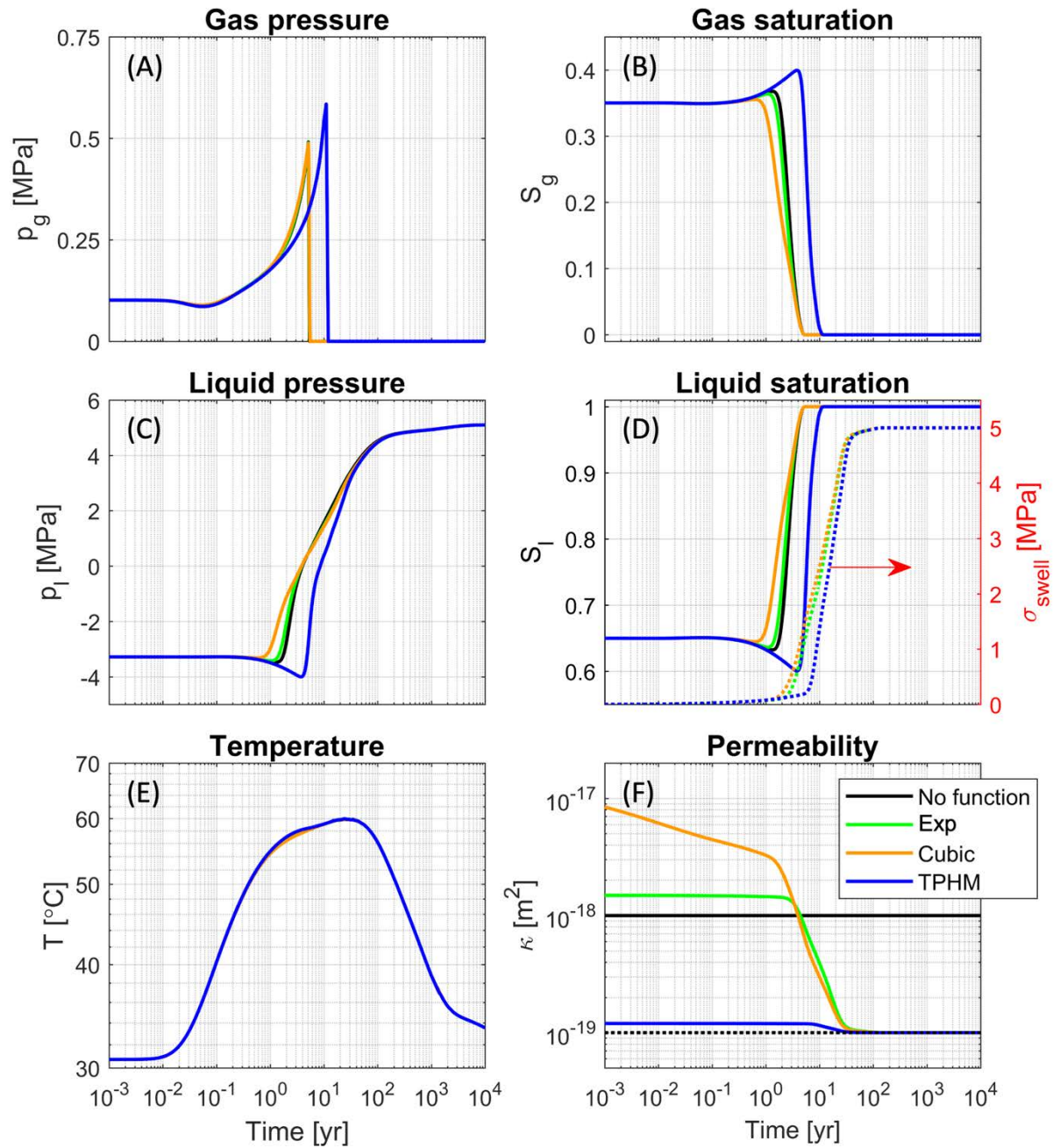


Figure 3-4. Evolution of physical quantities at the DRZ cell nearest the buffer for three cases with different stress-dependent permeability functions: (A) gas pressure, (B) gas saturation, (C) liquid pressure, (D) liquid saturation and swelling stress, (E) temperature, and (F) permeability. The host rock permeability is indicated by a black dash line in Figure F.

All three permeability relationships predict the DRZ permeability to converge to the initial permeability of the shale host rock, which was the basis for which the models were derived (i.e. DRZ permeability converges to the host rock permeability at maximum swelling stress). When the DRZ is characterized by Exp and Cubic functions, permeability decreases more quickly as a function of swelling stress than the TPHM, which results in faster re-saturation of the buffer and greater compressive stress on the DRZ in these models (Figure 3-4D). Correspondingly, the Exp and Cubic functions result in relatively larger reduction of the DRZ permeability than TPHM over a given change in water saturation in the buffer (Figure 3-4F). Note that the constant permeability case neglects swelling-driven elastic behaviors of DRZ and may exaggerate the intensity of fluid flow and solute transport through DRZ. These simulation results show that stress-dependent DRZ permeability changes similar to what is observed in fully coupled THM simulations implementing an exponential law as a function of effective stress (see Figure 11a of Sasaki and Rutqvist (2021)). This indicates that our reduced-order PFLOTRAN THC model can simulate geomechanical behaviors driven by buffer swelling without mechanical coupling.

### 3.1.3 Effects of shale permeability

The shale permeability is one of the key factors in assessing the efficiency of the natural barrier system (NBS) for safe nuclear waste disposal. In general, shales are characterized by very low permeability, typically less than  $1 \times 10^{-18} \text{ m}^2$ , from laboratory and regional studies (Neuzil 1994). The presence of heterogeneous features, i.e., transmissive fractures or pore structures, determines the spatio-temporal distribution of pressure fields and resultant flow and transport.

In this study, a sensitivity test was performed with more realistic lower shale permeability ( $1 \times 10^{-21} \text{ m}^2$ ). Figure 3-5 shows the temporal evolution of DRZ permeability and  $\text{Cl}^-$  concentration within the buffer nearby the waste package and DRZ with liquid saturation for the reference case (left column) and less permeable shale case (right column). The lower permeability of the shale host rock delays reduction of the DRZ permeability (Figures 3-5A and 3-5B) because the low-permeability shale retards the re-saturation process within buffer and DRZ, consequently causing slower increases of swelling stress (Figures 3-5C to 3-5D for buffer and Figures 3-5E to 3-5F for DRZ). Figures 3-5C to 3-5F indicate that  $\text{Cl}^-$  concentration within the DRZ decreases to achieve a steady state with the buffer while both buffer and DRZ are being heated. Once the buffer and DRZ are re-saturated,  $\text{Cl}^-$  concentrations increase due to influxes of  $\text{Cl}^-$  from the shale host rock. Lower shale permeability causes slower swelling that results in lower  $\text{Cl}^-$  concentration within DRZ before re-saturation (Figure 3-5F). This result implies that the host rock permeability will be one of the critical geologic parameters to determine the rate of buffer swelling and chemical transport into/out of the waste form. Note that hydraulic properties of the shale host rock may influence its thermal characteristics and corresponding heat transfer in the system, which has been neglected in this study. This suggests that the coupled THC process driven by stress-dependent thermo-hydrological variables needs to be considered in the safety assessment of the geological nuclear waste disposal.

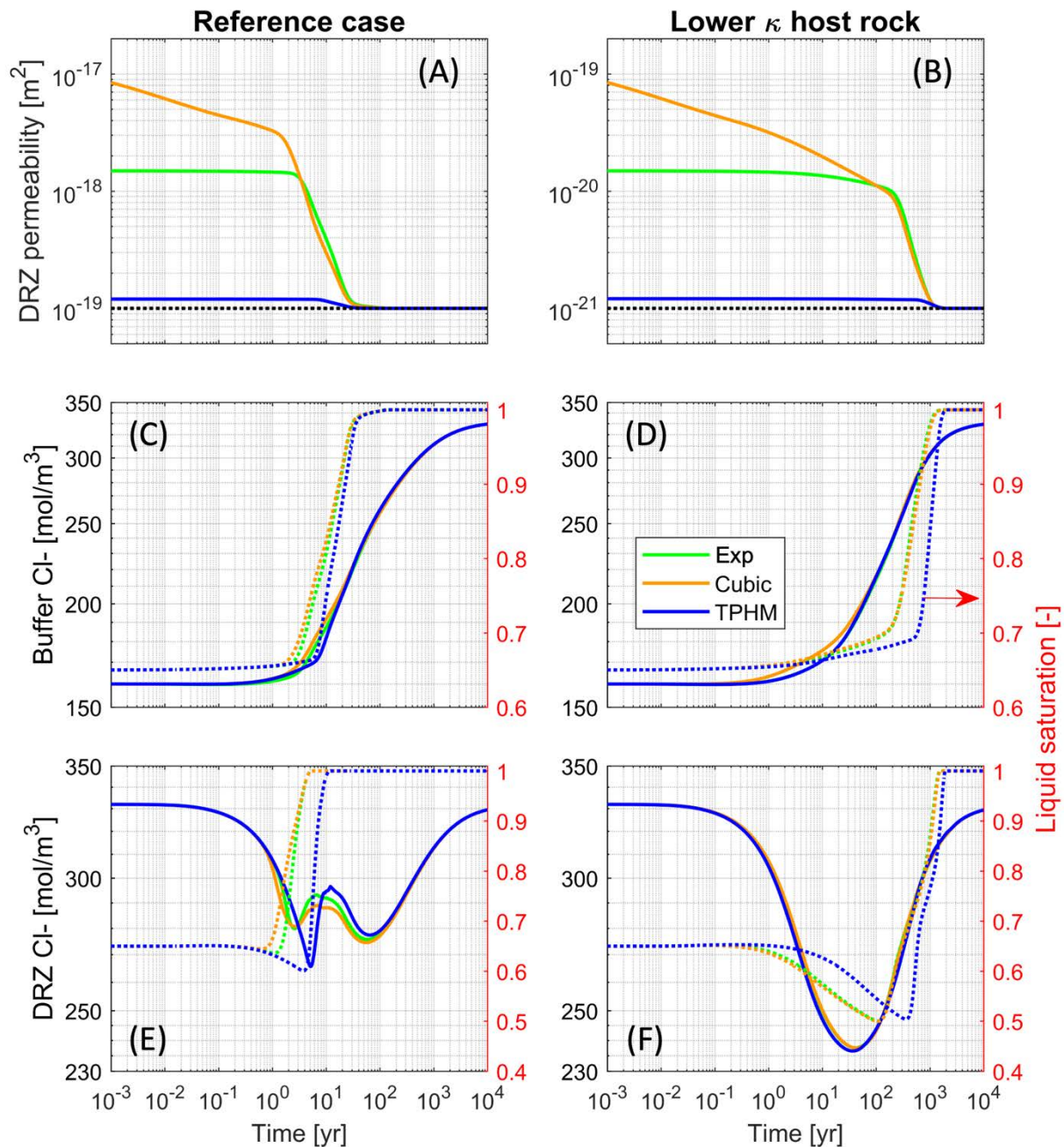


Figure 3-5. Sensitivity tests on shale host rock permeability: reference case ( $1 \times 10^{-19} \text{ m}^2$ ; left column) and less permeable shale ( $1 \times 10^{-21} \text{ m}^2$ ; right column). Temporal evolution of DRZ permeability (A–B), Cl<sup>-</sup> concentration and liquid saturation within buffer (C–D) and DRZ (E–F), respectively.

### 3.1.4 Geomechanical analysis

The local stress states within the DRZ can become altered in response to buffer swelling, which promotes their use as critical inputs to assess the geomechanical stability of the repository. This geomechanical analysis implements the method of wellbore stability analysis for hydraulic fracturing (Zoback 2007). If

the repository is envisioned as a horizontal and cylindrical wellbore, filled with fluids, parallel to the maximum horizontal stress ( $S_{H,max}$ ), the repository wall constitutes a principal stress plane because fluids filling the repository have no shear stress. This is schematically described in Figure 3-6.

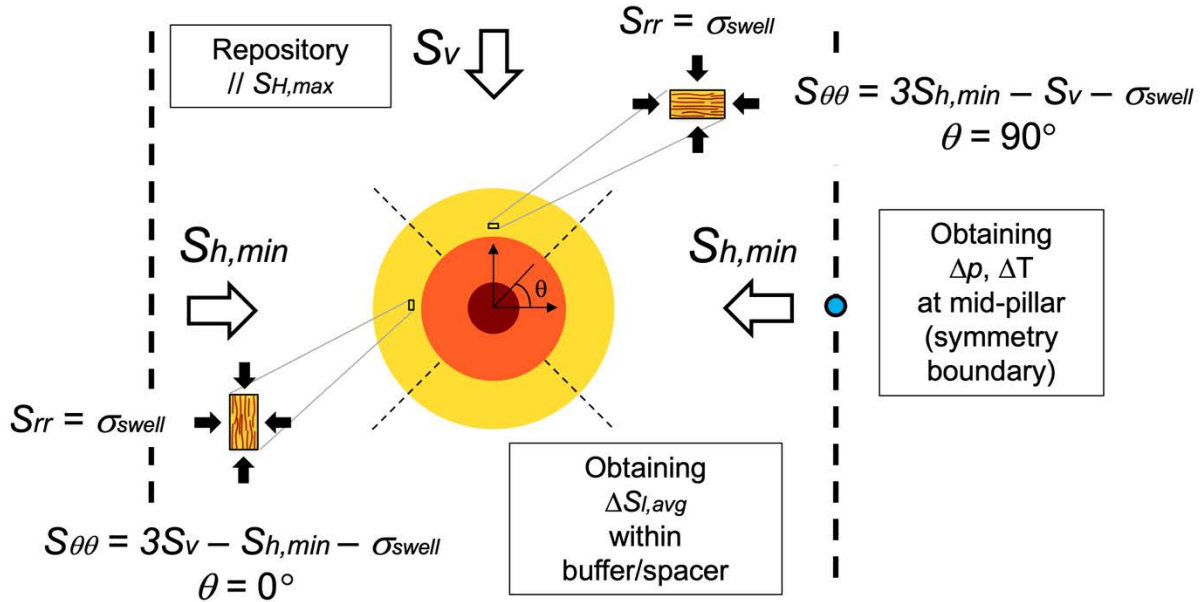


Figure 3-6. Schematic description of swelling-induced stresses acting on the repository system in all directions. The color of wp, engineered barrier, and DRZ follows the model domain shown in Figure 3-1B.

At the top and bottom boundaries of the repository, radial and hoop stresses are:

$$S_{rr} = \sigma_{swell} \quad (3-2)$$

$$S_{\theta\theta}(\theta = 90^\circ, 270^\circ) = 3S_{h,min} - S_v - \sigma_{swell} \quad (3-3)$$

The side boundaries of the repository model are closed and act as reflective boundaries, so that radial and hoop stresses are:

$$S_{rr} = \sigma_{swell} \quad (3-4)$$

$$S_{\theta\theta}(\theta = 0^\circ, 180^\circ) = 3S_v - S_{h,min} - \sigma_{swell} \quad (3-5)$$

The vertical stress is assumed to be constant throughout the duration of the simulation, and it can be predicted with a typical lithostatic pressure gradient of 23 kPa/m [Zoback, 2007]. The installation of waste packages perturbs the spatio-temporal fields of pore pressure ( $p$ ) and temperature ( $T$ ) which in turn affect the horizontal stress distribution over time:

$$\Delta\sigma_{h,p} = \alpha \frac{(1 - 2\nu)}{(1 - \nu)} \Delta p \quad (3-6)$$

$$\Delta\sigma_{h,T} = \alpha_T \frac{E}{(1 - \nu)} \Delta T \quad (3-7)$$

Where  $\alpha$  [-] is the Biot-Willis coefficient,  $\alpha_T$  [ $1/^\circ\text{C}$ ] is the thermal expansion coefficient,  $\nu$  [-] is Poisson's ratio for drained conditions, and  $E$  [Pa] is Young's modulus. Cooling of the waste package leads to solid shrinkage and stress relaxation (reducing compression), which should be taken into account for the calculation of the tensile fracture failure criteria. Installing waste packages with higher power will generate greater increase of local temperature within the DRZ, which can cause more intense thermally-induced stress. In this geomechanical analysis, temporal changes in pressure and temperature are obtained at the edge of the model domain, representing the symmetry boundary, as described schematically in Figure 3-6.

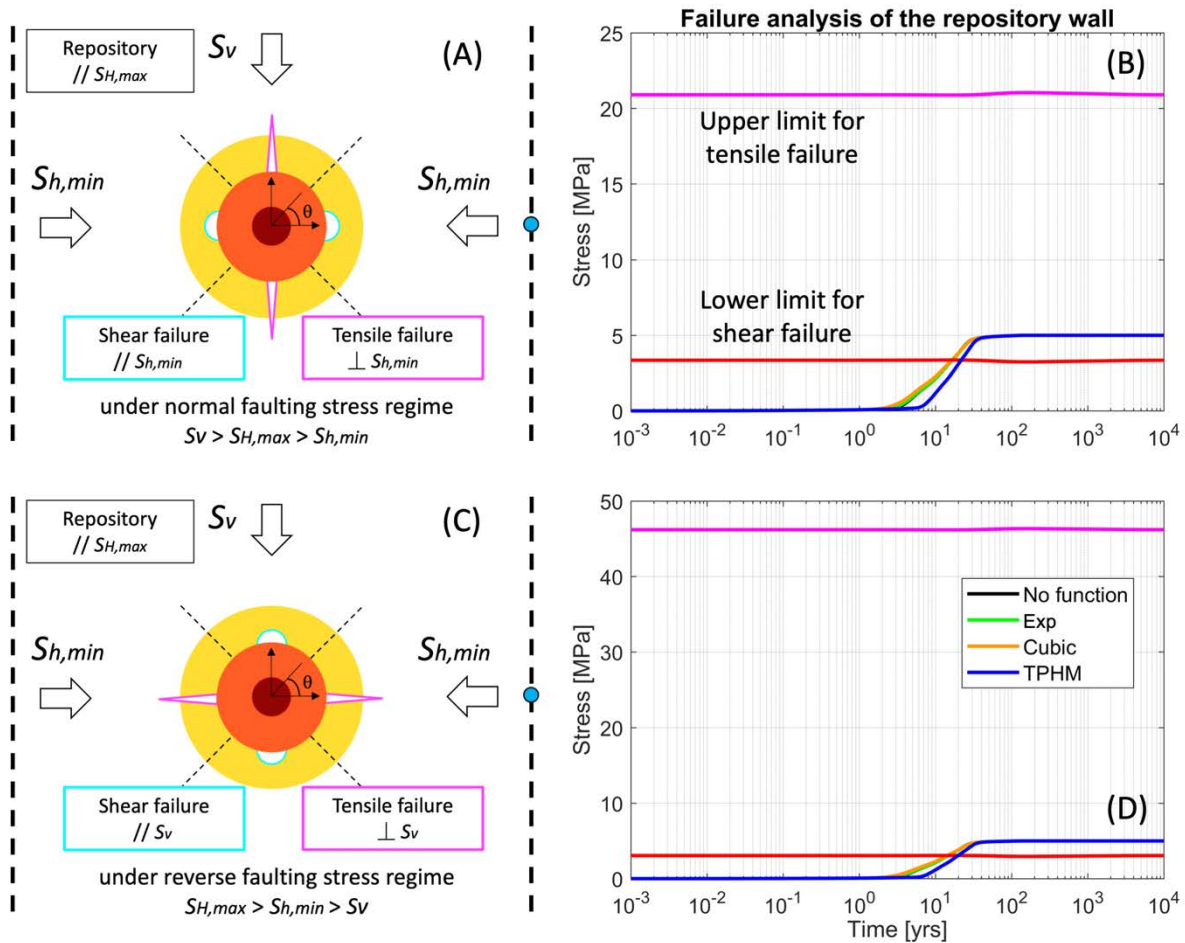


Figure 3-7. Geomechanical analysis of the DRZ stability: (A, C) schematic description of shear and tensile failure under the normal and reverse faulting stress states, respectively, and (B, D) lower and upper limits of  $\sigma_{swell}$  to prevent shear and tensile failure at given repository conditions and stress states; swelling stress staying between limits means that buffer swelling stabilizes the DRZ over time.

Depending on the faulting stress regime, the locations of minimal and maximal compression change. Shear failure (or breakout) results from elongation of the repository in the minimum stress direction, whereas tensile failure (or open-mode) initiates where hoop stress ( $S_{\theta\theta}$ ) becomes negative. Assuming that the repository is under the normal faulting (NF) stress regime ( $S_v > S_{H,max} > S_{h,min}$ ), the location of the least compression is at  $\theta = 90^\circ$  whereas the most compression occurs at  $\theta = 0^\circ$ . Accordingly, shear failure will occur parallel to the direction of  $S_{h,min}$ , whereas tensile failure will occur perpendicular to the direction of  $S_{h,min}$  where the least compressive stresses develop (Figure 3-7A). Shear failure will occur when effective stress anisotropy surpasses the shear strength limit of the formation. Under the reverse faulting stress regime where vertical stress is the lowest (Figure 3-7C) maximum anisotropy is found at  $\theta = 0^\circ$  and  $180^\circ$ , and the locations of shear and tensile failure are reversed.

$$S_1 = S_{\theta\theta} = 3S_v - S_{h,min} - \sigma_{swell} \quad (3-8)$$

$$S_3 = S_{rr} = \sigma_{swell} \quad (3-9)$$

Tensile fractures occur when the minimum principal stress ( $S_3$ ) on the repository wall goes below the limit for tensile stress: the tensile strength ( $T_s$ ). The minimum hoop stress is located on the wall and at  $\theta = 90^\circ$  and  $270^\circ$ :

$$S_{\theta\theta} = 3S_{h,min} - S_v - \sigma_{swell} \quad (3-10)$$

Note that the strike-slip faulting (SS) stress regime ( $S_{H,max} > S_v > S_{h,min}$ ) develops the same spots for shear and tensile failure at given orientation of the repository.

If the repository is under the reverse faulting (RF) stress regime ( $S_{H,max} > S_{h,min} > S_v$ ) can occur causing shear failure parallel to the direction of  $S_v$  and tensile failure perpendicular to the direction of  $S_v$  (Figure 3-7C). Shear failure can occur at  $\theta = 90^\circ$  and  $270^\circ$  with

$$S_1 = S_{\theta\theta} = 3S_{h,min} - S_v - \sigma_{swell} \quad (3-11)$$

$$S_3 = S_{rr} = \sigma_{swell} \quad (3-12)$$

whereas tensile stress can occur at  $\theta = 0^\circ$  and  $180^\circ$  with

$$S_{\theta\theta} = 3S_v - S_{h,min} - \sigma_{swell} \quad (3-13)$$

Assuming that the shale host rock is intact (no preexisting fractures), replacing  $S_1$  and  $S_3$  into a Mohr-Coulomb shear failure equation allows finding the swelling stress that would produce shear failure:

$$(S_1 - \Delta\sigma_{h,p} - \Delta\sigma_{h,T}) \leq (1 + F)(S_3 - \Delta\sigma_{h,p} - \Delta\sigma_{h,T}) + UCS \quad (3-14)$$

$$F = \left[ \sqrt{1 + \mu_i^2} + \mu_i \right]^2 \quad (3-15)$$

where  $m_i$  [-] is a frictional coefficient for intact rock, and UCS [Pa] is unconfined compression strength. Matching the lowest value of hoop stress with tensile strength ( $T_s$ ) allows finding the swelling stress which overcomes the breakdown pressure ( $\sigma_{\text{swell}} = P_b$ ) that would produce a tensile fracture:

$$-T_s \leq -P_b + (S_{\theta\theta} + \sigma_{\text{swell}}) - \Delta\sigma_{h,p} - \Delta\sigma_{h,T} \quad (3-16)$$

After obtaining the temporal evolution of  $\Delta S_i$  within the buffer, pressure, and temperature at the middle of symmetry boundary,  $\sigma_{\text{swell}}$ ,  $\Delta\sigma_{h,p}$ , and  $\Delta\sigma_{h,T}$  are calculated as a function of simulation time over the  $10^6$ -year simulation period using (3-1), (3-6), and (3-7). From the failure criteria (3-14) and (3-16), the lower and upper limits of swelling stress to prevent shear and tensile failure of DRZ can be calculated with assumed frictional characteristics ( $\mu_i = 1$ , UCS = 29 MPa, and  $T_s = 2.5$  MPa) under the normal faulting stress ( $S_v = 23$  MPa and  $S_{h,\text{min}} = 13.8$  MPa) and reverse faulting stress ( $S_v = 23$  MPa and  $S_{h,\text{min}} = 25.3$  MPa) states over the  $10^6$ -year simulation period.

The calibration shows that buffer swelling stabilizes the DRZ mechanically (staying above the lower limit of swelling stress; Figures 3-7B and 3-7D), and the TPHM function results in the slowest increase of  $\sigma_{\text{swell}}$  due to less reduction in the DRZ permeability (Figure 3-4F). This geomechanical analysis implies that buffer swelling compresses the DRZ and closes preexisting fractures within DRZ, which will secure the waste package as well as enhance the mechanical stability of the repository at the given in-situ stress condition.

### 3.1.5 Near-field multiphysics mechanism

As the PFLOTRAN simulation results show in Figures 3-4 and 3-5, the canisters containing heat-emitting nuclear waste will perturb the thermal field around the repository and affect the rate of de-/re-saturation of engineered barriers corresponding to the heat pulse. Note that the initial heat emission from the waste package and the heat capacity of the rock will determine the temperature distribution and control the resultant multiphysics processes (Zhao et al. 2014; Finsterle et al., 2019).

Water transport in the buffer at unsaturated conditions is a complex process which depends on temperature and water content in different parts of the buffer. The phase changes between water and steam cause evaporation and condensation. In addition, the thermal expansion and compression of water and air will affect the hydraulic conditions in the buffer and backfill. Thus, it is expected that advective fluxes of water and gas will be driven by liquid and gas pressure gradients, mechanical changes will occur in the engineered barriers, and subsequently solute diffusion and chemical reactions between the percolating fluids and the host rock will take place.

Thermally-driven mechanical impacts on rock properties are approximated by implementing the DRZ permeability changes as function of effective stress, which can provide reasonable estimate of stress perturbations without fully coupled THM simulations. However, the assumption of a pre-defined and constant volume of the DRZ may not be appropriate to describe long-term inelastic mechanical deformation (e.g., healing and sealing) associated with the surrounding host rock and overburden (Tsang et al., 2005). Such mechanical deformation can be critical to determine the transport of radioactive isotopes. If plastic behavior is dominant in the shale repository system, the DRZ deformation could occur in a manner that is uncoupled to elastic fracture opening and closure (Zaoui & Sekkal 2015) such that the permeability functions presented previously may not be appropriate to represent the effect of mechanical behaviors on the hydraulic characteristics of DRZ. Therefore, further studies are required to validate the accuracy of stress-dependent permeability changes as well as to advance this stress approximation method by including geomechanical impacts on other hydrological and thermal characteristics.

### 3.1.6 Future study

The fully coupled THC (Thermo-hydro-chemical) PFLOTRAN model with mechanical impacts of heat and pressure buildup on near-field characteristics will continue in the future, with a goal of integrating near-field process modeling into field-scale PA simulation in the GDSA Framework. In the short-term, stress-dependent porosity functions will be tested to generate a reasonable evolution of the DRZ porosity for a given scenario of nuclear waste disposal. The buffer re-saturation and corresponding stressing of the surrounding DRZ depends heavily on the waste package thermal loading, and thus, functions of thermal properties for buffer and DRZ will be integrated into the PFLOTRAN simulation. Afterwards, the reactive transport and waste package degradation process models will be included to examine how near-field perturbations in thermal and hydrological characteristics of DRZ affect the transport of radio-nuclides.

## 3.2 Thermal DPC studies

This project follows on from the DPC disposal thermal scoping analysis in Jones et al. (2021). In that report the unsaturated alluvium reference cases were unable to run to the one-million year simulation end. The exact reason the simulations did not complete is unclear. It may have been due to solver failures at the onset of the re-saturation process as the DPC cooled down, as was observed in a  $\frac{1}{4}$  waste package model in Sevougian et al. (2019b). Jones et al. (2021) also observed that there was a high level of grid orientation effects in the alluvium model at the end of the simulations. Grid orientation affects are also observed in the PA-scale unsaturated alluvium model in the present work, as discussed in Section 5 and shown in Figure 5-10.

In the present work a simplified model for the unsaturated alluvium case is meshed using Voronoi cells to see if grid orientation affects can be minimized and the simulations completed. Model height was increased to 500 m so that the waste package was vertically in the center of the domain, but x and y dimensions are the same at 35 m and 10 m, respectively.

In these models for the unsaturated alluvium case, the heterogeneity driven by layered system has been neglected. Instead, the host rock is assumed to be homogeneous by implementing the material properties for a confining unit where the waste package is placed (the model properties of “ubf\_conf” given in Table 4-1 of Jones et al. (2021)). The waste package, buffer and damage zone dimensions and properties are the same as Jones et al. (2021) Table 4-1. The initial condition is a linear distribution of pressure as a function of depth, and uniform gas saturation of 83% for the host rock, as this was the initial gas saturation near the waste package in Jones et al. (2021).

The DPC heat source simulations for the 50<sup>th</sup> percentile of Jones et al. (2021) are repeated here using PFLOTRAN GENERAL mode with PFLOTRAN default solvers and without characteristic curve smoothing.

### 3.2.1 Voronoi mesh generation

Surfaces for the  $\frac{1}{4}$  DPC alluvium mesh are generated using the LaGriT (LANL, 2017) software. The stratigraphic layering of the alluvium system is omitted for simplicity and the entire model is assigned properties representative of the fine-grained/playa sediment. Due to difficulty creating flat interior surfaces, the end of the waste package is not explicitly meshed. As a consequence, the length of the DPC heat source is only approximately enforced. The concentric cylinders of the waste package ( $r = 2.4$  m), backfill ( $r = 3.48$  m) and damage zone ( $r = 5.15$  m) are approximated piecewise by points on each half-circle spaced  $10^\circ$  apart, as can be seen on the mesh in Figure 3-8. The automated mesh coarsening algorithm is allowed to make the coarsest mesh that honors the input surfaces, which results in a model with 36,622 cells. The minimum connections between cells is 4, the maximum is 33 and the average is 11. (For comparison, the flexed hexahedral mesh has 109,872 grid cells, but just six connections at each

interior cell.) As shown in Figure 3-8, the mesh is highly refined near the DPC but becomes coarse in the far field.

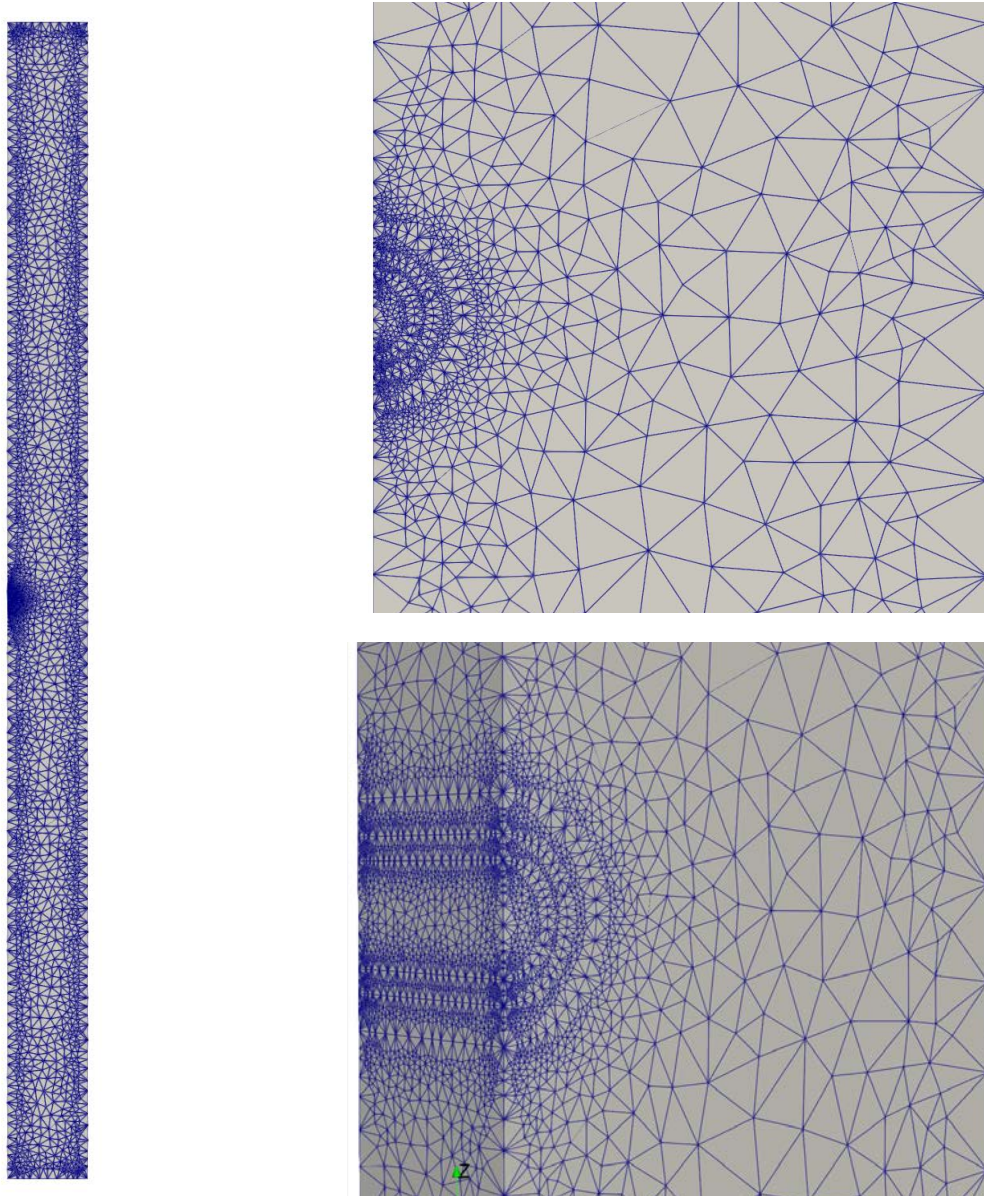


**Figure 3-8. Voronoi mesh for unsaturated alluvium DPC thermal study. Left: surface mesh on  $x=10\text{m}$  plane for the entire length of the model. Top Right: surface mesh on  $x = 10\text{ m}$  plane near the DPC. Bottom Right: isometric view of the surface mesh near the DPC.**

### 3.2.2 Modeling results

Both simulations run to the full the one-million year simulation time in the homogeneous approximation of the UZ repository. The computation times were similar, with the Voronoi mesh model taking 3.01 hours to complete and the flexed hexagonal mesh completing in 2.96 hours on a single core of a Macbook laptop. The flexed hexahedral mesh has approximately three times as many grid cells as the Voronoi mesh (109,872 vs 36,622), so the similarity in the computation times indicates how much more challenging it is to simulate on Voronoi meshes.

Figure 3-9 shows the spatial distribution of gas pressure and gas saturation at  $t = 100$  years for the two models implementing flexed hexagonal grids (Figures 3-9A and 3-9C) and Voronoi meshes (Figures 3-9B and 3-9D). For the case of flexed grids, numerical dispersion driven by grid orientation causes a lower maximum gas pressure in a waste package (10.878 MPa in Figure 3-9A vs 10.925 MPa for Voronoi mesh in Figure 3-B) and an extended region of fully unsaturated conditions in diagonal directions (Figure 3-9C). The Voronoi mesh reduces the grid orientation effects and allows the pressure and saturation perturbations to more closely correspond to the cylindrical geometry of the waste package and engineered barriers (Figures 3-9B and 3-9D).

Note that greater grid orientation effects may result from the heterogeneous material properties posed by the original layered system, and have been generally observed in the unsaturated alluvium models, including effects on the initial conditions caused by groundwater flow at depth as considered in the PA model in Section 5 and shown in Figure 5-10. Flexed hexagonal grids demonstrably cause a distorted distribution of pressure and saturation fields at the near-field adjacent to the waste package. Thus, this comparative study suggests that the Voronoi mesh may be more suitable to minimize the effect of grid orientation in future studies.

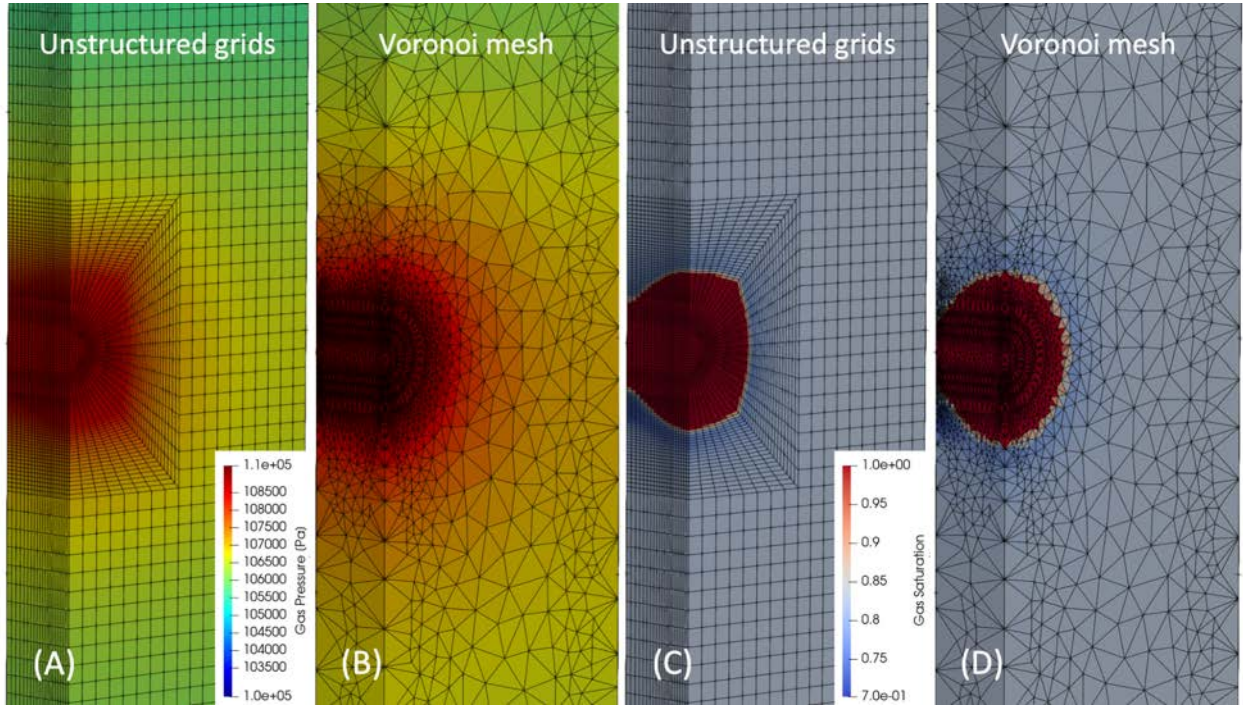


Figure 3-9. Results of gas pressure (A, B) and gas saturation (C, D) from PFLOTRAN models using a flexed hexahedral grid and Voronoi grid at  $t = 100$  years.

### 3.2.3 Future study

In the short-term, the implementation of Voronoi mesh will be improved to capture the waste package shape exactly and extended to the layered system in Jones et al. (2021) with groundwater flow for the unsaturated alluvium case to see if they are able to complete the full-complexity case. Future near-waste package studies in alluvium will be conducted with Voronoi meshes.

## 3.3 References

- Chang, K.W., Nole, M., and Stein, E.R. 2021. *Reduced-order modeling of near-field THMC coupled processes for nuclear waste repositories in shale*. *Comput. Geotech.* 138:104326.
- Finsterle, S., Muller, R.A., Baltzer, R., Payer, J., Rector, J.W. 2019. *Thermal Evolution near Heat-Generating Nuclear Waste Canisters Disposed in Horizontal Drillholes*. *Energies*. 12(4):596.
- van Genuchten, M.T. 1980. *A closed-form equation for predicting the hydraulic conductivity of unsaturated soils*. *Soil Sci. Soc. Am. J.* 44:892.
- Jones, P., Chang, K.W., and Hardin, E.L. 2021. *DPC disposal thermal scoping analysis*. SAND2021-7515R, Sandia National Labs. (SNL-NM), Albuquerque, NM.

- Jove-Colon, C.F., Hammond, G.E., Kuhlman, K.L., Zheng, L., Kim, K., Xu, H., Rutqvist, J., Caporuscio, F.A., Norskog, K.E., Maner, J., Palaich, S., Cheshire, M., Zavarin, M., Wolery, T.J., Atkins-Duffin, C., Jerden, J., Copple, J.M., Cruse, T., Ebert, W. 2016. *Evaluation of Used Fuel Disposition in Clay-Bearing Rock*. SAND2016-10311R. Sandia National Laboratories. Albuquerque, NM, USA.
- Liu, J.F., Song, Y., Skoczylas, F., Liu, J. 2016. *Gas migration through water-saturated bentonite-sand mixtures, CO<sub>2</sub> argillite, and their inter-faces*. Can. Geotech. J. 53(1):60–71.
- Los Alamos National Laboratory. 2017. *Los Alamos grid toolbox, LaGriT*. <http://lagrit.lanl.gov>
- Mualem, Y. 1976. *A new model for predicting the hydraulic conductivity of unsaturated porous media*. Water Resour. Res., 12:513–522.
- Neuzil, C.E. 1994. *How permeable are clays and shale?* Water Resour. Res., 30:145–150.
- Sasaki, T., Rutqvist, J. 2021. *Estimation of stress and stress-induced permeability change in a geological nuclear waste repository in a thermo- hydrologically coupled simulation*. Comput. Geotech. 129:103886.
- Sevougian, S. D., Stein, E. R., LaForce, T., Perry, F. V., Nole, M., Haukwa, C. B., and Chang, K. W. 2019b. *GDSA Repository Systems Analysis FY19 Update*. SAND2019-11942R. Sandia National Laboratories. Albuquerque, NM.
- Shelton, S.M. 1934. *Thermal conductivity of some irons and steels over the temperature range 100 to 500° C*. Bureau of Standards Journal of Research. 12(4/6):441–450.
- Tsang, C.F., Bernier, F., Davies, C. 2005. *Geohydromechanical processes in the excavation damaged zone in crystalline rock, rock salt, and indurated and plastic clays-in the context of radioactive waste disposal*. Int. J. Rock Mech. Min. Sci., 42:109–125
- Zaoui, A., Sekkal, W. 2015. *Can clays ensure nuclear waste repositories?* Sci. Rep. 5:8815.
- Zhao, H.G., Shao, H., Kunz, H., Wang, J., Su, R., Liu, Y.M. 2014. *Numerical analysis of thermal process in the near field around vertical disposal of high- level radioactive waste*. J. Rock Mech. Geotech. Eng. 6:55–60
- Zheng, J., Zheng, L., Liu, H.H., Ju, Y. 2015. *Relationships between permeability, porosity and effective stress for low-permeability sedimentary rock*. Int. J. Rock Mech. Min. Sci. 78:304–318.
- Zoback, M. 2007. *Reservoir Geomechanics*. Cambridge University Press. Cambridge, UK.

## 4. CONCEPTUAL MODEL OF THE SHALLOW GEOSPHERE IN A CRYSTALLINE ROCK ENVIRONMENT

### 4.1 Introduction

Disposal system modeling of the geosphere for the crystalline reference case has focused on a detailed representation of the crystalline host rock at repository depths, in particular the characteristics of fracture systems (Mariner et al. 2016). Features represented in the host rock have been informed by studies at the Forsmark site in Sweden (Mariner et al. 2016). Features of the sedimentary overburden are a simplified and generic representation of glacial deposits that includes reasonable values for thickness, permeability, porosity and transport properties (Mariner et al. 2016). A useful advancement in the development the crystalline reference case would be to develop a more detailed conceptual model of the shallow geosphere, that is, the upper 100 meters that includes the uppermost crystalline bedrock and the glacial deposits that overlie the bedrock. Studies at the Forsmark site in Sweden have led to well-developed models of the shallow geosphere including both the uppermost (“superficial”) crystalline bedrock and overlying glacial and other unconsolidated surficial deposits (Follin et al. 2008; Hedenstrom and Sohlenius 2008; Sohlenius et al. 2013). These models, including detailed representation of glacial deposits, are considered essential inputs for modeling radionuclide transport between the shallow geosphere and the biosphere (Lindborg 2010).

The purpose of this section is to begin development of a more refined model of the shallow geosphere in a representative crystalline environment of the U.S. We base this model on a region of the U.S. that has features in common with the crystalline environment at Forsmark in order to identify similarities and differences in the two settings that might influence how flow and transport is modeled in the shallow geosphere. This comparison will help guide future development of numerical models that incorporate features and processes representative of crystalline environments in the U.S.

### 4.2 Crystalline Rock Environments in the U.S.

Crystalline rocks include granitic rocks as well as less silicic plutonic rocks (e.g., granodiorite) and high-grade metamorphic rocks such as gneiss. Significant occurrences of crystalline rocks in the U.S. can be grouped into six major regions (from west to east): the Pacific border region, the Basin and Range region, the Rocky Mountain region, the Lake Superior Region, the Southern Appalachian Region and the Northern Appalachian Region (OCRD 1983; Table 4-1, Figure 4-1).

These regions can be grouped more generally in three main geographic and geologic terrains. The largest of these terrains occupies the western U.S. and includes Cenozoic to Archean granites of the North American Cordillera. Granites of the western Cordillera are in a geologic environment characterized by high topographic relief and high hydraulic gradient, reflecting active faulting and uplift, as well as significant areas of high to moderate seismicity. Archean granites of the Superior Province in the north-central U.S. (Lake Superior region) occupy a region characterized by relatively flat topography, low seismicity and a history of Quaternary glaciation (Harrison et al., 1983). Proterozoic to Paleozoic granites of the southern and northern Appalachian Mountains of the eastern U.S. occupy regions characterized by low to moderate topography and hydraulic gradients, low to moderate seismicity and a history of glaciation in the northern Appalachian Mountains (OCRD 1983; Figure 4-1). The combination of features found in the northern Appalachian Mountains (subdued topography, low hydraulic gradients, shallow crystalline bedrock with overlying glacial deposits) are similar to the geologic and hydrologic conditions of the crystalline rock environments in Finland and Sweden that have been extensively studied as host sites for HLW waste disposal.

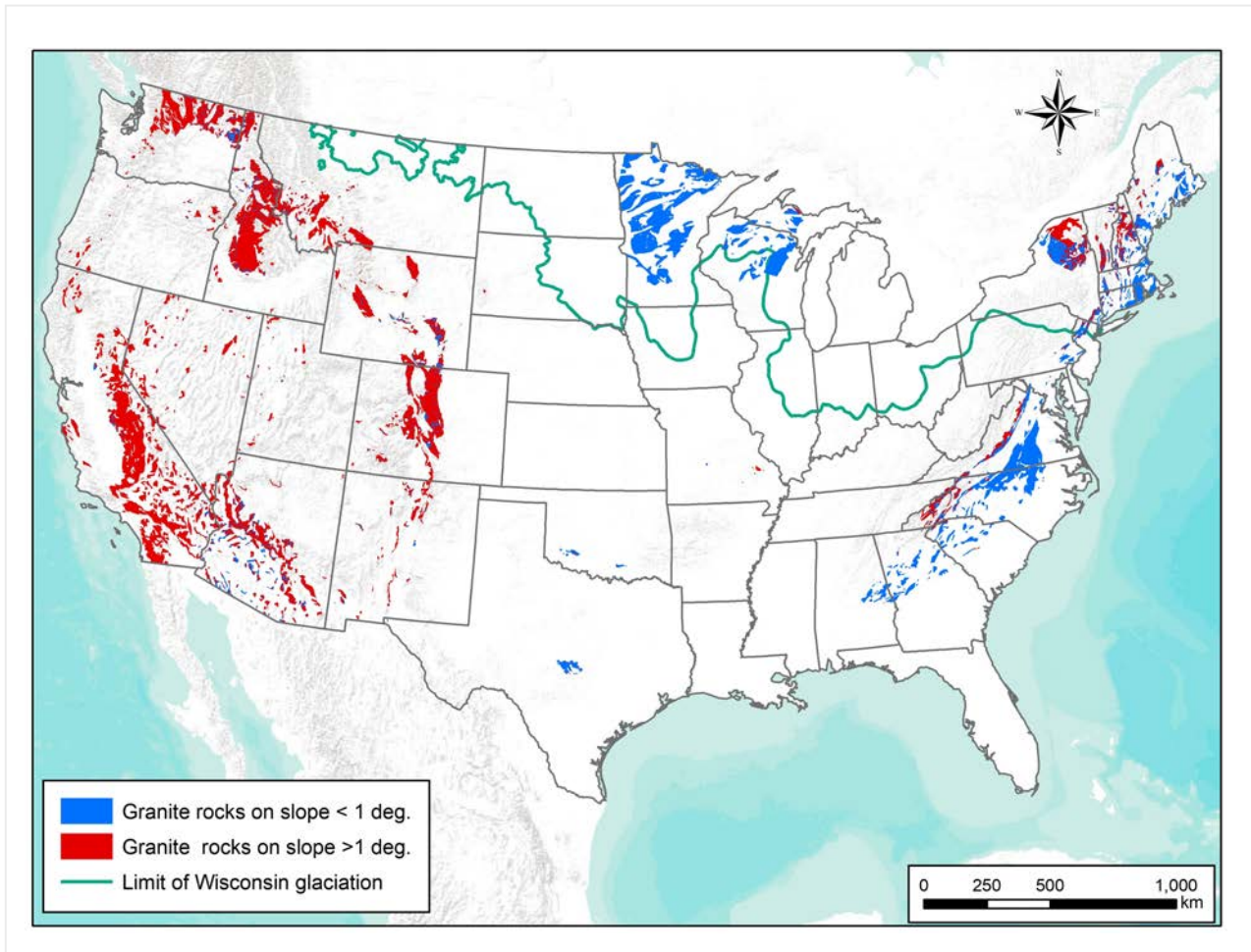


**Figure 4-1. Distribution of exposed or near-surface crystalline rocks (red) in the conterminous US from Perry et al. (2014). Crystalline rock occurrences are classified by smoothed local slope using a 3 km grid, illustrating that crystalline rocks in the eastern half of the US occur more frequently in areas of low topographic relief (slope <1 degree). The limit of Wisconsin glaciation is the southern extent of the most recent North American ice sheet.**

**Table 4-1. Crystalline Regions in the US after Mariner et al. (2011).**

<b>Region</b>	<b>Age and Location</b>	<b>Attributes</b>	<b>Comments</b>
Pacific Border Region	Triassic, Jurassic, and Cretaceous granites, California, Oregon, and Washington	Very high hydraulic gradient. Large vertical movement along the Sierra Nevada and Cascade Range. Large horizontal movement along the coast range. High seismic and volcanic activity. Regions of large expanses of granite.	
Basin and Range Region	Precambrian granites, Arizona, Jurassic and Triassic granites east of Sierra Nevada. Cretaceous granites in Nevada, California, and Arizona.	High hydraulic gradient. Large vertical movement. Many active faults, Major mining for mineral deposits. High heat flow region.	Some granitic areas in Arizona and Nevada have a relatively low incidence of seismicity, when compared to the California granites.
Rocky Mountain Region	Archean granite, Wyoming, and southern Montana. Precambrian granites, Front Range, Colorado. Mesozoic granite, Idaho batholiths, and Montana.	High hydraulic gradient. Large vertical movement. Moderate seismic activity. Large faults bound uplifted blocks. Major mineral deposits. Occurrence of large homogeneous masses of granite.	
Lake Superior Region	Precambrian granites, Minnesota, Wisconsin, and Michigan.	Low hydraulic gradient. Little vertical relief. Small number of faults. Very low seismic activity. No volcanic activity.	The most stable region of granite outcrops in the U.S. – part of the N. American Continent stable craton
Northern Appalachian and Adirondack Region	Precambrian crystalline rocks, New England and the Adirondacks.	Moderate to low hydraulic gradients. Moderate vertical uplift. No modern fault movement. Low seismic activity. No volcanic activity	
Southern Appalachian Region	Precambrian granite, Blue Ridge and Piedmont provinces.	High hydraulic gradient in the Blue Ridge. Intermediate to low hydraulic gradient in the Piedmont. Moderate vertical movement. Very few recent faults. Low seismicity. No volcanic activity. Large masses of granite.	

### 4.3 Representative Region for Identifying Features in the Conceptual Model of the Shallow Geosphere

Several features represented in the conceptual model for the GDSA crystalline reference case are based on features of the host rock that have been studied and documented at the Forsmark site in Sweden (Mariner et al. 2016). Selection of a region in the U.S. to guide development of a conceptual model of the shallow geosphere is premised on identifying a region that has an overall similarity to the crystalline environment at Forsmark. The goal is to facilitate comparison to the well-characterized and well-documented environment at Forsmark in order to gain insights into features of a U.S.-based conceptual model that are important to groundwater flow and transport. The northern Appalachian region of New England has several similarities to the Forsmark region including the fracture characteristics of shallow bedrock, low topographic relief and low hydraulic gradients, a stable tectonic setting and a Quaternary history of glaciation resulting in glacial deposits overlying the crystalline bedrock. Like the Forsmark region, New England has also experienced marine submergence and crustal rebound as continental glaciers have depressed the crust and then retreated following climate warming.

Within the New England region, we focus on two areas in Maine that include granitic plutons and glacial deposits that are typical of the region (Figure 4-2). These areas have been previously studied by DOE (1986), providing useful documentation and data related to their geology, hydrology and surface features. State organizations in Maine, such as the Geological Survey of Maine, provide online digital geologic data that aids in the development of the conceptual model of the shallow geosphere. Key GIS datasets available online from the Maine Geological Survey include bedrock geologic maps and maps of surficial geology (<https://www.maine.gov/dacf/mgs/pubs/index.shtml>). Other important datasets include the Maine Water Well Database (<https://www.maine.gov/dacf/mgs/pubs/digital/well.htm#data>), which provides data on overburden thickness and well yields.

The two areas of interest in Maine encompass the Sebago Lake Pluton in southwestern Maine and the Passadumkeag River Pluton in southeastern Maine (Figure 4-2). These two reference areas provide a representative sampling of near-surface crystalline rock environments that include glacial deposits and surface features such as lakes and wetlands. Both areas also lie close to the marine limit that marks the maximum area of marine submergence following the last glacial maximum and retreat (Figure 4-2). This limit is significant in that it marks the inland extent of fine-grained deposits of marine silts and clays that form an important regional confining unit. Although the data gathered by DOE (1986) and subsequent related studies provide a starting point to understand the geologic and hydrologic characteristics of the region, data from nearby areas within the same region are also used to gain a more complete understanding of features important for development of the conceptual model.

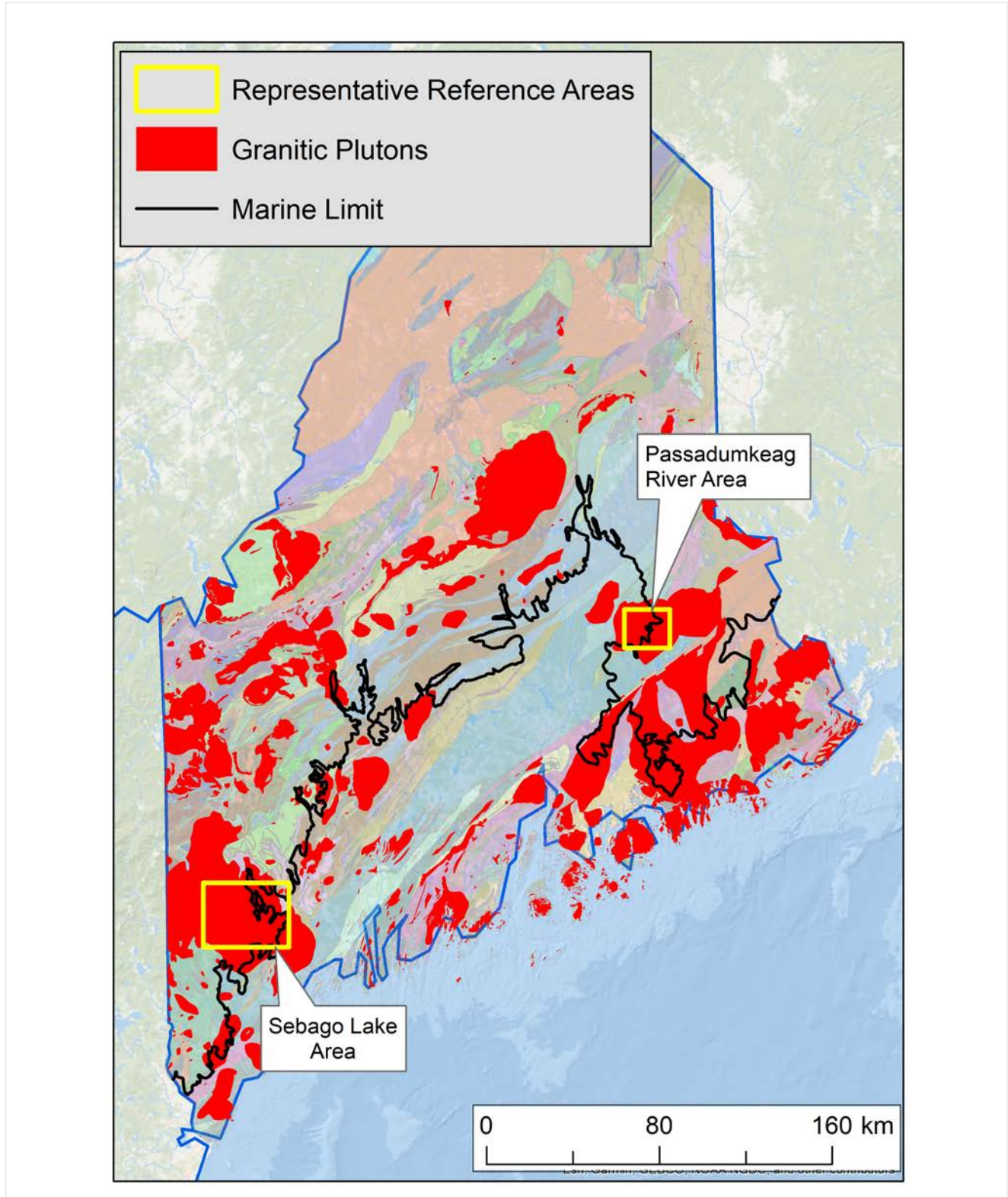


**Figure 4-2. Distribution of Paleozoic granitic plutons in Maine and boundaries of reference areas that include the Sebago Lake Pluton (southwestern Maine) and Passadumkeag River Pluton (southeastern Maine). Granitic plutons intrude several northeast trending metamorphic terranes.**

## 4.4 Regional Geology and Hydrology

### 4.4.1 Geology

The Northern Appalachians formed from a series of accretionary and collisional orogens during the Paleozoic Era. In Maine, these orogens produced regional metamorphism of sedimentary and volcanic rocks and a history of plutonism during and after the Acadian Orogeny that lasted for more than 100 Ma (Hogan and Sinha 1989). The granitic plutons intruded lower grade (greenschist) metamorphic rocks in the east and higher-grade metamorphic rocks (amphibolite facies) rocks in the west (Solar and Tomascak 2016). The majority of plutons in Maine, including the Passadumkeag River Pluton, were intruded as part of the Acadian Orogeny, between about 440 and 360 Ma (Hogan and Sinha 1989; Solar and Tomascak 2016). The Sebago Lake Pluton is a post-Acadian intrusion and one of the youngest major granitic plutons in the region with an age of 293 Ma (Solar and Tomascak 2016).

Episodes of granitic plutonism were followed by multiple episodes of regional uplift and erosion, which has left granitic bedrock at or near the surface throughout the region. Uplift and erosion of the crystalline terrain prior to Quaternary glaciation resulted in a relatively subdued landscape similar to the landscape of today (Thompson 2015).

In the most recent glacial cycle, continental ice sheets covered all of Maine and extended some distance past the current coastline. The weight of the ice sheets depressed the Earth's crust by about 240 meters (Stuiver and Borns 1975). With a warming climate, the ice sheets began to retreat about 14 thousand years ago and seawater submerged the southern coastal lowlands and valleys to the inland marine limit, as indicated by radiocarbon dating of shells found in marine clay and silt deposits (Figure 4.2; Stuiver and Borns 1975, Borns et al. 2004). Following deglaciation, the crust rapidly rebounded (~30m/ka, Borns et al. 2004) and the sea had largely retreated from the coastal lowlands by about 11 ka.

The advance and retreat of glaciers deposited several types of glacial deposits that overlie the crystalline bedrock (Thompson 2015). The oldest and most widespread is glacial till, composed of unsorted sand, silt, clay and cobbles that was deposited directly from glacial ice as glaciers moved over the landscape. The second most common deposit in the region are deposits of marine silt and clay that formed when fine-grained material was transported for some distance from the melting glacial front and deposited on the seafloor. Marine silt and clay deposits occur as far inland as the marine limit (Figure 4-2). Glaciofluvial sand and gravel are more localized, stratified deposits that form when glacial meltwater streams deposit coarser materials closer to the melting ice front (Thompson 2015). Because of their high permeability, sand and gravel deposits are the most significant aquifers in the region.

### 4.4.2 Hydrology

The two major aquifers in the region are the sand and gravel aquifers and the bedrock aquifers (Caswell 1987). Sand and gravel aquifers are the most productive aquifers in the region but are localized to channels or paleochannels that cover only a small percentage of the regional landscape. Bedrock aquifers are also localized and depend on the distribution and characteristics of shallow fractures. Till deposits, which cover most of the region, are poor aquifers. Marine silt and clay deposits are present in areas that were below the marine limit and act as a confining unit, impeding water movement from above and below due to their low permeability.

The regional topographic gradient of the region is towards the sea to the southeast. Near-surface hydraulic gradients in the region can be estimated from potentiometric surfaces presented in a site-specific study to the south of the Sebago Lake reference area (Nielsen et al. 1995). This study indicates an approximate gradient of 0.002 m/m to the southeast.

## 4.5 Data to Support the Crystalline Conceptual Model

The two reference areas in southern Maine encompass the Sebago Lake Pluton and the Bottle Lake complex, a composite intrusion that includes the Whitney Cove and Passadumkeag River plutons (DOE 1986; Figure 4-2). Data to support the conceptual model is focused on glacial deposits and the upper ~100 meters of the crystalline bedrock characterized by a system of horizontal fractures or sheet joints. Detailed properties of the crystalline rock (e.g., mineralogy and chemistry) are not considered as important to development of the conceptual model at this stage compared to shallow fracture features and the characteristics of the overlying glacial deposits. The two reference areas in Maine include glacial deposits that are representative of glacial deposits that occur throughout the larger region (Thompson 2015). For the purposes of developing a simplified conceptual model, we focus on till, outwash sand and gravel deposits and glaciomarine clay and silt deposits. These three glacial deposits are considered to be the most significant in terms of areal distribution, near-surface hydrology and flow and transport in surficial deposits (Thompson 2015).

### 4.5.1 Topography and Surficial Geology

Topographic and landscape data are represented using digital elevation models (DEM) and surface water data for each of the reference areas. A digital elevation model represents the topographic relief of the landscape. The relief in both reference areas is low to moderate with a total relief of about 300 meters (Figures 4-3 and 4-5). This compares to the relief on the land portion of the Forsmark site (a flat coastal site) of 50 meters (Strömberg and Brydsten 2013). The geology of surface deposits is based on the digital version of the Surficial Geology Map of Maine (Thompson and Borns 1985; MGS 2017). The geology of both reference areas is similar to Forsmark, consisting of crystalline bedrock overlain by a relatively thin layer of glacial and younger deposits.

#### 4.5.1.1 Sebago Lake Area

The landscape of the Sebago Lake reference area is characterized by generally north-south trending ridges separated by valleys that are typically filled by elongate lakes (Figure 4-3). Elevations in the reference area range from approximately 350 to 40 meters, with the lowest elevations in the southeastern corner of the area and the highest elevations in the more rugged terrain of the southwest corner (Figure 4-3).

The surface geology in the area of the Sebago Lake Pluton is shown in Figure 4-4 (MGS 2017). Outcrops of crystalline bedrock occur immediately to the east and southeast of the area (Figure 4-4). Glacial till is the oldest glacial deposit and covers 80-90% of the landscape. Glacial outwash deposits composed of sand and gravel form isolated, elongate deposits that fill valleys and paleo-valleys. Regionally, these deposits cover about 4 percent of the landscape. Fine-grained glaciomarine deposits are present on the eastern margin of the reference area. Other less significant surficial deposits within the reference area are ice contact deposits and stream alluvium. Based on GIS analysis of overburden thickness obtained from the Maine Water Well Database, the average thickness of overburden within the Sebago Lake reference area (all deposits above bedrock) is 9-10 meters, with a minimum of 0 and a maximum of 70 meters.

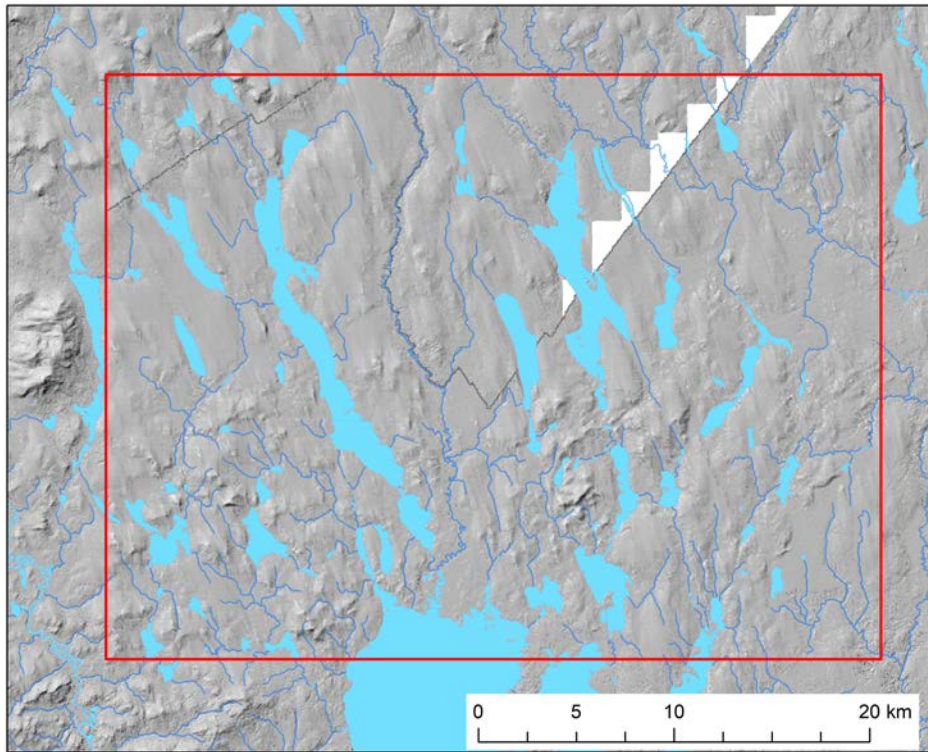


**Figure 4-3. Topography and surface features of the Sebago Lake Pluton reference area. Blue features are lakes and streams.**

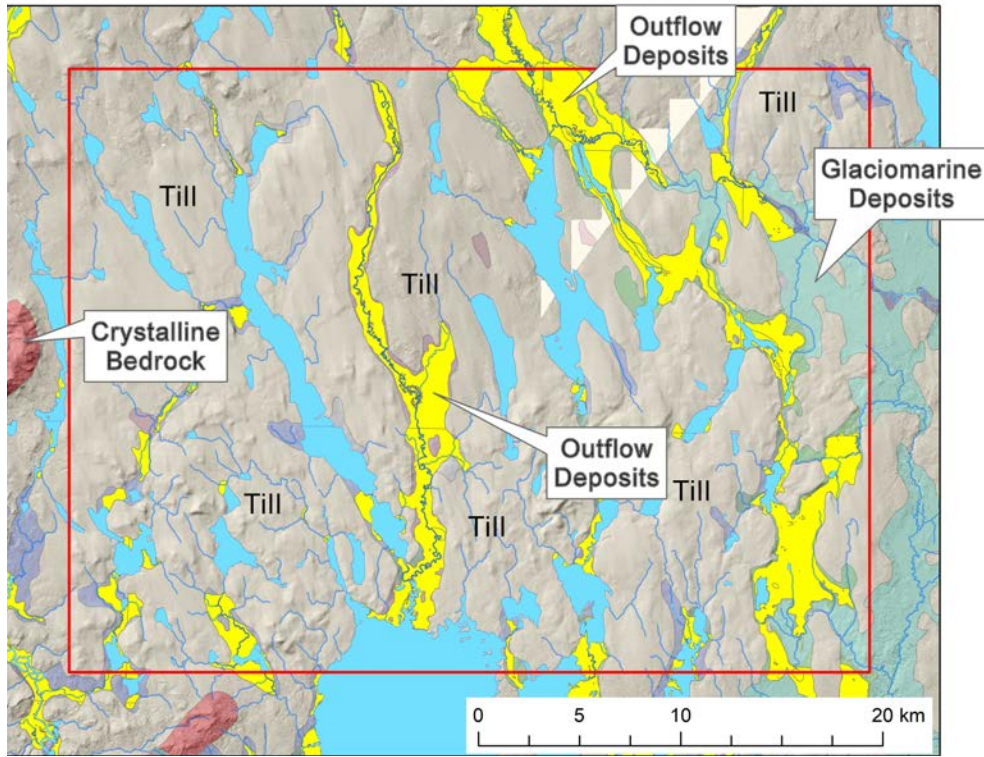
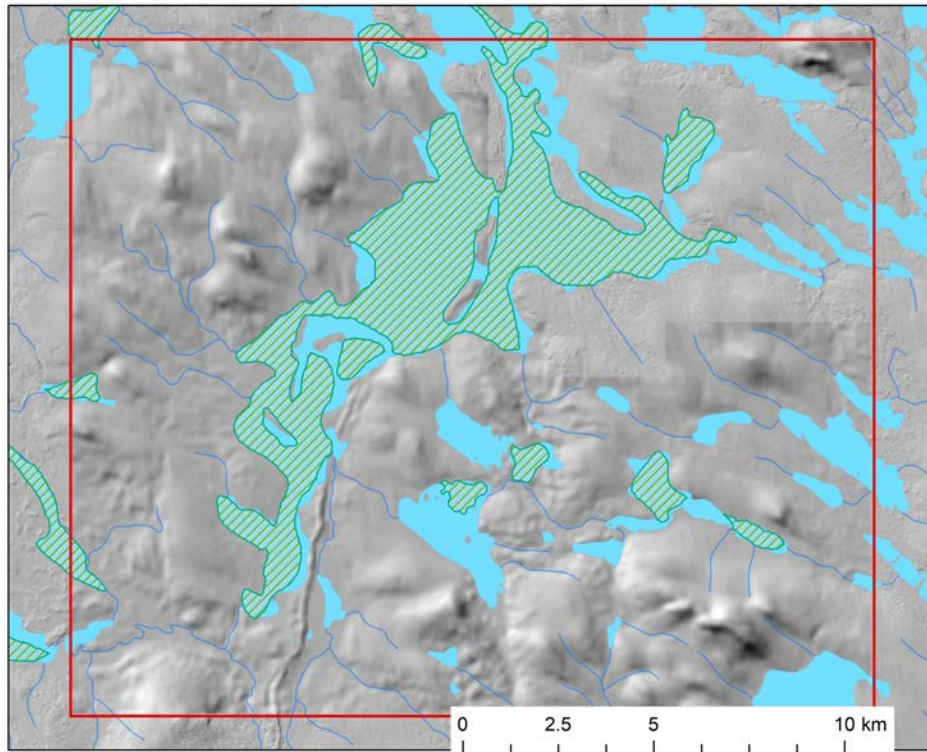


Figure 4-4. Surficial geology of the Sebago Lake Pluton reference area.

#### 4.5.1.2 Passadumkeag River Area

The landscape of the Passadumkeag River Pluton reference area is characterized by isolated hills and ridges with valleys, streams and lakes that are generally oriented towards the southeast (Figure 4-5). Elevations in the reference area range from approximately 370 to 60 meters, which is very similar to the relief of the Sebago Lake area. Elevations below 80 meters occur only in the southwestern corner of the area, Elevations above 260 meters occur along a ridge in the southeast corner of the area and at the highest point of a bedrock exposure at the southwest edge of the area, The southwestern area has the highest local relief with a difference of about 180 meters over a distance of about 2 kilometers. A prominent surface water feature of the Passadumkeag River area is a large wetland (the “1000-acre heath”) that occurs within the drainage area and floodplain of the Passadumkeag River (DOE 1986). The Passadumkeag River flows to the southwest while streams in the eastern half of the area flow to the southeast.

The surface geology of the Passadumkeag River Pluton reference area is shown in Figure 4-6 (MGS 2017). An outcrop of crystalline rock forms a ridge on the southwest margin of the reference area. Glacial till is the oldest surficial deposit and covers most of the landscape (Figure 4-6). Glacial outwash deposits composed of sand and gravel are not as prevalent as in the Sebago Lake area. They form isolated, elongate deposits that fill valleys and paleo-valleys. Fine-grained glaciomarine deposits occur in the southwestern corner of the reference area. The reference area is relatively unpopulated and only 9 water wells are recorded in the Maine well database. Based on these data, GIS analysis indicates the average thickness of total overburden is 13 meters with a minimum of 0 and a maximum of 29 meters.



**Figure 4-5. Topography and surface features of the Passadumkeag River Pluton reference area. Blue features are lakes and streams. Cross-hatched green areas are wetlands.**

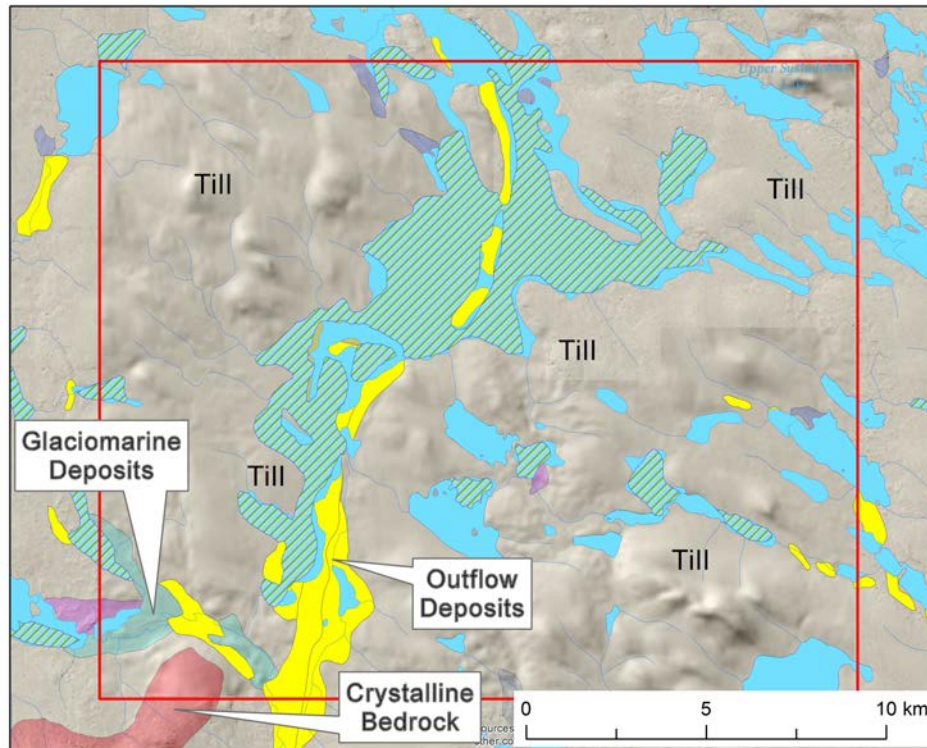


Figure 4-6. Surficial geology of the Passadumkeag River Pluton reference area

## 4.5.2 Characteristics of Crystalline Rocks

The crystalline rocks of interest in the region are granitic plutons that formed during and after the Acadian Orogeny. The mineralogy, petrology and composition of these rocks are typical of granitic rocks. In this section we are concerned primarily with the near-surface fracture systems of granitic plutons, which form the bedrock aquifer of the region. Bedrock wells have median yields of between 3 and 6 gallons per minute (gpm) (Tolman 2010). Approximately 35% of bedrock wells are reported to have yields >10 gpm (Tolman 2010). Maximum reported yields are typically 200-250 gpm.

### 4.5.2.1 Sebago Lake Pluton

The Early Permian Sebago Lake Pluton is a medium to coarse-grained two-mica granite composed primarily of plagioclase, alkali feldspar, quartz, biotite and muscovite with minor amounts of zircon, monazite, apatite and magnetite (DOE 1986). The granite intruded migmatitic country rock (high-grade metamorphic rock that has undergone partial melting) and has a crystallization age of 293 Ma (Tomascak et al. 1996; Solar and Tomascak 2016). Based on a more complete analysis of the relationship between the pluton and the migmatitic country rock, Solar and Tomascak (2016) estimate that the pluton has an area of approximately 400 km<sup>2</sup>, significantly less than previous estimates of >1600 km<sup>2</sup>.

Fisher (1962) reports on joint and fracture sets in the older Songo Pluton immediately adjacent and north of the Sebago Lake Pluton. The most dominant fracture set is nearly horizontal and interpreted as

resulting from regional unloading. Four vertical fractures sets are present with a northeast striking set interpreted as resulting from relaxing of northwest-southeast regional compression.

#### **4.5.2.2 Passadumkeag River Pluton**

The Late Devonian Passadumkeag River pluton is a granite intrusion with an area of approximately 700 km<sup>2</sup> (DOE 1986). It is part of the Bottle Lake complex that also includes the Whitney Cover pluton immediately to the east (DOE 1986; Ayuso et al. 1984). Both plutons intruded older metasedimentary rocks of Cambrian and younger age (Ayuso et al. 1984). The plutons have indistinguishable crystallization ages of approximately 380 Ma although the Passadumkeag River pluton is believed to be slightly younger based on field relationships (Ayuso et al. 1984). The Passadumkeag River pluton is a coarse-grained granite composed mainly of alkali and plagioclase feldspar and quartz, a few percent biotite and amphibole and several accessory minerals sphene, magnetite, zircon and apatite (Ayuso et al. 1984).

Data on direction and spacing of joint and fracture sets is available through photo-lineament studies and field measurements of brittle jointing (Hopeck 1990; Caswell, Eichler and Hill, Inc. 1990). Photo-lineament analysis and field measurements yield similar results with direction of vertical joint sets trending approximately N5W, N45E, N40W, N75W (Hopeck 1990). Joint orientation is near vertical and spacing was observed to vary from several centimeters to several meters, with one or two meters being typical (Hopeck 1990). Horizontal joints were not noted in these studies, either because they were not observed (as would be the case for photo-lineament analyses) or were not deemed significant in terms of understanding regional tectonics and relationship to contemporaneous faulting. It can be assumed, based on numerous other occurrences in New England, that horizontal joints are likely present the Passadumkeag River pluton.

#### **4.5.2.3 Shallow Horizontal Fractures**

Although there is no direct data on horizontal fractures for the reference areas, they are a common feature in the region (Figures 4-7 and 4-8). Fischer (1962) notes that they are the dominant fracture set at the Songo Pluton immediately north of the Sebago Lake Pluton. Horizontal fractures are also noted as significant transmissive features throughout southern Maine (e.g., Figure 4-7; Hansen et al. 1999).

Horizontal fractures are a primary feature of granites exposed in quarries within the region and are the reason that removal of granite by quarrying of joint-bounded rock sheets is feasible (Dale 1907, 1923; Figure 4-8). Based on numerous quarry exposures, Dale (1907, 1923) notes that horizontal joint spacing gradually increases with depth, from as little as 10-20 cm in the upper ~5 meters to typically 1-5 meters at greater depth. Horizontal joints and associated sheet structure have been observed in quarries at depths as great as 40 and 80 meters (Dale 1923). Joint spacings of 15-20 meters have been observed bounding the deepest sheets (Dale 1923). Horizontal joints generally bound lenticular sheets that gradually taper near their ends at joint intersections (Dale 1923; Figure 4-8). Individual fractures extend for lengths of at least several tens of meters (Figures 4-7 and 4-8). Horizontal fracture sets can form an interconnected system that may have significant lateral extent, although the overall dimensions are unknown within this region. Analogous horizontal fractures at Forsmark are interpreted to be hydraulically connected over distances of 2-3 km (Follin et al. 2008, Johansson 2008).



**Figure 4-7. Examples of horizontal fractures in crystalline rocks of southern Maine. Left: Groundwater flow (icicles) from a horizontal fracture exposed in a roadcut near Falmouth, Maine (MGS 2012). Right: horizontal fractures exposed in a quarry face in the Vinalhaven Pluton, Hurricane Island, Maine (Lemmond 2016).**

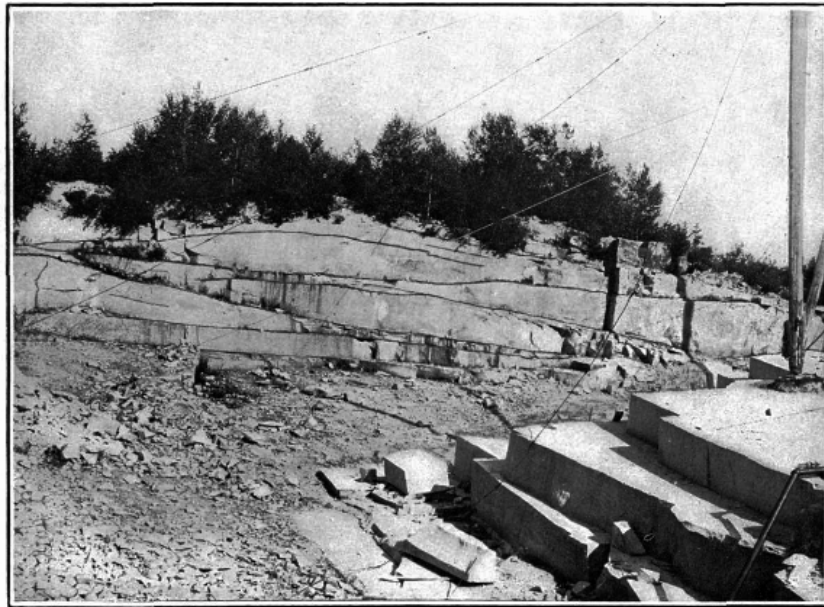


**Figure 4-8. Horizontal fractures and lenticular sheet structure in granite in quarry near Sullivan, Maine (Dale 1907). The sheets vary in thickness from 1-3 meters, except near tapered ends.**

### 4.5.3 Characteristics of Surficial Deposits

Three types of surficial deposits are represented in the conceptual model, based on the most widely distributed glacial deposits found in southern Maine. Glacial till covers most of the landscape and is composed of unsorted material deposited directly from glaciers. Glaciofluvial outwash deposits of sand and gravel are localized deposits that formed within meltwater channels and are the major surficial aquifers of the region. The Presumpscot Formation, composed of fine-grained marine silt and clay, was deposited during marine submergence of coastal lowlands following glacial retreat from the region.

#### 4.5.3.1 *Glacial Till*

Glacial Till is an unsorted and heterogeneous mixture of fine to coarse-grained material that is deposited directly from glacial ice (Figure 4-9). It consists of a matrix of sand, silt and clay that supports larger clasts derived from the local bedrock (Figure 4-9). The matrix of most till deposits in southern Maine have a sand content of greater than 50% (Thompson 2015).

Till deposits cover most of the regional land surface with thicknesses that range from a few meters or less to approximately 30 meters (Thompson 2015). Typical thickness is 2-3 meters. Till is largely absent on bedrock exposures or in modern stream channels where till has been eroded and replaced by modern alluvial deposits largely derived from eroded till.



Figure 4-9. Exposures of unsorted till deposits in southern Maine (Thompson 2015)

Based on data for horizontal hydraulic conductivity summarized in Nielsen and Locke (2012), till deposits in southern Maine are assigned a horizontal permeability of  $10^{-14}$  to  $10^{-13}$  m<sup>2</sup>. Based on a compilation of till hydraulic properties in southern New England, the porosity of till derived from crystalline rock sources ranges from 0.2 to 0.4 (Melvin et al. 1992). Till is a poor and rarely used aquifer, except in the case of limited-use hand dug wells that may yield 1-2 gpm of water. In areas where till is the only surficial deposit, wells are generally drilled through the till into the underlying shallow bedrock aquifer.

#### 4.5.3.2 *Glacial Sand and Gravel Deposits*

Melting of retreating glaciers created meltwater channels that carried large sediment loads which were deposited beyond the retreating glacial margins as glaciofluvial and glaciomarine deposits. Silt and clay particles in the meltwater were carried greater distances to lakes or the sea while coarser grained sand and gravel were deposited more proximally in inland stream channels (Thompson 2015). Sand and gravel

deposits have a typical thickness of 5-20 meters (Thompson 2015; Nielsen and Locke 2012). Examples of glaciofluvial sand and gravel deposits are shown in Figure 4-10.

Due to their high permeability, glaciofluvial sand and gravel deposits are the major aquifers in the region. Because their deposition was largely confined to channels in valleys and broad lowlands, their distribution in the region is highly localized (Figure 4-11). Based on GIS data, significant sand and gravel aquifers (well yields of >10 gpm) comprise about 4% of the surficial deposits in the region (Figure 4-11). This is potentially significant to both transport and biosphere models in that the most permeable deposits (and highest producing aquifers) occupy relatively small and discontinuous areas of the overall region. In addition, sand and gravel deposits above the marine limit are more likely to be open to recharge with recharge rates of approximately 25 inches/year (Nielsen and Locke 2015). Below the marine limit, sand and gravel deposits are more likely to be overlain by marine silt and clay deposits that act as a confining unit and limit recharge from above (Nielsen and Locke 2012).

Horizontal hydraulic conductivity values reported in Nielson and Locke (2012) for a representative sand and gravel aquifer indicate a permeability range of  $10^{-11}$  to  $10^{-10}$  m<sup>2</sup>. Porosity is estimated at 0.25 to 0.45 based on properties of unconsolidated sand and gravel deposits (Morris and Johnson 1967). Well yields from the sand and gravel aquifers typically range from 10 gpm to more than 1000 gpm (Williams et al. 1987).



**Figure 4-10. Exposures of glacial outwash sand and gravel deposits in southern Maine (Thompson 2015)**

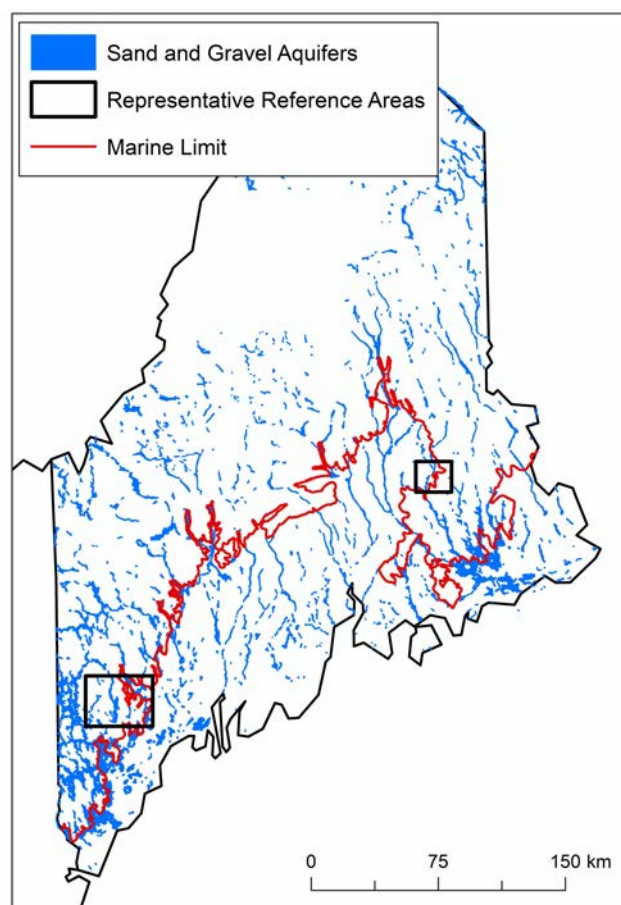


Figure 4-11. Distribution of sand and gravel aquifers in Maine.

#### 4.5.3.3 *Glacial Marine Silt and Clay Deposits*

The Presumpscot Formation is a distinctive marine sediment that covers much of the coastal lowlands of southern Maine (Thompson 1987). Its distribution defines the extent of marine submergence in southern Maine that followed glacial retreat and prior to rapid regional rebound (Figure 4-2 and 4-11). It is composed primarily of clay, silt and sand-sized particles carried to the sea by meltwater streams and deposited as a veneer over older glacial till and outwash deposits. The mineral grains are composed mainly of feldspar and quartz with minor clay and represent crystalline bedrock crushed by glacial action (“rock flour”, Thompson 1987). The thickness of the formation is variable but is typically in the range of 10-40 meters (Thompson 1987). An exposure of fine-grained deposits of the Presumpscot Formation is shown in Figure 4-12.

Measurements and calculations of the horizontal hydraulic conductivity of the Presumpscot Formation fall within a permeability range of  $10^{-17}$  to  $10^{-15}$  m<sup>2</sup> (Holland and Tolman 1987; Nielsen et al. 1995; Nielsen and Locke 2012). Vertical hydraulic conductivity is estimated to be one order of magnitude less than the horizontal permeability because sandy lenses in some parts of the deposit increase the average horizontal

permeability (Holland and Tolman 1987). Based on silt and clay content, researchers have assumed a porosity for the Presumpscot Formation of 0.4 (Nielsen et al. 1995; Brainard and Hebson 1999).

Due to its low permeability and widespread distribution, the Presumpscot Formation is the most significant confining unit of the glacial deposits in the region and plays an important role in regional groundwater studies (e.g., Nielsen et al. 1995; Nielsen and Locke 2012).



**Figure 4-12. Exposure of the Presumpscot Formation (Marine silt and clay) in southern Maine (Thompson 2015).**

## 4.6 Comparison between the Shallow Crystalline Environment in the U.S. and Forsmark, Sweden

Understanding the similarities and differences of shallow features at Forsmark and sites in similar geologic settings in the U.S. will help to build confidence in how to represent shallow features in the conceptual model for the crystalline reference case. Potential similarities and differences include the properties, relative abundances, thicknesses, and distribution of glacial deposits and the properties of shallow fracture systems in the crystalline bedrock.

### 4.6.1 Glacial Deposits

Determining the total thickness of glacial deposits overlying bedrock depends on borehole or geophysical data. The average overburden thickness at Forsmark (terrestrial and marine areas) is between 5 and 6 meters with a range of 0 to 42 meters (Hedenstrom and Sohlenius 2008). Based on well data from the two reference areas in Maine, average overburden thickness ranges from 9 and 13 meters with a total range of 0 to 70 meters. The total overburden thickness in the two reference areas is therefore approximately twice

the thickness of overburden at Forsmark. Several reports state that the thickness of glacial till throughout southern Maine is typically 2-3 meters.

Till distribution is similar in both regions in that it forms a near-continuous deposit overlying the crystalline bedrock (Figures 4-4 and 4-6; Hedenstrom and Sohlenius 2008). Low-permeability marine silt and clay deposits are common in the southern Maine region where they typically overlie till and glaciofluvial sand and gravel deposits. Where present, these deposits form a confining unit that impedes flow between the underlying deposits and the surface. At Forsmark, similar marine deposits are mostly present as offshore deposits in the present marine environment but are found locally in terrestrial areas.

Glaciofluvial sand and gravel deposits form localized and highly permeable deposits that would likely provide advective pathways for groundwater flow and transport. Glaciofluvial deposits cover ~4% of the land surface of Maine, based on GIS analysis of surficial mapping (Figure 4-11). As a somewhat equivalent comparison, glaciofluvial deposits occupy 6% of the areas covered by national surficial mapping in Sweden (Hedenstrom and Sohlenius 2008). Glaciofluvial deposits are rare in the “regional model area” of Forsmark, covering 1% of the landscape and forming a glacial esker in the southeast part of the area. The percent of area that a deposit covers within a specific area depends on the defined boundaries of the area and how common a deposit is within that area. The percent coverage is only a rough estimate in terms of defining a “generic” distribution of a deposit. GIS analysis of the Sebago Lake Pluton and Passadumkeag River Pluton reference areas indicate that glaciofluvial deposits cover 13% and 3% of the respective areas (Figures 4-4 and 4-6). These deposits are potentially significant to groundwater flow and transport in that, while they are localized on the landscape, they have significantly higher permeability than other glacial deposits and may therefore provide important flow pathways in the near-surface environment.

Estimates of horizontal permeability for the three major glacial deposits considered in the conceptual model are compared in Table 4-2 to best-estimate values for equivalent deposits at Forsmark (Johansson 2008).  $K_h/K_v$  is estimated at approximately 10 and 30 for equivalent deposits in Maine and Forsmark, respectively (Holland and Tolman 1987; Johansson 2008; Nielsen and Locke 2012). Overall, the agreement between permeability estimates of equivalent deposits in Maine and at Forsmark are remarkable, but perhaps not surprising given similar glacial processes in both regions.

**Table 4-2. Comparison of permeability estimates for glacial deposits. Values are for horizontal permeability.**

Glacial Deposit	Southern Maine (see Section 4.5.3 for references)	Forsmark (Johansson 2008)
Till	$10^{-14}$ to $10^{-13}$ m <sup>2</sup>	$1.0 \times 10^{-14}$ (fine-grained, depth > 0.6 m) $1.5 \times 10^{-13}$ (coarse-grained, depth > 0.6 m)
Glaciofluvial sand and gravel	$10^{-11}$ to $10^{-10}$ m <sup>2</sup>	$1.5 \times 10^{-11}$
Marine silt and clay	$10^{-17}$ to $10^{-15}$ m <sup>2</sup>	$1.5 \times 10^{-15}$ (lake or marine, depth > 0.6 m),

## 4.6.2 Shallow Horizontal Fractures

As discussed in Section 4.5.2.3, horizontal fractures in the New England region are observed in quarry exposures to have spacings of a meter or less to 10 meters or more, increasing with depth (Dale 1923). The deepest exposure of horizontal fractures is at a depth of 80 meters in a quarry and it can be assumed that they are present at greater depth. These fracture characteristics are similar to those in Forsmark, where horizontal fractures are interpreted to occur in the upper 100 - 150 meters of the bedrock (Follin 2008). Based on available data, the shallow horizontal fracture systems observed in the New England region and Forsmark are physically similar with no significant differences.

Estimates of the permeability of shallow horizontally fractured zones in the New England region are difficult to find. Lyford et al (1999) reports transmissivity values in fractured bedrock that suggest permeability range as high as approximately  $10^{-12}$  to  $10^{-11}$  m<sup>2</sup>. This compares to permeability values of shallow horizontal fractures at Forsmark of  $10^{-13}$  to  $10^{-10}$  m<sup>2</sup> (Johansson 2008). Given the physical similarities of shallow horizontal fracture systems in New England and Forsmark, it follows that permeability values would fall into similar ranges.

## 4.7 Conceptual Model of the Stratigraphy and Hydrology of the Shallow Geosphere

The spatial distribution, stratigraphy and hydraulic properties of unconsolidated glacial deposits control groundwater movement in the near-surface environment above crystalline bedrock. Understanding of these features is based on characteristics of glacial deposits documented in the region of the two reference areas. An example of the stratigraphic relationships of the primary glacial deposits is presented by Nielsen and Locke (2012) for an area to the southeast of the Sebago Lake Pluton where the three types of deposits occur together (Figure 4-13). The stratigraphic cross-section is normal to a north-south drainage system. It shows a thin, continuous layer of till above the bedrock and discontinuous glaciofluvial sand and gravel and glacial marine deposits of the Presumpscot Formation preserved mainly in drainage channels. Modern surficial units (alluvium) are present above the glacial deposits.

Based on the stratigraphic relationships observed in the region, a conceptual model of the stratigraphy can be constructed (Figure 4-14). The schematic stratigraphic cross-section includes the boundary of marine submergence to show differences in deposits from marine and terrestrial environments. The distribution and properties of glacial deposits are conceptualized as having a significant role in groundwater flow and transport at the interface between the crystalline basement and the biosphere. Till deposits with permeability of  $\sim 10^{-14}$  m<sup>2</sup> and a thickness of 2-3 meters can be assumed to be continuous over the entire landscape. Interspersed on the landscape at intervals on the order of 10 km are highly permeable ( $10^{-11}$  m<sup>2</sup>) glaciofluvial sand and gravel deposits that generally coincide with modern drainage channels (Figures 4-4 and 4-6). In some areas, sand and gravel was deposited on top of marine silt and clay (Figure 4-14; Thompson 1987). Sand and gravel deposits allow localized lateral groundwater flow in the surface environment, ultimately discharging into streams and lakes. Radionuclides are expected to be transported by advection and diluted as they move horizontally through the sand and gravel deposits. In areas below the marine limit, marine silt and clay deposits act as confining units that overlie either till or sand and gravel aquifers (Figure 4-13). A summary of the properties of the glacial deposits is presented in Table 4-3.

Crystalline bedrock depicted below the surficial deposits includes a shallow zone of horizontal, highly transmissive fractures that are discussed in Section 4.5.2.3. Based on analogous fractures at Forsmark (e.g., Follin et al. 2008), horizontal sheet fractures are expected to have a significant role in near-surface groundwater flow. Hydraulic properties of the shallow horizontal fracture system are only known through studies of analogous features at Forsmark (Follin et al. 2008; Johansson 2008). Permeability of the fractured zone is in the range of  $10^{-13}$  to  $10^{-10}$  m<sup>2</sup> (Johansson 2008). Shallow horizontal fractures extend to

a depth of ~100 - 150 meters at Forsmark and have been observed at a depth of 80 meters in quarry exposures in Maine.

Shallow horizontal fractures/sheet joints, believed to be analogous to those observed in Maine, have a significant role in conceptual models of shallow groundwater flow at Forsmark (Follin et al. 2008; Johansson 2008; Berglund et al. 2013). As understood from studies at Forsmark, transmissive horizontal fractures act as a groundwater drain that captures deep groundwater from below and recharge from above. As summarized in Johansson (2008) and Follin et al. (2008), horizontal fracture zones (corresponding to fracture domain FFM02 at Forsmark) are thought to be hydraulically connected over distances of 2-3 kilometers. When groundwater from depth intersects the shallow horizontal fractures, it can be impeded from discharging locally and is instead carried laterally to discharge at the edges of the horizontal fracture domain (Johansson 2008; Berglund et al. 2013). The findings at Forsmark suggest that the shallow horizontal fractures are not present uniformly beneath the landscape but are instead grouped into domains with an extent of a few kilometers (Follin et al. 2008). It is possible, but speculative, that this is the case in New England where quarries may have been preferentially located in areas of prominent horizontal jointing known from surface exposures.

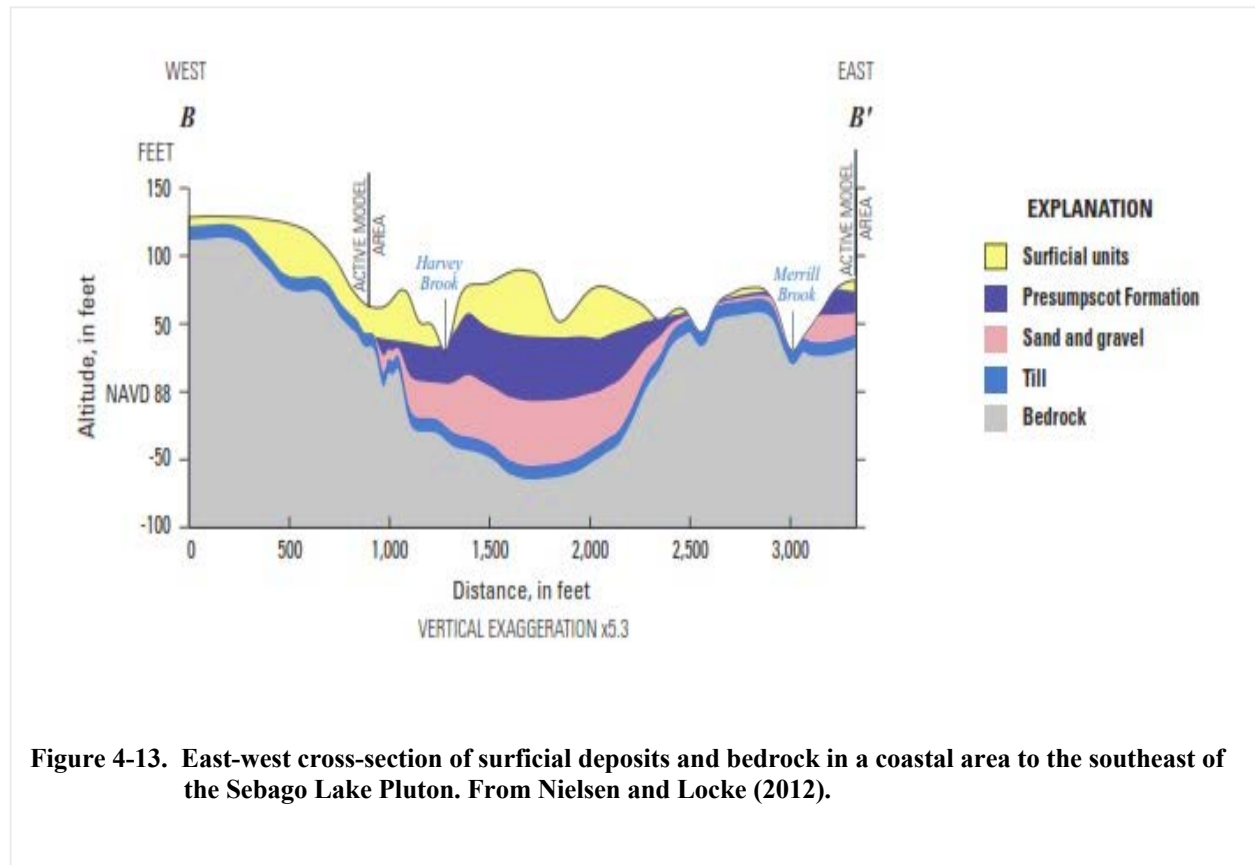


**Figure 4-13. East-west cross-section of surficial deposits and bedrock in a coastal area to the southeast of the Sebago Lake Pluton. From Nielsen and Locke (2012).**

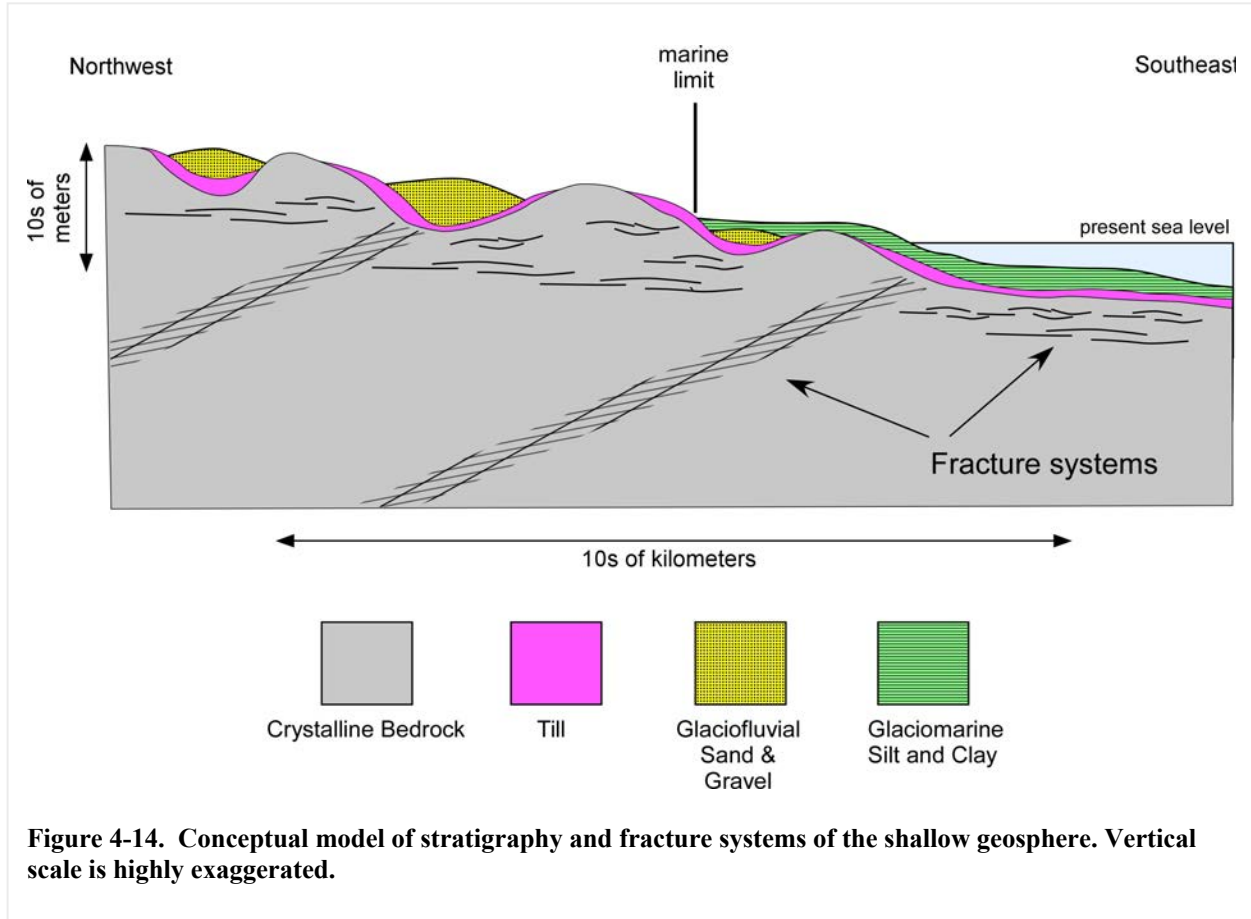


Table 4-3. Representative values of properties included in the conceptual model

Property	Till	Glaciofluvial sand and gravel	Marine silt and clay
Typical thickness (m)	2-3	5-25	10-40
Permeability (m <sup>2</sup> )	10 <sup>-14</sup> - 10 <sup>-13</sup> m <sup>2</sup>	10 <sup>-11</sup> - 10 <sup>-10</sup> m <sup>2</sup>	10 <sup>-17</sup> - 10 <sup>-15</sup> m <sup>2</sup>
Porosity	0.2 – 0.4	0.25 – 0.45	0.4
Typical well yield (gpm)	1-2	10-1000	NA

## 4.8 Conclusions

The New England region has overall similarities to the geologic and hydrologic setting of the Forsmark region of Sweden. Recognition of the similarities highlights the geologic and hydrologic features and properties to include in models of the shallow geosphere for the crystalline reference case. An important recognition is that the most permeable glacial deposits, which form sand and gravel aquifers, are highly

localized and generally are present in 10% or less of a particular area. The distribution of sand and gravel deposits between the two regions are similar on a regional scale but can differ in specific areas due to localized differences in their distribution across the landscape. Sand and gravel deposits are conceptualized as an important near-surface groundwater pathway that will influence radionuclide concentrations in the biosphere, as surface water and groundwater mix in lakes and streams. Conceptualizing the balance between groundwater and surface water inputs to biosphere objects (e.g., lakes and streams), which is influenced by the differing hydraulic properties of surface deposits, is a possible subject for future work.

The physical features of the shallow horizontal fracture system in crystalline bedrock are similar in both regions suggesting an overall similarity in hydraulic properties. The extents of horizontal fracture domains are estimated based on one example at Forsmark. This example indicates that the domains are localized on a scale of kilometers and are not present beneath an entire region (Follin et al. 2008). Upward groundwater flow can be captured in the high-transmissivity horizontal fracture systems where it is transported horizontally and discharged at the domain edges (Berglund et al. 2013).

## 4.9 References

- Ayuso, R.A., Arth, J.G., Sinha, A.K., Carlson, J. and Wones, JR. 1984. *Comparative geochronology in the reversely zoned plutons of the Bottle Lake Complex, Maine: U-Pb on zircons and Rb-Sr on whole rocks*. *Contr. Mineral. and Petrol.* 88:113–125.
- Berglund, S., Bosson, E., Selroos, JO, and Sassner, M. 2013. *Identification and Characterization of Potential Discharge Areas for Radionuclide Transport by Groundwater from a Nuclear Waste Repository in Sweden*. *AMBIO.* 42:435–446.
- Borns, Harold W. Jr.; Doner, Lisa A.; Dorion, Christosher C.; Jacobson, George L. Jr.; Kaplan, Michael R.; Kreutz, Karl J.; Lowell, Thomas V.; Thompson, Woodrow B.; and Weddle, Thomas K. 2004. *The Deglaciation of Maine, USA*. Earth Science Faculty Scholarship. 276.
- Brainerd, E.C., and Hebson, C.S. 1996. *Hydrogeology of Presumpscot clay-silt using isotopes*, in Loiselle, M., Weddle, T.K., and C. White, eds., *Selected papers on the hydrogeology of Maine: Augusta, Maine*, Geological Society of Maine, Bulletin 4:81–94.
- Caswell, WB. 1987. *Ground water handbook for the State of Maine*. Maine Geological Survey. Bulletin 39. 2nd ed. 135 p.
- Caswell, Eichler and Hill, Inc. 1990. *Photo-lineament Mapping at 1:40,000 Scale in the Sebago Batholith and Bottle Lake Complex of Maine*. Maine Geological Survey. OPEN-FILE NO. 90-25a. 11 p.
- Dale, TN. 1907. *The granites of Maine*. U. S. Geological Survey. Bulletin 313. 202 p.
- Dale TN. 1923. *The commercial granites of New England*. U.S. Geological Survey. Bulletin 738. 488 p.
- DOE. 1986. *Draft Area Recommendation Report for the Crystalline Repository Project*. U.S. Department of Energy, Office of Civilian Radioactive Waste Management. Crystalline Repository Project Office. DOE/CH-15(0).
- Fisher. I. S. 1962. *Petrology and structure of the Bethel Area*. *Maine. Geol. Soc. Amer. Bull.* 73:1385-1420.

- Follin S. 2008. *Bedrock hydrogeology Forsmark. Site descriptive modelling, SDM-Site Forsmark*. SKB R-08-95. Svensk Kärnbränslehantering AB.
- Follin S, Hartley L, Jackson P, Roberts D, Marsic N. 2008. *Conceptual model development and numerical modelling using CONNECTFLOW, Forsmark modelling stage 2.3*. SKB R-08-23. Svensk Kärnbränslehantering AB.
- Hansen, BP., Stone, JR., and Lane, JW. 1999. *Characteristics of fractures in crystalline bedrock determined by surface and borehole geophysical surveys, eastern surplus superfund site, Meddybemps, Maine*. Water-Resources Investigations Report. 99-4050. 27 p.
- Harrison, W., Edgar, D., Van Luik, A., Hinze, W., Braile, L., Kalliokoski, J., Pfannkuch, H., Wright, H., Tissue M. and Sood, M. 1983. *Geology, Hydrology, and Mineral Resources of Crystalline Rock Areas of the Lake Superior Region, United States*. Argonne National Laboratory Report. ANL/ES-134. 427 p.
- Hedenström A, and Sohlenius G. 2008. *Description of the regolith at Forsmark. Site descriptive modelling, SDM-Site Forsmark*. SKB R-08-04. Svensk Kärnbränslehantering AB.
- Hogan JP and Sinha AK. 1989. *Compositional Variation of Plutonism in the Coastal Maine Magmatic Province: Mode of Origin and Tectonic Setting*. Maine Geological Survey. Studies in Maine Geology. 4:1-33.
- Holland, WR and Tolman, AL. 1987. *Techniques of Ground Water Investigation and Modeling in Marine Clay: A Case Study*. Geologic and Geotechnical Characteristics of the Presumpscot Formation Maine's Glaciomarine "Clay" Symposium. Andrews, D.W., Thompson, W.D., Sandford, T.C., and Novak, I.D. Eds. Augusta, ME. 20 March 1987. 18 p.
- Hopeck, John T. 1990. *Tectonic fabrics of the Passadumkeag River pluton, Bottle Lake complex, Springfield and Scraggly Lake 15-minute quadrangles*, Maine Geological Survey, Open-File Report 90-25b. 7 p.
- Johansson P-O. 2008. *Description of surface hydrology and near-surface hydrogeology at Forsmark. Site descriptive modelling, SDM-Site Forsmark*. SKB R-08-08. Svensk Kärnbränslehantering AB.
- Lemmond, B. 2016. *Pieces, patterns, & processes: an ecological assessment of Hurricane Island, Maine. Field Naturalist Program*. The University of Vermont. 74 p.  
<https://www.hurricaneisland.net/current-research-and-data-projects>.
- Lindborg, T., ed. 2010. *Landscape Forsmark—Data, methodology and results for SR-Site*. Svensk Kärnbränslehantering AB. SKB TR-10-05. Stockholm, Sweden. Report. 252 pp.
- Lyford, FP., Garabedian, SP and Hansen, BP. 1999. *Estimated hydraulic properties for the surficial-and bedrock-aquifer system, Meddybemps, Maine*. Open-File Report 99-199. 27 p.
- Mariner, P. E., Stein, E. R., Frederick, J. M., Sevougian, S. D., Hammond, G. E., and Fascitelli, D. G. 2016. *Advances in Geologic Disposal System Modeling and Application to Crystalline Rock*. FCRD-UFD-2016-000440. SAND2016-96107R. Sandia National Laboratories. Albuquerque, NM.

- Melvin, R. L., de Lima, V., and Stone, B. D. 1992. *The Stratigraphy and Hydraulic Properties of Tills in Southern New England*. U.S. Geological Survey. Open-File Report. 91-481. 57p.
- MGS (Maine Geological Survey) Open Data. 2017. *Maine Surficial Geology 500K Units*, Available at <https://mgs-maine.opendata.arcgis.com/datasets/maine::maine-surficial-geology-500k-units/about>.
- MGS (Maine Geological Survey). 2012. *Water Resources in Maine* (website). <https://www.maine.gov/dacf/mgs/explore/water/facts/water.htm>.
- Morris, D.A. and Johnson, A.I. 1967. *Summary of Hydrologic and Physical Properties of Rock and Soil Materials, as Analyzed by the Hydrologic Laboratory of the U.S. Geological Survey, 1948-1960*. USGS Water Supply Paper: 1839-D.
- Nielsen, M.G., and Locke, D.B. 2012. *Simulation of groundwater conditions and streamflow depletion to evaluate water availability in a Freeport, Maine, watershed: U.S. Geological Survey Scientific Investigations Report 2011– 5227*. 72 p. at <http://pubs.usgs.gov/sir/2011/5227/>.
- Nielsen, M.G., and Locke, D.B. 2015. *Simulation of groundwater flow and streamflow depletion in the Branch Brook, Merriland River, and parts of the Mousam River watersheds in southern Maine: U.S. Geological Survey Scientific Investigations Report 2014–5235*. 78 p. <http://dx.doi.org/10.3133/sir20145235>.
- Nielsen, M.G., Stone, J.R., Hansen, B.P., and Nielsen, J.P. 1995. *Geohydrology, water quality, and conceptual model of the hydrologic system, Saco Landfill, area, Saco, Maine: U.S. Geological Survey Water-Resources Investigations Report 95–4027*. 94 p.
- OCRD (Office of Crystalline Repository Development). 1983. *A National Survey of Crystalline Rocks and Recommendations of Regions to Be Explored for High-Level Radioactive Waste Repository Sites OCRD-1*. Battelle Memorial Institute. Columbus, OH. 128 p.
- Sohlenius G, Strömngren M, and Hartz F. 2013. *Depth and stratigraphy of regolith at Forsmark. SR-PSU Biosphere*. SKB R-13-22. Svensk Kärnbränslehantering AB.Lindborg.
- Solar, Gary S., and Tomascak, Paul B. 2016. *The Migmatite-Granite Complex of southern Maine: Its structure, petrology, geochemistry, geochronology, and relation to the Sebago Pluton*: in Berry, Henry N., IV, and West, David P., Jr., editors. *Guidebook for field trips along the Maine coast from Maquoit Bay to Muscongus Bay*: New England Intercollegiate Geological Conference. p. 19-42.
- Strömngren, M. and Brydsten, L. 2013. *Digital elevation model of Forsmark*.
- Stuiver, M., and Borns, H. W., Jr. 1975. *Late Quaternary marine invasion in Maine: its chronology and associated crustal movement*: Geological Society of America. Bulletin. 86:99-104.
- Thompson, W. B., and Borns, H. W., Jr. 1985. *Surficial geologic map of Maine: Augusta*. Maine Geological Survey. 1:500,000 map. [http://digitalmaine.com/mgs\\_maps/15](http://digitalmaine.com/mgs_maps/15).
- Thompson, W.B. 1987. *The Presumpscot Formation in Southwestern Maine*. In *Geologic and Geotechnical Characteristics of the Presumpscot Formation Maine’s Glaciomarine “Clay”*

- Symposium, Andrews, D.W., Thompson, W.D., Sandford, T.C., and Novak, I.D., Eds. Augusta, ME. 20 March 1987. 22 p.
- Thompson, WB. 2015. *Surficial geology handbook for southern Maine*: Maine Geological Survey. Bulletin 44. 97 p. Maine Geological Survey Publications 2. [http://digitalmaine.com/mgs\\_publications/2](http://digitalmaine.com/mgs_publications/2).
- Tolman, S.S. 2010. *Bedrock well yields in the Lewiston 30x60 minute quadrangle*. Maine Geological Survey. Open-File Map. 10-51.
- Tomascak, PB, Krogstad, EJ, and Walker, RJ. 1996. *U-Pb monazite geochronology of granitic rocks from Maine: implications for late Paleozoic tectonics in the northern Appalachians*. Journal of Geology. 104:185-195.
- Williams, JS., Tepper, DH., Tolman, AL., and Thompson, WB. 1987. *Hydrogeology and water quality of significant sand and gravel aquifers in parts of Androscoggin, Cumberland, Oxford, and York Counties, Maine*. Maine Geological Survey. Open-File Report 87-1a. 121 p.

## 5. UNSATURATED ALLUVIUM

This section presents an update of the unsaturated zone (UZ) alluvium reference case first introduced in Mariner et al. (2018), continued in Sevougian et al. (2019a), and in Sevougian et al. (2019b). The present study is focused on setting up more realistic simulations with the use of newly developed PFLOTRAN solvers and options. This includes setting bottom conditions open to fluid and with heat flux representative of the geothermal gradient, setting characteristic curves to be different for upper basin fill (UBF) as well as upper basin fill confining (ubf\_conf) materials, setting infiltration to the top of the model to 10 mm/yr., modifying thermal conductivity for the drift, setting the repository to be in a low permeability region, and generating a new mesh that corrected a zig-zag boundary issue along the disturbed rock zone (DRZ).

This reference case considers thick alluvial valleys of the Great Basin in the western United States and the low-permeability playa/lacustrine sediments found there. Several features of this type of host rock are favorable to waste isolation, including low groundwater fluxes, low permeability, and low water saturation. This type of environment is favorable to the disposal of dual-purpose canisters (DPCs) since low water saturation greatly reduces the possibility of criticality events. Mariner et al. (2018) goes into detail of the natural barrier system, movement of water through sediments, and the physical and chemical characteristics of the host rock.

These next sections touch on the model setting, description of the model domain, repository layout, simulation set up, results of completed runs, and future work considerations.

### 5.1 Model Setting

Two schematics, shown in Figures 5-1 and 5-2, take their inspiration from the thick alluvial valleys of the Great Basin in the western United States. Figure 5-1 is a schematic of the hydrology and geology of a UZ repository (Mariner et al., 2018). Figure 5-2 shows the cross section of a UZ model where the repository is represented by the red block at a depth of 250 m and lies within the UZ that is between a depth of 0 m to 450 m. Within the UZ, there are impermeable fine-grained playa sediments, fluvial deposits, and the UBF consisting of unconsolidated gravel, sand, silt, and clay. The saturated zone (SZ) is located below the UZ at a depth of 450 m to 1,000 m. The SZ consists of an alluvial aquifer at a depth of 450 m to 500 m, which is a higher-permeability sand/gravel aquifer that lies at the base of the UBF and above the lower basin fill (LBF) at a depth between 500 m to 1,000 m which is made up of consolidated gravel, sand, silt, and clay.

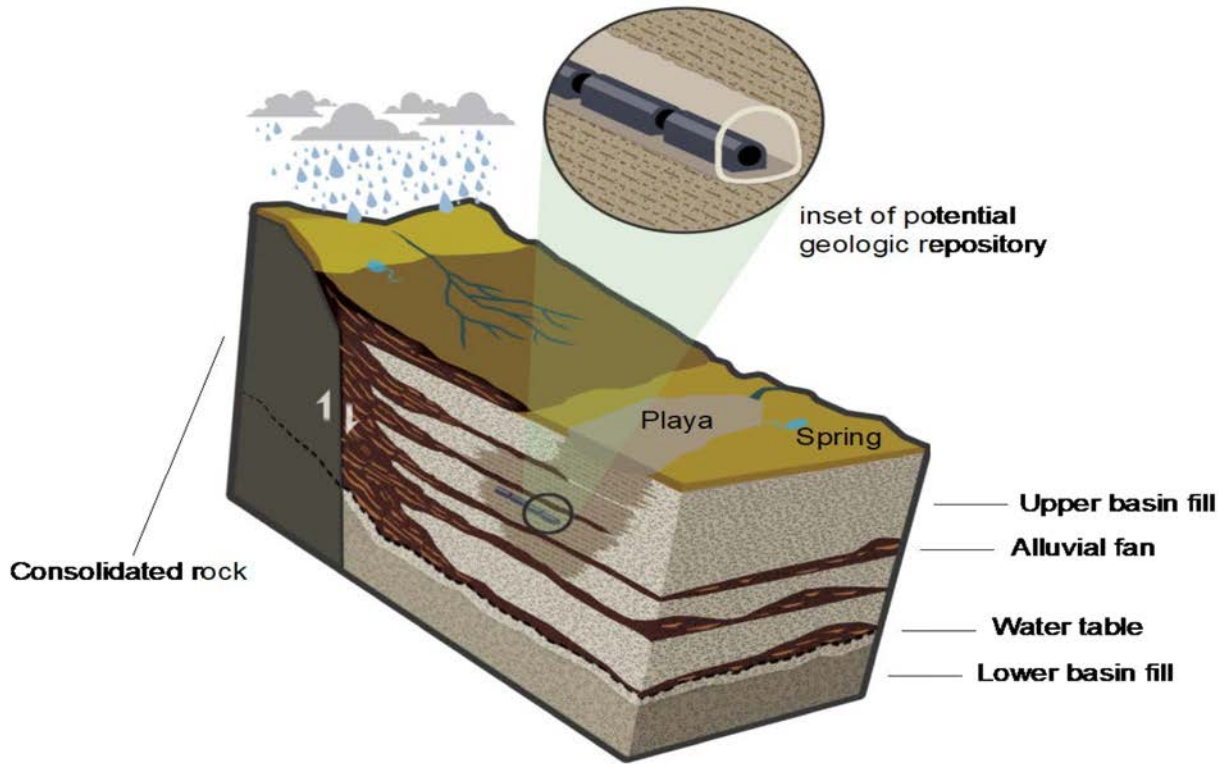


Figure 5-1 A schematic showing a potential unsaturated zone geologic repository. Figure 5-2 of Mariner et al. (2018). A possible location for a repository would be in the playa deposits, which are impermeable fine-grained sediments and are located towards the center of this schematic. Also notice the lithologic heterogeneity depicted here that is expected in basin-fill valleys where alluvial fans, fluvial systems, spring discharge areas, and playas are common features.

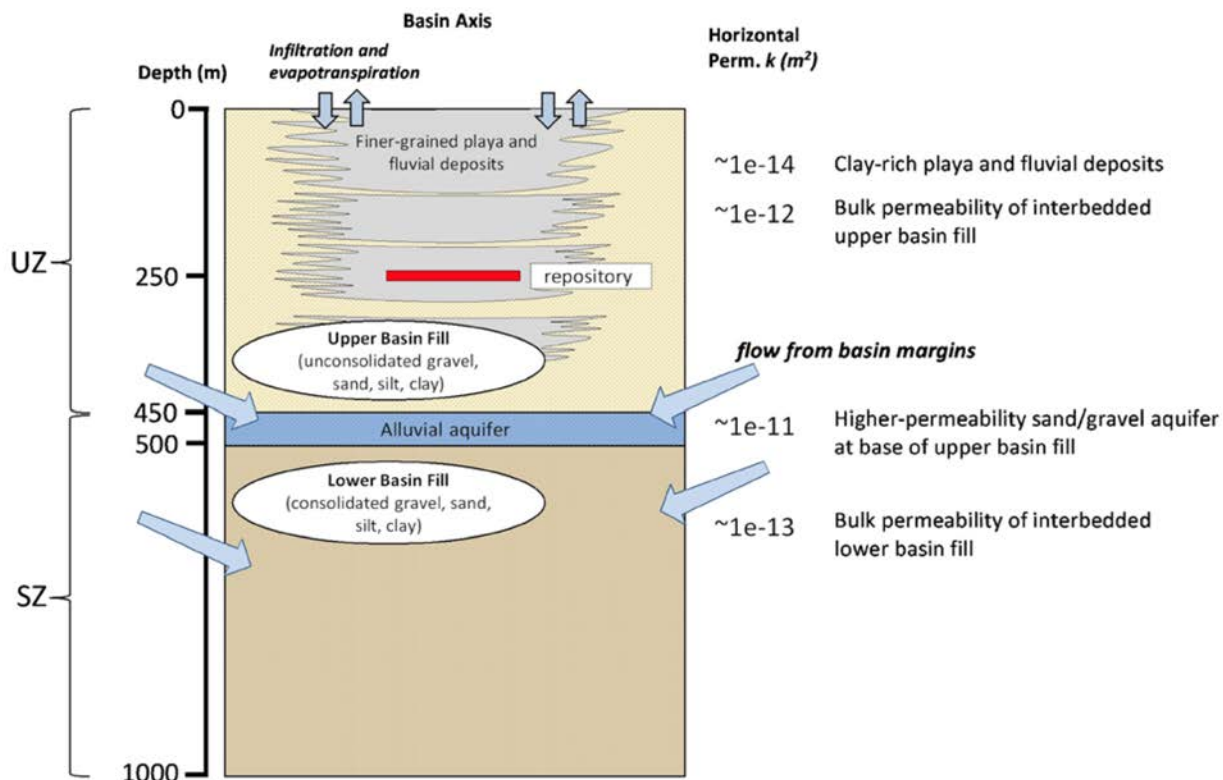


Figure 5-2 Schematic cross section of the unsaturated zone model (Mariner et al., 2018). UZ = unsaturated zone; SZ = saturated zone

## 5.2 Simulation

The mesh for the model domain originally proposed by Mariner et al. (2018) for field-scale simulations of the UZ reference case has since been slightly modified due to a “zig-zag” issue in the DRZ edge that has been addressed for the deterministic simulations presented in this section and later discussed in section 5.3. The configuration for the model domain used this year is shown in Figure 5-3, is colored by material ID and has the same domain size of 3915 m x 1065 m x 1005 m as in Mariner et al., (2018). The repository lies within ubf\_conf which is material ID 3, colored in turquoise.

Figure 5-4 shows an XY slice through the repository that is colored by material ID. Within this model the repository is assumed to be 250 meters below the surface. The zoom box on the top left of the figure shows four WPs in red, buffer in yellow, DRZ in burgundy, and ubf\_conf in turquoise.

Many preliminary simulations with varying levels of complexity were run using PFLOTRAN. The two final simulations were run using 24-PWR, 100 y OoR, 40 GW-d/MTU burn-up WPs in a field-scale half-symmetry model with 27 drifts and 25 WPs per drift (675 24-PWR waste packages for half-symmetry). Drift spacing is 50 m, and center-to-center spacing of packages along the drift is 20m. The model has no-flow boundary condition at the south face, which acts as a reflector, meaning the total number of WPs represented in the model is 1350. The field-scale PA unstructured mesh used for the final simulations was gridded with Cubit (Blacker et al. 2016) and has 2,996,313 grid cells, nearly 600,000 more than the mesh in previous studies. Simulations of two-phase flow and temperature were run with PFLOTRAN (Hammond et al. 2014). Model domain visualizations have been generated using ParaView (Ayachit 2015).

Previously, simulation attempts failed at around 180 years. Using newly developed PFLOTRAN solvers and smoothed characteristic curve options, these same simulations were run up to 1 million years without failure in GENERAL mode. The updated simulations presented later in this section were set up to end at 100,000 years since there is no transport and pressure, saturation and temperature have returned to initial values by this time. The simulation runs consist of two PFLOTRAN simulations that differ only in the water infiltration rate that is set for them. The first has a water infiltration rate set to what was previously used in Sevougian et al. (2019a) which is 1 mm/yr and the second is set to a water infiltration rate of 10 mm/yr, a value more consistent with what is expected in the Great Basin (Mariner et al. 2018). These simulations were run to 100k years using 540 cores of a parallel HPC cluster on the new UZ mesh. The first run completed in 5.94 hours and the second in 5.29 hours. A comparison between the runs is presented later in the section with more emphasis on the more realistic second run.

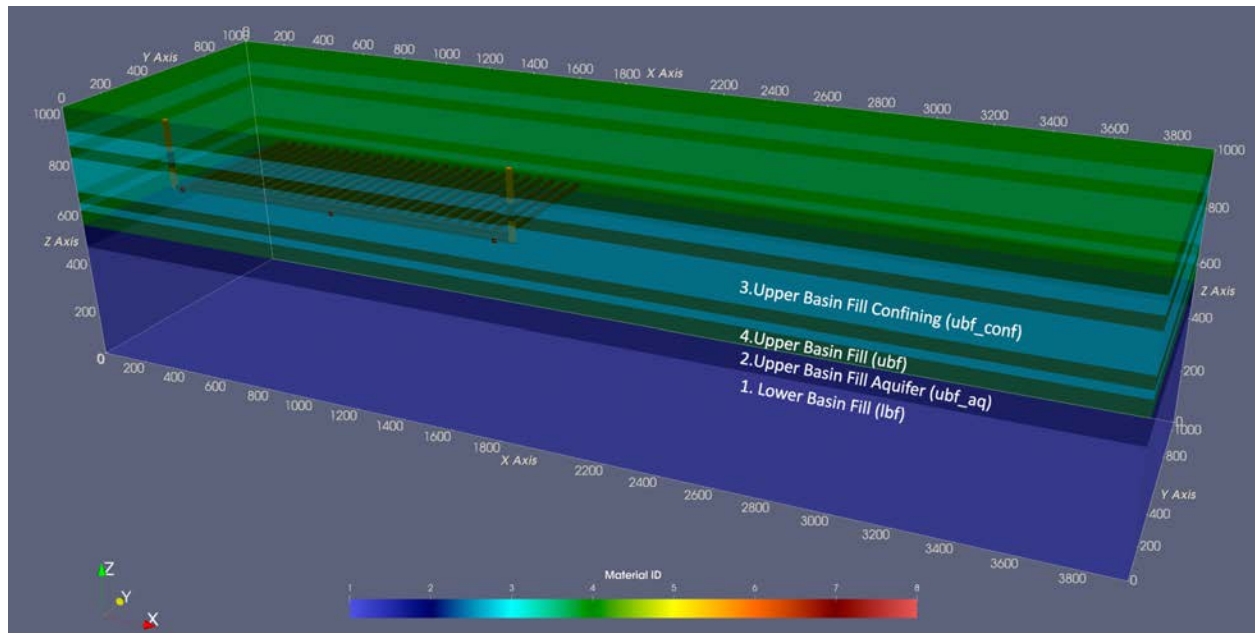


**Figure 5-3** Configuration of the repository and natural barrier system that was generated using Cubit, simulated in PFLOTRAN and visualized on ParaView. Turquoise color (material ID 3) represents the upper basin fill confining (ubf\_conf) units (the centermost contains the repository as seen there), green (material ID 4) represents UBF, dark blue (material ID 2) represents the UBF aquifer, and blue (material ID 1) represents LBF. Distances along the axes are in meters, where 1000 m is land surface and 0 m is the bottom of the model domain. The left side of the figure represents a western direction.

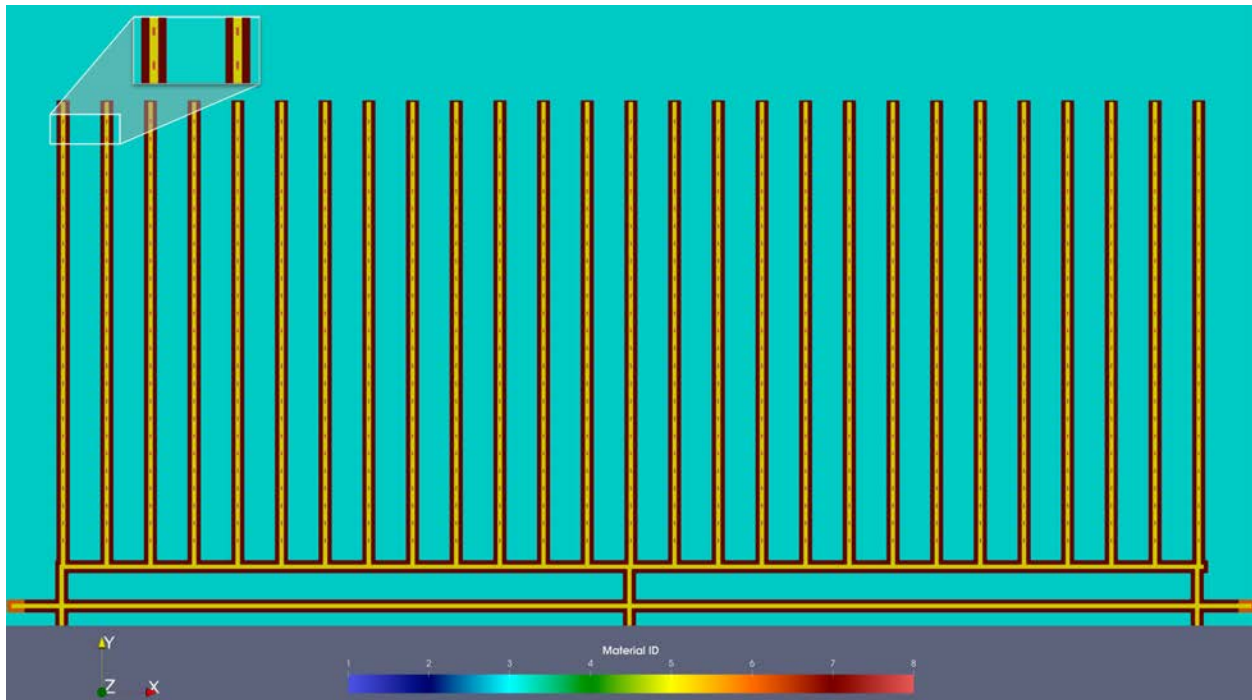


Figure 5-4 XY slice through the repository colored by material ID. The repository is assumed to be 250 meters below the surface. The zoom in box on the top left shows a close-up of four waste packages (WPs), colored in red, buffer in yellow, DRZ in burgundy, and ubf\_conf in turquoise. Visualized using ParaView.

### 5.2.1 New PFLOTTRAN Solver and Options

Newly developed PFLOTTRAN solvers and options allowed for completion of the UZ simulations that had previously failed. Figure 5-5 shows text taken from the working PFLOTTRAN input deck used to run the simulations. The bold text represents the required keywords needed for use with the newly developed Newton Trust-Region Dogleg Cauchy (NTRDC) nonlinear solver. Here NTRDC adds steepest-descent solution update to the Newton solution if it optimizes better than Newton solution alone within the trust region (Nole et al. 2021).

The box on the top includes the `NEWTONTRD_HOLD_INNER_ITERATIONS` keyword that is recommended if the simulation is expected to go through many state changes throughout the simulation. Using this keyword, the inner iteration will evaluate the residuals once and if there is a phase state change of any cell, it will not allow further phase state changes in the inner iterations until the solution is optimized. If converged, it will force extra Newton steps to make sure the phase state change does not occur further. If not converged, it continues to the next outer iteration.

The box on the bottom left within the same figure includes a `RESCUE_MODE` keyword that is activated when GENERAL mode simulations get stuck in hundreds of small time-steps, because it cannot cross over the barrier of phase state changes. `RESCUE_MODE` will recognize this and perturb the time step by a large factor called `RESCUE_FACTOR` (default is 1,000 times larger than  $\Delta t$ ) to advance the simulation. `RESCUE_FACTOR` is the number multiplied by  $\Delta t$  in the next time step to perturb the simulation. `RESCUE_STEP_THRESHOLD` is set to a small number ( $1.0d-5$ ) and controls how small of a time step it

uses to trigger the RESCUE\_MODE. It counts the number when RESCUE\_STEP\_THRESHOLD is greater than  $\Delta t/t$ . The successive number of time steps with size smaller than RESCUE\_STEP\_THRESHOLD are added up. RESCUE\_MODE is triggered when this number is larger than RESCUE\_FREQUENCY. RESCUE\_FREQUENCY, set to a value of 50, controls how often it triggers the RESCUE\_MODE by having PFLOTTRAN inject artificial large time steps.

In the NEWTON\_SOLVER block in the NUMERICAL\_METHODS FLOW box, MAXIMUM\_NUMBER\_OF\_ITERATIONS is the maximum number of Newton iterations before reporting failed convergence and is recommended to be set between 15 and 20 (default 8) because NTRDC is a much more robust solver than Newton. Directly below, the NEWTONTRD keyword allows for options such as USE\_CAUCHY TRUE and AUTO\_SCALE FALSE. USE\_CAUCHY TRUE enables the Cauchy solution update evaluation, NTRDC. AUTO\_SCALE FALSE disables solution update scaling meaning that the solution update evaluation will focus more on pressure than other unknowns. With these options NTRDC performs better and with fewer spurious phase state changes.

The box on the bottom right of Figure 5-5 shows two bold keywords that are applied to the characteristic curves block of the input deck. Shown here is only one of the two characteristic curves included in the simulation, in which these same keywords are applied. The first bold keyword is LOOP\_INVARIANT which is a necessary optimization technique to pre-calculate the piecewise junction point (Nole et al. 2021). That means, if the characteristic curve is “loop-invariant”, (i.e., not changing alpha, m, etc. within a loop) then the piecewise junction point is fixed, and it only needs to be found once per simulation, which speeds up the simulations.

The second bold keyword is UNSATURATED\_EXTENSION which aims at preserving continuity of the van Genuchten model and its derivative at the residual saturation while also modeling the matrix potential of thin films below the residual (Nole et al. 2021). The LCPC keyword that is used in combination with UNSATURATED\_EXTENSION is one of the few listed options in PFLOTTRAN. LCPC allows the user to specify the tangent line at a chosen junction point to ensure the “capillary pressure” extension is piecewise smooth and continuous with the van Genuchten curve. The “L” in LCPC stands for linear, while “CPC” stands for capped capillary pressure.

```

#===== flow mode =====
SIMULATION
SIMULATION_TYPE SUBSURFACE
PROCESS_MODELS
  SUBSURFACE_FLOW flow
  MODE GENERAL
  OPTIONS
    WINDOW_EPSILON 1.d-3
    CHECK_MAX_DPL_LIQ_STATE_ONLY
    NEWTONTRD_HOLD_INNER_ITERATIONS
  /
/

#===== numerical methods=====
NUMERICAL_METHODS FLOW

TIMESTEPPER
  TS_ACCELERATION 10
  NUM_STEPS_AFTER_TS_CUT 2
  RESCUE_MODE
    RESCUE_FACTOR 1000.
    RESCUE_FREQUENCY 50
    RESCUE_STEP_THRESHOLD 1.0d-5
  END
/

NEWTON_SOLVER
  VERBOSE_LOGGING
  USE_INFINITY_NORM_CONVERGENCE
  RESIDUAL_INF_TOL 1.d-4
  MAXIMUM_NUMBER_OF_ITERATIONS 15
  NEWTONTRD
    USE_CAUCHY TRUE
    AUTO_SCALE FALSE
  END
/

LINEAR_SOLVER
  SOLVER ITERATIVE
  MAXIMUM_NUMBER_OF_ITERATIONS 2000
/

END

#===== Characteristic Curves =====
#===== saturation functions =====
CHARACTERISTIC_CURVES cc1
  SATURATION_FUNCTION VAN_GENUCHTEN
  LOOP_INVARIANT
  UNSATURATED_EXTENSION LCPC
  LIQUID_RESIDUAL_SATURATION 0.1d0
  M 0.5
  ALPHA 1.d-3
/
  PERMEABILITY_FUNCTION MUALEM_VG_LIQ
  M 0.5
  LIQUID_RESIDUAL_SATURATION 0.1d0
/
  PERMEABILITY_FUNCTION MUALEM_VG_GAS
  M 0.5
  LIQUID_RESIDUAL_SATURATION 0.1d0
  GAS_RESIDUAL_SATURATION 0.1d0
/
END
    
```

Figure 5-5 Text from the PFLOTRAN input deck used to set up the simulations. Bold text represents the keywords used for the new solver and characteristic curve smoothing options. Lighter text is included to show where these keywords are located within the input deck.

### 5.2.2 Initial Conditions

The initial pressure is atmospheric at the top of the model domain. The initial temperature conditions are a surface temperature of 25 °C and a natural geothermal temperature gradient of 0.025°C/m. The east and west boundary conditions are based on equilibrated one-dimensional simulations corresponding to these constraints. The full model domain temperature, pressure and saturation are simulated without drifts, waste packages or damage zone until a convergence tolerance is reached. This guarantees quasi-steady-state initial condition for the simulations within filtration. Also, as in Sevougian et al., (2019b), there is no east to west hydraulic gradient.

### 5.2.3 Boundary Conditions

The bottom condition for the model was set to be Dirichlet so it is open to fluid flow and has temperature based on a heat flux of 44 °C, which is representative of the geothermal gradient. These parameters were taken from the previously used input deck used in Mariner et al., (2018). There is also no cross-repository flux at this time but will be considered for future PA modeling. At the top boundary water infiltration rates are different for two different simulations: the first is set to have a rate of 1 mm/yr while the second is set to 10 mm/yr.

### 5.2.4 Material Properties

Material properties are discussed in Sections 4.1 and 4.2 of Sevougian et al. (2019a). Values used in the simulations are summarized in Table 5-1, which has been modified from the original table found in Sevougian et al. (2019a), Table 4-7. The modification made includes setting the unsaturated thermal conductivity of the backfill to a value of 1.0 (previously 2.0) and also inserted a row of values for the upper basin fill DRZ model region that is now included the simulation. Future simulations will have a more realistic grain density value for the upper basin fill DRZ.

**Table 5-1 Parameter values used in simulations (Modified from Sevougian et al. 2019a, Table 4-7). Modifications include backfill unsaturated thermal conductivity is now set to 1.0 (previously set to 2.0) and included a row of values for the upper basin fill DRZ.**

Model Region	Permeability (m <sup>2</sup> )	Porosity $\phi$	Tortuosity exponent <sup>1</sup> $\tau$	Saturated Thermal Conductivity (W/m/K)	Unsaturated Thermal Conductivity (W/m/K)	Heat Capacity (J/kg/K)	Grain Density (kg/m <sup>3</sup> )
Upper basin fill (UBF)	$1 \times 10^{-12}$	0.40	1.4	2.0	1.0	830	2700
Upper confining zone (ubf_conf)	$1 \times 10^{-14}$	0.40	1.4	2.0	1.0	830	2700
Basin fill below water table (LBF)	$1 \times 10^{-11}$	0.40	1.4	2.0	1.0	830	2700
Confining zone below water table	$1 \times 10^{-13}$	0.40	1.4	2.0	1.0	830	2700
Upper basin fill DRZ	$1 \times 10^{-11}$	0.435	1.4	2.0	1.0	830	1600
Backfill	$1 \times 10^{-13}$	0.40	1.4	2.0	1.0	830	2700
Waste Package (WP)	$1 \times 10^{-13}$	0.50	1	16.7	16.7	488	5000

<sup>1</sup>  $\tau = \phi^{1.4}$  (Van Loon and Mibus 2015)

## 5.3 Simulation Results and Discussion

Figures 5-6, 5-7 and 5-8 show the temperature, gas pressure, and liquid saturation in the repository after 0.5, 10, and 300 years of disposal. These times correspond roughly to peak WP pressure, peak WP temperature and a point in time in which the liquid saturation of all WPs goes to zero, respectively.

As can be seen in Figure 5-6, the temperature reaches a maximum of about 228°C in the waste packages after around 10 years of disposal. The regions of high temperature are in the immediate vicinity of the drifts, with little or no change in temperature outside the array.

The gas pressure at the WPs peaks to around 200,000 Pa just after half a year, nearly doubling from the initial gas pressure value. This is due to WP temperature reaching the boiling point of water (100°C) around the same time. The gas pressure declines after hitting its maximum value as can be seen in Figure 5-7.

In Figure 5-8 it can be seen that the liquid saturation after 0.5 years at the WPs is zero. By this time the temperature of the waste packages has reached over 100°C. At 10 years the region with liquid saturation of zero has expanded outward towards the buffer from the WPs. By 300 years a liquid saturation value of zero has reached the DRZ for several of the inner repository WP locations. The scale on Figure 5-8 shows that the liquid saturation data range resulted in a negative bottom value (-2.3e-02) in some waste packages. This small numerical error will be investigated in the future.

Figure 5-9 shows the temperature, gas saturation, gas pressure, and liquid saturation as a function of log time at a single observation point called “Fwp\_inside”, which is inside the centermost WP of the half-symmetry repository for the two PFLOTRAN simulations. Table 5-2 lists results for these runs at specific times of interest. Both simulations took 12 days before the water in the “Fwp\_inside” begins to boil off. It took 0.24 years for all the water to boil off for the 1 mm/yr infiltration rate run and 0.5 years for the 10 mm/yr run. The maximum temperature at the WP is reached after 13.1 years (238.3°C) and 11.7 years (227.6°C) for the 1 mm/yr and 10 mm/yr infiltration rate runs respectively. Water begins to re-saturate the waste package after year 10,044 for the 1 mm/yr run and year 1,779 for the 10 mm/yr run. All of these results are expected based on the lower initial saturation in the 1 mm/yr simulation and the slower re-saturation of the repository. Re-saturation to initial conditions is reached and exceeded by end of both the 100k year simulations. The reason why the liquid saturation at 100K years is different from the initial for both the runs is that the initial saturation is based on equilibrated ubf\_conf, but the final saturation is in equilibrated WP material.

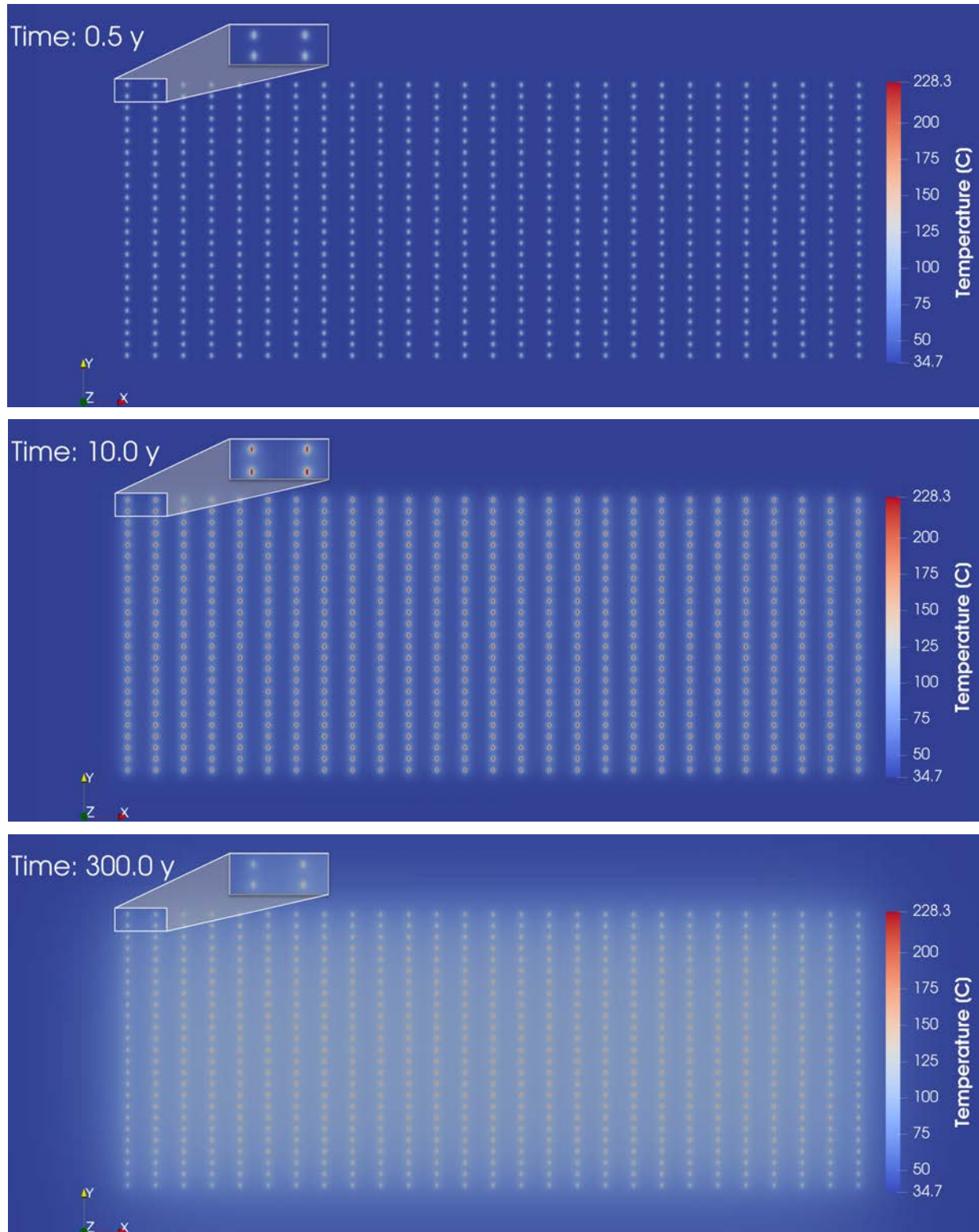


Figure 5-6 XY slice through the repository colored by temperature (°C) at years 0.5, 10, and 300 for the 10 mm/yr infiltration rate simulation. Temperature range has been scaled over all timesteps.

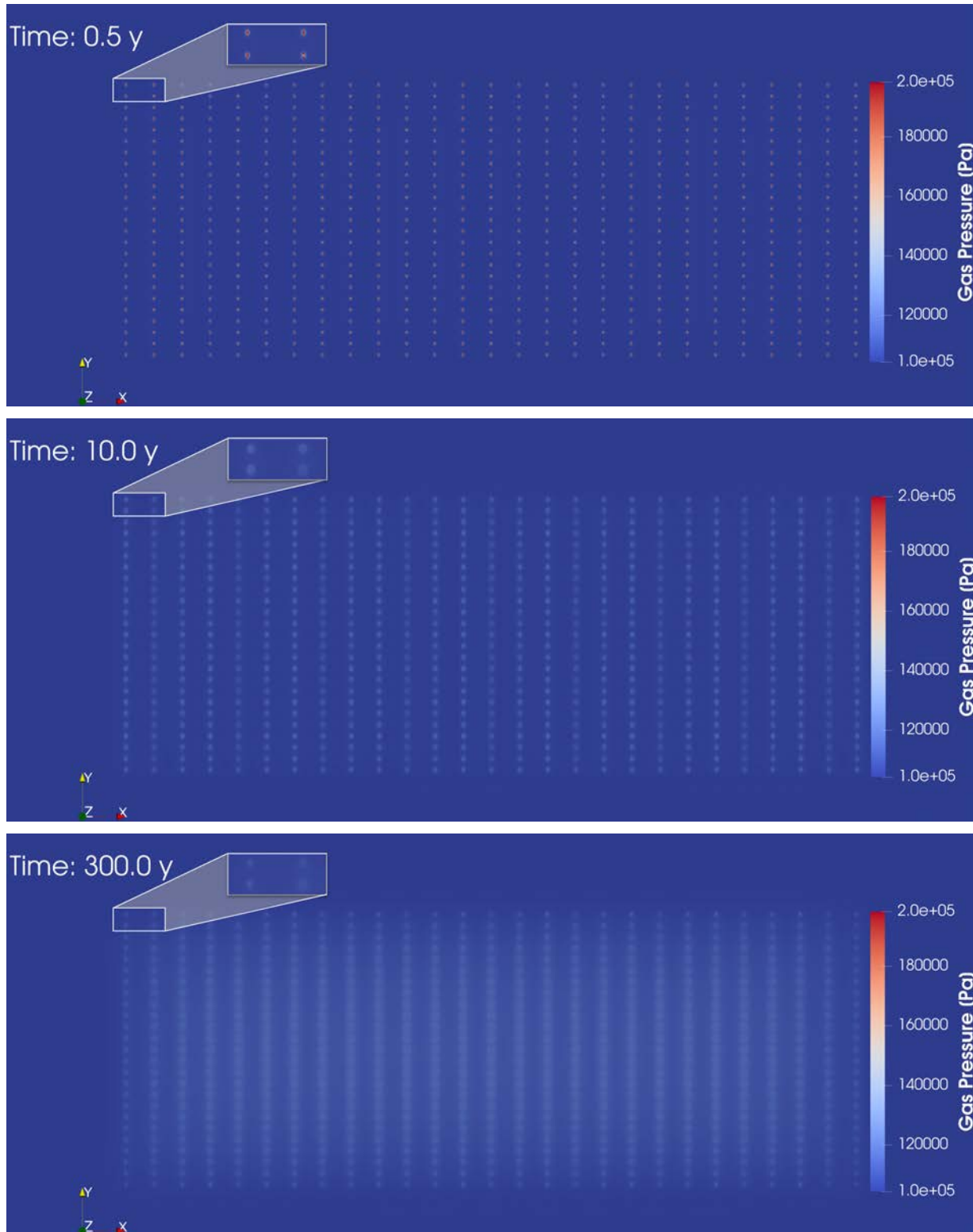


Figure 5-7 XY slice through the repository colored by gas pressure (Pa) at years 0.5, 10, and 300 for the 10 mm/yr infiltration rate simulation. Pressure range has been scaled over all timesteps.

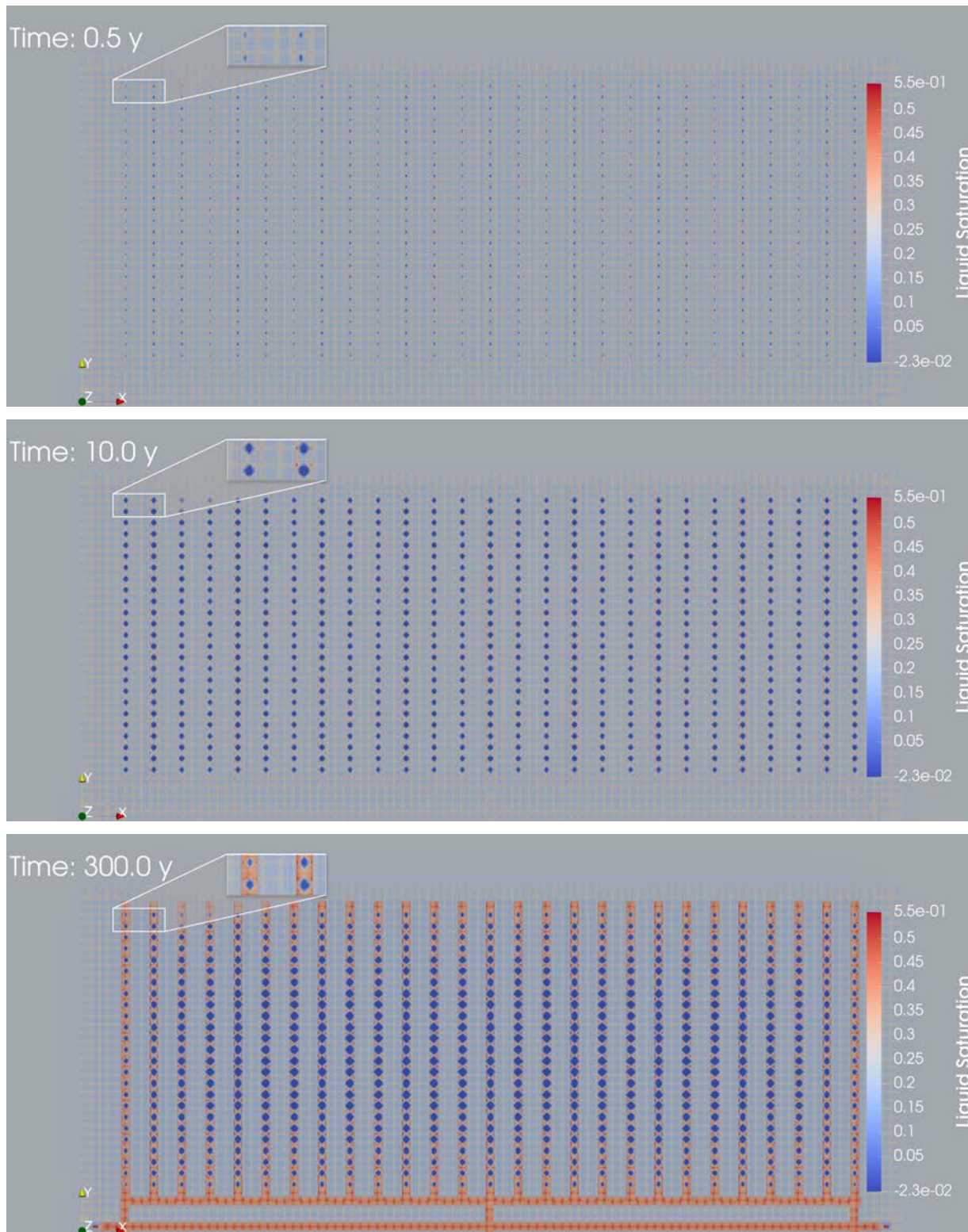


Figure 5-8 XY slice through the repository colored by liquid saturation at years 0.5, 10, and 300 for the 10 mm/yr infiltration rate simulation. Saturation range has been rescaled over all timesteps.

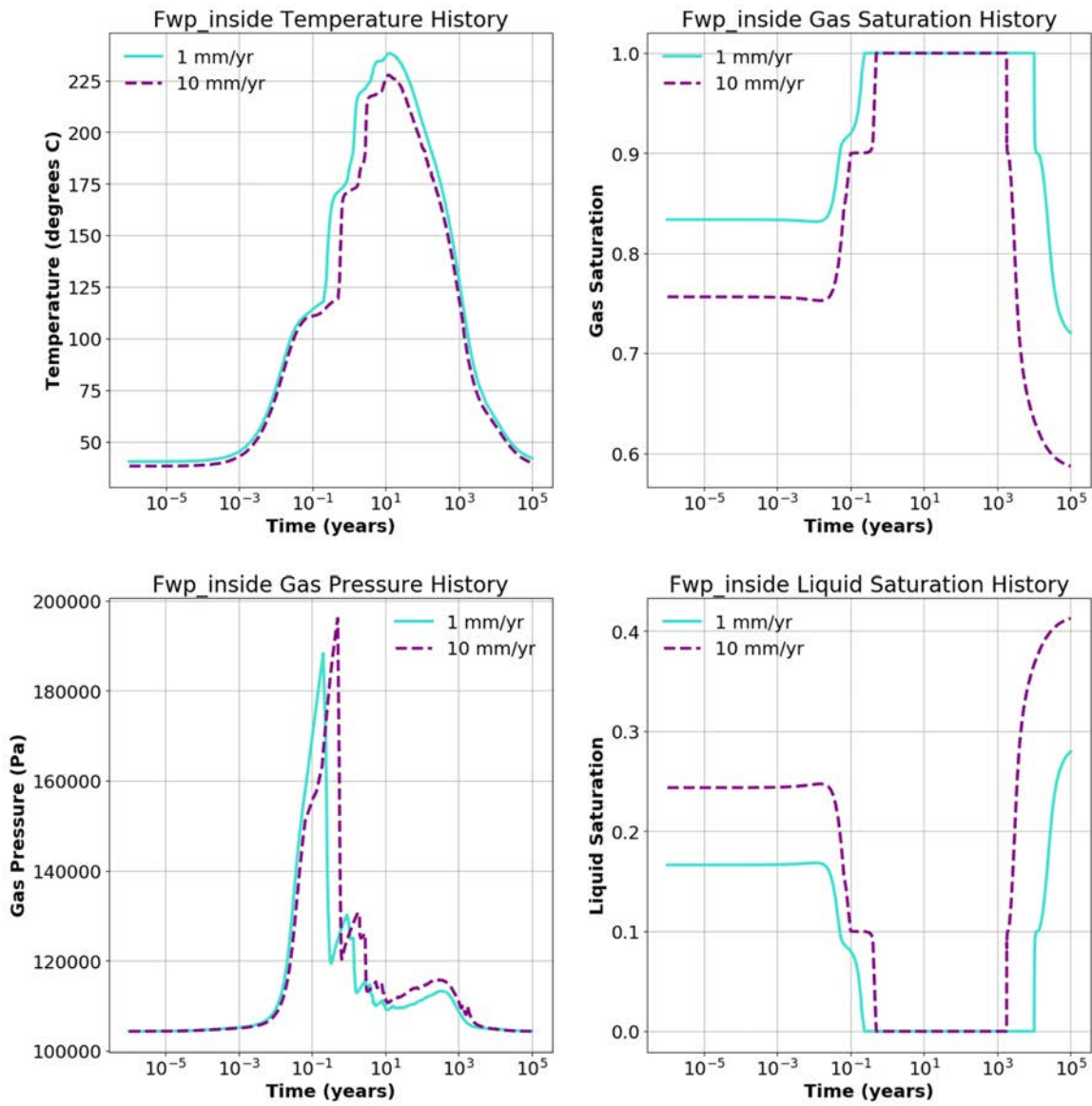
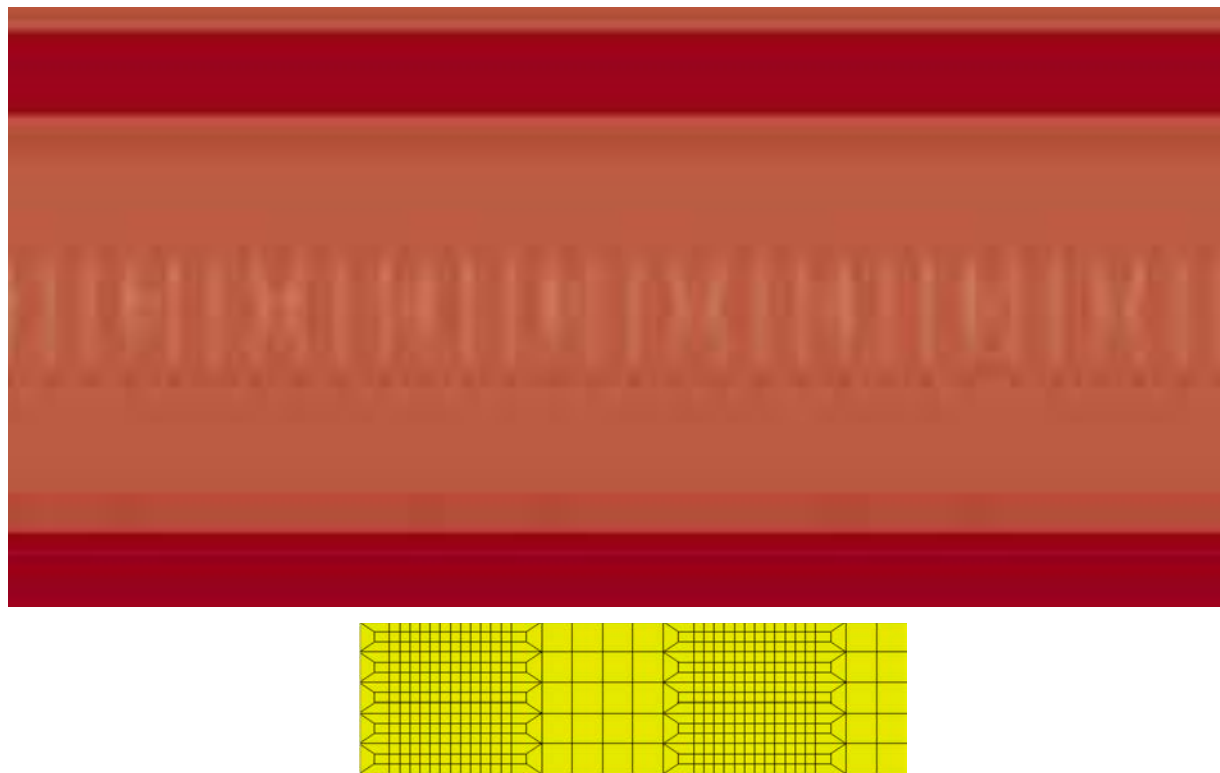


Figure 5-9 Temperature, gas saturation, gas pressure and liquid saturation history plots at observation point “Fwp\_inside” for the two PFLOTRAN simulations.

**Table 5-2 Results for the PFLOTRAN simulations at observation point “Fwp\_inside”.**

<b>Simulation:</b>	<b>1 mm/yr infiltration rate run</b>	<b>10 mm/yr infiltration rate run</b>
<b>Initial temperature:</b>	40.4°C	38.1°C
<b>Maximum temperature:</b>	238.3°C at 13.1 years	227.6°C at 11.7 years
<b>Temperature at 100K years:</b>	42°C	39.7°C
<b>Initial gas pressure:</b>	104,324 Pa	104,321 Pa
<b>Maximum gas pressure:</b>	188,280.6 Pa at 0.2 years	196,080 Pa at 0.5 years
<b>Gas pressure at 100K years:</b>	104,345.9 Pa	104,339 Pa
<b>Initial liquid saturation:</b>	0.16	0.24
<b>Liquid saturation goes to zero:</b>	from year 0.24 to year 10,044	from year 0.5 to year 1,779
<b>Liquid saturation at 100K years:</b>	0.28	0.41
<b>Initial gas saturation:</b>	0.83	0.76
<b>Gas saturation at value 1:</b>	from year 0.24 to year 10,044	from year 0.5 to year 1,779
<b>Gas saturation at 100K years:</b>	0.72	0.59

Grid orientation effects were observed in the model, as can be seen in Figure 5-10. These are caused by the “zig-zags” at the edges of the refined area of the repository, as shown on the bottom of Figure 5-10. In the previous mesh the “zig-zags” could also be seen in the x direction but the new UZ mesh with nearly 600,000 additional grid cells near the repository does not have this issue. This is due to having to increase the area of grid refinement around the DRZ to avoid the “zig-zag” boundary. Nevertheless, grid orientation effects are still present in the new mesh. This does not appear to happen in any other reference case. Possible solutions for grid orientation effects will be investigated in the future.



**Figure 5-10** Top: Zoomed XZ slice showing equilibrated gas saturation through the center of the half-symmetry repository showing grid orientation effects. Bottom: Slice showing ‘zig-zag’ pattern of the mesh refinement between two drifts (not to scale). There are also ‘zig-zags’ above and below the repository.

## 5.4 Conclusions and Considerations for Future Work

This year’s study on the UZ model has reached new heights. A combination of the PFLOTRAN NTRDC solver and characteristic curve smoothing options allowed for simulations to run past the re-saturation process. Simulations came close to reaching initial conditions by the end of the 100k year runs.

The simulation results show that in both cases the pressure in the WP nearly doubles, and the waste package completely dries out in less than a year. Temperature continues to increase for over 10 years and reaches over 200 °C. These high temperatures and pressures may be unacceptable in the field and higher thermal-conductivity engineered backfill may be required.

As seen in Figure 5-8, the liquid saturation legend range rescaled over all timesteps of the simulation reveals some negative saturation values that will need to be investigated. Future simulations will also need to have the current grain density for the upper basin fill DRZ seen in Table 5-1 modified to a higher value similarly to the other materials found in the table.

The next possible steps to include:

1. Implement flow from west to east of model. This is still unclear on how to initialize. Previous methods used for other references cases won’t work since this one is unsaturated.
2. Look into possible solutions for the observed grid orientation effects.

3. Set up UZ simulations using the GDSA Framework Graphical Workflow as described in section 3.2.1 of Mariner et al., (2020).
4. Uncertainty quantification (UQ) and sensitivity analysis (SA) for the UZ model using Dakota.
5. Full-scale PA with new PFLOTRAN transport model.

## 5.5 References

- Ayachit, U. 2015. *The ParaView Guide: A Parallel Visualization Application*, Kitware, ISBN 978-1930934306
- Blacker, T., Owen, S. J., Staten, M. L., Quador, R. W., Hanks, B., Clark, B., Meyers, R. J., Ernst, C., Merkley, K., Morris, R., McBride, C., Stimpson, C., Plooster, M., and Showman, S. 2016. *CUBIT Geometry and Mesh Generation Toolkit 15.2 User Documentation*, SAND2016-1649R, Sandia National Laboratories, Albuquerque, NM.
- Hammond, G.E., Lichtner, P.C. and Mills, R.T. 2014. *Evaluating the performance of parallel subsurface simulators: An illustrative example with PFLOTRAN*. Water Resources Research, 50(1), 208-228. doi: 10.1002/2012wr013483
- Mariner, P. E., Stein, E. R., Sevougian, S. D., Cunningham, L. J., Frederick, J. M., Hammond, G. E., Lowry, T. S., Jordan, S., and Basurto, E. 2018. *Advances in Geologic Disposal Safety Assessment and an Unsaturated Alluvium Reference Case*, SFWD-SFWST-2018-000509, SAND2018-11858R, 130 p.
- Mariner, P.E., Nole, M.A., Basurto, E., Berg, T.M., Chang, K.W., Debusschere, B.J., Eckert, A.C., Ebeida M.S., Gross\*, M., Hammond, G.E., Harvey, J., Jordan, S.H., Kuhlman K.L., LaForce, T.C., Leone, R.C., McLendon III, W.C., Mills, M.M., Park, H.D., Perry, F.V., Salazar III, A., Seidl, D.T., Sevougian, S.D., Stein, E.R., Swiler, L.P. 2020. *Advances in GDSA Framework Development and Process Model Integration*. SAND2020-10787 R
- Nole, M., Leone, R.C., Park, H.D., Paul, M., Salazar, A., Hammond, G.E., and Lichtner, P.C. 2021. *PFLOTRAN Development FY2021*. SAND2021- 8709 R. Sandia National Laboratories, Albuquerque, New Mexico, July 21, 2021.
- Sevougian, S. D., Stein, E. R., LaForce, T., Perry, F. V., Lowry, T. S., Cunningham, L. J., Nole, M., Haukwa, C. B., Chang, K. W. and Mariner, P. E. 2019a. *GDSA Repository Systems Analysis Progress Report*. SAND2019-5189R. Sandia National Laboratories, Albuquerque, NM.
- Sevougian, S. D., Stein, E. R., LaForce, T., Perry, F. V., Nole, M., Haukwa, C. B., and Chang, K. W. 2019b. *GDSA Repository Systems Analysis FY19 Update*. SAND2019-11942R. Sandia National Laboratories, Albuquerque, NM.
- Van Loon, L.R. and J. Mibus. 2015. *A modified version of Archie's law to estimate effective diffusion coefficients of radionuclides in argillaceous rocks and its application in safety analysis studies*. Applied Geochemistry. 59, 85-94. doi: 10.1016/j.apgeochem.2015.04.002

## 6. INVESTIGATION INTO SIMULATIONS ON VORONOI MESHES

Three years ago, an integration project with the Sandia (1464) VoroCrust developers was initiated to test the viability of using VoroCrust meshing software (Abdelkader et al. 2018, 2020) to generate meshes for use in PFLOTRAN simulations. The long-term goal of this study is to integrate an open-source version of VoroCrust into the GDSA Framework (<https://pa.sandia.gov/>). With rigorously correct, automated VoroCrust meshing it may be possible to study errors that arise from meshes and uncertainty in geological features as part of GDSA sensitivity and uncertainty analysis.

PFLOTRAN simulations on VoroCrust meshes of increasing complexity have been documented in Sevougian et al. (2019) and LaForce et al. (2020). This year the goal of demonstrating the ability of VoroCrust to create meshes for accurate PFLOTRAN simulations has largely been achieved, as demonstrated by the PFLOTRAN simulations in the following sections and in Section 3.2. However, the VoroCrust simulation meshes generated thus far are not as complex as will be required for PA-scale simulations.

### 6.1 FY 2021 Improvements to VoroCrust

Two significant improvements have been made to the VoroCrust software this year:

1. The first improvement is the ability of VoroCrust to create meshes in the exodus II format. This is a significant development that was unexpectedly-difficult to achieve. The exodus mesh file can be coupled with PFLOTRAN simulation output to create publication-quality visualizations in ParaView (Ahrens et al. 2005), as demonstrated by the figures in Section 6. The exodus II format may also allow researchers to use VoroCrust meshes with other simulation software, which will create a larger community of users and accelerate VoroCrust development. In particular, it is hoped that researchers at LANL will be able to use VoroCrust meshes for their in-house simulator FEHM for future GDSA collaborative projects.
2. The second improvement is the capability for regional refinement. In previous versions of VoroCrust users could uniformly refine or coarsen the entire model by choosing a single maximum grid-cell size parameter. The new capability allows for definition of the maximum grid-cell size at an arbitrary number of individual points within the domain. Users can now define different levels of refinement in different regions, resulting in a mesh that is fine in regions of interest and that rapidly coarsens away from them, resulting in fewer grid cells overall and more efficient computation in PFLOTRAN simulations. An example of this is shown in Section 6.3.

### 6.2 Four Test Cases Revisited

In this section four common reservoir structures are meshed for benchmarking. Each case represents a common geometrical feature in heterogeneous subsurface geological models. The four geometries are horizontal layering, pinch-out of the center layer in a three-layered model, an interior lens with pinch-out on all sides, and offset fault in a three-layered model, as shown in Figure 6-1. Four benchmark simulations of increasing complexity are run on each structure.

The test problems were originally presented in Gross et al. (2019) where they were also meshed using tetrahedral grid cells in LaGriT (Los Alamos National Laboratory 2017). The benchmark simulations were run on these four test case geometries in two subsurface flow simulators, FEHM (Los Alamos National Laboratory 2018) and PFLOTRAN (Lichtner et al. 2020). The results of this study are detailed in Section 8 and 9 of Gross et al. (2019). Simulations on the four test structures have also been run using

Voronoi meshes from a previous version of Vorocrust and hexahedral grid cells in CUBIT (Skroch et al. 2019) as detailed in Section 3.2 of Sevougian et al. (2019).

The 16 test simulations of Gross et al. (2019) are revisited here with some adaptations. All simulations are run in PFLOTRAN using Vorocrust meshes. Five of the simulations are quantitatively benchmarked against analytical solutions. The quality of simulation results is quantitatively assessed on 14 of these 16 benchmark simulations. Mesh refinement is studied on the on the pinch-out case and simulation reproducibility is studied on the interior lens case.

Each of the test volume meshes in this section have a similar resolution to the tetrahedral meshes in Gross et al. (2019). In that work the layered model, Test Case 1, has a relatively coarse mesh while the pinch-out model, Test Case 2, and interior lens model, Test Case 3, required a large number of grid cells to stair-step the angled interfaces with tetrahedral elements. This wide range of mesh resolutions serves to test the meshing algorithm and simulator on problems from tens of thousands to over a million grid cells. Voronoi meshes of these geometries do not require as many cells to capture the material interfaces, and grid refinement will be addressed in a subsequent section.

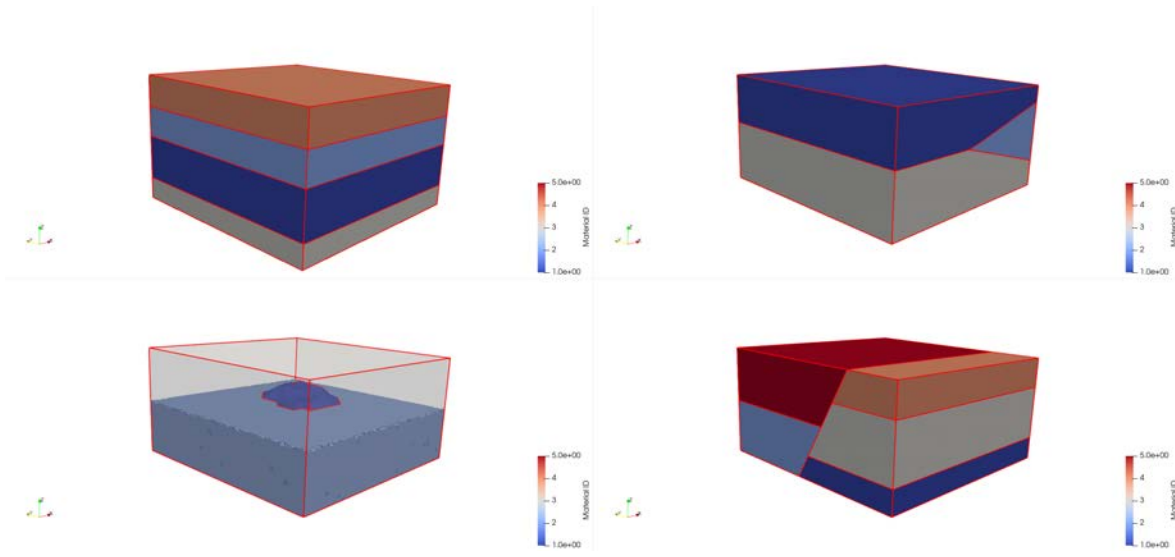


**Figure 6-1 Stratigraphy for all four Test Case volumes. Top Left: Test case 1 with 4 horizontal layers. Top Right: Test Case 2 with a pinch-out. Bottom Left: Test Case 3 with an interior lens. Bottom Right: Test Case 4 with layering and an offset fault.**

## 6.2.1 Meshing

### 6.2.1.1 Test Structure 1: layered media

Test structure 1 is a simple layered system as shown on the top left of Figure 6-1. The model is  $20 \times 20 \times 12.0766$  m. The layer thickness from top to bottom is 2.9661, 2.8597, 5.8258, and 2.0766 m. The Voronoi mesh is shown in Figure 6-2 and has 40,439 elements.

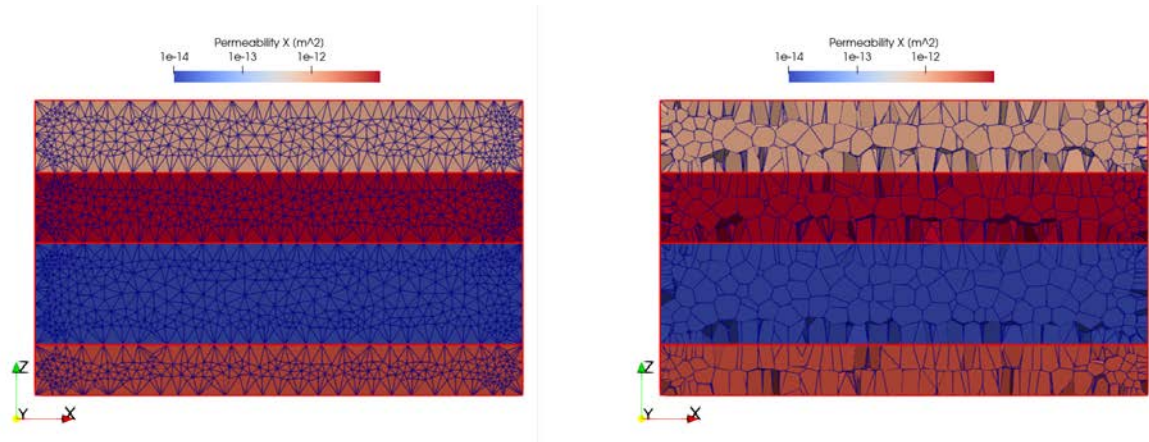


Figure 6-2 Test structure 1 layered example. Left: Surface mesh. Right: Interior mesh on a slice on the plane  $y = 10$  m. Permeabilities shown are for Test Case 1.2.

### 6.2.1.2 Test Structure 2: pinch-out

Test structure 2 contains three materials with material 2 pinching out in the interior of the model as shown on the top right of Figure 6-1. The volume is  $20 \times 20 \times 10$  m and the Voronoi mesh is shown in Figure 6-3. The Voronoi mesh is highly refined and has 1,059,151 elements. As in test structure 1, the Voronoi mesh has smaller elements on the surface (left) and larger elements in the interior (right).

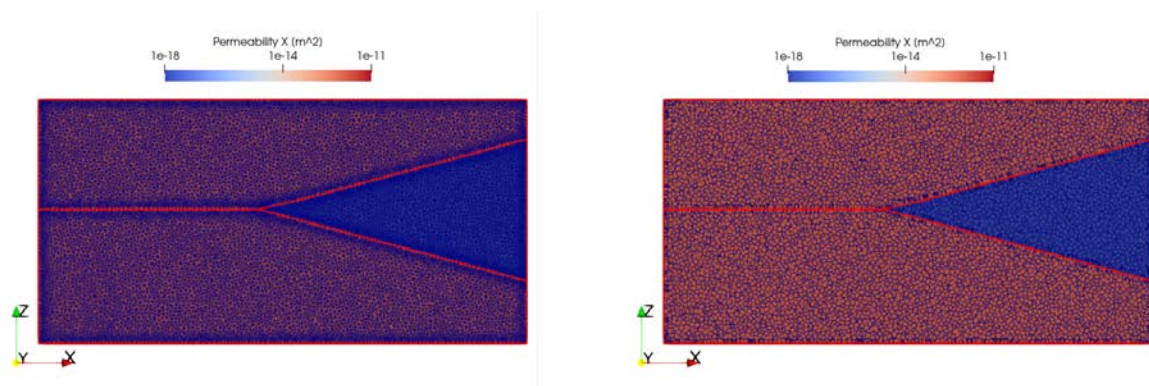


Figure 6-3 Test structure 2 pinch out example. Left: Surface mesh. Right: Interior mesh on a slice on the plane  $y = 10$  m. Permeabilities shown are for Test Case 2.2.

### 6.2.1.3 Test Case 3: interior lens

Test structure 3 contains an interior lens by surrounded on all sides by a different material as shown on the bottom left of Figure 6-1. The volume is  $20 \times 20 \times 10$  m, with  $z$  in the range  $(-10,0)$ . The lens has a flat bottom at  $z = -4$  m and a top surface with varying height. It pinches to zero thickness on all sides. The Voronoi mesh for Test structure 3 is shown in Figure 6-4. The Voronoi mesh has 442,994 elements. The elements are again smaller at boundaries and material interfaces, and larger in the interior. This mesh is also highly refined, it is possible to create a VoroCrust Voronoi mesh of this model with just 22,000 cells as shown in Sevougian et al. (2019).

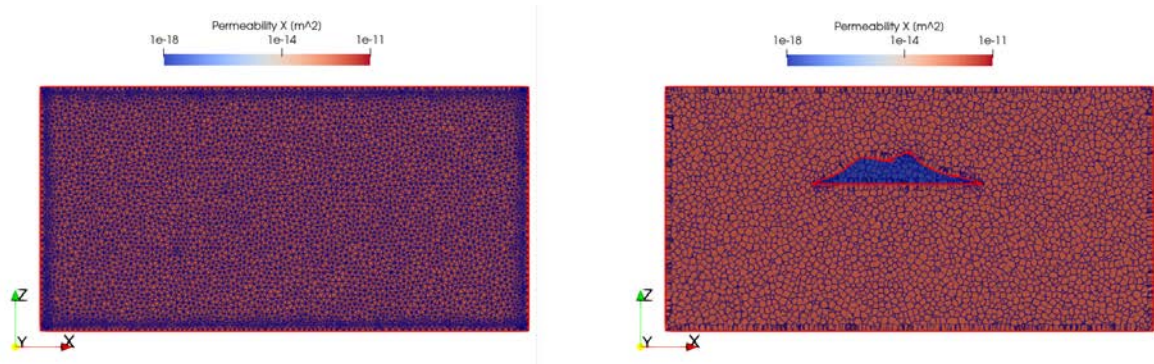


Figure 6-4 Test structure 3 interior lens example. Left: Surface mesh. Right: Interior mesh on a slice on the plane  $y = 10$  m. Permeabilities shown are for Test Case 3.2.

#### 6.2.1.4 Test Case 4: offset fault

Test structure 4 contains three material layers which are offset across a fault that passes through the model at an angle as shown on the bottom right of Figure 6-1. The volume is  $20 \times 20 \times 10$  m and the Voronoi mesh for Test structure 4 is shown in Figure 6-5. The Voronoi mesh has 228,965 cells. Like the other test structures, the grid cells are largest in the interior and smaller on the faces of the model and a short distance from material intersections.

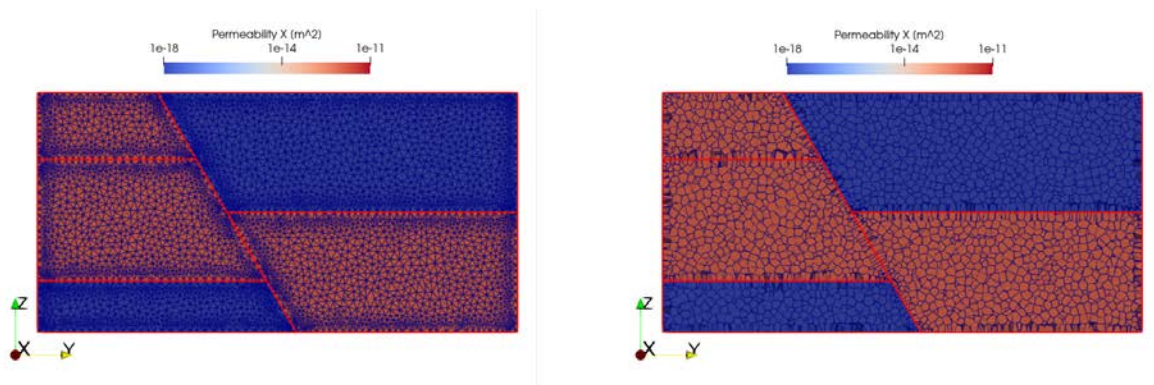


Figure 6-5 Test structure 4 offset fault example. Left: Surface mesh. Right: Interior mesh on a slice on the plane  $x = 10$  m. Permeabilities shown are for Test Case 4.2.

### 6.2.2 Test case simulations

#### 6.2.2.1 Single-phase homogeneous: Test Cases 1.1-4.1

Test Cases 1.1-4.1 are single-phase Richard's flow through a homogeneous porous medium with an enforced pressure gradient driving flow upwards. The simulations assume no gravity for simplicity. The purpose of this benchmark is to check for grid orientation effects caused by the internal material boundaries in each domain. The simulation parameters are shown on Table 6-1.

For Test Cases 1.1-4.1, the vertical flux through the simulation is calculated analytically using the equation:

$$q = A\rho \frac{k}{\mu} \nabla P \tag{6-1}$$

In all the cases cross sectional area  $A = 400 \text{ m}^2$ , and  $k = 1 \times 10^{-12} \text{ m}^2$ , while liquid viscosity and density are fixed in the simulator at  $\mu = 1.0 \times 10^{-3} \text{ Pa s}$ ,  $\rho = 998.6 \text{ kg/m}^3$ , respectively.

For Test Cases 1.1 and 2.1 the enforced pressure gradient is  $\nabla P = 1 \times 10^5/12.0 \text{ Pa/m}$ , which gives flux  $q = 3.33 \text{ kg/s}$ . This is matched to 7 significant figures in the Test Case 1 simulation, and to 5 significant figures for the Test Case 2.1 simulation. For Test Cases 3.1 and 4.1, the enforced pressure gradient is  $\nabla P = 1 \times 10^5/10.0 \text{ Pa/m}$ , which gives flux  $q = 3.9944 \text{ kg/s}$ , which is matched exactly to the 10 significant figures in the output file for both Test Cases 3.1 and 4.1. This demonstrates that there is little to no grid effect on the simulated flux for this benchmark.

**Table 6-1 Parameters for the 16 simulations on four test structures (after Gross et al. (2019)). RICHARDS mode is single-phase isothermal flow. GENERAL mode is full two-phase flow with thermal capability. All GENERAL mode simulations in the present work are isothermal with temperature  $T = 20 \text{ }^\circ\text{C}$ . Variable permeability properties and their distribution are given in Tables 6-2 and 6-3 and 6-4.**

Scenario	Permeability [m <sup>2</sup> ]	Mode	Gravity	Top Boundary	Bottom Boundary	Simulation Time
1.1, 3.1, 4.1	$1.00 \times 10^{-12}$	RICHARDS	No	$P = 1 \times 10^6 \text{ Pa}$	$P = 1.1 \times 10^6 \text{ Pa}$	1 hr
2.1	$1.00 \times 10^{-12}$	RICHARDS	No	$P = 1 \times 10^6 \text{ Pa}$	$P = 1.08 \times 10^6 \text{ Pa}$	1 hr
1.2, 3.2, 4.2	Variable	RICHARDS	No	$P = 1 \times 10^6 \text{ Pa}$	$P = 1.1 \times 10^6 \text{ Pa}$	1 hr
2.2	Variable	RICHARDS	No	$P = 1 \times 10^6 \text{ Pa}$	$P = 1.08 \times 10^6 \text{ Pa}$	1 hr
1.3, 2.3, 3.3, 4.3	$2.65 \times 10^{-12}$	GENERAL	Yes	$q = 4 \times 10^3 \text{ kg/y}$	$P = 1.1 \times 10^5 \text{ Pa}$ $S_w = 0.5$	5000 yr
1.4, 2.4, 3.4, 4.4	Variable	GENERAL	Yes	$q = 4 \times 10^3 \text{ kg/y}$	$P = 1.1 \times 10^5 \text{ Pa}$ $S_w = 0.5$	5000 yr

### 6.2.2.2 Single-phase heterogeneous: Test Cases 1.2-4.2

Test Cases 1.2-4.2 are single-phase isothermal Richard’s flow through a heterogeneous porous medium with an enforced pressure gradient driving flow upwards. Gravity is neglected for simplicity. The purpose of this benchmark is to compare the difference in the result from having heterogeneous media in each domain. The simulation parameters except for permeability are shown in Table 6-1 and are identical to Gross et al. (2019). The permeability distribution for each case are shown in Figures 6-2 to 6-5 and on Table 6-2.

The simulated pressure profiles for Test Cases 1.2-4.2 are shown on a slice through the interior of the domain in Figure 6-6. The flux for Test Case 1.2 is calculated analytically by substituting in the harmonic average of the layer permeabilities for  $k$ , as the layers are flat and continuous across the domain. The harmonically averaged permeability for Test Case 1.2 is  $k = 2.375 \times 10^{-14} \text{ m}^2$ , which gives an analytical flux of  $q = 9.486 \times 10^{-2} \text{ kg/s}$ . The simulated flux out of the top of the domain is  $q = 9.566 \times 10^{-2} \text{ kg/s}$ , a relative error of 0.00847.

Test Cases 2.2-4.2 do not have analytical solutions. Figure 6-6 shows that in Test Cases 2-2 and 3-2 the liquid pressure gradient indicates that flow is around the partial barriers created by the low-permeability region, as expected. In Test Case 4.2 the low-permeability material extends across the full domain in the  $x$  and  $y$  directions, as shown in Figure 6-5, so fluid must pass through the low-permeability region. The result is a large region of high-pressure in the thick part of the low-permeability region on the right of Figure 6-6.

**Table 6-2 Permeability in  $\text{m}^2$  for Test Case 1.2, 2.2, 3.2 and 4.2. Porosity is 0.1 for all materials. Permeabilities are also shown in Figures 6-2 to 6-5.**

Test Case 1.2	Top	Second	Third	Bottom
	$1 \times 10^{-12}$	$1 \times 10^{-11}$	$1 \times 10^{-14}$	$5 \times 10^{-12}$
Test Case 2.2	Outside Wedge	Inside Wedge		
	$1 \times 10^{-12}$	$1 \times 10^{-18}$		
Test Case 3.2	Outside Lens	Inside Lens		
	$1 \times 10^{-12}$	$1 \times 10^{-18}$		
Test Case 4.2	Top Left (two layers)	Bottom Left	Top Right	Bottom Right
	$1 \times 10^{-12}$	$1 \times 10^{-18}$	$1 \times 10^{-18}$	$1 \times 10^{-12}$

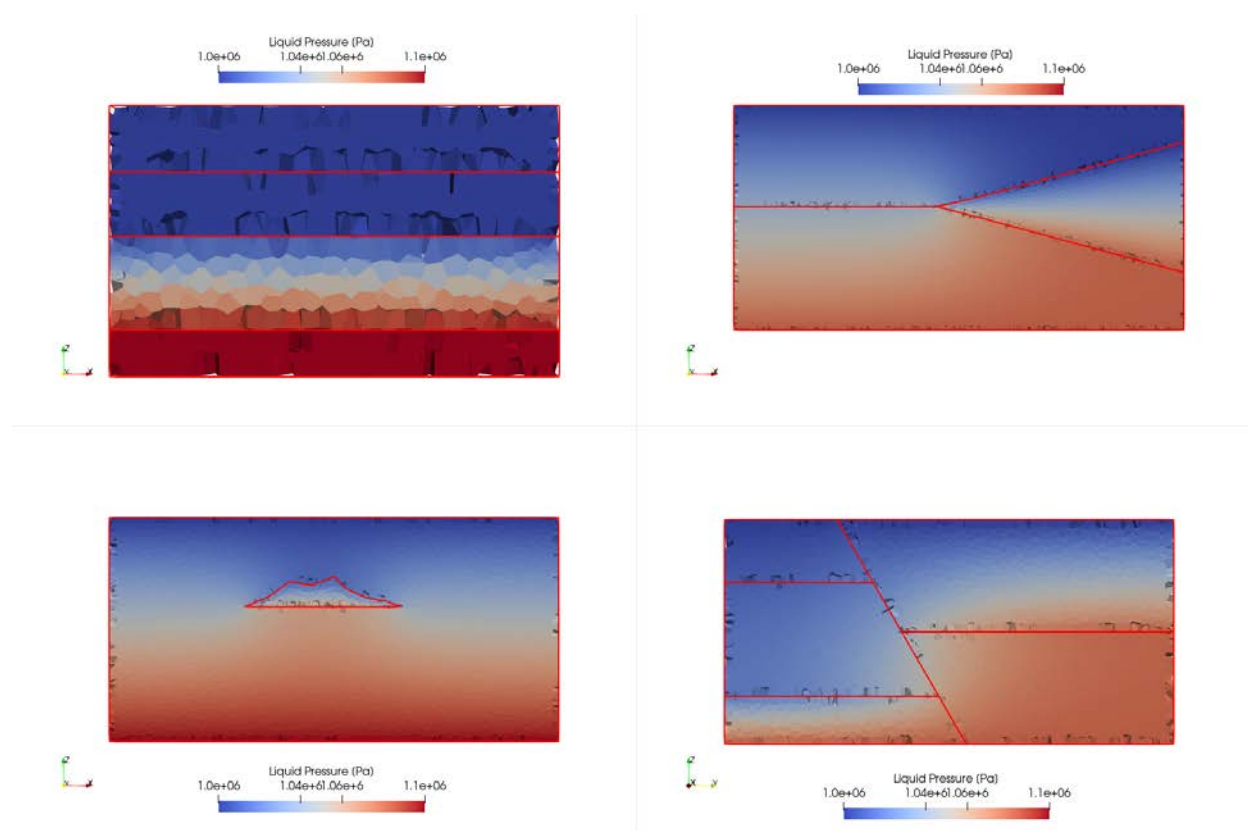


Figure 6-6 Steady-state pressure for Test Case 1.2 (top left), 2.2 (top right), 3.2 (bottom left) and 4.2 (bottom right). Test Cases 1-3 are shown on the XZ plane on a slice through the plane  $y = 10$  m, while solution for Test Case 4 is shown on the YZ plane on a slice through the plane  $x = 10$  m.

### 6.2.2.3 Two-phase homogeneous: Test Cases 1.3-4.3

This benchmark simulation tests for grid orientation effects in homogeneous models for two-phase flow. The boundary conditions are given in Table 6-1 and the permeability and two-phase flow properties for all the models are given by the Santa Fe rock properties in Table 6-3. The simulation is isothermal with fluid properties representative of air and water at  $T = 20$  °C.

This simulation is slightly different than in Gross et al. (2019). The present model has fixed pressure at the bottom of the domain instead of the top, and the constant liquid saturation at the base is 50% instead of 10%. The infiltration rate is the same at 4,000 kg/yr. The new boundary conditions were chosen to avoid with high suction when the Otowi formation is at the top boundary of the domain in Test Case 4.4 in the next section.

The simulation results are shown in Figures 6-7 and 6-8. There are no obvious grid orientation effects in the simulated profiles, though it can clearly be seen that the coarseness of the mesh in Test Case 1.3 results in a larger region of high water saturation at the base of the model. This indicates that the mesh with 40,439 does not have grid sufficient resolution to capture the thin high-saturation liquid layer at the base of the model created by bottom boundary condition  $S_w = 0.5$ .

The other three saturation and pressure profiles are very similar. As Test Cases 2.3-4.3 all have the same volume, it is possible to compare the total liquid mass in the three models to see if they are all giving the same result. The total water mass in the liquid phase are 9.818 kg, 9.821 kg, and 9.823 kg in Test Cases 2.3, 3.3, and 4.3, respectively. This indicates that three meshes are high enough resolution to accurately capture the steady-state saturation profile and also that they are not having grid effects due to the internal

boundaries in the meshes. The coarsest of these meshes is Test Case 4 with 228,965 grid cells and the finest is Test Case 2 with 1,036,237 grid cells.

**Table 6-3 Santa Fe and Otowi rock properties and two-phase flow parameters (after Gross et al. (2019)).**

	<b>Santa Fe</b>	<b>Otowi</b>
Permeability [m <sup>2</sup> ]	$2.65 \times 10^{-12}$	$2.32 \times 10^{-13}$
Porosity	0.35	0.44
Capillary Pressure Function	van Genuchten	van Genuchten
Liquid Relative Permeability Function	Mualem/van Genuchten	Mualem/van Genuchten
Gas Relative Permeability Function	Mualem/van Genuchten	Mualem/van Genuchten
M (-)	0.6269	0.4318
$\alpha$ (1/Pa)	$5.100 \times 10^{-4}$	$6.018 \times 10^{-5}$
P <sub>c,max</sub> (Pa)	$2.0 \times 10^6$	$2.0 \times 10^6$
Liquid Residual Saturation (-)	0.01	$4.3 \times 10^{-3}$
Gas Residual Saturation (-)	0.0	0.0

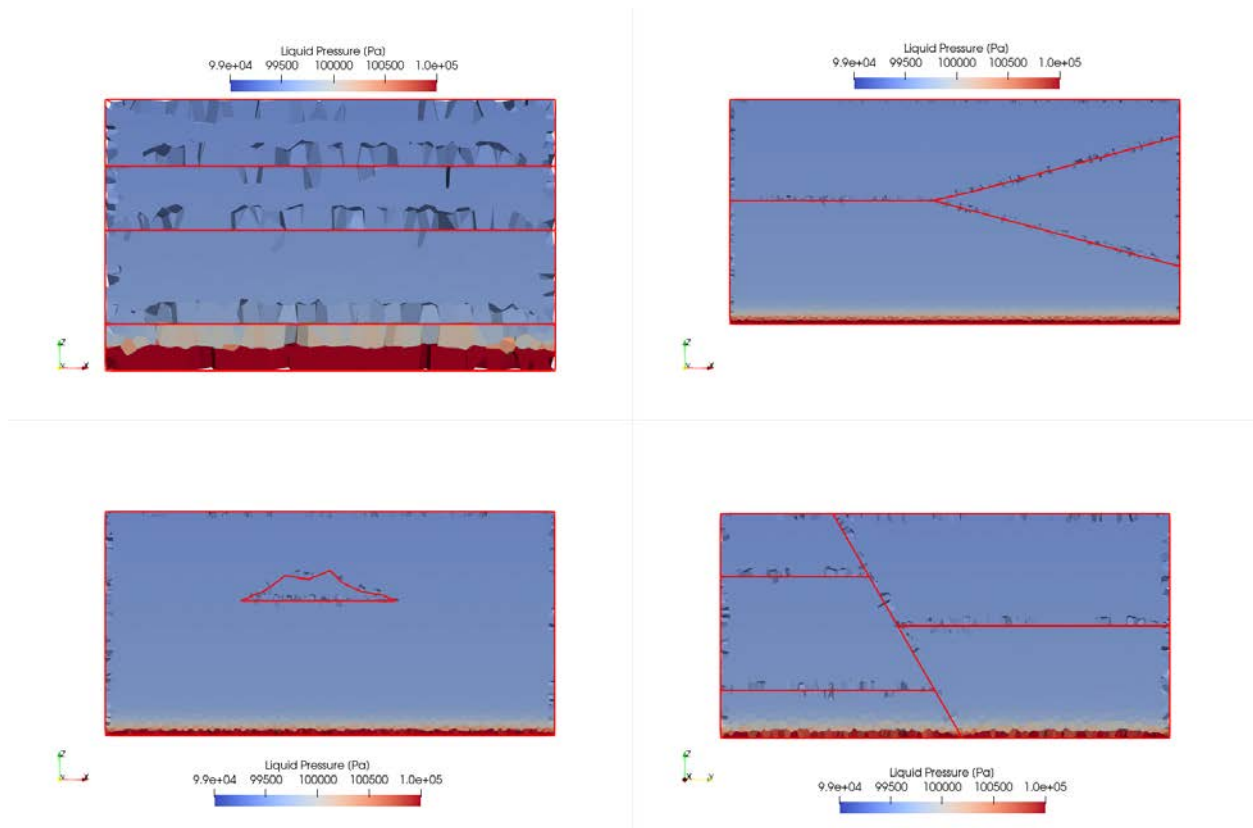


**Figure 6-7 Steady-state liquid pressure for Test Case 1.3 (top left), 2.3 (top right), 3.3 (bottom left) and 4.3 (bottom right). Test Cases 1-3 are shown on the XZ plane on a slice through the plane y = 10 m, while solution for Test Case 4 is shown on the YZ plane on a slice through the plane x = 10 m.**

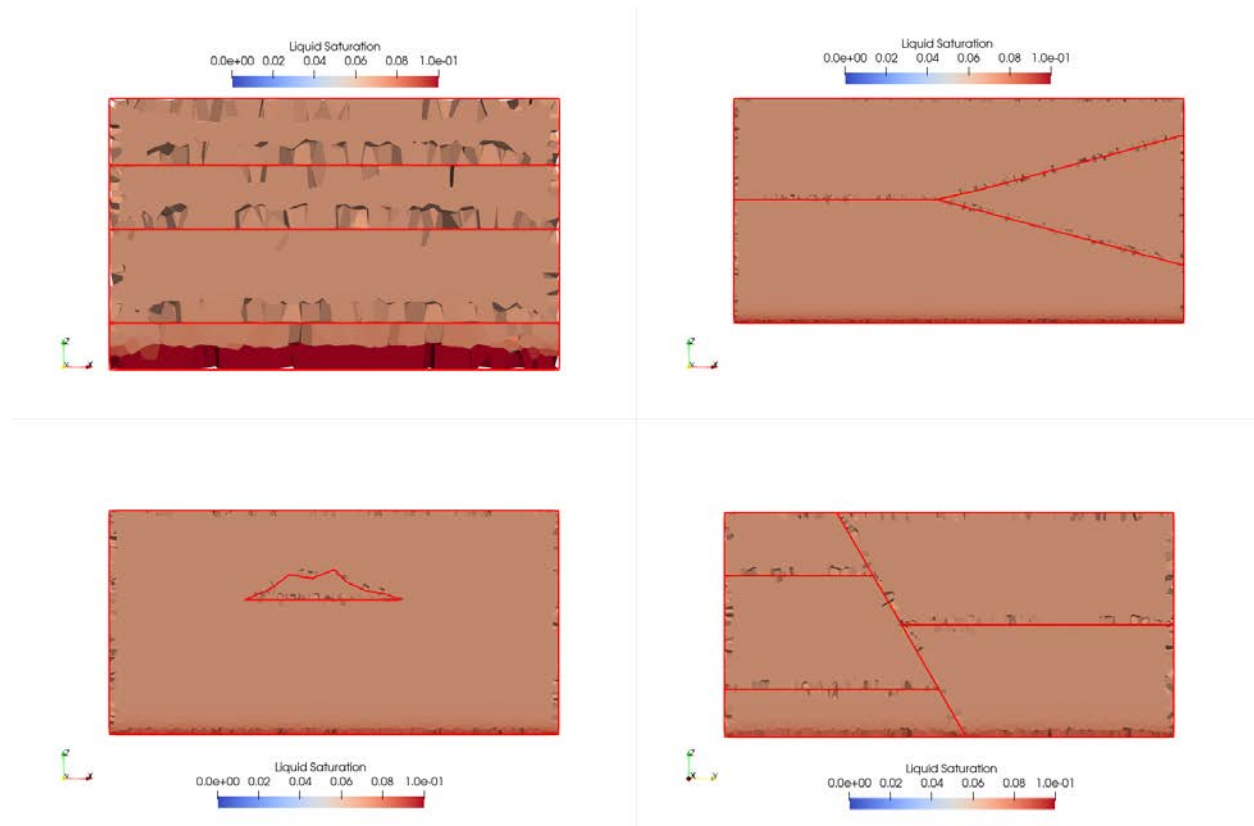


Figure 6-8 Steady-state liquid saturation for Test Case 1.3 (top left), 2.3 (top right), 3.3 (bottom left) and 4.3 (bottom right). Test Cases 1-3 are shown on the XZ plane on a slice through the plane  $y = 10$  m, while solution for Test Case 4 is shown on the YZ plane on a slice through the plane  $x = 10$  m.

#### 6.2.2.4 Two-phase heterogeneous: Test Cases 1.4-4.4

This benchmark simulation tests the capability of the simulation model to accurately capture two-phase flow with large property contrasts between regions. The boundary conditions are given in Table 6-1 and are identical to Test Cases 1.3-4.3 in the preceding section.

The permeability and two-phase flow properties for all the models are given by the Santa Fe or Otowi rock properties in Table 6-3, as described in Table 6-4. This simulation is isothermal with fluid properties representative of air and water at  $T = 20$  °C.

The simulation results are shown in Figures 6-9 and 6-10. As can clearly be seen, there are two distinct equilibrium saturation profiles for the high and low permeability regions. In the low-permeability and high capillary pressure Otowi formation, the liquid saturation at the bottom of the region is above 50% and decreases upwards. The exception to this is the Otowi region at the lower left corner of Test Case 4.4. This region has lower saturation because of the imposed saturation  $S_w = 0.5$  and pressure  $P = 1.1 \times 10^5$  Pa at the base of the model.

In the Santa Fe formation, liquid saturation is on the order of 6-7% and relatively uniform across an entire region. In the Santa Fe liquid saturation is low because fluid can flow at a low saturation through the model as a result of the higher permeability, relative permeability to water and lower capillary pressure. The pressure is lowest in the areas adjacent to the Otowi regions because of the lower pressure in the Otowi regions. Notice that all the pressures in the Santa Fe are on the order of the imposed pressure at the base, while pressures in the Otowi are about  $1 \times 10^4$  Pa lower, with a sharp transition between the two. This is due to the different capillary pressure curves in the two media.

**Table 6-4 Heterogeneous properties for Test Case 1.4, 2.4, 3.4 and 4.4 are defined according to geological formations as shown below. Properties are given in Table 6-3.**

Test Case 1.4	Top	Second	Third	Bottom
	Santa Fe	Otowi	Otowi	Santa Fe
Test Case 2.4	Outside Wedge	Inside Wedge		
	Santa Fe	Otowi		
Test Case 3.4	Outside Lens	Inside Lens		
	Santa Fe	Otowi		
Test Case 4.4	Top Left (two layers)	Bottom Left	Top Right	Bottom Right
	Santa Fe	Otowi	Otowi	Santa Fe

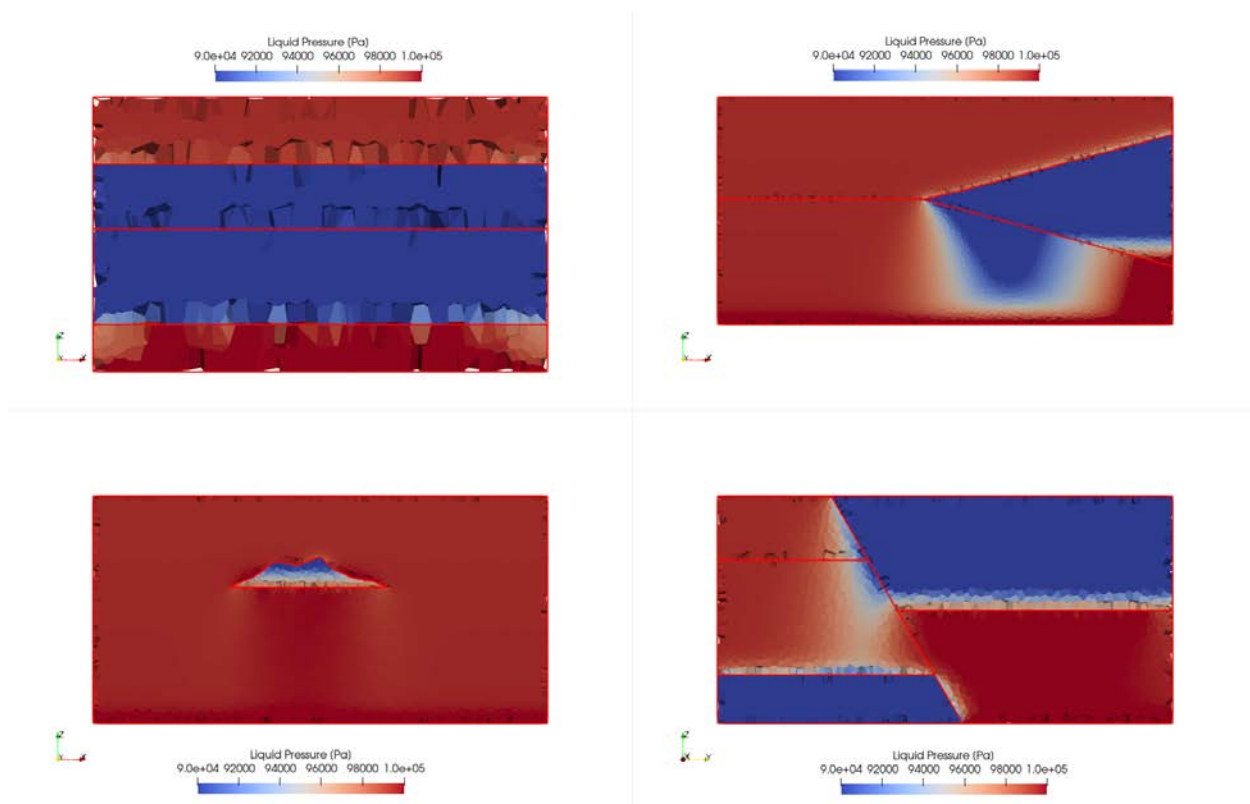


**Figure 6-9 Steady-state liquid pressure for Test Case 1.4 (top left), 2.4 (top right), 3.4 (bottom left) and 4.4 (bottom right). Test Cases 1-3 are shown on the XZ plane on a slice through the plane  $y = 10$  m, while solution for Test Case 4 is shown on the YZ plane on a slice through the plane  $x = 10$  m.**

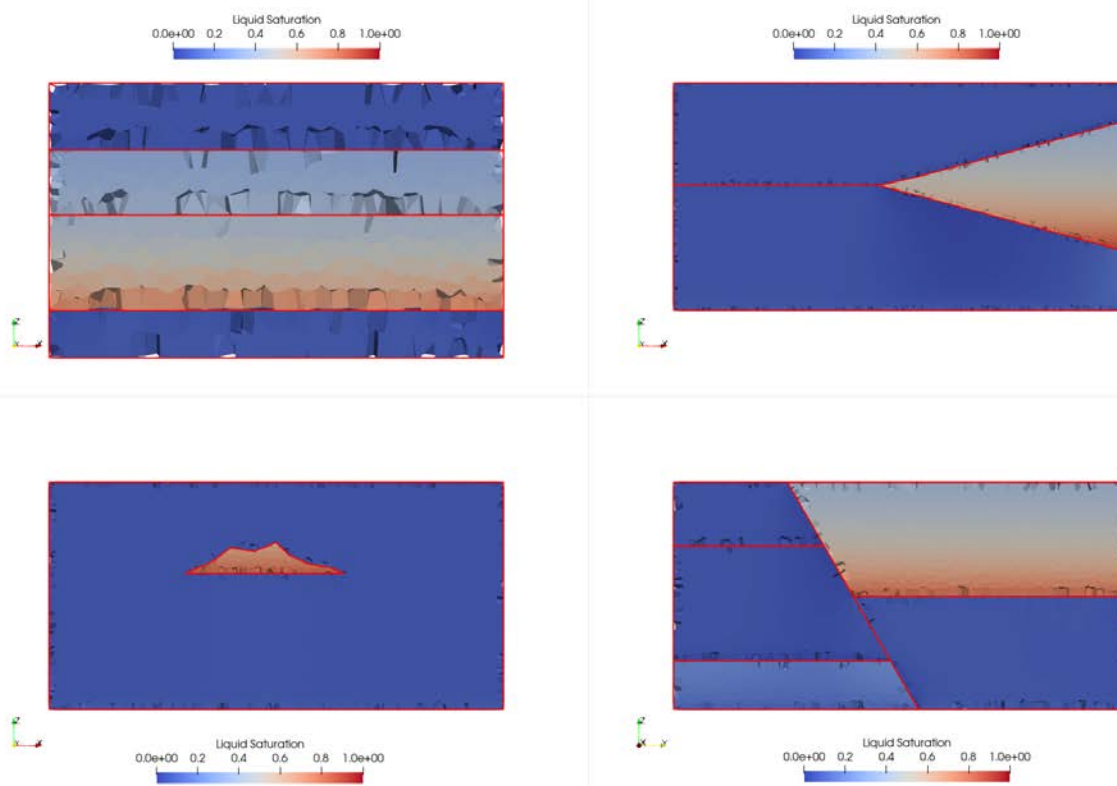


**Figure 6-10** Steady-state liquid saturation for Test Case 1.4 (top left), 2.4 (top right), 3.4 (bottom left) and 4.4 (bottom right). Test Cases 1-3 are shown on the XZ plane on a slice through the plane  $y = 10$  m, while solution for Test Case 4 is shown on the YZ plane on a slice through the plane  $x = 10$  m.

### 6.2.3 Error analysis

This section analyzes the error in simulations both within and between meshes for a subset of the 16 Test cases outlined in the preceding section. The difference in liquid pressure and liquid saturation (where applicable) between monitoring points is calculated using the relative integral difference over time:

$$D = \frac{\int_{t=0}^{t_{max}} |Q_i - Q_j|}{\int_{t=0}^{t_{max}} Q_i} \quad (6-2)$$

where  $Q_i$  is liquid pressure or liquid saturation at monitoring point  $i$ , and  $Q_j$  is the same quantity at another monitoring point that is expected to have the same value. Calculation of the integral in Eq. 6-2 is most accurate if monitoring point quantities are output at the same times.

To calculate the dimensionless difference,  $D$ , between two monitoring points using Eq. 6-2, the liquid pressure is output every 0.02 hours for the duration of the 1-hour simulations of the eight single-phase cases, Test Cases 1.1-4.1 and 1.2-4.2. Linear scaling in time is chosen because the equilibrium pressure is reached almost immediately, so this tests the accuracy of the equilibrated single-phase solutions. For the eight two-phase cases, Test Cases 1.3-4.3 and 1.4-4.4, liquid pressure and liquid saturation are output in a

log-increasing fashion: every 0.1 year for the first year, every 1.0 year for the first 10.0 years, etc, for the 5000 years of the simulation. Log-increasing time output was chosen to capture calculated errors at early-time and thus test the accuracy of the solutions during the equilibration process. The simulations take different amounts of time to equilibrate, and equal-size time-steps in Eq. 4-2 would miss early errors and strongly weigh the error towards the late-time, particularly for homogeneous cases with higher permeability. The monitoring points for the test cases are shown in Table 6-5.

**Table 6-5 Monitoring point locations for Test Cases 1.1-4.4. All points with the same ID are expected to have the same solution due to symmetry of the problem.**

	Location	ID		Location	ID
Test Case 1	(10, 10, -1.5), (10, 1, -1.5), (1, 10, -1.5)	1.a	Test Case 3	(10, 10, -1.6)	3.a
	(1, 10, -4), (10, 1, -4)	1.b		(4, 10, -3.5)	3.b
	(1, 10, -8), (10, 1, -8), (10, 10, -8)	1.c		(10, 10, -3.5)	3.c
	(1, 10, -11), (10, 1, -11)	1.d		(16, 10, -3.5)	3.d
				(10, 4, -3.5)	3.e
Test Case 2	(15, 10, -1.5), (15, 1, -1.5)	2.a		(10, 16, -3.5)	3.f
	(5, 1, -2.5), (5, 10, -2.5)	2.b		(10, 10, -5)	3.g
	(9, 1, -2.5), (9, 10, -2.5)	2.c			
	(5, 1, -5), (5, 10, -5)	2.d	Test Case 4	(1, 5, -1.5), (10, 5, -1.5)	4.a
	(9, 1, -5), (9, 10, -5)	2.e		(1, 10, -2.5), (10, 10, -2.5)	4.b
	(15, 1, -5), (15, 10, -5)	2.f		(1, 15, -2.5), (10, 15, -2.5)	4.c
	(5, 1, -7.5), (5, 10, -7.5)	2.g		(1, 5, -5), (10, 5, -5)	4.d
	(9, 1, -7.5), (9, 10, -7.5)	2.h		(1, 5, -9), (10, 5, -9)	4.e
	(15, 1, -8), (15, 10, -8)	2.i		(1, 10, -7.5), (10, 10, -7.5)	4.f
				(1, 15, -7.5), (10, 15, -7.5)	4.g

**6.2.3.1 Mesh quality**

One readily available test of mesh quality is the difference between monitoring points in the simulation that are expected to have the same solution. The monitoring points in each of the Test Cases are in given in Table 6-5. For the homogenous cases all points with the same depth are duplicate monitoring points. Notice that the heterogeneous Test Cases 3.2 and 3.4 have no duplicate monitoring points, as this mesh has no planes of symmetry.

For intra-mesh error calculations,  $Q_i$  is either liquid pressure or liquid saturation at an arbitrarily chosen monitoring point  $i$  and  $Q_j$  is any other monitoring point in Table 6-5 with the same point ID for heterogeneous cases, and any other monitoring point with the same depth for homogeneous cases. For every Test Case and every monitoring point the simulated difference between duplicate monitoring points is smaller than 0.5% for 13 of the 14 simulations that contain duplicate monitoring points. The only simulation with intra-mesh error greater than 1% are monitoring points 4.f and 4.g in Test Case 4.4.

The liquid saturation at monitoring points 4.f and 4.g in Test Case 4.4 have maximum difference of 3-4%. The difference in liquid pressure at these points is less than 0.3%. These are the regions of Test Case 4.4 with Santa Fe properties, which has higher permeability. As a result, they equilibrate to the highest liquid pressure and lowest saturation, as can be seen in Figures 6-9 and 6-10. Figure 6-11 shows that the two monitoring points 4.f have very similar liquid pressure and saturation during the equilibration process, but equilibrate to slightly different values, which causes the difference between the monitoring points. Figure 6-12 shows the pressure and saturation at monitoring points 4.f on a very small scale. The difference in the equilibrated pressure and saturation appears to be a boundary effect caused by (1,10, -7.5) being just a few grid cells away from the  $x = 0$  m boundary of the domain.

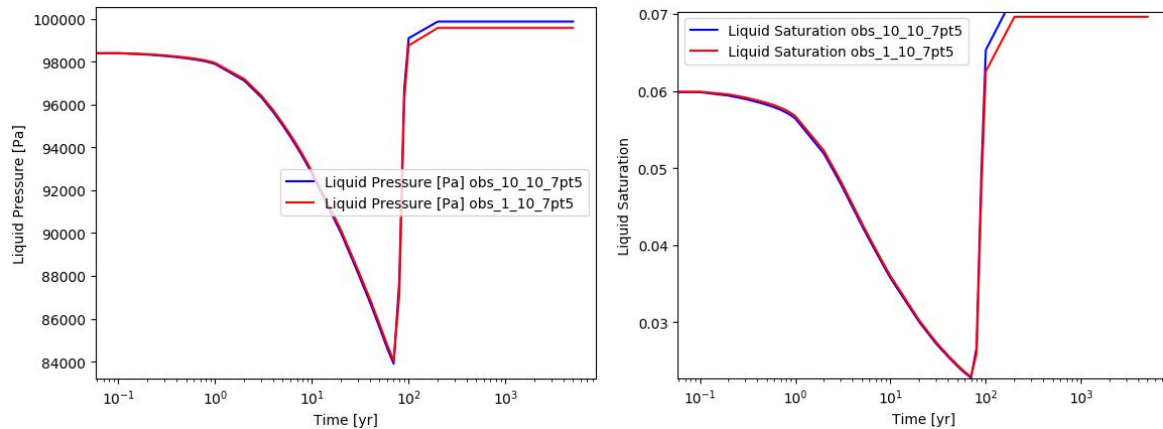


**Figure 6-11 Liquid pressure and saturation profiles for equivalent monitoring points vs log of time for heterogeneous two-phase Test Case 4.4.**

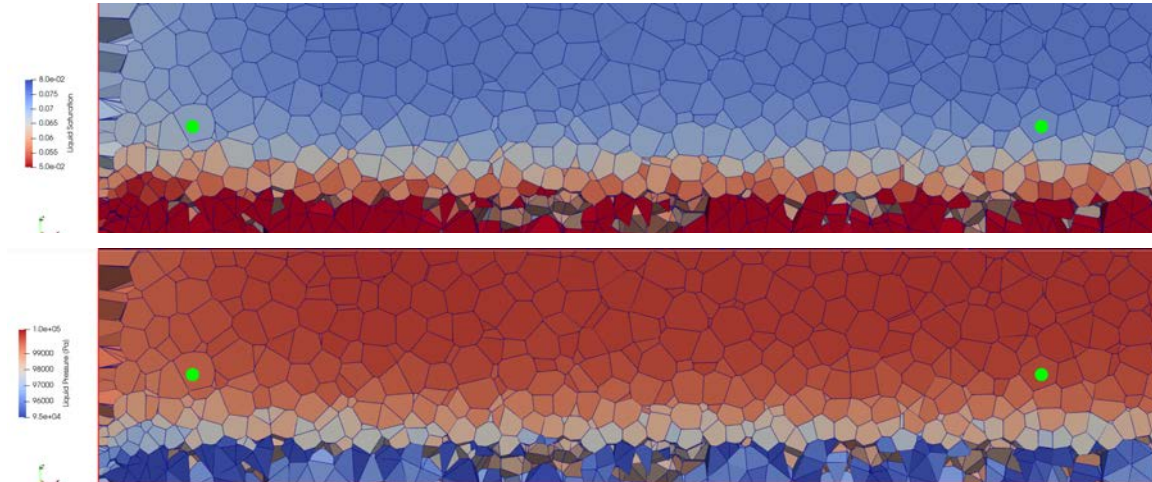


**Figure 6-12 Side view of the equilibrated saturation (top) and pressure (bottom) distribution near the monitoring points (10,10,-7.5) m and (1,10,-7.5) m for heterogeneous two-phase Test Case 4.4. Very small scales have been chosen in the colorbars to emphasize the difference in quantities between the two points.**

### 6.2.3.2 Mesh resolution

In this subsection a series of simulations are run on all the test structure 2 scenarios with three levels of resolution to explore the impact of mesh refinement on simulations. Meshes are generated with maximum radius in the meshing sphere-generating algorithm of 0.7, 0.14 and 0.28, which results in meshes with size increasing by a factor of approximately five. The coarsest mesh has 37,560 grid cells, medium mesh has 194,157 grid cells, and finest is the mesh from the preceding section and has 1,059,151 grid cells.

The monitoring points are repeated in the left column of Table 6-6. Some of the monitoring points are at  $y = 1.0$  m and some are at  $y = 10$  m and not all of the monitoring points are in the coarsest mesh. Other than the mesh resolution, simulations are identical to the one presented in Subsection 6.2.2.

For Test Cases 2.1, 2.2 and 2.3 there is virtually no impact of grid resolution on the simulation results. In Test Case 2.1 fluid flux through the problem is identical to 9 significant figures for the three meshes, while for Test Case 2.2 there is a general trend for slightly lower flux with coarser mesh resolution. The integral relative difference in pressure from the benchmark monitoring point all monitoring points in Test Cases 2.1-2.3 is always less than 0.001 and the difference in saturation for Test Case 2.3 is always less than 0.003.

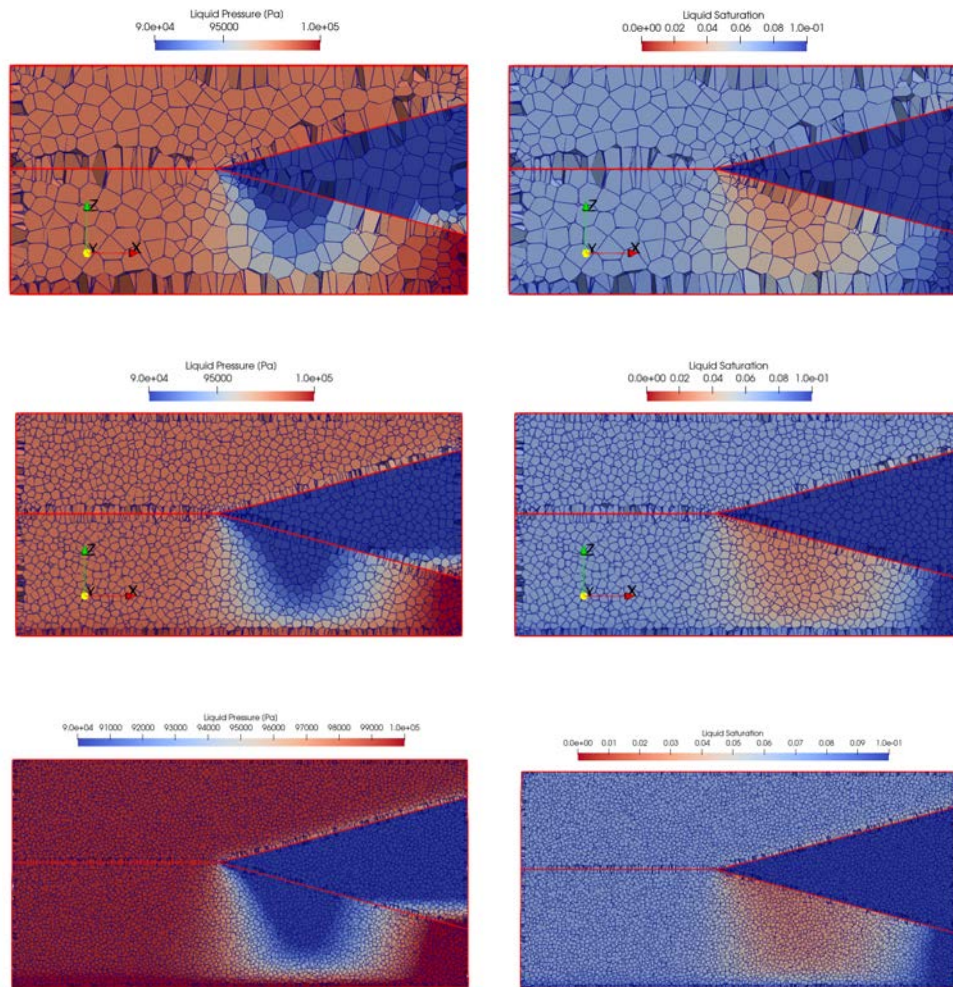
Test Case 2.4 is more challenging and has correspondingly larger differences in simulation results. The difference in pressure and saturation from the arbitrarily chosen benchmark monitoring point on the fine mesh are shown in Table 6-6. There is a clear increase in difference from the fine mesh simulation result with coarser meshes. There is also a general trend of difference increasing with  $x$  at similar depth: Error increases 2.b  $\rightarrow$  2.c, 2.d  $\rightarrow$  2.e  $\rightarrow$  2.f and 2.g  $\rightarrow$  2.h. This is likely because the top and bottom regions become narrower with increasing  $x$  due the broadening of the wedge material.

Table 6-6 shows that the maximum integral relative pressure difference from the benchmark on the intermediate mesh is  $8.25 \times 10^{-3}$  [-] at point 2.i. Relative difference in saturation is about an order of magnitude higher. This result indicates that the intermediate mesh is suitable for this simulation, as the simulated results are consistent with the fine mesh to within a few percent. This can also be seen in the similarity of the pressure and saturation profiles on Figure 6-13.

The monitoring points with by far the largest integral relative pressure difference are 2.f and 2.i on the coarsest mesh, with relative difference  $1.34 \times 10^{-2}$  [-] and  $3.59 \times 10^{-2}$  [-]. The largest saturation difference occurs for the monitoring point 2.i and is unacceptably large at 0.32. Figure 6-14 shows that on the intermediate and fine mesh, pressure and saturation decrease uniformly upwards to the material boundary. Conversely, the pressure and saturation distributions are nonuniform on the coarse mesh. This demonstrates that the coarse mesh is simply not sufficiently refined in this region to capture the pressures or saturation distribution for Test Case 2.4 accurately.

**Table 6-6 Dimensionless integral relative difference in Test Case 2.4 solutions at monitoring points in meshes with different resolution. The monitoring point used as benchmark are those with N/A. (-) indicates that the monitoring point is not in the mesh.**

ID	Location	Liquid Pressure Difference [-]			Liquid Saturation Difference [-]		
		Fine (1,059,151)	Medium (194,157)	Coarse (37,560)	Fine (1,059,151)	Medium (194,157)	Coarse (37,560)
2.a	(15, 1, -1.5)	$2.15 \times 10^{-6}$	$8.25 \times 10^{-5}$	$1.25 \times 10^{-4}$	$2.88 \times 10^{-5}$	$1.12 \times 10^{-3}$	$1.69 \times 10^{-3}$
	(15, 10, -1.5)	N/A	$9.02 \times 10^{-5}$	$4.98 \times 10^{-4}$	N/A	$1.22 \times 10^{-3}$	$6.67 \times 10^{-3}$
2.b	(5, 1, -2.5)	$8.20 \times 10^{-9}$	$1.56 \times 10^{-7}$	$6.37 \times 10^{-7}$	$9.43 \times 10^{-8}$	$2.26 \times 10^{-6}$	$7.92 \times 10^{-6}$
	(5, 10, -2.5)	N/A	$1.68 \times 10^{-7}$	$1.05 \times 10^{-6}$	N/A	$2.36 \times 10^{-6}$	$1.35 \times 10^{-5}$
2.c	(9, 1, -2.5)	$1.07 \times 10^{-7}$	$9.11 \times 10^{-6}$	$2.88 \times 10^{-5}$	$1.81 \times 10^{-6}$	$1.24 \times 10^{-4}$	$3.92 \times 10^{-4}$
	(9, 10, -2.5)	N/A	$8.84 \times 10^{-6}$	$3.09 \times 10^{-5}$	N/A	$1.21 \times 10^{-4}$	$4.19 \times 10^{-5}$
2.d	(5, 1, -5)	$8.85 \times 10^{-9}$	$1.92 \times 10^{-6}$	$6.18 \times 10^{-6}$	$5.34 \times 10^{-7}$	$2.64 \times 10^{-5}$	$8.31 \times 10^{-5}$
	(5, 10, -5)	N/A	$2.26 \times 10^{-6}$	-	N/A	$3.11 \times 10^{-5}$	-
2.e	(9, 1, -5)	$9.41 \times 10^{-5}$	$1.91 \times 10^{-3}$	$3.06 \times 10^{-3}$	$9.86 \times 10^{-4}$	$2.04 \times 10^{-2}$	$3.31 \times 10^{-2}$
	(9, 10, -5)	N/A	$2.92 \times 10^{-3}$	-	N/A	$3.15 \times 10^{-2}$	-
2.f	(15, 1, -5)	$1.26 \times 10^{-4}$	$4.71 \times 10^{-3}$	$1.33 \times 10^{-2}$	$8.22 \times 10^{-5}$	$5.88 \times 10^{-3}$	$1.67 \times 10^{-2}$
	(15, 10, -5)	N/A	$5.16 \times 10^{-3}$	-	N/A	$6.16 \times 10^{-3}$	-
2.g	(5, 1, -7.5)	$1.10 \times 10^{-8}$	$2.10 \times 10^{-5}$	-	$1.40 \times 10^{-7}$	$2.85 \times 10^{-4}$	-
	(5, 10, -7.5)	N/A	$2.54 \times 10^{-5}$	$5.62 \times 10^{-5}$	N/A	$3.44 \times 10^{-4}$	$7.62 \times 10^{-4}$
2.h	(9, 1, -7.5)	$3.82 \times 10^{-5}$	$7.37 \times 10^{-4}$	$1.61 \times 10^{-3}$	$4.25 \times 10^{-4}$	$8.27 \times 10^{-3}$	$1.82 \times 10^{-2}$
	(9, 10, -7.5)	N/A	$7.41 \times 10^{-4}$	$2.59 \times 10^{-3}$	N/A	$8.31 \times 10^{-3}$	$2.97 \times 10^{-2}$
2.i	(15, 1, -8)	$1.09 \times 10^{-3}$	$4.30 \times 10^{-3}$	$1.34 \times 10^{-2}$	$7.17 \times 10^{-3}$	$2.95 \times 10^{-2}$	$9.82 \times 10^{-2}$
	(15, 10, -8)	N/A	$8.25 \times 10^{-3}$	$3.59 \times 10^{-2}$	N/A	$5.84 \times 10^{-2}$	$3.20 \times 10^{-1}$



**Figure 6-13** Side view of the equilibrated pressure and saturation distribution for heterogeneous two-phase Test Case 2.4 on a slice through  $y = 10$  m. Top: simulated result on the coarse mesh. Middle: simulated result on the intermediate mesh. Bottom: simulated result on the fine mesh.

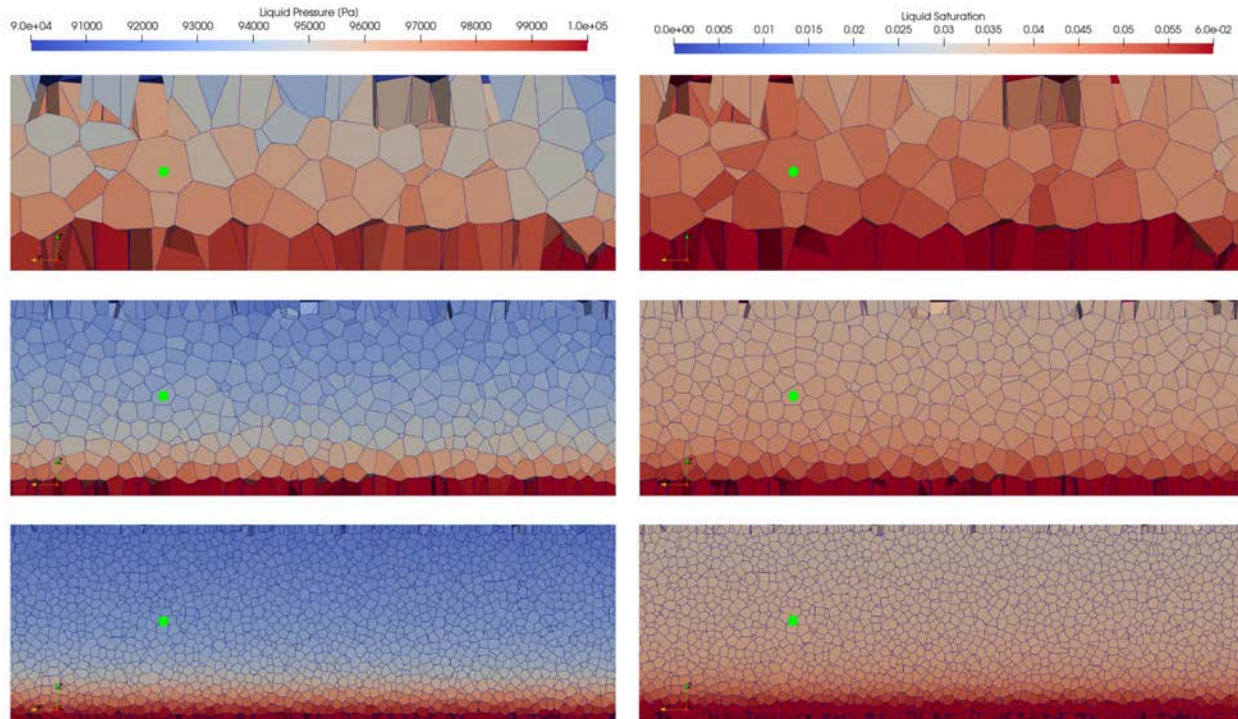


**Figure 6-14** Side view on a slice along the plane  $x = 15$  m of the equilibrated pressure (left) and saturation (right) distribution near the monitoring point (15, 10, -8) m for heterogeneous two-phase Test Case 2.4. The range  $z = (-7.5, -10)$  m and  $y = (8, 18)$  m is shown. The green circle indicates the centroid of the monitoring point cell. Top: simulated result on the coarse mesh. Middle: simulated result on the intermediate mesh. Bottom: simulated result on the fine mesh. Very small temperature and pressure ranges have been chosen to emphasize differences between the simulated result in this area.

### 6.2.3.3 Mesh reproducibility

In this subsection ten meshes of identical resolution are generated and the simulation for Test Case 3.4 is run. The purpose of this example is to demonstrate mesh quality and reproducibility. The meshes had between 440,593 and 444,217 cells, indicating good reproducibility of mesh size. The simulations for Test Case 3.4 take around an hour to complete, with the shortest at 0.977 hr and the longest at 1.266 hr. This demonstrates consistency in the simulation time on the different realizations of the mesh.

The difference in simulated results from the base case shown in Figures 6-9 and 6-10 (Subsection 6.2.2.3) was calculated using Eq. 6-2 at the seven monitoring points in the domain as shown in Table 6-7. One point was inside the lens, near the center at (10,10,-3.5) m, one was directly above the lens at (10,10,-1.6) m, one was directly below the lens at (10,10,-5) m. Four points were outside the lens and at depth  $z = -3.5$  m so that they were in a plane parallel to the  $z$ -axis that intersects the lens: (4,10,-3.5) m, (16,10,-3.5) m, (10,4,-3.5) m, (10,16,-3.5) m.

The largest difference in liquid pressure and saturation at any monitoring point was below the lens at (10,10,-5), which had an integral relative difference in pressure of  $4.350 \times 10^{-4}$  [-] on mesh 9. The differences in saturation (not shown) followed a similar trend, though the differences were about an order of magnitude larger, like the example in the preceding section. There was a tendency for mesh 9 to have largest difference from the base case simulated pressure and for mesh 4 to have the smallest, as shown in

Table 6-7, but the simulated differences are uniformly small. This indicates a high degree of precision and reproducibility for the meshes.

**Table 6-7 Monitoring point locations for ten realizations of Test Case 3.4. Minimum and maximum dimensionless integral relative pressure difference from the base case are shown, along with the mesh that had the largest or smallest difference.**

ID (Location)	Minimum Pressure Difference (Mesh ID)	Maximum Pressure Difference (Mesh ID)
3.a (10,10,-1.6) m	$4.537 \times 10^{-7}$ (mesh 4)	$6.223 \times 10^{-6}$ (mesh 6)
3.c (10,10,-3.5) m	$2.138 \times 10^{-5}$ (mesh 6)	$1.608 \times 10^{-4}$ (mesh 7)
3.g (10,10,-5.0) m	$2.699 \times 10^{-5}$ (mesh 7)	$4.350 \times 10^{-4}$ (mesh 9)
3.b (4.0,10,-3.5) m	$1.572 \times 10^{-8}$ (mesh 3)	$5.156 \times 10^{-7}$ (mesh 4)
3.d (16,10,-3.5) m	$5.508 \times 10^{-9}$ (mesh 4)	$3.004 \times 10^{-8}$ (mesh 3)
3.e (10,4.0,-3.5) m	$6.224 \times 10^{-7}$ (mesh 4)	$5.320 \times 10^{-6}$ (mesh 9)
3.f (10,16,-3.5) m	$7.495 \times 10^{-9}$ (mesh 3)	$1.115 \times 10^{-7}$ (mesh 9)

## 6.3 Wyoming uplift simulation

In this section the full workflow for generating a mesh and simulating a complex model are demonstrated on a field-scale CO<sub>2</sub> storage project. The example geology and conceptual model are based on a potential CO<sub>2</sub> injection site that has been studied extensively by Stauffer et al. (2009), Deng et al. (2012) and Harp et al. (2017). A different part of the uplift is used in the present study, along with simplifications to allow for studying meshing the geological structure.

### 6.3.1 Meshing

The surfaces for input are assumed to be available as height maps on regularly spaced grids as this is the format generated by geological mapping software. A slice of the Rock Springs uplift in Wyoming from EarthVision (Dynamic Graphics, 2021) commercial software is shown in Figure 6-15.

To mesh a simulation domain containing only part of the structure, the geological surfaces are trimmed to the area of interest and encapsulated into a single volume with watertight intersections between all surfaces. Using LaGriT software, three surfaces representing the top Phosphoria caprock, top Weber Sandstone reservoir and top Madison limestone are preserved and clipped to an approximately 20km by 20km box. A flat bottom surface is created in the crystalline basement. The selected area is shown on the top of Figure 6-16. The simulation domain includes one flank of the uplifted structure, where CO<sub>2</sub> will be injected and the crest where the CO<sub>2</sub> is expected to migrate and pool.

In most of the domain it is desirable to have the mesh as coarse as possible to reduce the number of grid cells and thus computation time. In the entire Phosphoria overburden and crystalline basement underburden Vorocrust is allowed to mesh as coarsely as possible. As can be seen in the center subfigure of Figure 6-16 the resulting mesh is very coarse in places, particularly in the crystalline basement. A moderately refined mesh is desired throughout the Weber sandstone storage interval. In the simulation domain the Weber is only 100-200m thick and largest grid cell radius allowable by the meshing algorithm is 50 to 100m, or around half the layer thickness. This was felt to be sufficient away from CO<sub>2</sub> plume.

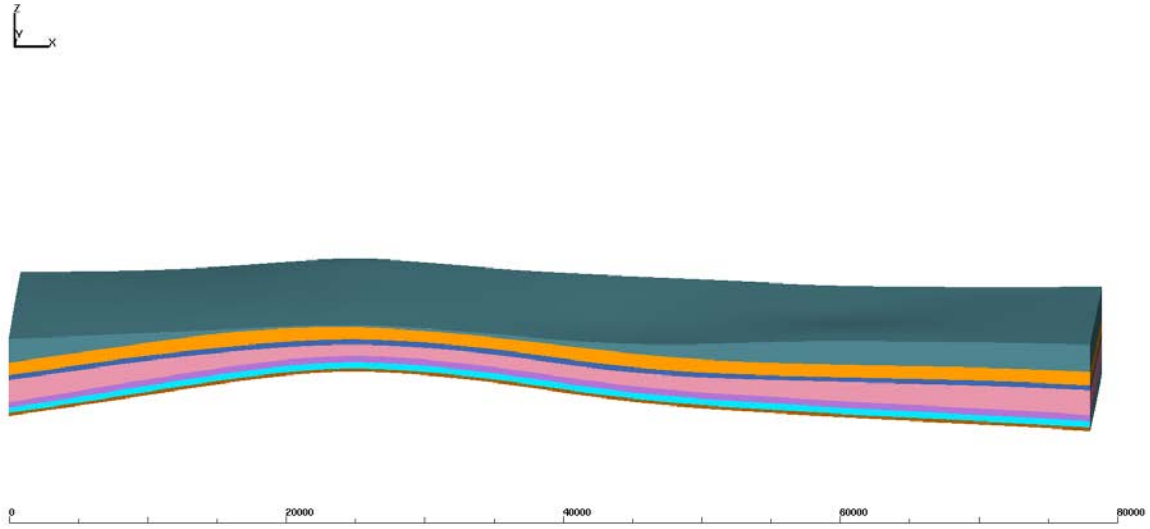


Figure 6-15 Geological surfaces for the Rock Springs uplift from geological mapping software.

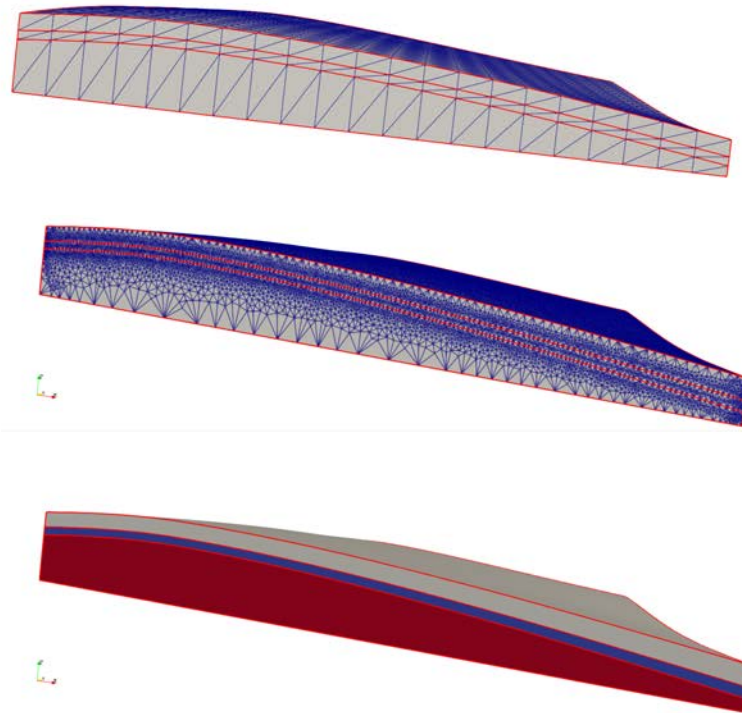


Figure 6-16 Top: Clipped region containing only the Phosphoria top, Weber top, and Madison top surfaces integrated into a water-tight volume with a flat base. Middle: Surface mesh of the reservoir. Bottom: Reservoir layers colored by material type. The Phosphoria caprock is shown in gray, Weber sandstone injection interval is blue and crystalline basement is red.

### 6.3.1.1 *Local grid refinement*

A simulation of the proposed injection scheme was run to 100 years to see where the plume traveled. The plume was limited to the area shown in the darker 'L' shape shown on the bottom left of Figure 6-17. The area in the 'L' is the location of desired refinement.

Using the top Weber geological surface, a series of points spaced approximately 300 m apart in x and y were defined covering the predicted plume area at the top of the Weber reservoir. The refinement can be seen for the whole top Weber and near the wells in Figure 6-17. The desired maximum radius at each point was defined based on the x-distance from the injection wells. The area immediately around the wells was refined to a maximum cell radius of 20 m, gradually increasing to a maximum of 50 m along the top of the structure. Radius was increased gradually in increments of 3 to 5 m at a time, as large changes in mesh refinement were observed to bias simulation results. The mesh coarsening up and down dip of the injection wells can be seen on the bottom right of Figure 6-17.

Two parallel surfaces with maximum cell radius 10,000 m to allow for the coarsest possible mesh were defined in the Phosphoria, 40 m above and in the Weber sandstone, 120 m below the Weber top surface. This prevented the automatic mesh refinement algorithm from refining the mesh outside the immediate vicinity of the Weber top surface. The refined mesh along the top Weber with coarsening above and below can be seen in the y-slice shown in Figure 6-18. The mesh is finest at the top Weber and coarsens both downward and upward into the other formations.

Refined regions were also defined near each of the injection wells (18500, 8500, -1390) m, (18500, 9500, -1390) m, (19500, 8500, -1515) m and (19500, 9500, -1515) m to a depth of 50-55 m below the well completion. The injection wells are shown as red circles in Figures 6-18 and 6-19. Figure 6-19 shows that the refined region extends further down into the Weber sandstone at and between the wells, to allow for more accurate modelling of the CO<sub>2</sub> plume in the near-well region and as it travels vertically up to the caprock. The resultant mesh has 762,763 grid cells.

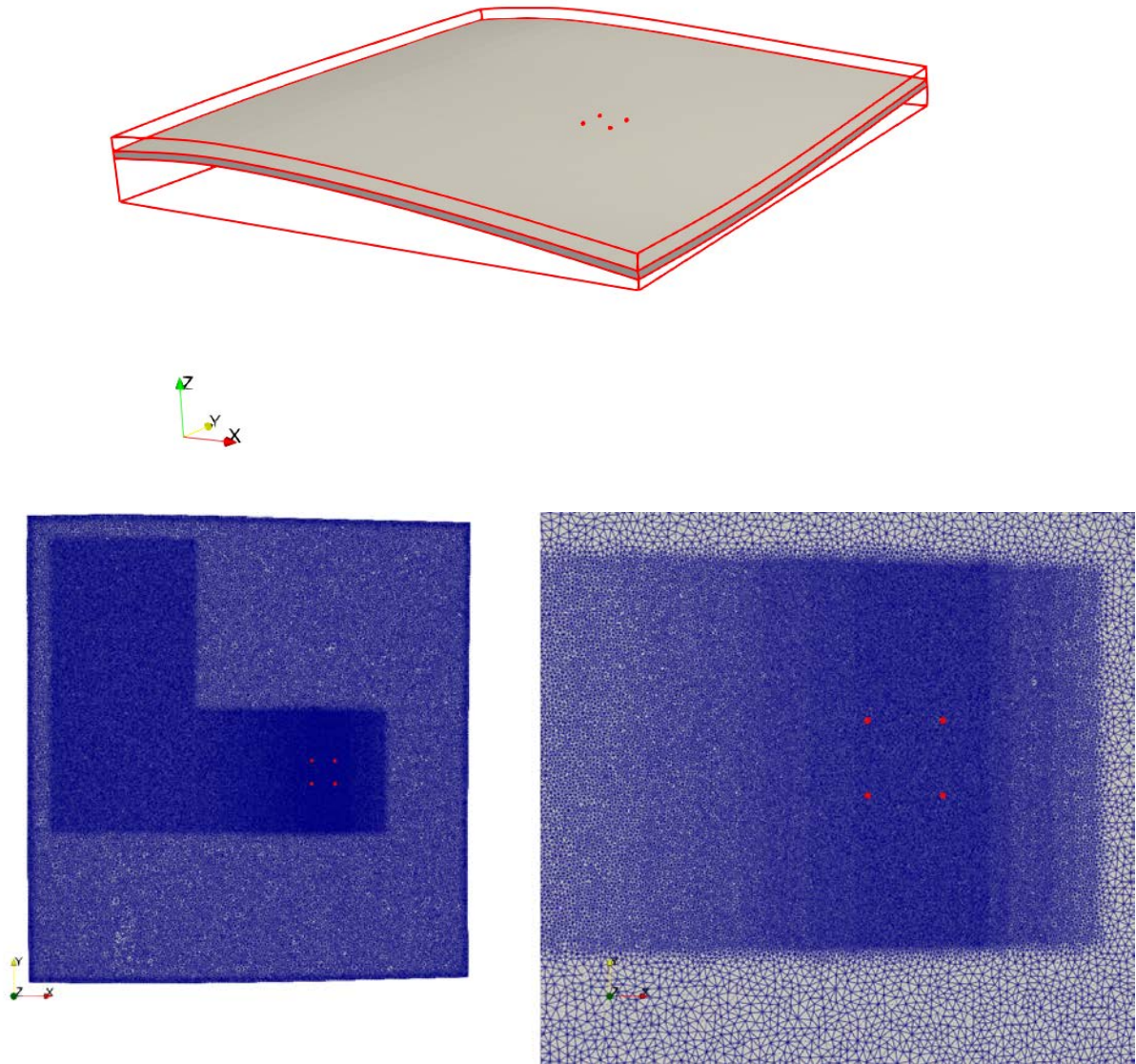


**Figure 6-17 Top: isometric view of the Weber sandstone in the full simulation model. Bottom Left: Top mesh for the full Weber sandstone layer. Bottom Right: Top mesh for the Weber sandstone layer near the injection wells showing finely refined region gradually coarsening away from the wells. Injection wells are shown as red circles on all subfigures.**

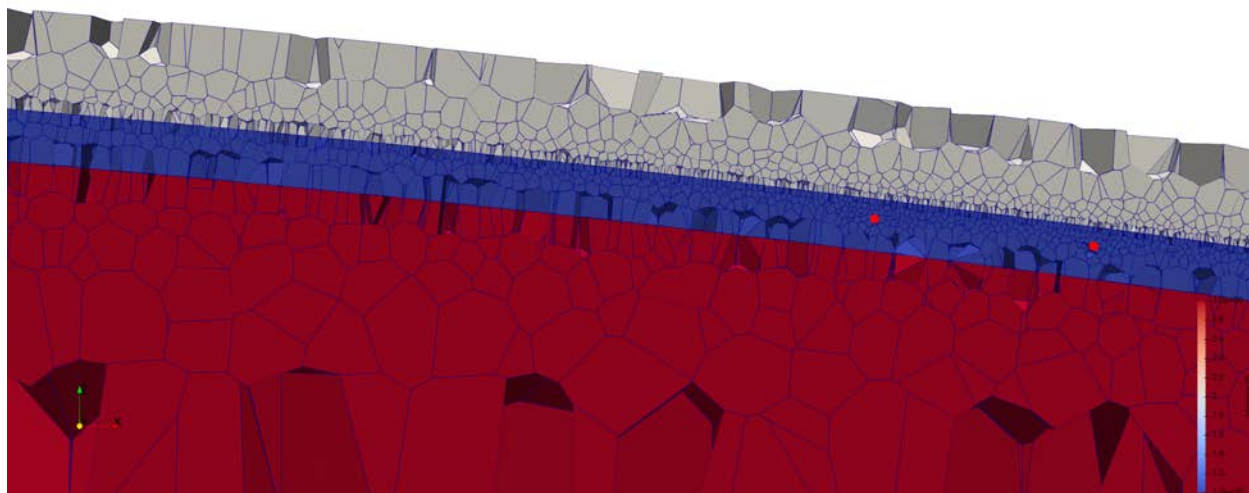


**Figure 6-18** Slice through two of the injection wells at  $y = 8500$  m showing the refined mesh near the wells. The Phosphoria caprock is shown in gray, Weber sandstone injection interval is blue and crystalline basement is red. Injection well locations are shown as red circles.

### 6.3.1.2 Simulation implementation

The permeability and porosity of the regions are taken to be the mean of the high case from Deng et al. (2012), as shown in Table 6-8. Within each region the properties are homogeneous. The vertical to horizontal permeability of the Weber and crystalline basement are 0.1, while for the Phosphoria the ratio is 0.001, to prevent vertical intrusion of  $\text{CO}_2$  into the overburden. The high case was chosen so that only 4 injection wells at 1 km spacing were required to inject  $\text{CO}_2$  at the desired rate of 10 kg/s into each well, for a total of 1.26 million metric tons per year for 100 years. Water is also injected in each well at a rate of  $1 \times 10^{-5}$  kg/s to prevent dryout. Each well is assumed to be a point source in the reservoir and no explicit well model is used. The simulations are isothermal. These simplifications from the cases considered in Stauffer et al. (2009), Deng et al. (2012) and Harp et al. (2017) speed up the simulation and allow study of the impact of meshing and the geological structure.

The relative permeability parameters for the simulation model are the same in each rock type and are shown in Table 6-9. The van Genuchten capillary pressure curve and the Mualem-van Genuchten relative permeability curves are used with the residual saturations taken from Deng et al. (2012). These proved to be faster to simulate in PFLOTRAN than the linear curves used in Deng et al. (2012) due to the way they are implemented in PFLOTRAN (Nole et al. 2021).

The small and large  $x$  boundaries are open to flow and assigned initial reservoir properties. The large and small  $y$  boundaries are closed to represent sealing faults on either side of the structure. These fault seals are not present in the original geological model and are introduced so that  $\text{CO}_2$  will pool at the top of the structure instead of migrating out of the model updip in the positive  $y$  direction.

Due to the complexity of simulating two-phase flow on highly unstructured Voronoi meshes, new experimental solvers were also used in the simulation. A novel Newton solver that has recently been implemented into PETSC and PFLOTRAN called Newton Trust-Region Dog-Leg (Park et al. 2021; Nole et al. 2021) is used. NTRDC is more capable of resolving complex nonlinear constitutive models than traditional Newton-Raphson solvers. The linear solver used is the newly implemented Flexible

Generalized Minimum Residual (FGMRES) with constrained pressure residual (CPR) conditioner using the alternate-block factorization (ABF) decoupler. The combination of FGMRES, CPR, and ABF seems to be effective for simulation domains with large contrast in permeability and unstructured grids. These solver options are also discussed Section 5 on the unsaturated alluvium PA model and in more detail in Nole et al. (2021).

**Table 6-8 Rock parameters for the Rock Springs Uplift example.**

Formation	Phosphoria (caprock)	Weber Sandstone (reservoir interval)	Crystalline basement (underburden)
Horizontal permeability (m <sup>2</sup> )	$1.2603 \times 10^{-15}$	$3.3300 \times 10^{-12}$	$1.000 \times 10^{-18}$
Vertical permeability (m <sup>2</sup> )	$1.2603 \times 10^{-18}$	$3.3300 \times 10^{-13}$	$1.000 \times 10^{-19}$
Porosity (-)	0.1015	0.2488	0.0100

**Table 6-9 Fluid flow parameters for the Rock Springs Uplift example.**

	Capillary pressure	Liquid phase	Gas phase
M (-)	0.2	0.6	0.6
$\alpha$ (1/Pa)	0.5	N/A	N/A
Liquid residual	0.1	0.1	0.1
Gas residual	N/A	N/A	0.1

### 6.3.1.3 Rock Springs uplift simulation results

The liquid saturation in the Weber Sandstone is shown in Figures 6-19 and 6-20. The CO<sub>2</sub> travels updip in the negative x-direction to top of the anticline structure at early time. At 10 years the CO<sub>2</sub> has begun to pool in a local high point in the structure, and by 20 years (not shown) it is visibly migrating in the positive y-direction towards the highest point in the anticline, which is at the top (largest-y) in the model. Migration in the y-direction is slower and much more uniform because the incline is very small compared to the flank of the structure, as can be seen in Figure 6-17. By 50 years (not shown) the CO<sub>2</sub> is pooling against the sealing fault at the top of the structure, and the structure fills downward until 100 years, at the end of the simulation.

The CO<sub>2</sub> saturation on the flank of the anticline is never high, due to the relatively rapid flow of CO<sub>2</sub> in a thin plume towards the crest of the structure, as can be seen in Figure 6-19. Once the CO<sub>2</sub> reaches a local highpoint in x the saturation increases until the gas spills into the next, higher point in the structure. Finally, the gas fills the structure downward, back towards the injection wells.

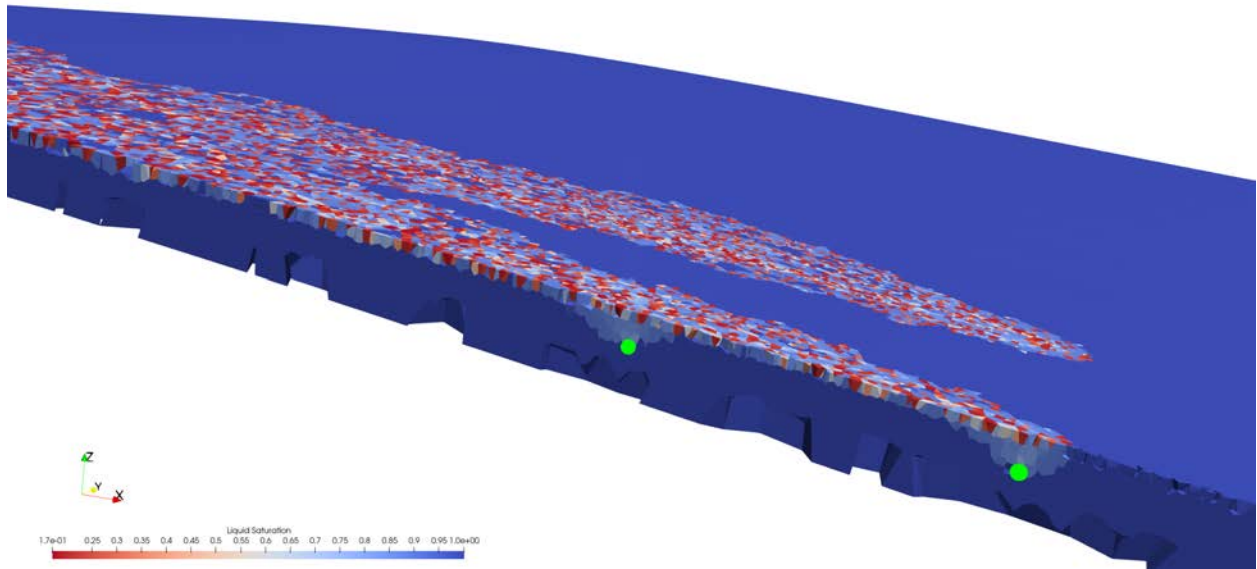


**Figure 6-19 Isometric view of the liquid saturation in the Weber sandstone after 10 years of injection. Only the Weber formation is shown and slice is at  $y = 8500$  m. Green circles mark two of the well locations, which are 1 km apart.**

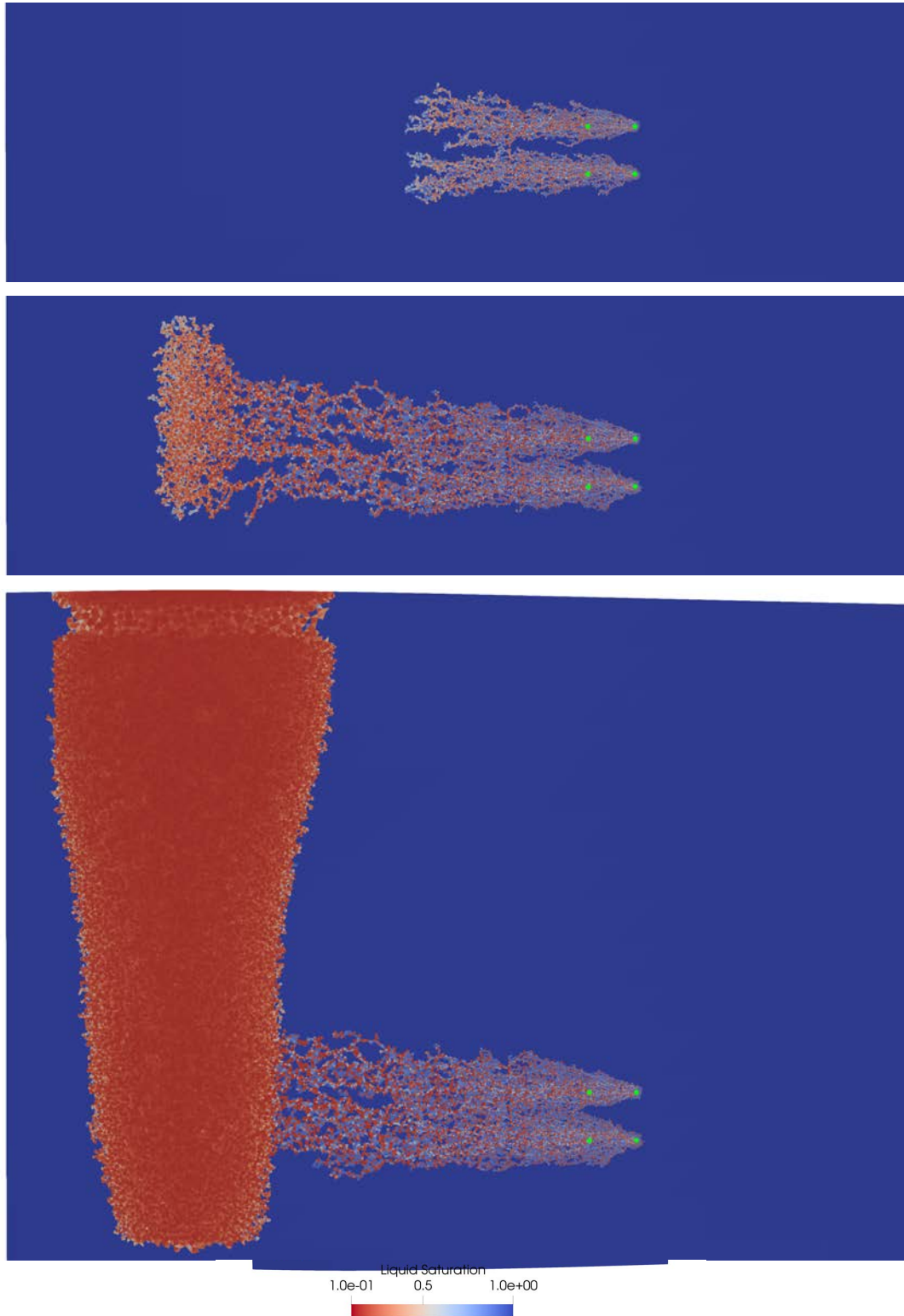


**Figure 6-20** Top view of the liquid saturation at the top of the Weber Sandstone. Green circles mark well locations. Top: 2.5 years of CO<sub>2</sub> injection. Middle: 10 years. Bottom: 100 years.

#### **6.3.1.4 Rock Springs uplift conclusions and observations**

The buoyancy-driven flow of CO<sub>2</sub> under a small incline is an extremely difficult problem to solve numerically due to small pressure gradients in the flow field. The migration of CO<sub>2</sub> in this example is a viscous-unstable displacement and forms fingers, even in homogeneous media. Using structured meshes, these fingers are very difficult to model accurately because the uniformity of the grid smooths the gas invasion fronts. Due to random orientation of the grid cells, there is no such smoothing using the randomly generated Voronoi meshes, and gas fingering is observed from the first 2.5 years of injection, as shown in the top of Figure 6-20. The combination of the new PFLOTRAN solvers and the highly refined Voronoi mesh enable high-level resolution of the plume in the subsurface.

### **6.4 Conclusions and Future Work**

The long-term goal of the collaborative project presented in Section 6 is to develop a meshing tool that is open-source, flexible and well-suited for large-scale fluid flow simulations for integration in the GDSA Framework (<https://pa.sandia.gov/>). Building on the work of Sevougian et al. (2019) and LaForce et al. (2020) and utilizing the recently implemented local grid-refinement capability of VoroCrust, significant progress has been made towards that goal this year.

Sixteen benchmark simulations were completed on meshes of four common reservoir structures (layering, pinch-out, interior lens, and offset fault). Five simulation results have compared with analytical solutions and three quantitative error analyses have been conducted on the benchmark problems. The first analysis showed that intra-mesh error is generally small, indicating high mesh quality. The second analysis demonstrated that simulation results are reliable when the mesh is sufficiently refined. The final analysis demonstrated that mesh realizations and simulation results on them are very similar in terms of size, computation time and simulation result, which indicates high consistency across mesh realizations.

An example of CO<sub>2</sub> storage in the subsurface is also presented. Though not of direct interest to GDSA, this example demonstrates the capability of the presented workflow to mesh subsurface features from geological mapping software with a realistic scale and level of complexity and run numerically challenging simulations on the resultant meshes.

#### **6.4.1 Future PFLOTRAN/VoroCrust integration studies**

Two integration studies that would demonstrate the suitability of VoroCrust meshes in problems of practical interest for GDSA which are proposed for the near future are:

- Complete the near-DPC thermal study initiated in Jones et al. (2021) using VoroCrust meshes for the unsaturated alluvium model, as flexed hexagonal meshes show clear grid-orientation effects for this case (See Section 3.2).
- Create a simplified PA-scale model and run a SA/UQ analysis that includes mesh resolution and/or geological structure uncertainty in the sampled parameters.

#### **6.4.2 Future VoroCrust development**

Two additional developments in VoroCrust need to be achieved before it can be integrated into the GDSA Framework, both of which are research goals for the near future are:

- An open-source version of VoroCrust will be developed that is available to users outside of the National Laboratories.
- Addition of the ability to explicitly add Voronoi cells representing waste packages and have the mesh conform to them, but not mesh within them in order to simulate individual waste packages at the PA-scale.

Other desirable VoroCrust capabilities would be to mesh faults that terminate within the model, always retain user-specified monitoring points in the final mesh, and anisotropic Voronoi meshing to significantly reduce the number of grid cells in thin layers.

## 6.5 References

- Abdelkader A., Bajaj C.L., Ebeida, M.S., Mahmoud, A.H., Mitchell, S.A., Owens, J.D., Rushdi, A.A. 2018. *Sampling conditions for conforming Voronoi meshing by the VoroCrust algorithm*. Leibniz international proceedings in informatics. 99.
- Abdelkader A., Bajaj C.L., Ebeida, M.S., Mahmoud, A.H., Mitchell, S.A., Owens, J.D., Rushdi, A.A. 2020. *VoroCrust: Voronoi meshing without clipping*. ACM Transactions on Graphics (TOG). 39(3):1–16.
- Ahrens, J., Geveci, B., Law, C. 2005. *ParaView: An End-User Tool for Large Data Visualization*. Visualization Handbook. Elsevier.
- Deng, H., Stauffer, P.H., Dai, Z., Jiao, Z., Surdam, R.C. 2012. *Simulation of industrial-scale CO<sub>2</sub> storage: Multiscale heterogeneity and its impacts on storage capacity, injectivity and leakage*. International Journal of Greenhouse Gas Control. 10:397–418.
- Dynamic Graphics I. 2021. EarthVision. [https://www.dgi.com/earthvision/evarticles/ev\\_articles.html](https://www.dgi.com/earthvision/evarticles/ev_articles.html).
- Gross, M., Bussod, G., Gable, C., Kelley, R., Lavadie-Bulnes, A., Milazzo, D., Miller, E., Miller, T., Roback, R., Stauffer, P.H., and Swanson, E. 2019. *Progress report on the development of a geologic framework model capability to support GDSA*. Technical Report LA-UR-19-27943, Los Alamos National Lab., Los Alamos, NM.
- Harp, D.R., Stauffer, P.H., O'Malley, D., Jiao, Z., Egenolf, E.P., Miller, T.A., Martinez, D., Hunter, K.A., Middleton, R.S., Bielicki, J.M., et al. 2017. *Development of robust pressure management strategies for geologic CO<sub>2</sub> sequestration*. International Journal of Greenhouse Gas Control. 64:43–59.
- LaForce, T., Chang, K.W., Perry, F., Lowry, T.S., Basurto, E., Jayne, R.S., Brooks, D.M., Jordan, S.H., Stein, E., Leone, R.C., et al. 2020. *GDSA Repository Systems Analysis investigations in FY2020*. Technical report. Sandia National Lab.(SNL-NM). Albuquerque, NM.
- Lichtner, P.C., Hammond, G.E., Lu, C., Karra, S., Bisht, G., Andre, B., Mills, R.T., Kumar, J., Frederick, J.M. 2020. *PFLOTRAN Web page*. <http://www.pflotran.org>.
- Los Alamos National Laboratory. 2017. *Los Alamos grid toolbox, LaGriT*. <http://lagrit.lanl.gov>.
- Los Alamos National Laboratory. 2018. *Finite element heat and mass transfer code, FEHM*. <https://fehmlanl.gov/>
- Nole, M., Leone, R.C., Park, H.D., Paul, M., Salazar, A., Hammond, G.E., and Lichtner, P.C. 2021. *PFLOTRAN Development FY2021*. SAND2021- 8709 R. Sandia National Laboratories, Albuquerque, New Mexico, July 21, 2021.

- Park, H.D., Hammond, G.E., Valocchi, A.J., LaForce, T. 2021. *Linear and nonlinear solvers for simulating multiphase flow within large-scale engineered subsurface systems*. *Advances in Water Resources, to appear*.
- Sevougian, S., Stein, E., LaForce, T., Perry, F., Nole, M., and Chang, K. 2019. *GDSA Repository Systems Analysis FY19 update*. Technical Report SAND2019-11942 R. Sandia National Lab.(SNL-NM) Albuquerque, NM.
- Stauffer, P.H., Surdam, R.C., Jiao, Z., Miller, T.A., Bentley, R.D. 2009. *Combining geologic data and numerical modeling to improve estimates of the CO<sub>2</sub> sequestration potential of the rock springs uplift, Wyoming*. *Energy Procedia*. 1(1):2717–2724.